



Making galaxies passive
Insights from resolved studies of nearby galaxies

Miguel Querejeta
Max-Planck-Institut für Astronomie



Heidelberg 2016

Dissertation in Astronomy
submitted to the
Combined Faculties of the Natural Sciences and Mathematics
of the Ruperto-Carola-University of Heidelberg, Germany,
for the degree of
Doctor of Natural Sciences

Put forward by
Miguel Querejeta
born in Donostia-San Sebastián, Spain

Oral examination: 25.05.2016



Making galaxies passive
Insights from resolved studies of nearby galaxies

Miguel Querejeta
Max-Planck-Institut für Astronomie



Referees: Prof. Dr. Hans-Walter Rix
Dr. Simon Glover

A mis padres

Wie, hör' ich das Licht?

RICHARD WAGNER: *Tristan und Isolde*

Abstract

The rapid suppression of star formation, or quenching, is thought to be an important process in the evolution of the most massive galaxies, but the mechanisms involved are still hotly debated. Here, we consider two agents that control star formation and can ultimately lead to its suppression: AGN feedback and galaxy mergers.

In the first part of the thesis, we study the interplay between stellar structure, nuclear activity, and molecular gas in the context of AGN feeding and feedback. We start presenting our catalogue of stellar mass maps for more than 1500 nearby galaxies, which has been publicly released. Using the stellar mass map of the spiral galaxy M51, we show that there is sufficient molecular gas inflow to feed the AGN ($\sim 1 M_{\odot}/\text{yr}$), and feedback effects which include a nuclear molecular outflow (at a rate comparable to the inflow), as well as a large-scale radio jet which pushes molecular gas laterally, inducing shocks and turbulence.

In the second part, we address the role of galaxy mergers in the buildup of a passive population of lenticular galaxies (or S0s). While lenticulars are the most common early-type galaxies in the Universe, their formation channels remain elusive. We use numerical simulations to show that even major mergers of spiral galaxies can result in lenticulars, with a bulge-disc coupling in agreement with observations. We also find that major mergers can simultaneously account for the difference in angular momentum and concentration between spirals and S0s, as recently found by the CALIFA team.

Globally, our results show that both internal processes (transport of gas and AGN feedback) and external mechanisms (mergers) have the ability to regulate and eventually suppress star formation in galaxies. Current and future instrumental advancements (ALMA, NOEMA, JWST) will permit to confirm our findings with other galaxies and further assess their relative importance.

Zusammenfassung

Die rasche Abnahme der Sternentstehung („quenching“) ist ein wichtiger Prozess in der Entwicklung der massereichsten Galaxien, aber die verantwortlichen Mechanismen sind nach wie vor heiß umstritten. In dieser Dissertation betrachten wir zwei Prozesse, die die Sternentstehung regulieren und deren Abnahme ermöglichen: AGN-Feedback und die Verschmelzung von Galaxien.

Im ersten Teil der Dissertation untersuchen wir das Wechselspiel von stellarer Verteilung, nuklearer Aktivität, und molekularem Gas. Zuerst wird unser Katalog von Sternmassenkarten beschrieben. Danach zeigen wir anhand der Sternmassenkarte der Spiralgalaxie M51, dass genügend Gas Richtung Zentrum fließt, um den AGN zu füttern ($\sim 1 M_{\odot}/\text{yr}$). Anschließend folgt eine Beschreibung der Entstehung des großen Feedback-Effekts durch große Radiojets, die das molekulare Gas zur Seite drücken und Schocks sowie Turbulenzen zur Folge haben.

Im zweiten Teil beschäftigen wir uns mit der Rolle von großen Galaxienverschmelzungen („major mergers“) bei der Entstehung der Lentikulargalaxien (oder „S0s“). Lentikulargalaxien sind die häufigste Form der so genannten „early-type galaxies“ des lokalen Universums, doch ihre Entstehungsweise ist immer noch ungeklärt. Das Scheiben-zu-Bulge-Verhältnis wurde als Argument gegen eine Entstehung durch Verschmelzungen benutzt. Mithilfe numerischer Simulationen zeigen wir jedoch, dass sogar „major mergers“ S0s produzieren können, die dem richtigen Verhältnis entsprechen. Zudem können solche „major merger“ Simulationen die kinematischen Unterschiede von Spiral- und Lentikulärgalaxien erklären.

Insgesamt zeigen unsere Ergebnisse, dass die beiden internen Prozesse (der Transport von Gas und AGN-Feedback) und auch externe Mechanismen (Galaxienverschmelzungen) die Regulierung und Abnahme der Sternentstehung ermöglichen. Gegenwärtige wie zukünftige Instrumente (ALMA, NOEMA, JWST) werden unsere Ergebnisse und deren Bedeutung bestätigen können.

Acronyms

ACS:	Advanced Camera for Surveys
AGB:	Asymptotic giant branch
AGN:	Active galactic nucleus
ALMA:	Atacama Large Millimeter/submillimeter Array
CALIFA:	Calar Alto Legacy Integral Field Area survey
CR:	Corotation
ETG:	Early-type galaxy
FFT:	Fast Fourier transform
FR:	Fast rotator
FWHM:	Full width at half maximum
GMC:	Giant molecular cloud
HERACLES:	HERA CO Line Extragalactic Survey
HST:	Hubble Space Telescope
IC:	Index catalogue
ICA:	Independent component analysis
ILR:	Inner Lindblad resonance
IMF:	Initial mass function
IR:	Infrared
IRAC:	Infrared Array Camera
IRSA:	NASA/IPAC infrared science archive
ISM:	Interstellar medium
JWST:	James Webb Space Telescope
LINER:	Low-ionisation nuclear emission-line region
LMC:	Large Magellanic Cloud
LTG:	Late-type galaxy
M/L:	Mass-to-light ratio
NED:	NASA extragalactic database
NGC:	New general catalogue
NIR:	Near-infrared
NIRCam:	Near infrared camera

NLR:	Narrow line region
NOEMA:	Northern Extended Millimeter Array
OLR:	Outer Lindblad resonance
PA:	Position angle
PAH:	Polycyclic aromatic hydrocarbon
PAWS:	PdBI Arcsecond Whirlpool Survey
PCA:	Principal component analysis
PdBI:	Plateau de Bure interferometer
PSF:	Point spread function
QSO:	Quasi-stellar object
RC3:	Reference catalogue 3
RSG:	Red supergiant
SDSS:	Sloan Digital Sky Survey
SED:	Spectral energy distribution
SF:	Star formation
SFH:	Star formation history
SFR:	Star formation rate
S⁴G:	Spitzer Survey of Stellar Structure in Galaxies
SMBH:	Supermassive black hole
S/N:	Signal-to-noise ratio
SPH:	Smoothed Particle Hydrodynamics
SR:	Slow rotator
SSC:	Short spacings correction
SSFR:	Specific star formation rate
SSP:	Simple stellar population
THINGS:	The HI Nearby Galaxy Survey
TiRiFiC:	Tilted Ring Fitting Code
UHR:	Ultraharmonic resonance
UV:	Ultraviolet
VLA:	Very Large Array
XNC:	Extra-nuclear cloud

Contents

1	Introduction	1
1.1	Star formation suppression and morphological transformations	2
1.2	AGN and their relation to quenching	5
1.3	Passive discs: the origin of lenticular galaxies	7
1.4	The key role of stellar mass	11
1.5	Quenching in the ALMA/NOEMA era	13
1.6	Scope of thesis: questions	14
2	Stellar mass maps for nearby galaxies	15
3	Molecular gas inflow in M51	35
4	AGN feedback in M51	55
5	Making discs passive with major mergers: photometry	77
6	Making discs passive with major mergers: kinematics	101
7	Summary and discussion	109

7.1	Conclusions of the thesis	109
7.1.1	An important observational tool: stellar mass maps	109
7.1.2	AGN feeding and feedback in M51	111
7.1.3	Creating lenticular galaxies with mergers	113
7.1.4	Towards an integral picture of star formation suppression in galaxies	115
7.2	Open questions and future perspectives	116
	Bibliography	119
	Acknowledgements	125

Chapter 1

Introduction

It is remarkable how much our understanding of galaxies and the structure of the Universe has evolved in the last century; after all, it was less than 100 years ago that galaxies were proven to be external to our own Milky Way. The number of known galaxies has greatly increased in this time, from a few thousand in the early catalogues compiled by John Louis Emil Dreyer (New General Catalogue and Index Catalogues, 1888-1908) to the more than 200 million galaxies identified so far by the Sloan Digital Sky Survey (SDSS, Data Release 12; Alam et al. 2015). Additionally, extrapolations from deep fields with the *Hubble* Space Telescope (HST) suggest that the number of galaxies in the observable Universe is at least $N \sim 10^{11}$ (Illingworth et al. 2013). It was also less than 100 years ago that the Universe was proven to be expanding (Hubble 1929), which quickly led to the establishment of the Big Bang theory (Lemaître 1927). The discovery of the cosmic microwave background (CMB; Penzias & Wilson 1965) strongly supports the Big Bang theory. From that initial explosion to the present day, the observable Universe has changed dramatically, giving rise to a wealth of structure which is composed of some basic units: galaxies.

A galaxy can be defined as a large collection of baryonic mass (stars, gas, dust, etc.) which is bound together by gravity and is sitting in the potential well of a dark matter halo. They are thought to have originated from the hierarchical buildup of matter in the early Universe, from small clumps due to quantum fluctuations which eventually got amplified; the anisotropies in the CMB provide the fossil record of these primordial fluctuations, and the incontestable probe of the Big Bang (Bennett et al. 1996). Since their infancy, galaxies have evolved to their present state by a number of different processes, both hierarchical and secular, as we will see later on.

The discovery that baryonic matter makes up only a small fraction of the total mass in the Universe has enormous implications for our understanding of the cosmos; for example, non-baryonic matter is invoked to explain the mismatch between virial mass and total light in galaxy clusters (Zwicky 1933), or the approximately flat rotation curves in spiral galaxies (Rubin & Ford 1970; Bosma 1978). Dark matter is now routinely implemented in cosmological simulations, which have triumphed in mimicking the large-scale structure of the Universe down to individual galaxies (e.g. Millennium simulation, Springel et al. 2005; Illustris simulation, Vogelsberger et al. 2014). Baryons are all we can detect observationally (although the possibility to detect gravitational waves now seems confirmed, opening up new possibilities; Abbott et al. 2016), but dark matter leaves its footprints on dynamics. Although we will assume Newtonian dynamics in the present thesis, it is fair to mention that alternative theories

of gravity exist in which dark matter can be avoided (e.g. MOND; Milgrom 1983; see also Famaey & McGaugh 2012 for a broad review on these alternative models).

One of the most fundamental challenges of modern astrophysics is understanding the process by which gas transforms into stars, and how this process is orchestrated in the context of galaxies and as a function of environment. Star formation regulates the interchange of energy between stars, gas, and dust, explains the chemical enrichment of the interstellar medium (ISM), and, overall, it can determine the structure and ultimate fate of a given galaxy. However, studying star formation in galaxies is challenging, as it involves multi-scale processes, and can only be successfully understood by combining observations across different wavelengths, ideally assisted by numerical simulations. In this thesis, we will consider two specific mechanisms that have the ability to control and suppress star formation in galaxies: feedback from an active galactic nucleus (AGN) and galaxy mergers. In the next pages, we introduce the context and a number of concepts which will be used in the thesis.

1.1 Star formation suppression and morphological transformations

At fixed stellar mass, galaxies are known to show a bimodality in terms of colour (Baldry et al. 2004; Brinchmann et al. 2004); in a colour-mass (or colour-magnitude) diagram, the relative scarcity of galaxies between the so-called *blue cloud* and *red sequence* has been recognised as evidence of the short timescales over which star formation is suppressed (Faber et al. 2007). This is illustrated by Fig. 1.1, which shows colour-mass diagrams based on $\sim 25\,000$ nearby galaxies imaged by the SDSS and morphologically classified by *Galaxy Zoo*, an online citizen science project (Lintott et al. 2008). The *green valley* at intermediate optical colours corresponds to an under-abundance of galaxies compared to the blue cloud and red sequence; this means that, as a population, galaxies cannot spend a long time in this intermediate stage, and this has led authors to conclude that the suppression of star formation, or *quenching*, must occur rapidly (~ 1 Gyr).

At the same time, Fig. 1.1 emphasises the strong correlation that exists between colour and morphology, suggesting an evolutionary connection: ellipticals and lenticulars (*early-type galaxies*, ETGs) tend to be passive and red, implying low degrees of star formation, as opposed to actively star-forming blue spirals and irregulars (*late-type galaxies*, LTGs). There are some interesting exceptions to this general trend which have been studied by the *Galaxy Zoo* team: blue ETGs (Schawinski et al. 2009) and passive red spirals (Masters et al. 2010), which could be transition objects.

It is important to state at this point that ETGs tend to have limited gas and dust masses *relative to their stellar mass*: it is not true that they are devoid of gas and star formation, and in fact some of them have cold gas reservoirs which are comparable, in absolute terms, to the amount of molecular gas present in the Milky Way (Young et al. 2011). ETGs also have inner components and peculiar kinematic features (e.g. kinematically decoupled cores; Krajnović et al. 2011); therefore, they are more complex than once thought.

Many processes have been proposed to explain how LTGs transform into ETGs, and to account

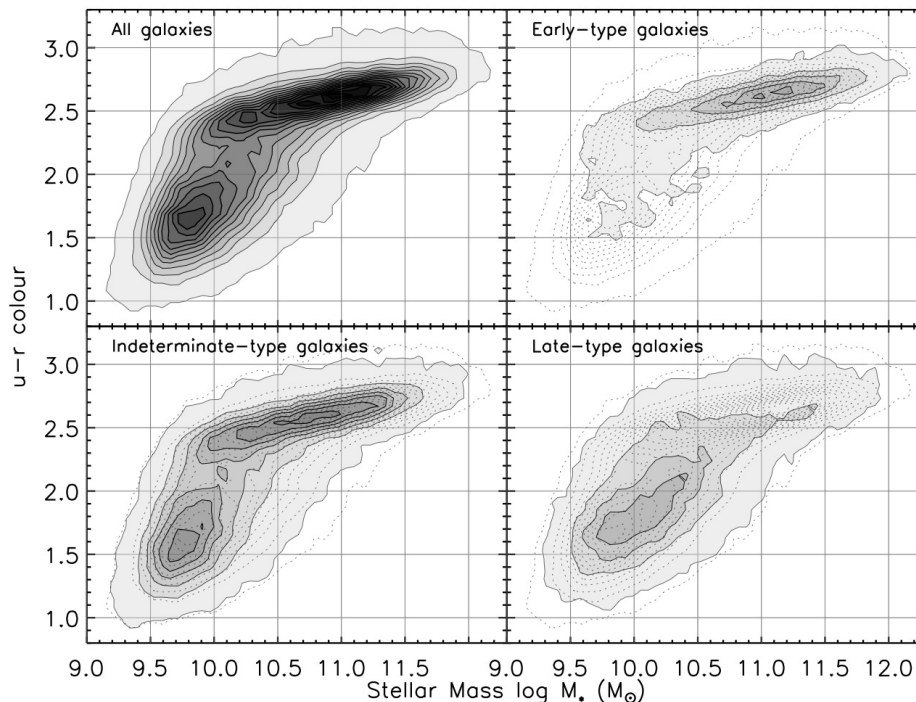


Figure 1.1: Four colour-stellar mass diagrams based on $\sim 25\,000$ nearby galaxies in the SDSS, according to the morphological classifications from the *Galaxy Zoo* project (adapted from Schawinski et al. 2014). The *blue cloud* covers the lower part of the plots, mostly in the range $u-r = 1.5-2$, and stands out in the bottom-right panel (among late-type galaxies); the *red sequence* appears in the upper part of the plots, essentially with $u-r = 2.5-2.7$ (clearly associated with early-type galaxies, top-right panel); the *green valley* covers the parameter space between these two groups, approximately around $u-r = 2-2.5$.

for the evolution of galaxies in general. Fig. 1.2, adapted from Kormendy & Kennicutt (2004), summarises some of the most important mechanisms proposed so far, with fast processes at the top, and slow processes at the bottom; the left-hand side reflects internal galactic mechanisms, while the right-hand side lists external (environmental) factors; in the centre, aspects common to all means of galaxy evolution appear. By *fast*, it should be understood that these processes span timescales comparable to a dynamical time (or free-fall time, $t_{\text{dyn}} \sim (G\rho)^{-1/2}$), whereas *slow* secular evolution operates over several galaxy rotation periods. From the observed scarcity of galaxies in the green valley and the idea that quenching must be quick, it follows that processes in the top-right corner should be dominant in the transformation from LTGs to ETGs (mergers, ram-pressure stripping¹). However, this is over-simplistic: on the one hand, even if the transition through the green valley is quick, this is only reflecting one property of galaxies (colour), and it does not rule out secular processes, either sequen-

¹We will introduce ram-pressure stripping, mergers, harassment, and other evolutionary mechanisms in Sect. 1.3, in the context of the origin of lenticular galaxies.

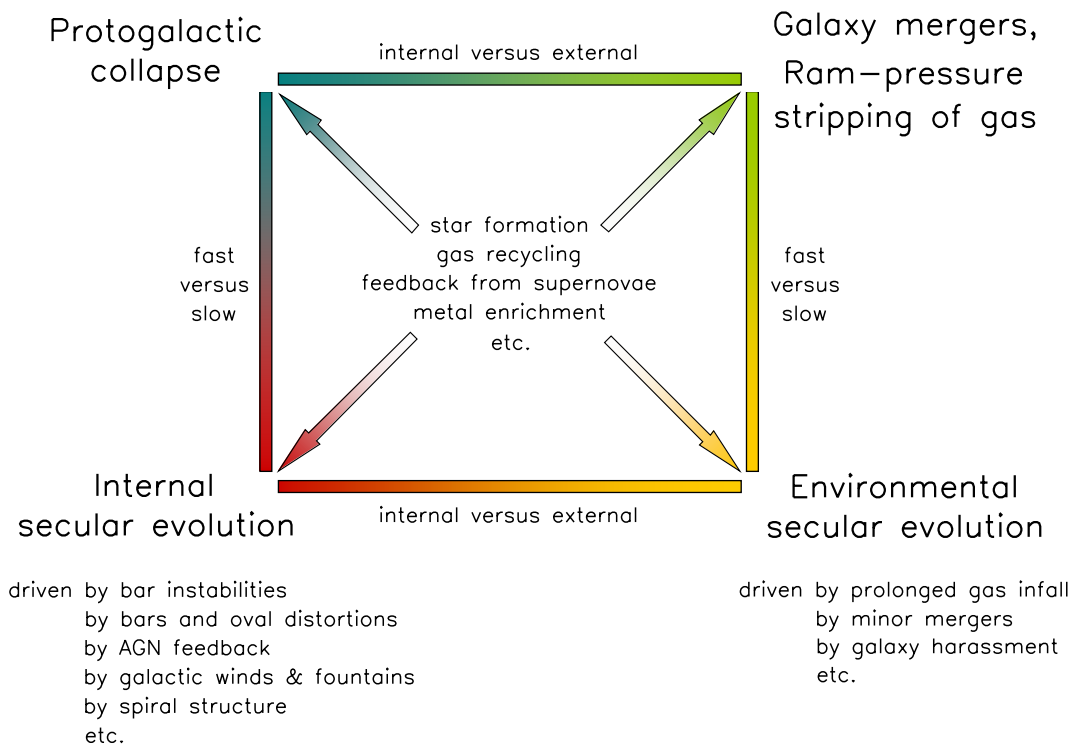


Figure 1.2: Diagram synthesising the most relevant galaxy evolution mechanisms, grouped vertically according to whether they are fast or slow, and horizontally depending on whether they are internal or external (adapted from Kormendy & Kennicutt 2004). In this thesis, we will focus on the top-right and bottom-left processes in the context of star formation suppression.

tially or in parallel to fast processes; on the other hand, internal processes such as AGN feedback² can be reasonably quick, so they should also be considered (as we will see in Chapter 4).

In essence, it is the suppression or enhancement of star formation (both locally and globally) that drives most of these evolutionary processes, most obviously in the quenching case (through sudden suppression of star formation). Star formation is thought to take place at the scales of giant molecular clouds (GMCs): there is a stronger correlation in galaxies between molecular gas surface density and star formation rates (SFRs; e.g. Bigiel et al. 2008) than between atomic gas surface density and SFRs (the well-known Schmidt-Kennicutt law; Schmidt 1959; Kennicutt 1998). There might be an even narrower correlation between star formation and the *dense* phase of molecular gas (for example, as traced by HCN; Gao & Solomon 2004; Liu et al. 2015), which suggests that it is in the cores of GMCs where the star formation process is most active. Contrary to the traditional view that GMCs have *universal properties* (Solomon et al. 1987; Bolatto et al. 2008), the PAWS survey of molecular gas in M51 has demonstrated that this is not the case, but rather the opposite: GMC properties strongly depend on the dynamical environment (Hughes et al. 2013b,a; Colombo et al. 2014), which has motivated a new paradigm for the dynamical regulation of star formation at GMC scales (Meidt et al.

²AGN feedback is introduced in detail in Sect. 1.2.

2013). Therefore, to understand the regulation of star formation in galaxies, it is important to study molecular gas in its interplay with stellar structure and, possibly, nuclear activity.

1.2 AGN and their relation to quenching

Active galactic nuclei are recognised as some of the most energetic sources of the Universe, with the potential to dramatically influence the evolution of their host galaxy: their bolometric luminosities are in the range of $10^5 - 10^{13} L_{\odot}$, in some cases sufficient to outshine their host (Robson 1996). Active nuclei also play a pivotal role in reconciling cosmological simulations with observations; specifically, AGN feedback is invoked to explain the lower stellar-to-total mass ratio in the halo of the most massive galaxies (Moster et al. 2010). Implemented this way, sufficiently strong baryonic feedback (in tandem with energy input from star formation in low-mass galaxies) can solve the most challenging problems that cosmological simulations have encountered (‘cooling flow’, ‘too big to fail’, ‘cusp-core problem’; see Springel 2010 for a review). However, it remains to be confirmed whether the strong feedback effects introduced *ad hoc* by simulators bear a direct connection with reality.

Simple arguments of variability timescales, radiative efficiency, and the spatial scales involved in AGN exclude nuclear fusion as their possible source of energy. Now, it is well accepted that transformation of gravitational energy into radiation must be the main mechanism responsible for producing these large luminosities, as the result of accretion of gas onto a central supermassive black hole (SMBH; Hoyle & Fowler 1963; Rees 1977). Indeed, most luminous galaxies in the local Universe have a SMBH (with mass $10^6 - 10^{10} M_{\odot}$; Ferrarese & Ford 2005; Gültekin et al. 2009); the fact that not all local galaxies host currently active nuclei could be explained as the result of variations in the availability of fuel, or changes in the efficiency with which the gravitational potential energy of the infalling gas is transformed into radiation.

AGN present themselves in a number of different flavours. The first difference is motivated by the width of the high-excitation optical emission lines found in the spectrum of the nuclear source. While Seyfert 1 galaxies³ show both broad and narrow emission lines, in Seyfert 2 galaxies only the narrow lines can be directly observed. A variant of Seyfert galaxies with emission lines arising from atoms which are not so strongly ionised is known as LINER (low-ionisation nuclear emission-line region; Heckman 1980). In both cases (LINER and Seyfert), in addition, radio emission can be associated with the nucleus, and typically also arises from plasma jets and extended structures (e.g. lobes, rings) which produce synchrotron emission. This justifies a further subdivision of the ‘AGN zoo’ into radio-loud and radio-quiet galaxies (Fanaroff & Riley 1974). Finally, quasars (quasi-stellar radio sources), QSOs (quasi-stellar objects), and BL Lacertae objects are extremely powerful AGN, in which the central source often outshines the host galaxy (Schmidt 1963; Stein et al. 1976).

According to the AGN unification model, all these manifestations can be explained as the result of the variation of a few intrinsic properties (mainly, luminosity and radio emission), and the viewing angle (Antonucci 1993). The differences between Seyfert 1 and 2 are thought to arise from the obscu-

³These galaxies are named after their discoverer, Carl Seyfert, who first described them back in the 1940s (Seyfert 1943).

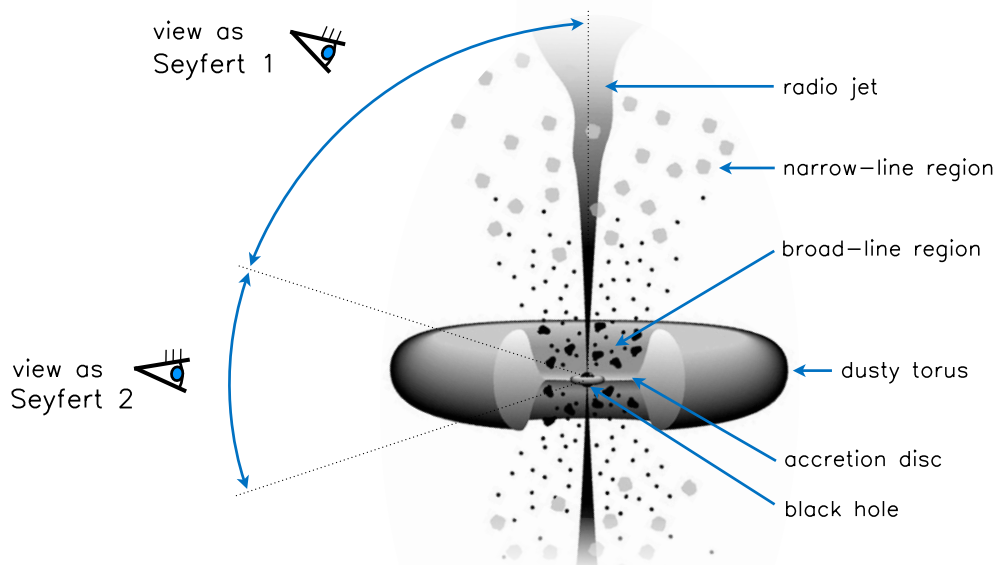


Figure 1.3: Diagram illustrating the unification model for AGN. Depending on the viewing angle, the same active galaxy appears as Seyfert 1, when both the narrow- and broad-line regions are directly visible, or as Seyfert 2, when the broad-line region is blocked by the obscuring torus (adapted from Urry & Padovani 1995).

ration of the innermost regions of the nucleus by a dusty torus which is preventing us from directly seeing the broad-line region in Seyfert 2 galaxies (see Fig. 1.3). This theory finds strong support in the observations of the broad-line region in polarised light in the Seyfert 2 case, which can be due to scattering of light by the dusty torus. The rest of the AGN types (radio galaxies, quasars, etc.) could result from details of the accretion process which are still not fully understood (e.g. amount of fuel available and its transport to small scales, radiative efficiency of the accretion process, coupling to magnetic fields). For more details, the reader is referred to the books by Robson (1996) and Osterbrock & Ferland (2006).

In this thesis, we will pay special attention to AGN feedback through radio jets. This type of feedback is known as the kinetic or radio mode (introduced by Croton et al. 2006, as opposed to the radiative or quasar mode; Fabian 2012), and it is naturally associated with radio-loud galaxies. The emission detected at radio-wavelengths must arise from a highly ionised plasma, which is typically strongly collimated when it leaves the nucleus (the ‘radio jet’), with velocities close to the speed of light. In some cases, these jets are seen to abruptly terminate in two lobes (e.g. Centaurus A), while in others the transition is more smooth, giving rise to a multitude of structures connected to the jet (e.g. M51, Crane & van der Hulst 1992). It is still unclear how exactly the accretion of gas to the central SMBH can produce these highly collimated radio jets, but it is believed that it must be a combination of thermal pressure, centrifugal forces, and the so-called Blandford-Znajek process (Blandford & Znajek 1977). The latter consist in a spinning black hole in a magnetic field which is anchored to the rotating accretion disc; it has been successfully implemented in numerical simulations

(e.g. Fendt & Sheikhnezami 2013). Only recently have simulators started to tackle the problem of the interaction of the expanding radio plasma with the interstellar medium of the host galaxy (e.g. Wagner et al. 2012; Cielo et al. 2014). The jet-ISM interaction is important, as it might hold the key to explain the outflows of gas which are observed in nearby and distant galaxies (involving ionised, atomic, and molecular gas; e.g. Ciccone et al. 2012); we will examine this in more detail later in this thesis (Chapter 4).

Another critical piece in the puzzle of AGN activity and its potential relation to star formation suppression is the transport of gas to the centre. Naturally, in the absence of fuel to power the central engine, feedback effects cannot be sustained in time; therefore, the ability of gas to flow towards the nucleus (*gas inflow*) can indirectly control any feedback effects. Studying the mechanisms that drive gas flows in galaxies affords the interesting possibility of connecting nuclear activity to the large-scale galaxy structure and secular processes. Dynamical regulation of the rates at which material is funnelled towards the AGN has been proposed as a mechanism to explain the connection between the nuclear SMBH and the stellar structure of the bulge; in particular, the tight scaling relations observed between the SMBH and bulge masses (Håring & Rix 2004), and between the mass of the SMBH and the stellar velocity dispersion of the bulge (Ferrarese & Merritt 2000). However, attempts to relate nuclear activity and gas flows have been fairly inconclusive so far (García-Burillo et al. 2007), possibly due to the different timescales involved, or partially because gas flows are very difficult to quantify observationally, as we will see in detail in Chapter 3.

1.3 Passive discs: the origin of lenticular galaxies

Disc-dominated lenticular galaxies represent the majority of early-type galaxies in the local Universe (71.4% of ETGs in RC3; de Vaucouleurs et al. 1991); therefore, far from being exceptional examples, they constitute one of the most important end-products of galaxy evolution. They have some transversal properties, in the sense that they share with elliptical galaxies red colours and low levels of star formation (relative to their stellar mass), while they contain large-scale galactic discs, in analogy to spiral galaxies. In this sense, they have long been regarded as a transition class (Hubble 1936), to the point that they might constitute a *Rosetta stone* of galaxy evolution, holding important information to understand how galaxies transform from late to early morphological types. However, in spite of their cosmological relevance, the evolutionary tracks that lead to lenticular galaxies are still poorly characterised.

A number of arguments suggest that, generally speaking, spirals must be the progenitors of lenticular galaxies. We know that at high redshift the gas content of galaxies was much larger than in the local Universe (Genzel et al. 2015; Popping et al. 2015); in the past, the incidence of discs was also higher (van der Wel et al. 2011), presumably associated with spiral morphologies (Wuyts et al. 2011). Therefore, in general terms, evolution is expected to proceed from LTGs to ETGs (Gonçalves et al. 2012; Moustakas et al. 2013).

Three independent studies have recently brought further attention to the similarity in properties

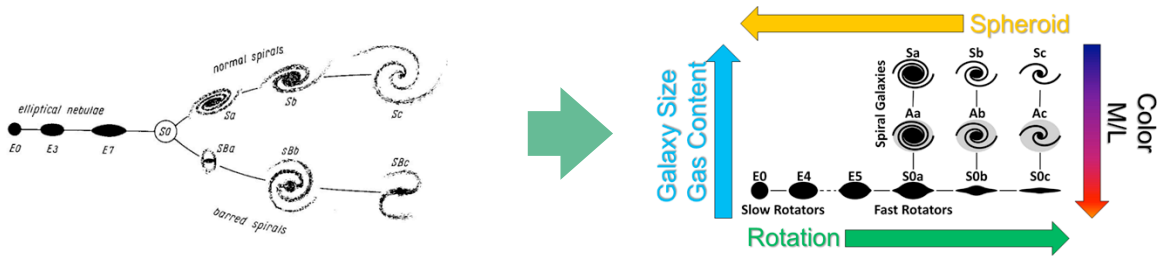


Figure 1.4: *Left*: Traditional Hubble tuning fork diagram, depicting S0 galaxies between ellipticals and spirals (Hubble 1936). *Right*: ATLAS^{3D} comb, reflecting the change in our understanding of S0s, now forming a whole sequence parallel to that of spirals (Cappellari et al. 2011a,b).

between spiral and lenticular galaxies. Lenticulars cover a large range of bulge-to-disc luminosity ratios (Laurikainen et al. 2010; Kormendy & Bender 2012), and their rotational support also takes a range of values similar to that spanned by spiral galaxies (Cappellari et al. 2011b). To reflect these morphological and dynamical differences among S0s, a modification to Hubble’s tuning fork diagram has been proposed by these authors, in which lenticulars are subdivided into S0a, S0b, and S0c, and they are placed in parallel to spirals (see Fig. 1.4). This idea had already been proposed by Spitzer & Baade (1951) and van den Bergh (1976), and, altogether, it triggers the question as to what extent the parallelism in properties between spirals and lenticulars is reflecting an underlying genetic connection: are lenticular galaxies *faded* spirals?

While there is ample consensus that elliptical galaxies form through mergers of discs (which simultaneously quench star formation and give rise to a predominantly spheroidal component, e.g. Toomre 1977; Schweizer et al. 1990), the origin of lenticular galaxies remains a controversial topic. A number of theories have been put forward to explain their formation, but tension exists both in terms of observations and simulations, with a number of puzzling and even conflicting results. Next, we will summarise the most successful mechanisms proposed so far and the observations that support them.

Arguably, the most popular process invoked to explain the emergence of lenticular galaxies is *ram-pressure stripping*, which is thought to play an important role in the dense environment of galaxy clusters. As a spiral galaxy enters a cluster, the intracluster medium can create hydrodynamical (ram) pressure which is high enough to expel most of the interstellar medium of the infalling galaxy (Gunn & Gott 1972). Deprived of the fuel to form new stars, the galaxy will undergo a rapid quenching of its star formation, and the stellar populations will gradually age. Provided that, on average, discs in spiral galaxies are composed of younger stars than bulges, the fading of the stellar populations will eventually lead to higher bulge-to-disc luminosity ratios; at the same time, the lack of gas is expected to lead to the disappearance of spiral arms, and result in a reasonably smooth disc. However, this mechanism is not expected to affect the stellar kinematics or other structural properties of the progenitor galaxy.

Along similar lines, the so-called *strangulation* might also account for the transformation from spiral into lenticular morphological types (Larson et al. 1980). It relies on the removal of the large-

scale reservoir of gas from the halo of the galaxy, which would have a slower, more gradual impact on star formation (because the gas in the galaxy would be retained, and only the reservoir for *future* gas supply would be eliminated; see also Bekki et al. 2002). Similarly to ram-pressure stripping, strangulation is also a simple fading mechanism, but the main difference is that it operates over longer timescales.

Another alternative that has been proposed is *harassment* as the result of repeated tidal interactions, which are expected to be very frequent in the cluster regime (Moore et al. 1996), but can also be relevant in galaxy groups. Harassment could occur either by the tidal interaction exerted by the cluster gravitational potential, or by close encounters with companions in the group or cluster (Bialas et al. 2015). As opposed to the mechanisms introduced above, harassment could suppress star formation, resulting in fading, but it could also imprint some dynamical signatures on the host galaxy. Tidal torques can also result in significant gas inflow, which can subsequently trigger nuclear starburst or AGN activity (see Chapter 3).

Mergers have also been considered as mechanisms that can give rise to S0s (Bekki 1998; Bournaud et al. 2007). As opposed to the simple fading mechanisms, mergers would be especially relevant in the context of galaxy groups; in massive galaxy clusters, the relative velocities are too high for merging (Eliche-Moral et al. 2012), but mergers could play a role in pre-processing galaxies before they enter the cluster domain (Vijayaraghavan & Ricker 2013). So far, minor and intermediate mergers⁴ have been considered, both isolated and as part of a series. However, major mergers have typically been ignored so far, under the assumption that they are too destructive to give rise to disc-dominated lenticular galaxies (even though some studies have pointed to the possibility of preserving discs in mergers, especially when the gas fractions are high: Robertson et al. 2004; Springel & Hernquist 2005; Hopkins et al. 2009).

One of the strongest arguments in favour of simple fading is the morphology-density relation observed in galaxy clusters. Dressler (1980) showed that, as the cluster-centric distance decreases, the fraction of S0s becomes larger, and the proportion of spirals decreases at a similar rate; this can be explained as the result of the loss of gas and subsequent truncation of star formation in the infalling galaxy as it approaches the densest regions of the cluster. Dressler et al. (1997) claimed that at $z \sim 0.5$ the fraction of S0s in clusters was a factor of 2-3 lower than at $z \sim 0$, while the fraction of spirals was a factor of 2 higher. In spite of the admitted incompleteness of the sample, this has been interpreted as further evidence of spirals transforming into S0s in clusters, now witnessed in time (e.g. through ram-pressure stripping; but see the objections raised by Andreon 1998 regarding the redshift dependence of the uncertainties in the morphological types).

In this context, Aragón-Salamanca et al. (2006) compared the specific frequency of globular clusters (defined as the number of globular clusters in a galaxy per unit *V*-band luminosity) in two independent samples of spiral and lenticular galaxies, concluding that globular clusters are a factor of three more frequent in S0s. Since the globular cluster specific frequency is fairly constant in spiral galaxies, the authors take it as a fossil record of how bright an observed S0 galaxy was when it was a spiral,

⁴We define minor mergers as those with mass ratios higher than 7:1, intermediate mergers in the range 7:1-4:1, and major mergers as those with mass ratios below 4:1.

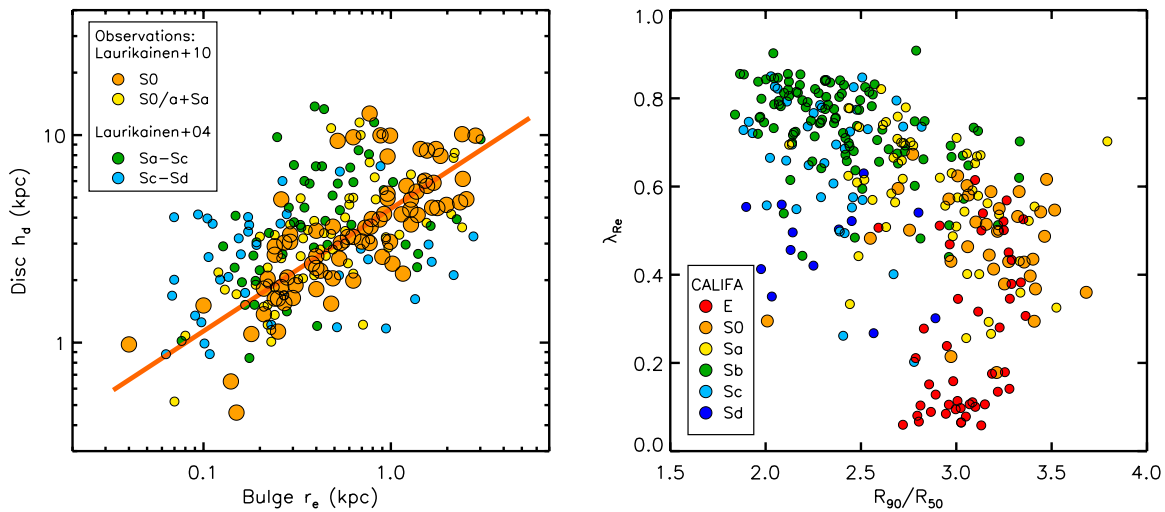


Figure 1.5: *Left*: highlight from Fig. 10b in Laurikainen et al. (2010), demonstrating the scaling relation that exists between disc scalelength and bulge effective radius for lenticular galaxies (orange), even tighter than the equivalent correlation for spiral galaxies. *Right*: stellar angular momentum (λ_{Re}) plotted against light concentration (R_{90}/R_{50}) for the galaxies observed by CALIFA (Falc3n-Barroso et al. 2015); both λ_{Re} and R_{90}/R_{50} correspond to an edge-on view.

and show that the reduction in luminosity implied by the change in specific frequency of globular clusters matches the dimming expected from stellar population synthesis models in about 3 Gyr. This relies on the hypothesis that the transformation process does not alter the number of globular clusters significantly, and that they are so old that their relative ageing is negligible. Bedregal et al. (2006) also showed that the Tully-Fisher relation for S0s in the B band is offset by 1.4 mag from the relation for spirals (with a scatter of ~ 1 mag), which they interpret as further evidence in favour of simple fading.

From their photometric structural decompositions for more than 100 lenticular galaxies in the K band, Laurikainen et al. (2010) find strong scaling relations for S0s, which they interpret as evidence against a possible merger origin of these systems, supporting simple fading models instead (see Fig. 1.5, left). They also identify pseudo-bulges in S0s, also known as ‘discy bulges’ because their profiles have Sérsic indices closer to $n \sim 1$ (typical of discs) than to $n \sim 4$ (the so-called de Vaucouleurs profile of elliptical galaxies, which explains well the light distribution of classical bulges). The presence of pseudo-bulges in S0s has been used to favour ‘gentle’ processes such as simple fading and secular evolution instead of mergers (Kormendy & Kennicutt 2004; Laurikainen et al. 2010).

On the other hand, evidence against simple fading includes the fact that S0s in clusters exist outside the region where gas-stripping mechanisms are expected to be effective, and the observation that the bulges of S0s are systematically brighter than those of spirals (Dressler 1980). Along similar lines, the stellar population synthesis models from Bruzual & Charlot (2003) predict a dimming of 0.75 mag in the K band from spirals to S0s due to simple fading. However, Burstein et al. (2005) compiled a comprehensive census of galaxy magnitudes for a range of distances and environments, using K band to minimise potential problems with dust, and showed that S0s are not dimmer than

spirals (in fact, they are slightly brighter on average), which constitutes a strong piece of evidence against simple fading of lenticulars as a class. One last counter-argument against simple fading has been recently raised by the CALIFA team: from IFU observations for hundreds of nearby galaxies, they have determined that there is a systematic offset between spirals and S0s when both specific angular momentum (λ_{Re}) and the light concentration (R_{90}/R_{50}) are simultaneously taken into account; there is some overlap for early-type spirals (Sa), but the dichotomy becomes extreme between Sb-Sd and lenticulars (see Fig. 1.5; Falc3n-Barroso et al. 2015). Since simple fading is not expected to significantly change the angular momentum of the galaxy undergoing the truncation of star formation, this constitutes an important challenge to that paradigm.

In this thesis, we will explore whether mergers of galaxies can account for this mismatch, with special attention to major mergers. We will show how, even though major mergers initially destroy the pre-existing discs, under favourable orbital conditions, the debris from the collision settles down into a disc soon after coalescence. The remnant would be classified as an S0, and, somewhat surprisingly, the disc and bulge of the resulting galaxy obey the photometric scaling relations observed in real lenticulars. The merger mechanism has the great advantage that, in addition, it can successfully explain the evolution on the plane of specific angular momentum–concentration, in agreement with the observations from CALIFA.

1.4 The key role of stellar mass

While light is the most direct observable in astrophysics, the evolution of galaxies is largely constrained by their *mass* distribution. In particular, stellar mass determines most of the action in terms of secular evolution; deviations from axisymmetry (e.g. bars) produce gravitational torques, which play an important role in redistributing matter and energy in galaxies (Athanasoula 2013). Therefore, it is important to have an accurate knowledge of the stellar mass surface density in galaxies, and not only the total integrated mass.

Stellar mass is also closely related to star formation in galaxies through the so-called main sequence of star formation. Indeed, the relation between star formation rates and stellar mass (Daddi et al. 2004; Noeske et al. 2007; Elbaz et al. 2007) has been shown to have an intrinsic width of as little as ~ 0.2 dex (Speagle et al. 2014), with a strong evolution of the normalisation factor with redshift (star formation rates at fixed stellar mass are ~ 20 times lower at $z = 0$ than at $z = 2$) and probably also more subtle changes in the slope of the relation across cosmic times. This is essentially the same as the concept of *blue cloud* that we introduced in Sect. 1.1 when galaxies are pre-selected to be star-forming.

In conjunction with estimates for total dynamical masses (e.g. from rotation curves), measuring the stellar mass surface density in galaxies can help us constrain the fraction of baryonic to nonbaryonic matter in these systems, and infer how dark matter is distributed. Stellar mass is also instrumental to any calculations of specific star formation rates, which is a useful normalised indicator of how actively a given galaxy is forming new stars.

The stellar component of a galaxy can be modelled as the superposition of discrete *simple stellar populations* (SSPs), in each of which all stars are characterised by having the same age and initial metallicity. The initial mass function (IMF) of an SSP describes the distribution of initial masses for that population of stars; the best-known IMFs are Salpeter (1955), Kroupa (2001), and Chabrier (2003), with significant differences arising mostly in their low-mass end. On the other hand, the star formation history (SFH) of a galaxy tells us how many of these SSPs have been formed as a function of time. Therefore, in principle, if we know the IMF, the SFH and the metallicity enrichment, assuming that our stellar evolution models are correct, we can predict the amount of light that will be radiated at a given wavelength for a total stellar mass; alternatively, we can turn this around to deduce the stellar mass from flux measurements in a given band. This can be achieved thanks to stellar population synthesis, which combines models of stellar evolution with radiative transfer equations (e.g. Bruzual & Charlot 2003; Maraston 2005).

However, serious problems appear when one attempts to measure stellar masses in practice: at the optical wavelengths, the newest generations of stars dominate the emission, and reduce the M/L_* in such a way that it becomes difficult to link the observed flux to the total stellar mass (since young stars bias our view of where most stellar mass is located). Additionally, starlight does not translate linearly into detected radiation, as it can be absorbed by dust and re-emitted at longer wavelengths; therefore, a good treatment of dust attenuation (and emission) is essential to correctly estimate stellar masses. Finally, stellar population synthesis models still face some uncertainties, mostly associated with the unclear last stages of stellar evolution (such as thermally pulsing asymptotic giant branch stars, TP-AGB); see Courteau et al. (2014) for a recent review.

Motivated by the quick variations of M/L_* in the optical as the result of recent bursts of star formation, the near-infrared (NIR) has been exploited as a more robust window to estimate stellar masses (Elmegreen & Elmegreen 1984; Rix & Zaritsky 1995; Meidt et al. 2014; Norris et al. 2014). It has also been recognised that M/L_* is strongly correlated with colours, and these have been employed to better constrain the mass due to stars (Bell & de Jong 2001), with the most sophisticated approach consisting in combining both optical and NIR colours to break the age-metallicity degeneracy and reduce the problems associated with dust (Zibetti et al. 2009). Alternatively, spectral energy distribution (SED) fitting can be performed using multi-wavelength data, but this limits the opportunities to obtain high-resolution 2D stellar mass maps to relatively galaxies.

The IMF is the most important systematic uncertainty affecting stellar mass measurements. However, because the slope of the IMF does not change substantially for $M_* > 1M_\odot$ (at least among Salpeter, Kroupa, and Chabrier), the choice of IMF introduces only a constant offset in the output stellar mass. Upper limits can be obtained independently from dynamical mass estimates (e.g. from galaxy rotation curves; Bell & de Jong 2001). Altogether, ignoring the offset due to the IMF, relative masses between galaxies can be obtained with accuracies of 0.2 – 0.3 dex, at best, employing the most sophisticated techniques described above. In Chapter 2, we demonstrate how $3.6\mu\text{m}$ imaging from the *Spitzer* Space Telescope, together with an algorithm to correct those images for dust emission (from the $3.3\mu\text{m}$ PAH feature and dust continuum) permits to calculate stellar masses with even higher accuracy, and affords the great advantage of allowing for the algorithm to be implemented automatically.

This has resulted in an increase by an order of magnitude in the amount of resolved stellar mass maps available so far, which we have made publicly available.

1.5 Quenching in the ALMA/NOEMA era

Astronomy is undergoing a revolution as the result of current advancements in instrumentation. While HST was an unprecedented breakthrough in the decade of 1990, revealing details that had remained hidden before, ALMA is called to take over in our days, opening up a comparable new window in the mm to sub-mm wavelength regime. With completion of the whole array achieved, full capabilities will be offered to observers in the next few years. More than 50 antennas will be operative in total (7 m-12 m in diameter each), with baselines that will provide a resolution as high as 10 milliarcseconds. In parallel, the extension of the Plateau de Bure interferometer from 6 to 12 antennas, becoming the Northern Extended Millimeter Array (NOEMA), opens up new exciting opportunities in the northern hemisphere.

Observations in the (sub-)mm band are critical to understand the process of star formation and its potential quenching, and in general how energy is regulated in the ISM. ALMA and NOEMA provide access to a myriad of molecular lines, which fall in the different atmospheric bands of the interferometers as the lines get redshifted (depending on how far from us they were emitted). Specifically, in this thesis we will describe observations of CO(1-0) and HCN(1-0) line emission. These are the lowest-energy rotational transitions of the CO and HCN molecules, respectively. Most of the molecular gas in nearby galaxies is in the form of H₂, but since this molecule does not have a permanent dipole moment (because it is linear and symmetric), CO is routinely used to trace molecular gas instead; HCN, on the other hand, traces a denser phase of molecular gas (critical density $n_{\text{cr}} \sim 10^6 \text{ cm}^{-3}$, as opposed to CO, $n_{\text{cr}} \sim 10^3 \text{ cm}^{-3}$).

In this context, since many new galaxies will be mapped to unprecedented detail in molecular tracers, it will be useful to obtain measurable quantities such as molecular gas inflow and outflow rates. Thus, it is important to have a good handle on the methodological limitations and uncertainties that we will potentially face, as well as any complementary tools that will be required (e.g. stellar mass maps). In other words, we need to be ready by knowing *what to expect*. ALMA and NOEMA can make important contributions to our understanding of the quenching of star formation: observations of molecular gas in ETGs are now possible (e.g. Young et al. 2011; Alatalo et al. 2014), and the modes of star formation suppression are now also starting to be explored in detail (e.g. AGN feedback; García-Burillo et al. 2014; Morganti et al. 2015).

Overall, the new instrumental capabilities in the (sub-)mm bands make this a timely thesis, which does not only aim to address important questions, but also tries to prepare for challenges that are expected to arise in the immediate future. To a large extent, this thesis can be regarded as an attempt to lay the foundations for future studies, including some necessary tools (stellar mass maps, Chapter 2), what we can learn about strategies and limitations from a case study (M51, Chapters 3 and 4), and how we can profit from synergies between observations and numerical simulations (Chapters 5 and 6).

1.6 Scope of thesis: questions

Within the context of star formation quenching, the work presented in this thesis is motivated by the following questions:

1. An important observational tool: stellar mass maps

- How accurately can we estimate stellar masses in nearby galaxies? → CHAPTER 2
- What type of data do we need? What are our limitations and uncertainties? → CHAPTER 2

2. AGN feeding and feedback in M51

- Is there evidence for molecular gas inflow towards the active nucleus of M51? What are the inflow rates and how accurately can we constrain them? → CHAPTER 3
- How large is the impact of AGN feedback on molecular gas? How exactly is this process orchestrated? → CHAPTER 4

3. Creating lenticular galaxies with mergers

- Can major mergers of spiral galaxies simultaneously quench star formation and preserve discs? → CHAPTER 5
- Do the scaling relations observed between bulges and discs of lenticular galaxies rule out (major) mergers as their possible origin? → CHAPTER 5
- Can mergers explain the mismatch between spiral and lenticular galaxies in terms of specific angular momentum and light concentration? → CHAPTER 6

In CHAPTER 7, we will come back to these points and close the thesis with some conclusions, new questions that our investigation has triggered, and an outlook into the future.

Chapter 2

Stellar mass maps for nearby galaxies

In this chapter we present a catalogue of stellar mass maps for more than 1500 nearby galaxies, based on $3.6\ \mu\text{m}$ imaging from the *Spitzer* Space Telescope. This paper has been published in *The Astrophysical Journal Supplement Series*, 219, 5 (Querejeta et al. 2015c), and the catalogue has been publicly released through IRSA¹. The chapter develops an observational tool which will be essential for future studies; specifically, in Chapter 3, we will use one of these maps of stellar mass surface density to quantify gravitational torques and gas inflow in the spiral galaxy M51.

¹<http://irsa.ipac.caltech.edu/data/SPITZER/S4G>

THE *SPITZER* SURVEY OF STELLAR STRUCTURE IN GALAXIES (S⁴G):
PRECISE STELLAR MASS DISTRIBUTIONS FROM AUTOMATED DUST CORRECTION AT 3.6 μm

MIGUEL QUEREJETA¹, SHARON E. MEIDT¹, EVA SCHINNERER¹, MAURICIO CISTERNAS^{2,3}, JUAN CARLOS MUÑOZ-MATEOS⁴,
KARTIK SHETH^{5,6,7}, JOHAN KNAPEN^{2,3}, GLENN VAN DE VEN¹, MARK A. NORRIS¹, REYNIER PELETIER⁸, EJA LAURIKAINEN^{9,10},
HEIKKI SALO⁹, BENNE W. HOLWERDA¹¹, E. ATHANASSOULA¹³, ALBERT BOSMA¹³, BRENT GROVES¹, LUIS C. HO^{12,19},
DIMITRI A. GADOTTI⁴, DENNIS ZARITSKY¹², MICHAEL REGAN¹⁴, JOANNAH HINZ¹⁵, ARMANDO GIL DE PAZ¹⁶,
KARIN MENENDEZ-DELMESTRE¹⁷, MARK SEIBERT¹², TRISHA MIZUSAWA¹⁸, TAEHYUN KIM¹⁹, SANTIAGO ERROZ-FERRER^{2,3},
JARKKO LAINE⁹, AND SÉBASTIEN COMERÓN^{9,10}

¹Max-Planck-Institut für Astronomie, Königstuhl 17, D-69117 Heidelberg, Germany; querejeta@mpia.de

²Instituto de Astrofísica de Canarias, Spain

³Departamento de Astrofísica, Universidad de La Laguna, Spain

⁴European Southern Observatory, Chile

⁵National Radio Astronomy Observatory, Charlottesville, VA, USA

⁶Spitzer Science Center, Pasadena, CA, USA

⁷California Institute of Technology, Pasadena, CA, USA

⁸Kapteyn Astronomical Institute, University of Groningen, The Netherlands

⁹University of Oulu, Finland

¹⁰Finnish Centre of Astronomy with ESO (FINCA), University of Turku, Finland

¹¹Leiden Observatory, Leiden University, Leiden, The Netherlands

¹²The Observatories of the Carnegie Institution for Science, Pasadena, CA, USA

¹³Laboratoire d'Astrophysique de Marseille (LAM), France

¹⁴Space Telescope Science Institute (STScI), Baltimore, MD, USA

¹⁵MMT Observatory/University of Arizona, Tucson, AZ, USA

¹⁶Universidad Complutense de Madrid (UCM), Spain

¹⁷Observatório do Valongo, Brazil

¹⁸Florida Institute of Technology, Melbourne, FL, USA

¹⁹Kavli Institute for Astronomy and Astrophysics, Peking University, Beijing, China

Received 2014 May 10; accepted 2014 August 6; published 2015 July 1

ABSTRACT

The mid-infrared is an optimal window to trace stellar mass in nearby galaxies and the 3.6 μm IRAC band has been exploited to this effect, but such mass estimates can be biased by dust emission. We present our pipeline to reveal the old stellar flux at 3.6 μm and obtain stellar mass maps for more than 1600 galaxies available from the *Spitzer* Survey of Stellar Structure in Galaxies (S⁴G). This survey consists of images in two infrared bands (3.6 and 4.5 μm), and we use the Independent Component Analysis (ICA) method presented in Meidt et al. to separate the dominant light from old stars and the dust emission that can significantly contribute to the observed 3.6 μm flux. We exclude from our ICA analysis galaxies with low signal-to-noise ratio ($S/N < 10$) and those with original [3.6]–[4.5] colors compatible with an old stellar population, indicative of little dust emission (mostly early Hubble types, which can directly provide good mass maps). For the remaining 1251 galaxies to which ICA was successfully applied, we find that as much as 10%–30% of the total light at 3.6 μm typically originates from dust, and locally it can reach even higher values. This contamination fraction shows a correlation with specific star formation rates, confirming that the dust emission that we detect is related to star formation. Additionally, we have used our large sample of mass estimates to calibrate a relationship of effective mass-to-light ratio (M/L) as a function of observed [3.6]–[4.5] color: $\log(M/L) = -0.339(\pm 0.057) \times ([3.6] - [4.5]) - 0.336(\pm 0.002)$. Our final pipeline products have been made public through IRSA, providing the astronomical community with an unprecedentedly large set of stellar mass maps ready to use for scientific applications.

Key words: galaxies: evolution – galaxies: formation – galaxies: photometry – galaxies: structure

1. INTRODUCTION

Cosmological studies have revealed a close relation between stellar mass and star formation rates (SFRs) in galaxies (e.g., Daddi et al. 2007; Noeske et al. 2007; González et al. 2011), which implies that stellar mass controls to a great extent their growth and evolution. However, even more illuminating than the total mass of a galaxy is the actual spatial distribution of its baryonic mass. This snapshot of the present-day gravitational potential constitutes a fossil record of the evolutionary history that led to its current state. Therefore, reliable maps of the stellar mass distribution provide a vital tool to probe the baryonic physics responsible for shaping galaxies to their present state.

Maps of the stellar mass distribution have played an important role in understanding many structural and evolutionary effects in galaxies that are thought to be linked to secular evolution (see Kormendy & Kennicutt 2004, for a review). For example, stellar mass maps traced by near-IR imaging have been used to study torques exerted by the stellar structure (e.g., Zaritsky & Lo 1986; Foyle et al. 2010). They are also critical to evaluate the role of bars (e.g., Scoville et al. 1988; Knapen et al. 1995, 2000; Sheth et al. 2005; Elmegreen et al. 2007; Salo et al. 2010) and to confirm theoretical predictions for bar formation (Athanasoula 1992, 2013). Studies of the spiral structure (e.g., Elmegreen & Elmegreen 1984; Elmegreen et al. 1989; Regan &

THE ASTROPHYSICAL JOURNAL SUPPLEMENT SERIES, 219:5 (19pp), 2015 July

QUEREJETA ET AL.

Elmegreen 1997) and inner stellar components in galaxies (e.g., Erwin & Sparke 2002; Falcón-Barroso et al. 2006; Eliche-Moral et al. 2011) also benefit from the use of the true underlying stellar mass distribution.

Similarly, knowing how the stellar mass is organized is essential if we want to understand how the gravitational potential influences the gas distribution and dynamics. For instance, mass maps have been used to infer the gravitational torques acting on the gas to determine nuclear inflows or outflows (see, for instance, Knäpen et al. 1995; García-Burillo et al. 2005; Jogee et al. 2005; Hunt et al. 2008; Haan et al. 2009). In a recent study, knowledge of the gravitational torques has been applied to assess the role of dynamics and stability of giant molecular clouds in the nearby galaxy M51 (Meidt et al. 2013). Therefore, stellar mass maps are an important tool when it comes to understanding the response of gas to the underlying gravitational potential.

While several strategies can be used to measure the total mass of a galaxy (see recent review by Courteau et al. 2013), unbiased stellar mass maps of galaxies are not trivial to obtain, and they often involve large uncertainties. Optical images have been used along with prescriptions to calculate the mass-to-light ratio ($M/L \equiv Y$, in the most sophisticated case obtained using two color images, see Zibetti et al. 2009). Alternatively, kinematic information can be used to derive the total mass within a given radius (e.g., Cappellari et al. 2006), which, in combination with a model for the dark matter halo, can provide an independent measure of the baryonic mass distribution for a given galaxy. Newer strategies include fitting stellar population models to IFU spectral data-cubes, from which an estimate of surface mass density can be obtained (such as those of CALIFA, Cid Fernandes et al. 2013). In any case, the instrumental requirements or the methodological complexities of these strategies have so far prevented researchers from obtaining maps of the stellar mass distribution for large samples (of more than ~ 100 galaxies).

In this paper, we apply a novel technique to infrared images, first introduced in Meidt et al. (2012a), which allows us to automatically produce high-quality mass maps for a large fraction of the galaxies in the *Spitzer* Survey of Stellar Structure in Galaxies (S⁴G, Sheth et al. 2010). S⁴G provides deep imaging for 2352 nearby galaxies ($D < 40$ Mpc) at the wavelengths of 3.6 and 4.5 μm , probing stellar surface densities down to $\sim 1M_{\odot} \text{pc}^{-2}$. The near- to mid-infrared regime provides a very good window to trace stellar mass, as the light emitted at these wavelengths is dominated by K- and M-type giant stars, tracing the old stellar populations that dominate the baryonic mass budget of nearby galaxies (e.g., Rix & Rieke 1993). As extinction is a strong function of wavelength, any stellar light emitted in the mid-infrared is significantly less affected than in the optical or at shorter wavelengths. Consequently, these data allow us to probe the mass distribution very well even in moderately inclined galaxies. While extinction is of little concern, emission from dust can significantly contribute to the flux detected in the 3.6 and 4.5 μm filters, in particular from the 3.3 μm PAH feature and hot dust arising from massive star-forming regions or around active nuclei (Meidt et al. 2012a).

In order to effectively separate the old stellar light from this dust emission which has a very different spectral energy distribution from the stars, we use a method based on Independent Component Analysis (ICA). Our method typically

identifies the main dust contribution at 3.6 and 4.5 μm (diffuse dust; Meidt et al. 2012a) and also allows one to remove the localized flux arising from circumstellar dust related to the late phases of red stars with lower M/L (Meidt et al. 2012b). After removing this dust emission, we are left with a smooth distribution of essentially old stars (age $\tau \sim 2\text{--}12$ Gyr). According to Meidt et al. (2014) and Norris et al., the age and metallicity dependence of the M/L at 3.6 μm for old stars is so modest that even a single $M/L \equiv Y_{3.6} = 0.6$ provides a conversion into mass accurate within ~ 0.1 dex.

We have constructed a pipeline (S⁴G Pipeline 5) to automatically remove dust emission from the 3.6 μm images in the large S⁴G survey of galaxies. Application of an appropriate M/L (see Meidt et al. 2014) to these cleaned maps results in stellar mass maps. All the maps of the old stellar light, along with those of the identified dust emission, will be made publicly available through the NASA/IPAC Infrared Science Archive (IRSA).²¹

In this paper we explain the details of our pipeline and analyze some properties of the two components identified by ICA for the wide range of galaxies present in S⁴G. After presenting the data in Section 2, the ICA method to remove dust emission is physically motivated and briefly explained in Section 3, followed by our description of the detailed pipeline in Section 4. Our iterative approach of ICA is presented here, along with a brief justification of the different steps involved in the process and an account of the uncertainties. In Section 5 we describe the conversion to mass maps and the public product release. Section 6 is an account of the final sample and general properties of solutions, whereas results are presented Section 7. We close the paper with a summary and some conclusions in Section 8.

2. OBSERVATIONS AND DATA PROCESSING

S⁴G (Sheth et al. 2010) has imaged 2352 galaxies using the Infrared Array Camera (IRAC, Fazio et al. 2004) at 3.6 and 4.5 μm , the bands which are still available within the post-cryogenic mission of the *Spitzer Space Telescope*. The selection of galaxies corresponds to a volume ($d < 40$ Mpc), magnitude ($m_{B,\text{corr}} < 15.5$ mag) and size limit ($D_{25} > 1'$), and provides deep images reaching $\mu_{3.6 \mu\text{m}}(\text{AB})(1\sigma) \sim 27$ mag arcsec⁻² (about $1M_{\odot} \text{pc}^{-2}$).

All the images have been processed using the S⁴G pipeline, which consists of five steps. The first four steps are summarized in Sheth et al. (2010), and will be described in detail in separate papers (Muñoz-Mateos et al. 2015, Salo et al. 2015). The process that we present here corrects for emission from dusty sources in the IRAC bands, and it constitutes the fifth stage of the S⁴G pipeline system.

1. *Pipeline 1* transforms the raw data into science-ready FITS images by mosaicking and matching the background levels, providing a resulting pixel scale of 0.75 arcsec pixel⁻¹ (Regan et al. 2015, in preparation). The point-spread function (PSF) has a typical FWHM of 1".7 and 1".6 at 3.6 and 4.5 μm , respectively.
2. *Pipeline 2* generates masks, first based on SExtractor identifications, and then checked and modified by eye (Muñoz-Mateos et al. 2015, in preparation).

²¹ irsa.ipac.caltech.edu

3. *Pipeline 3* takes care of measuring sky levels, determining the center and obtaining isophotal values (intensity, surface brightness, ellipticity, position angle; Muñoz-Mateos et al. 2015, in preparation).
4. *Pipeline 4*, performs GALFIT photometric structural decompositions of the sample (Salo et al. 2015, in preparation).
5. *Pipeline 5*, presented here, relies on previous pipeline steps and is the application of the ICA method to separate the light from old stars and dust.

Additionally, at some points in this paper, and especially for the analysis of results (Section 7), we will make use of a set of ancillary information. For distances, whenever available, we rely on the mean redshift-independent distance provided by the NASA Extragalactic Database (NED); otherwise, they are based on the observed radial velocity, also from NED (compiled by Muñoz-Mateos et al. 2015, in preparation). We utilize the morphological classification at $3.6\ \mu\text{m}$ from Buta et al. (2010) and Buta et al. (2015). SFRs are derived from IRAS photometry at $60\ \mu\text{m}$ and $100\ \mu\text{m}$ obtained from NED following Larsen & Richtler (2000).

3. THE ICA TECHNIQUE

3.1. Expected Sources at 3.6 and 4.5 μm and Their Colors

For nearby galaxies, the light detected in the IRAC $3.6\ \mu\text{m}$ filter arises mainly from two components: the photospheres of (old) stars and from dust emission. Old stars dominate the stellar flux, as their atmospheres are cold and their blackbody curves peak close to $3.6\ \mu\text{m}$; additionally, due to CO absorption at $4.5\ \mu\text{m}$, old K and M giants exhibit blue $[3.6]-[4.5]$ colors (Pahre et al. 2004; Willner et al. 2004). Younger (hotter) stars are not expected to contribute significantly to the observed stellar emission. However, due to their strong UV fluxes, these younger stars can heat their surrounding dust, which, in turn, re-radiates at longer wavelengths and can also account for a significant fraction of the light at $3.6\ \mu\text{m}$ (Meidt et al. 2012b). Models show that the dust emission arises from the PAH bands (specifically, the $3.3\ \mu\text{m}$ feature) and the continuum radiation from very small grains (e.g., Li & Draine 2001), and this (hot) dust emission becomes more prominent near the sites of star formation, where the presence of young stars leads to stronger radiation fields.

According to the measurements of Flagey et al. (2006), PAHs should have colors $[3.6]-[4.5] \sim 0.3$, including both the $3.3\ \mu\text{m}$ PAH feature and the underlying PAH continuum detected, e.g., in Milky Way reflection nebulae. In the absence of the PAH continuum, the $[3.6]-[4.5]$ color is bluer (as low as $[3.6]-[4.5] \sim -0.1$), although this scenario will likely be uncommon here, given unavoidable mixing at our resolution. For the continuum dust component, we expect $[3.6]-[4.5] \sim 1.0$, adopting the power-law approximation $f_\nu \propto \nu^{-\alpha}$ to the Wien side of the dust spectral energy distribution (SED) with $\alpha = 2$, which Blain et al. (2003) suggest better accounts for the observed dust SED shape than a modified blackbody in the near-IR. As shown in Figure 1, the diffuse mixture of PAH and continuum dust emission will exhibit resulting colors in the range $0.2 < [3.6]-[4.5] < 0.7$.

The relative flux contributions of the PAH and continuum at $3.6\ \mu\text{m}$ can be estimated from the ratio of the $6.2\ \mu\text{m}$ PAH feature to the $6.2\ \mu\text{m}$ continuum measured by Peeters et al. (2002). For normal spiral galaxies, this ratio is between

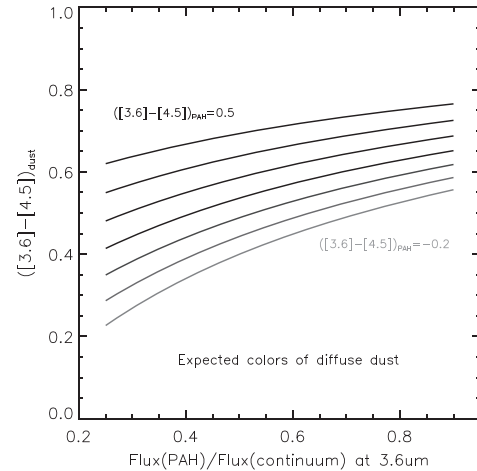


Figure 1. Observed $[3.6]-[4.5]$ color as a function of the relative contribution to flux from diffuse dust continuum and PAH. The different curves correspond to different intrinsic PAH colors $[3.6]-[4.5]_{\text{PAH}} = -0.2$ to 0.5 in steps of 0.1 . For reasonable fractions of such a mixture, we find that the resulting dust color is constrained within the range $0.2-0.7$ (see text for details).

$0.72-1.16$ (on average ~ 1) and can be as low as 0.1 in QSOs and the nuclei of Seyfert galaxies. The ratio of the $3.3-6.2\ \mu\text{m}$ PAH features measured in H II regions, star-forming regions and in planetary nebulae falls in the range $0.15-0.25$ (Hony et al. 2011). With the Blain et al. power-law dust continuum, this implies that the ratio of the $3.3\ \mu\text{m}$ PAH emission to the underlying continuum is $\sim 0.4-0.9$, or as low as 0.1 in galaxy nuclei or other regions dominated by hot dust.

Figure 1 shows the resulting colors for the diffuse dust at $3.6\ \mu\text{m}$ adopting this range of PAH flux fractions for a wide range of possible PAH colors and assuming a fixed continuum color. As found by Meidt et al. (2012b), the primary non-stellar emission detectable with ICA is in the form of this “diffuse dust” component, i.e., the mixture of PAH and the dust heated by the ambient interstellar radiation field, away from star-forming regions. As considered later in Section 4.3 and in Appendix B, some galaxies also exhibit additional emission from hot dust, isolated in star-forming H II regions. This dominant component in H II regions, which can be thought of as the far end of the spectrum exhibited by the “diffuse dust,” should have $[3.6]-[4.5]$ colors closer to 1.

In the implementation of our S⁴G pipeline we make use of the fact that regions containing hot dust (and negligible PAH) have colors that are distinguishable from the nominal diffuse dust component. We also make use of the fact that the colors of the dust and the old stellar population are very different. The colors for old stellar populations lie in the range $-0.2 < [3.6]-[4.5]_{\text{stars}} < 0$, according to the observed colors of giant stars (Meidt et al. 2014). This is consistent with the observed colors of early-type galaxies, in the absence of significant dust emission (Peletier et al. 2012, and Norris et al. 2015). The non-stellar $[3.6]-[4.5]$ color, on the other hand, always appears positive in these bands ($[3.6]-[4.5]_{\text{dust}} > 0$), although it can span a wider range, as seen in Figure 1.

Table 1 summarizes the colors expected for the different sources of emission at $3.6\ \mu\text{m}$. These sources combine together to produce the observed $[3.6]-[4.5]$ colors plotted in Figure 2. There we show representative colors for young, relatively

Table 1
Main Sources at 3.6 μm and Their [3.6]–[4.5] Colors

Source	Typical [3.6]–[4.5] Range
Old stars ^a	–0.2–0
Diffuse dust	~0.2–0.7
PAH emission ^b	~0.3
Dust in H II regions ^c	~1.0

Notes. Main sources identified with ICA, and typical values of their colors.

^a Willner et al. (2004), Pahre et al. (2004), Peletier et al. (2012), Meidt et al. (2014), Norris et al.

^b Dominated by PAH emission. Approximate estimation based on Flagey et al. (2006).

^c Representative number based on Blain et al. (2003); it can either correspond to hot dust, e.g., in H II regions, or, in the most extreme case, to hot dust heated to large temperatures near an AGN.

metal-poor, late-type galaxies and their old, metal-rich early-type counterparts (with bluer [3.6]–[4.5] colors),²² adopting the dust contamination fractions estimated in Appendix A. The latter consistently exhibit [3.6]–[4.5] < 0, whereas the addition of even a little bit of dust emission will move the [3.6]–[4.5] colors of late-type galaxies above zero.

3.2. ICA

Here, we introduce the ICA method and the nomenclature that we will use. The method has already been described and validated by Meidt et al. (2012a), so we will only provide a short summary here.

Similar to Principal Component Analysis (PCA), ICA is a means of *blind source separation* which we use to extract measurements of the flux and the wavelength-dependent scaling of individual components from linear combinations of the input data. But in contrast to PCA, ICA maximizes the statistical independence of the sources rather than requiring that the sources are orthogonal (with zero covariance). We use the *fastICA* realization of the method developed by Hyvärinen (1999) and Hyvärinen & Oja (2000), which achieves statistically independent solutions by maximizing the non-Gaussianity of the source distributions.

In practice, given N input images (e.g., at N different wavelengths), ICA will identify at most N underlying distinct sources that contribute to the flux in each of the N images, under the assumption that each image is a linear combination of the sources. Because S^4G provides images of each galaxy in two channels, ICA can identify two distinct components through solution of the following equation:

$$\mathbf{x} = \mathbf{A} \cdot \mathbf{s}, \quad (1)$$

where \mathbf{x} is the $2 \times P$ measurement set, with as many columns as pixels P in the analysis region, \mathbf{s} is the $2 \times P$ source solution set, and $A_{i,j}$ is an invertible 2×2 matrix of “mixing coefficients” determined simultaneously with \mathbf{s} .

As first considered by Meidt et al. (2012a), ICA provides a way to distinguish between the old stellar population that dominates the light in the IRAC bands and additional emission present to varying degrees (depending on the nature of the source), without a priori

²² As a result of CO absorption in the 4.5 μm band, the metallicity dependence of the [3.6]–[4.5] color identified by Meidt et al. (2014) is the reverse of that exhibited by optical or optical-NIR colors; the [3.6]–[4.5] color becomes more blue with increasing metallicity (see also Norris et al.).

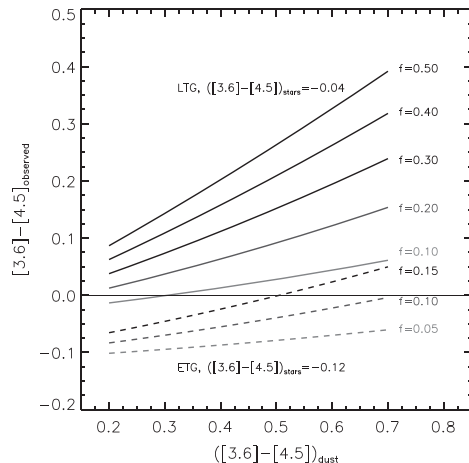


Figure 2. Observed [3.6]–[4.5] colors that arise from mixing stars with dust emission. Stars have colors $-0.2 < [3.6]–[4.5]_{\text{stars}} < 0$, and dust emission typically covers the range $0.2 \lesssim [3.6]–[4.5]_{\text{dust}} \lesssim 0.7$. Here, we show the resulting color for realistic combinations of dust colors and fractions, for two fixed stellar colors. One of them is representative of late-type galaxies (LTG, $[3.6]–[4.5]_{\text{stars}} = -0.04$), and the other one is standard of early-type galaxies (ETG, $[3.6]–[4.5]_{\text{stars}} = -0.12$). The fractions of dust emission at 3.6 μm (f) are also limited to the maximum expected fractions in early- and late-type galaxies, as estimated in Appendix A. Virtually all possible combinations lead to global negative colors in the case of early-type galaxies, whereas essentially all realizations produce positive global colors for late-type galaxies, in which the contribution from dust can be more significant.

knowledge of the relative proportions of the sources or their colors between 3.6 and 4.5 μm . In six prototypical star-forming disk galaxies, Meidt et al. (2012a) showed that ICA can identify and remove the combined PAH and continuum dust emission (tracing star formation, as observed at longer wavelengths) and localized emission from dusty asymptotic giant branch (AGB) and red supergiant (RSG) stars. The ICA correction leaves a cleaned, smooth map of the old stellar light consistent with expectations for an old, dust-free stellar population.

Our pipeline implementation of ICA includes an estimate of the uncertainties on both components by running the ICA sequence 48 times, based on 48 perturbations to the mixing matrix. As an initial guess for the mixing coefficients we adopt the expected color range of stars and dust ($-0.2 < [3.6]–[4.5]_{\text{stars}} < 0$ and $0 < [3.6]–[4.5]_{\text{dust}} < 1.5$), but we find that ICA solutions quickly depart from the initial seeds and converge to the final solution. The perturbations to the mixing matrix correspond to small steps in dust and stellar color in a count-controlled nested loop. The primary loop implements a change in the stellar color by 0.04 mag, during which the secondary iterates the dust color in steps of 0.3 mag (at fixed stellar color).

3.3. Notation

For each of the two original input images we obtain two source images, which we refer to as s_1 and s_2 , providing a total of four images (which we could in principle name $s_{1,3.6}, s_{2,3.6\mu\text{m}}$ and $s_{1,4.5}, s_{2,4.5\mu\text{m}}$). At either wavelength it will always hold that $(s_1 + s_2) = \{\text{original image}\}$. However, since the two source images at 4.5 μm are scaled replicas of the two source images at 3.6 μm , with scalings set by the colors of the solutions ($[3.6]–[4.5]_{s_1}$ and $[3.6]–[4.5]_{s_2}$), throughout the paper we will, by default, refer to the 3.6 μm solutions as s_1 and s_2 .

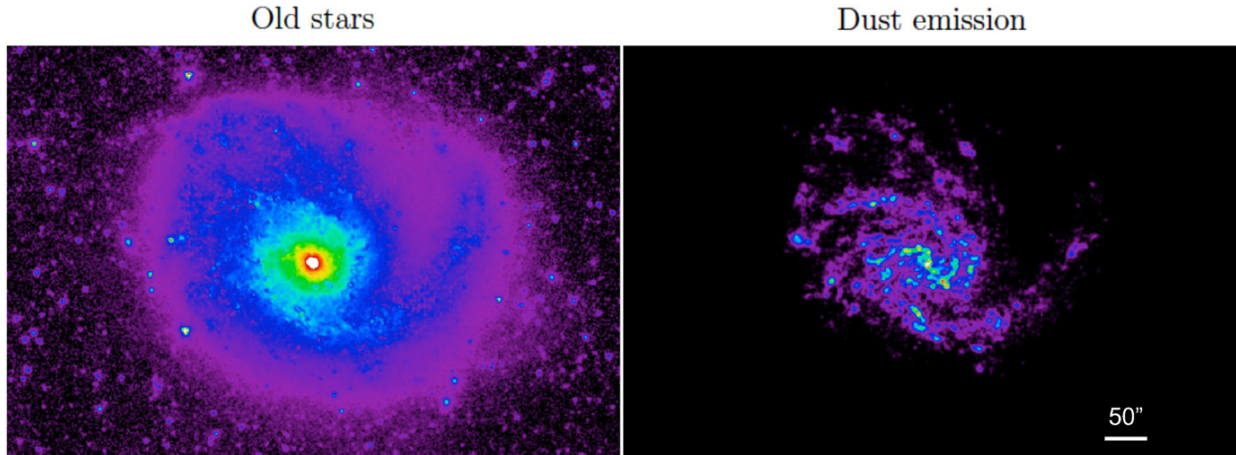


Figure 3. NGC 4254 as a prototypical example of the ICA decomposition of the $3.6\ \mu\text{m}$ image into old stars ($s1$, left) and dust emission ($s2$, right). This is the standard case for star-forming disk galaxies, with a dust color of $[3.6]-[4.5]_{s2} = 0.17$ and finding a color of the old stellar component of $[3.6]-[4.5]_{s1} = -0.02$, in agreement with the values expected for K and M giants. Here, and throughout the paper, $s1$ maps are shown in square root intensity scale, with $I_{3.6}^{\text{max}} = 10\ \text{MJy/sr}$, whereas $s2$ maps are displayed in linear scale, with $I_{3.6}^{\text{max}} = 5\ \text{MJy/sr}$ (in both cases $I_{3.6}^{\text{min}} = 0$).

With this notation, ICA typically separates the emission arising from old stars (which we identify with $s1$) from dust ($s2$), as is illustrated by Figure 3. The secondary emission that arises from dust can have a number of physical origins, covering different color ranges (see Table 1), but is always redder than old stars in these bands, which allows ICA to perform the separation into two distinct components.

4. S⁴G PIPELINE 5

In this section we summarize our approach for applying the ICA technique to the S⁴G sample, exploiting the powerful resources available from S⁴G (images at 3.6 and $4.5\ \mu\text{m}$ and pipeline products). We introduce and describe our iterative implementation of ICA, which is designed to ignore all pixels that contain emission different from the dominant two (e.g., background galaxies, foreground stars), thus allowing ICA to produce better results.

Given the size and diversity of the sample, it is not surprising that there are some galaxies for which we cannot expect to apply ICA under optimal conditions. In the same way that a low signal-to-noise ratio (S/N) can degrade the quality of color information that can be extracted from 2D images, low S/N provides inadequate leverage on the spectral shapes of the two components between 3.6 and $4.5\ \mu\text{m}$ which is necessary for ICA to obtain a robust solution. Our testing of the method confirms that ICA cannot correctly separate images into two components when the average signal to noise is low.²³ Therefore, we have adopted a conservative approach and apply our pipeline only to those galaxies with average signal-to-noise above $S/N > 10$.

Obtaining dust-free flux maps in an automatic fashion with ICA involves a number of steps (masking, second ICA iteration, thresholding, postprocessing) that will be introduced and justified in the present section. For clarity, the steps involved in the pipeline are presented in a flow chart (Figure 4),

²³ Our analysis of the set of galaxies with S/N below 10 confirms that S/N is a major determinant in the quality of solutions; we find that 67% of these cases have solutions with an $s1$ component with colors outside the expected range for old stars. We therefore leave out those galaxies with the poorest data quality, by definition.

with a reference in *italics* to the specific section where they are discussed.

4.1. Defining the ICA Solution Area

Because our implementation of ICA seeks to maximize the non-Gaussianity of the source distributions (Hyvärinen & Oja 2000), ICA is sensitive to extreme outliers in color, even if these cover only a small region. This means that a few pixels with very different color from the dominant color can bias the whole solution (not only the area they cover), yielding an unrepresentative separation of the original image into two components. Consequently, properly masking any foreground stars or background galaxies is particularly important.

We have developed a specific masking strategy that builds on masks already available from S⁴G Pipeline 2, but includes further corrections to ensure that bright regions belonging to the galaxy are not masked in a first attempt. Pipeline 2 masks were developed primarily for galaxy photometric decompositions (Pipeline 4), and that is the reason why this subtle yet important modification is necessary to make the masks applicable for our purposes here.

Specifically, we remove from the Pipeline 2 masks any contiguous regions that are small (maximum area in pixels of $8000\ \text{Mpc}^2/d^2$) and have colors $-0.3 < [3.6] - [4.5]_{\text{orig}} < 0.75$, as they tend to be bright regions intrinsic to the target galaxy (e.g., H II regions). The distance-dependent cut in size corresponds to a radius of $\sim 150\ \text{pc}$, covering well even the largest H II regions (see Whitmore et al. 2011), whereas the color criterion matches roughly the range spanned by emission from old stars and dust, leaving out saturated field stars and observational artifacts, which usually exhibit colors outside this range.

Therefore, the set of pixels to which we apply ICA (the ICA *solution area*) is defined to contain all emission out to the edge of the galaxy and avoid external sources such as field stars and background galaxies. The area is centered on the photometric center defined in Pipeline 3 and extends out to the $25.5\ \text{mag arcsec}^{-2}$ isophote (Muñoz-Mateos et al. 2015, in preparation), excluding the masked regions. At this early stage,

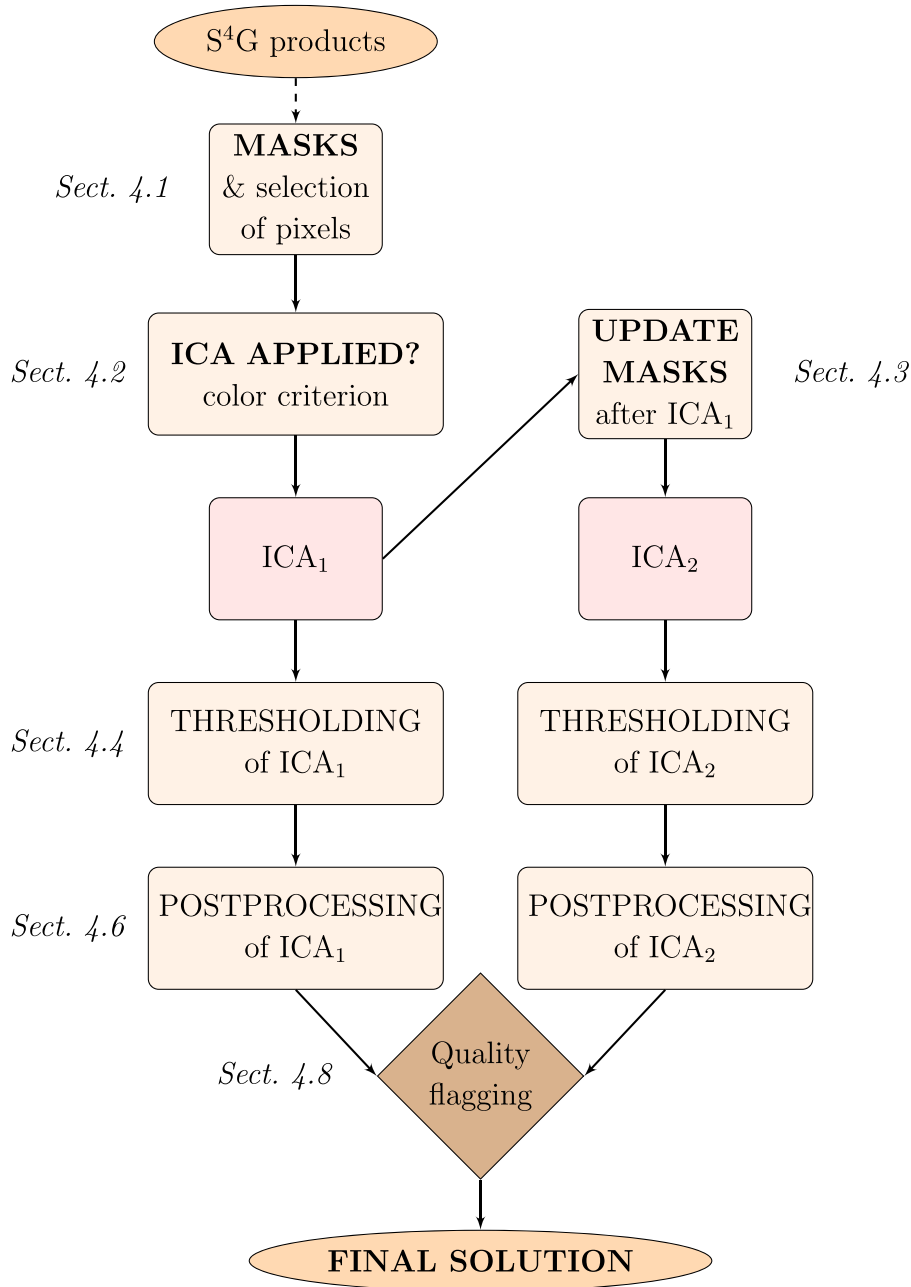


Figure 4. Flow diagram showing the different steps involved in S⁴G Pipeline 5. The blocks shaded in light orange are executed in IDL, whereas the parts in light red correspond to C++.

we also correct for PSF effects by convolving both images with the IRAC 4.5–3.6 μm PSF kernel from Aniano et al. (2011).

4.2. Deciding Whether ICA Should be Applied

The expected color for an old stellar population of ages $\tau \sim 2\text{--}12$ Gyr is $-0.2 < [3.6]\text{--}[4.5] < 0$ (see references in Table 1). Some of the galaxies in S⁴G have original [3.6]–[4.5] global colors in that range, which implies that they are already compatible with an old stellar population. As shown in Figure 2, an originally blue color is indicative of little to no dust emission; we therefore do not apply ICA to these galaxies. We have found that these cases can be best identified by

calculating the *weighted mean* of the original color for the pixels in our ICA solution area; the weights are chosen as the inverse of the variances ($w_i = 1/\sigma_i^2$, where σ_i is the original color error, as described in Section 4.7). By adopting the weighted mean we avoid the bias of low signal-to-noise regions, from which color information is less reliable. A total of 376 galaxies in S⁴G (16% of the sample) have colors originally compatible with old stars, and are therefore excluded from the further ICA analysis.

Inspection of the 2D color maps confirms very little contamination from dust in galaxies where the original negative color is consistent with that of old stars, although dust may not

be entirely absent. Still, we prefer not to run ICA in these cases, since our testing suggests that more uncertainty in the old stellar light map can be introduced under these circumstances than if the non-stellar emission is simply retained. In particular, we have found that when emission from dust becomes negligible, the separation starts to be dominated by spatial fluctuations in the original color due to noise. As shown in Appendix A, a low fractional dust contamination leads to the largest errors on the stellar flux obtained from the ICA separation.

4.3. Iterative ICA: Reducing the Number of Sources of Emission

As described in Section 3.1, the primary non-stellar emission detectable with ICA is in the form of a “diffuse dust” component, i.e., a mixture of PAH and dust continuum. Some galaxies also exhibit secondary non-stellar emission from hot dust isolated in star-forming H II regions or near an active nucleus. Even in these cases, it is most common that the diffuse dust, which is spatially more extensive than the dust in H II regions, dominates the ICA solution. But as the hot dust regions are assigned a color that is unrepresentative (and, in particular, less red than their true color), the flux in this secondary dust component can be overestimated (see Section 4.6 below).

In other cases (e.g., a high number of H II regions, or very pervasive star formation), ICA will favor the hot dust. While this may provide the best description of the non-stellar emission in some galaxies (with genuinely more hot than diffuse dust), often the emission from the diffuse dust component is still present, but underestimated by ICA (since it is assigned a color redder than its intrinsic value). As we are more interested in isolating dust emission in the disk (tracing star formation, heating from hot evolved stars, etc.), we prefer to completely avoid these very red, hot dust-dominated regions by performing a second iteration of ICA with the corresponding areas masked.

This same iterative process is useful in general for reducing the number of sources of emission present in the *solution area*. Extremely bright nuclear point-like sources have a very similar effect on ICA solutions as the bright field stars and background galaxies described in Section 4.1. In some cases, they initially completely dominate the secondary component identified with ICA. Ignoring the central source helps ICA identify other types of secondary sources of emission, as can be seen in Figure 5.

The relative contributions of the additional sources determines the degree to which ICA identifies a realistic secondary source. When, for example, the second component is dominated by the diffuse dust emission, and hot dust appears in only small localized H II regions, ICA successfully describes the dominant source (in this case diffuse dust; see Meidt et al. 2012a, and Appendix B). This is close to the optimum decomposition and is characteristic of most star-forming disk galaxies. However, when the contributions of the two sources become comparable (e.g., when they cover similarly sized areas in the disk), ICA finds a compromise between the two. In some cases, this compromise is an acceptable outcome, but it is often possible to obtain a noticeably improved solution for one of the components by running ICA again, now with pixels containing the other source masked. This is confirmed by the tests described in Appendix A, and, for the interested reader,

the details of this empirically optimized strategy are described below (Section 4.3.1).

In our automatic pipeline, the second ICA iteration is determined to be effective when the second ICA s_2 is bluer than the first ICA s_2 (i.e., the reddest sources have been removed from the dust map). This is the case for 66% of the objects, in which $[3.6]-[4.5]_{s_2}$ is effectively reduced after the second iteration and ICA₂ is chosen. The improvement in the solution for these cases is also associated with a decrease in the color uncertainties (in 79% of those objects $[3.6]-[4.5]_{s_2}^{\text{ICA}_2}$ has a smaller uncertainty than $[3.6]-[4.5]_{s_2}^{\text{ICA}_1}$). Even in these cases, the fractional change to the total old stellar flux (and, thus, total mass) is not dramatic, typically on the order of ~5%, but of course this can locally become more significant.

We have confirmed that running a third iteration of ICA would introduce a change which is negligible, smaller than the uncertainty in 98% of the cases. Therefore, for simplicity, we have only implemented two iterations in the final pipeline.

4.3.1. Technical Details on Second Iteration, ICA₂

In practice, all the pixels with original colors redder than the global color of the dust component ($[3.6]-[4.5]_{s_2}$) are selected. This is, by definition, equivalent to selecting the pixels in which oversubtractions in the stellar map have occurred (i.e., negative values in the stellar map after the first iteration of ICA). To prevent masking any spurious isolated red pixels (i.e., those that arise from local fluctuations at low signal-to-noise), the regions identified as oversubtractions are radially dilated by 1 pixel. We then check if, after the dilation, contiguous pixels still correspond to a region with original integrated color greater than $[3.6]-[4.5]_{s_2}$. If this is the case, the given region will be masked for the second iteration.

Additionally, we analyze the distribution of fluxes in the map of dust and mask all the regions that are above 5σ (σ meaning now the standard deviation in the distribution of the identified dust fluxes) if a given contiguous region has an integrated color that exceeds either $[3.6]-[4.5]_{s_2}$ or an empirically set limit of $[3.6]-[4.5]_{\text{orig}} = 0.1$.

Finally, to account for the reddest nuclear dust emission, often related to active galactic nucleus (AGN) activity, we perform one more modification on the masks of the galaxies in which the first ICA solution had an s_1 color redder than old stars ($[3.6]-[4.5]_{s_1} > 0$). Such a red s_1 color indicates that the spatially dominant diffuse dust emission has not yet been removed with ICA, as an even redder nucleus is identified as virtually the only component by ICA in the s_2 map. Therefore, in the second iteration, we mask the contiguous region in the s_2 map which has the highest average flux, provided that it covers an area smaller than 200 px. This is about the maximum area we can expect to be covered by the PSF (Aniano et al. 2011) due to a point source; if the area is larger, we instead mask the circular region with a diameter of 10 px that maximises the s_2 flux contained.

We confirm that most of the galaxies with $[3.6]-[4.5]_{s_1}^{\text{ICA}_1} > 0$ can be attributed to AGN activity (55% of these are classified as AGN in Simbad, whereas the global fraction of such AGN-classified galaxies in S⁴G is only 8%; see Véron-Cetty & Véron 2010). A substantial portion of the remaining 45% has, conversely, been identified to have nuclear star formation (so-called H II nuclei). In any case, masking that central region allows ICA to identify the more extended dust emission, and in 70% of the objects, this second iteration

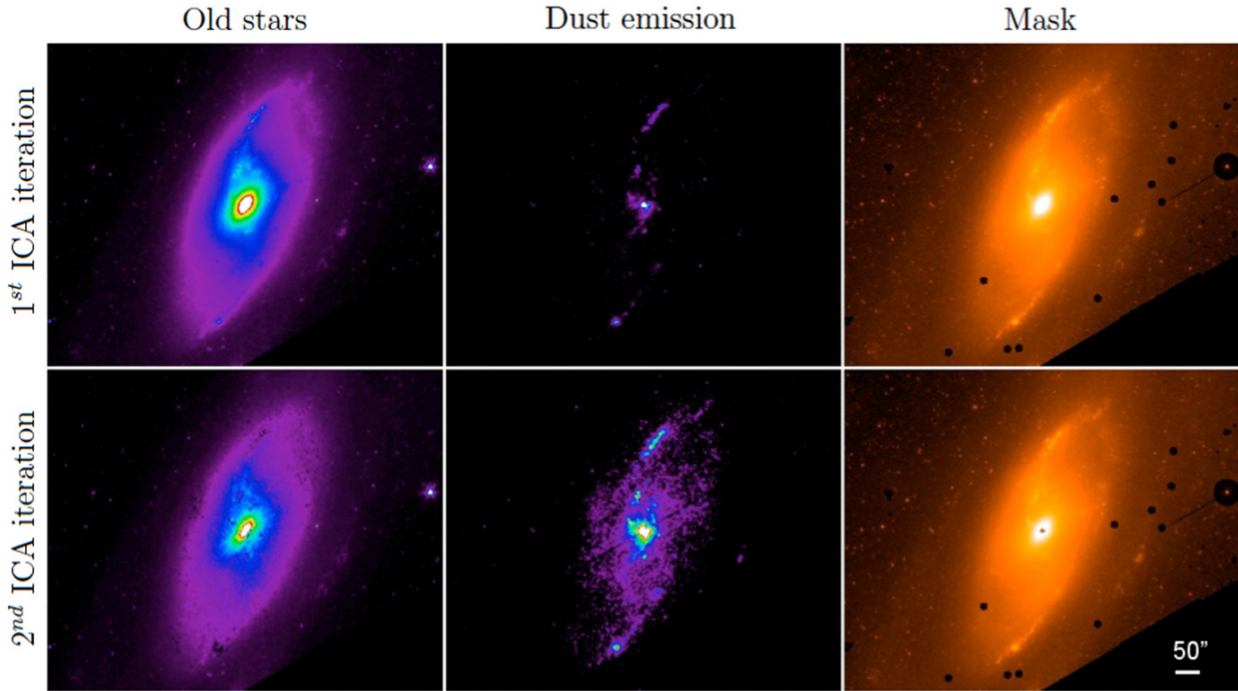


Figure 5. Example of how a second iteration of ICA with extreme color and flux outliers masked can reveal different components. Here, the first (top) and second (bottom) iterations are presented for NGC4258, a LINER galaxy. The left map corresponds to the old stellar flux (s_1), the central column represents the dust map (s_2), and the right column shows the mask used in each case (regions attenuated by 5 mag against the original $3.6 \mu\text{m}$ image). For the first iteration, ICA finds a dust color of $[3.6]-[4.5]_{s_2}^{\text{ICA}_1} = 0.697$ and a stellar color of $[3.6]-[4.5]_{s_1}^{\text{ICA}_1} = -0.028$. The second iteration effectively makes the dust color less red ($[3.6]-[4.5]_{s_2}^{\text{ICA}_2} = 0.138$), and the final stellar color is then $[3.6]-[4.5]_{s_1}^{\text{ICA}_2} = -0.063$.

makes the s_1 color match the expected values for an old stellar population (shifting from $[3.6]-[4.5]_{s_1}^{\text{ICA}_1} > 0$ to $[3.6]-[4.5]_{s_1}^{\text{ICA}_2} < 0$).

4.4. Determining Significant Secondary Emission: Thresholding

ICA provides a solution for each pixel in the *solution area* using information from all other pixels in the area. But not all pixels contain a genuine secondary source; consequently, some low-level noise is systematically introduced throughout the analysis area. These low-level pixels can either be positive or negative, since ICA does not impose non-negative solutions, and they are clearly artificial, as they fluctuate nearly uniformly around zero. To prevent arbitrary removal (or addition) of flux from the stellar map, we conservatively impose a minimum flux of s_2 above which the emission is arguably genuine. We base our threshold on the map of propagated uncertainties, which we are able to compute following the recipe described and justified below.

4.4.1. Technical Details on Thresholding

We define the threshold relative to the map of propagated uncertainties, with the additional simple assumption that the noise randomly introduced by ICA is symmetric about zero. In principle, there is no mechanism within ICA that should asymmetrically bias the noise toward positive values, and this is confirmed by the histograms of the flux distribution of s_2 over areas where no dust emission is expected (e.g., in the outermost part of the galaxy). For a randomly selected sample of galaxies, these histograms are indeed very symmetric

distributions centered around zero (some are shown in Figure 6 for illustrative purposes).

In light of the symmetric distribution of noise around zero, we adopt a variable threshold, which we set to M times the propagated map of uncertainties, where M is defined by the 95th percentile in the noise distribution measured from the negative pixels in s_2 divided by the average propagated noise:

$$\text{flux threshold} = \left(- \frac{95\text{th percentile of negatives}}{\text{average propagated noise}} \right) \times \text{map of propagated noise.} \quad (2)$$

As we assume that the distribution of negative pixels is representative of the global noise distribution, such that a symmetrical cut in the 95th percentile toward positive values removes all negative noise and also 95% of the artificially introduced positive noise. What is left is primarily the significant emission in s_2 .

The fluxes at these threshold locations are returned back to the map s_1 , which, as a result, once again becomes identical to the original image for those positions. We note that some genuinely identified low-level dust emission may be returned to the stellar map. (At low flux values, where the distributions of genuine dust emission and noise overlap, there is no way to uniquely determine their true contributions.) In effect, we modify the picture of the old stellar light map supplied by the original image by removing flux only if we are confident that it corresponds to dust emission. This prevents the introduction of additional structure by artificially removing flux consistent with noise.

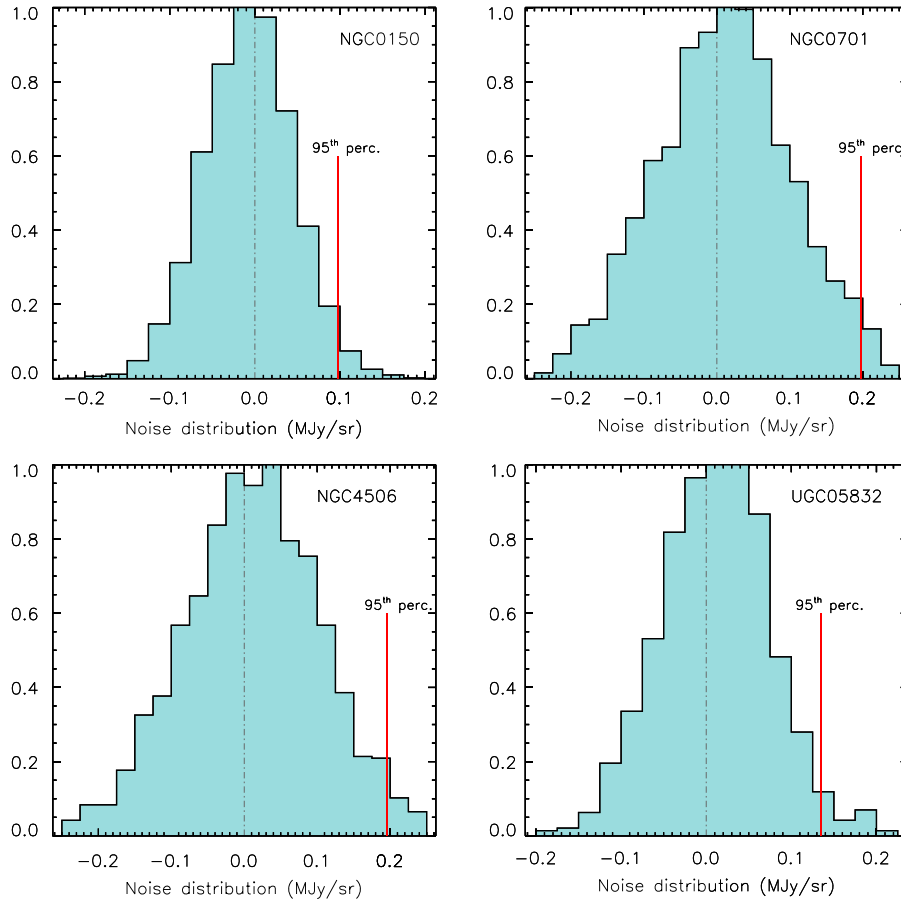


Figure 6. Histograms showing the flux distribution on areas of s_2 where virtually no dust emission is expected (i.e., the noise distribution). It follows a highly symmetrical distribution around zero, based on which we define a threshold to remove noise from our final maps (threshold set by the red vertical line, the 95th percentile of the negative noise distribution).

4.5. Choosing the Best Solution

Because ICA optimally separates two sources in two images, the second iteration, for which the number of sources has been reduced, supplies in principle our best solution. In practice, this translates into a dust color which becomes less red after the second iteration, as a combination of hot dust, evolved star regions and possibly red nuclei have been masked, to converge on a color representative of the spatially dominant diffuse dust emission.

However, when the second iteration returns solutions that are unphysical (i.e., the ICA colors of one or both sources fall outside the range of colors expected for old stars or dust emission, or the identified dust color turns redder after the second iteration), then we take this as an indication that the solution has been biased by the masking of noisy pixels rather than by a true additional secondary source. The solution from the first iteration is chosen in this case (34% of the cases).

4.6. Solution Postprocessing

Independently of the choice of solution, a posteriori processing is necessary, as the light from old stars will be over- or under-estimated in pixels containing dust properties that deviate from the dominant ones. There are two cases when we choose to adjust a posteriori the information in map s_1 . In

the first case, when pixels contain dust with redder colors than the ICA $[3.6]-[4.5]_{s_2}$ color and these are unmasked, the solution overestimates the true secondary flux in these pixels. This manifests itself in oversubtractions on the stellar flux map, which we find to be an acceptable price to pay for the high quality with which a larger fraction of the dust emission can be described with ICA. In these cases we opt to linearly interpolate over the regions of oversubtraction, which are typically small, effectively filling them in with information about the old stellar light from neighboring pixels.

A second case arises when those red regions have been masked in the second iteration (i.e., regions with the reddest dust emission). Since we do not want to leave that extra flux in the stellar map, we also linearly interpolate over all those masked regions (since they are typically of the order of a few pixels). The map of dust emission is then adjusted in this case, by taking the difference between the original image and the adjusted old stellar map.

Naturally, the colors of the sources are also recalculated after these slight flux modifications.

4.7. Quantifying Uncertainties

Several uncertainties combine to set the level of accuracy that we can obtain in our maps of the distribution of old stellar light, due to both systematic and measurement errors. For

Table 2
Uncertainties Involved in the Pipeline^a

Uncertainty	Typical Value (mag)
Error of original global color	0.001
ICA bootstrapping error	0.074
Propagated photometric error [3.6]–[4.5] _{s1}	0.028
2nd iteration change on [3.6]–[4.5] _{s1}	0.036

Note.

^a Typical values understood as the median values of the distributions.

clarity, Table 2 summarizes the typical values of the different uncertainties involved.

The 3.6 and 4.5 μm images on which we base our separation have photometric uncertainties, which propagate through the ICA method into the final maps we produce. The original photometric uncertainties are quantified via the sigma maps (σ_1 , σ_2) that we obtain from the S⁴G weight maps and, according to Equation (1), they propagate in to the following uncertainties:

$$\sigma_{11}^2 = \frac{\text{ZP}^2}{10^{0.8(cs1)} - 10^{0.8(cs2)}} \left[\left(\sigma_1^2 + \Delta\text{sky}_1^2 \right) + \frac{10^{0.8(cs2)}}{\text{ZP}^2} \left(\sigma_2^2 + \Delta\text{sky}_2^2 \right) \right], \quad (3)$$

and

$$\sigma_{12}^2 = \frac{\text{ZP}^2}{10^{0.8(cs2)} - 10^{0.8(cs1)}} \left[\left(\sigma_1^2 + \Delta\text{sky}_1^2 \right) + \frac{10^{0.8(cs1)}}{\text{ZP}^2} \left(\sigma_2^2 + \Delta\text{sky}_2^2 \right) \right], \quad (4)$$

where $\text{ZP} = 280.9/179.7$, $cs1 = [3.6] - [4.5]_{|s1}$, $cs2 = [3.6] - [4.5]_{|s2}$, and Δsky_1 and Δsky_2 refer to the uncertainties in the determination of the sky for a given galaxy in each of the bands. In particular, there are two sky uncertainties computed within S⁴G Pipeline 3: one reflects Poisson noise, while the other refers to the large-scale background errors (rms calculated within and among different sky boxes; Muñoz-Mateos et al. 2013, see also Muñoz-Mateos et al. 2009 for a detailed discussion). Our global estimate of the sky error is calculated as $\Delta\text{sky} = \sqrt{\Delta\text{sky}_{\text{Poisson}}^2 + \Delta\text{sky}_{\text{large scale}}^2}$, which has a typical (median) value of 0.013 MJy/sr for both bands. Here, we neglect any uncertainties associated to the photometric zero points.

There is also uncertainty intrinsic to the ICA method, namely the reliability or uniqueness of a solution identified in any given measurement set. Our algorithm includes a quantification of the uniqueness of the solution by performing ICA on each measurement set N times, each time with a different initial seed matrix of mixing coefficients (bootstrapping). Perturbations to the initial seed are fixed for all galaxies in the sample and represent N possible realistic mixtures of old stars and dust emission. Optimally, ICA quickly converges to its final solution independent of the initial seed (Meidt et al. 2012a). The range of final mixing coefficients sets the uncertainty on the final average solution, and this ICA color uncertainty corresponds typically to values of order ~ 0.07 mag. The ICA

tests presented in the appendices confirm the meaningfulness of these uncertainties.

The $s1$ color change associated with the second iteration is typically of the order of ~ 0.04 mag. Interestingly, in 88% of the cases, this color change is well constrained by the initial ICA bootstrap uncertainty (i.e., the change occurs within the $s1$ color error bar). Taking this into account, and considering the typical values listed in Table 2, we can state that the ICA bootstrap error is the dominant source of uncertainty, and provides a good estimate of how accurate our solutions are (see Appendix B).

4.8. Quality Flagging

To account for the varying quality of solutions, flags are provided along with the final products. Flagging has been independently performed by two of the authors (Sharon Meidt, Miguel Querejeta) and an external classifier (Emer Brady), according to well-defined criteria.

1. Is the physical distribution of the identified dust in accordance with the signatures that appear in the color map?
2. Are there significant oversubtractions in the map of old stellar flux?
3. Are there any artifacts that prevent ICA from obtaining a correct solution?

Three quality flags have been established: 1—*excellent*, 2—*acceptable*, 3—*bad*, and the statistical mode is chosen as the final classification (cases in which all three classifiers disagree have been revised and individually discussed). Depending on the specific application of the mass maps, only those galaxies classified as either 1 or both 1 and 2 will be suitable; also, some of the solutions classified as 3—*bad* correspond to galaxies in which the input data was contaminated by artifacts (e.g., mux bleeds or saturated PSFs), and a personalized case-by-case treatment of the masks can potentially improve the quality of those solutions (but we have not done it to avoid introducing a subjective component, and for homogeneity of the pipeline results).

It should be noted that, within the group of more than 1200 galaxies that constitute our final *science sample* (Section 6), very few have the *bad* quality flag, “3” (only 3.5%). This is, to a great extent, because we have conservatively excluded from the analysis all galaxies with low S/N, which systematically lead to solutions of poorer quality.

5. STELLAR MASS MAPS AND PRODUCTS RELEASED

The dust-free flux maps that we produce with our Pipeline 5 can be directly converted into mass maps by choosing the appropriate M/L and assumed distance. In Section 5.1 we refer to a possible strategy to choose M/L , including the necessary conversions into appropriate units. In Section 5.2 the product release of S⁴G Pipeline 5 is described.

5.1. Converting to Stellar Mass Maps

Using the IRAC zero magnitude flux density at 3.6 and 4.5 μm , $\text{ZP}_{3.6\mu\text{m}} = 280.9$ Jy and $\text{ZP}_{4.5\mu\text{m}} = 179.7$ Jy (Reach et al. 2005), and the corresponding absolute magnitude of the Sun, $M_{\odot}^{3.6} = 3.24$ mag (Oh et al. 2008), we obtain the

following relationship for the $3.6\ \mu\text{m}$ IRAC band:

$$1\ \text{MJy/sr} = 704.04\ L_{\odot}/\text{pc}^2. \quad (5)$$

Starting from an ICA-corrected flux surface density measurement $S_{3.6\ \mu\text{m}}$ in *Spitzer* units of MJy/sr, the stellar mass contained by a pixel ($0.75''$) can be obtained as

$$\frac{M}{M_{\odot}} = 9308.23 \times \left(\frac{S_{3.6\ \mu\text{m}}}{\text{MJy/sr}} \right) \times \left(\frac{D}{\text{Mpc}} \right)^2 \times \left(\frac{M/L_{3.6\ \mu\text{m}}}{M_{\odot}/L_{\odot}} \right). \quad (6)$$

For a detailed discussion on how to choose the optimal $3.6\ \mu\text{m}$ M/L , the reader is referred to Meidt et al. (2014) and Norris et al. Here we adopt a single $M/L = 0.6$ (assuming a Chabrier IMF), which according to both sets of authors can convert the $3.6\ \mu\text{m}$ old stellar flux (with dust removed) into stellar mass with an accuracy of ~ 0.1 dex. Given that the dependence on age and metallicity of the M/L at $3.6\ \mu\text{m}$ is relatively small for old stellar populations, Meidt et al. (2014) advocate for this constant M/L and its uncertainty assuming a universal age–metallicity relation, together with the constraint on metallicity (and thus age) provided by the $[3.6]–[4.5]$ color. Following an independent, empirical strategy, Norris et al. argue for a comparable value, without invoking such an argument. A M/L of 0.6 is also found to be representative in stellar population synthesis models, extended to the wavelength range of $2.5–5\ \mu\text{m}$ using empirical stellar spectra by Röck et al.

5.2. Public Data Products

To give users the opportunity to choose their preferred distance and M/L , we release the map of the old stellar flux (map *s1*), along with the dust map (*s2*). To allow for the choice of a spatially varying M/L , we also provide a color map for the old stars. This color map conserves the original $[3.6]–[4.5]$ color in all pixels without non-stellar emission (i.e., where $s2 = 0$ after thresholding), and $[3.6]–[4.5]_{s1}$ elsewhere. Additionally, the quality flags, colors and integrated fluxes of each component are made public in a table format.

Our recommended post-processing strategy is explained in Section 4.6, which includes interpolation over masked areas. However, a myriad of interpolation techniques exist, and some users may even prefer to leave all the original flux unchanged for those regions. Therefore, we also provide the masks used, making it possible for different strategies to be applied. In a final step, for aesthetical purposes, dust maps have been smoothed in the areas of significant dust emission using a Gaussian kernel of $\sigma = 2$ px and conserving total flux between *s1* and *s2*, but unsmoothed maps are available upon request. The release of Pipeline 5 products takes place on the NASA/IPAC Infrared Science Archive (IRSA).

6. FINAL SAMPLE WITH ICA SOLUTIONS

In Section 4 we introduced an initial cut in signal-to-noise to make sure that we apply ICA in a regime in which it can perform correctly. Excluding all galaxies with $S/N < 10$ made 667 objects be initially discarded. Additionally, it was explained in Section 4.2 that 376 galaxies from $S^4\text{G}$ (16.3% of total) have original colors which are already compatible with an old stellar population. On those objects, and using the weighted mean of the original color to discriminate, we do not apply ICA, given that the fractional contamination from dust is

Table 3
Fraction of $S^4\text{G}$ Galaxies to Which ICA has been Applied

Group/Class	Number of		Criterion
	Galaxies	Fraction ^a	
All $S^4\text{G}$	2352
Good P3 data ^a	2308	100%	...
Low S/N: discarded	644	28.0%	$S/N < 10$
Little dust: ICA not applied	376	16.3%	$[3.6]–[4.5]_{\text{orig,weighted}} < 0$
ICA applied	1288	55.8%	$[3.6]–[4.5]_{\text{orig,weighted}} > 0$
1. <i>s1</i> compatible with old stars	1251	54.2%	$-0.2 < [3.6]–[4.5]_{s1} < 0$
2. <i>s1</i> incompatible with old stars	37	1.6%	rest
Total good mass maps	1627	70.5%	...

Note.

^a At the time of running our pipeline, not all of $S^4\text{G}$ galaxies had Pipeline 3 (P3) data available; the ones that failed at P3 are typically those with the poorest data quality, and even if some have been added later on, we prefer not to include them in the analysis, as they are few and likely problematic. The *fraction of total* is therefore referred to the 2308 galaxies with good P3 data at the moment we ran this Pipeline 5.

low (typically below $\sim 15\%$). We have shown (see Appendix A) that uncertainties become large under those conditions, and we risk incurring a larger error by inaccurately removing the dust emission present, if any, than not correcting for it.

In fact, the group of 376 galaxies with original blue colors to which we do not apply ICA is clearly dominated by early-type galaxies. The majority (201 galaxies) are ellipticals or S0s, and the rest are predominantly early-type spirals. For those early-type galaxies, based on scaling relations from longer wavelengths, we can assume a maximum fraction of flux due to dust of $\sim 15\%$, which constrains the maximum global error due to not applying a dust correction (see Appendix A).

Once galaxies with low signal to noise and original blue colors have been excluded, the optimized algorithm explained in Section 4 has been applied to the rest of the $S^4\text{G}$ sample, which includes galaxies across the whole Hubble sequence, covering a wide range of masses and SFRs. This extends the work by Meidt et al. (2012a) to a much broader range of galaxy types and observational characteristics. Table 3 summarizes the different groups of galaxies that we have just mentioned.

We find that, after applying ICA, 1251 galaxies have *s1* colors compatible with those expected for old stars, $-0.2 < [3.6]–[4.5]_{s1} < 0$. The former range matches the colors expected for K and M giants (see Meidt et al. 2014, and as observed in old, dust-free E/S0 galaxies, Peletier et al. 2012, and in globular clusters, Norris et al.). Only 37 galaxies have final *s1* colors that do not match the range expected for old stars. Adding the (mainly early-type) galaxies to which we did not apply ICA because they already had original colors compatible with old stars, this means that we have a total of more than 1600 galaxies with good mass maps.

Figure 7 shows the distribution of the galaxies in our final ICA-corrected catalog according to distance, morphological type and SFRs, proving that it covers a representative range in all three properties. For reference, the distribution of galaxies to which we did not apply ICA due to original colors compatible with old stars is overlaid in red, and an empty black line shows the global distributions for the entire $S^4\text{G}$.

THE ASTROPHYSICAL JOURNAL SUPPLEMENT SERIES, 219:5 (19pp), 2015 July

QUEREJETA ET AL.

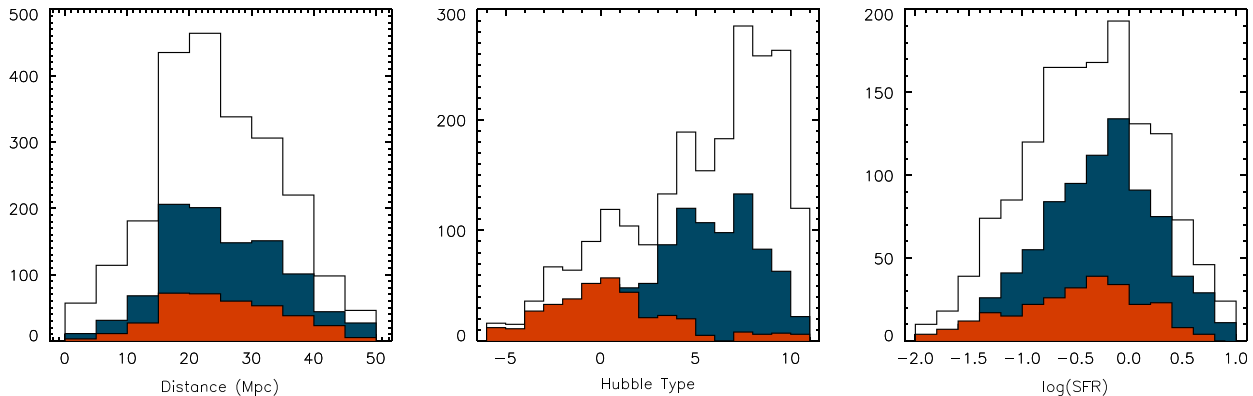


Figure 7. Histograms showing the distances, morphological types and star formation rates spanned by the galaxies in our science sample (blue). Overplotted in red is the distribution of the galaxies to which ICA was not applied (compatible with old stars). The global S^G distributions are shown by the empty black histograms.

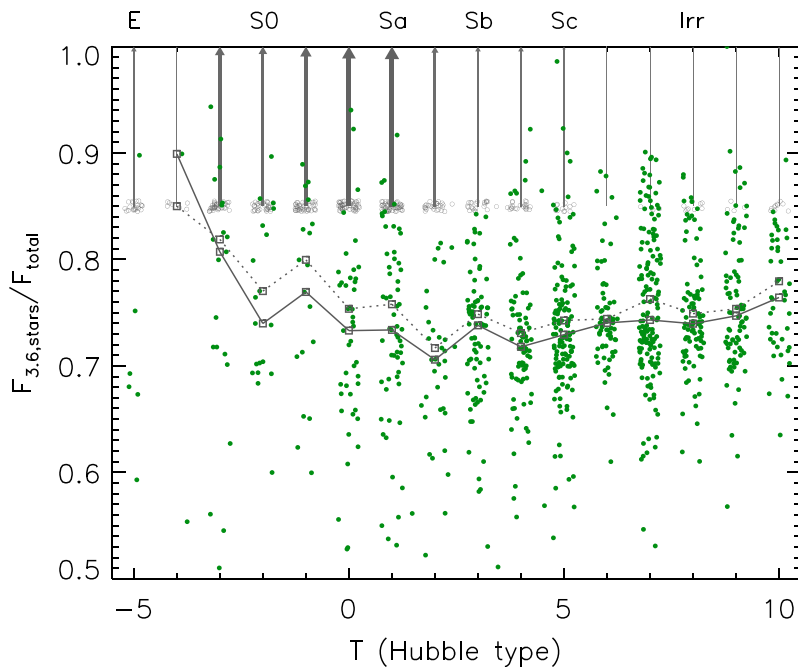


Figure 8. Fraction of total observed $3.6 \mu\text{m}$ flux arising from old stars as a function of Hubble type. The open circles located at $F_{\text{stars}}/F_{\text{total}} \approx 0.85$ correspond to the galaxies with original blue colors to which ICA was not applied; they are included here as lower limits for reference (maximum expected contamination of 15%, see Appendix A; thickness and darkness of arrows are proportional to the number of galaxies in each bin). We see that contamination becomes more severe toward later T , tracking an increase in dust content until the latest types, where dust and PAHs are fewer. The gray squares joined by a continuous line represent the running medians in each bin, excluding lower limits, while the squares joined by a dotted line are the equivalent considering the lower limits.

7. RESULTS

7.1. Trends with Hubble Type

Here we explore how the stellar flux fraction ($s1/\text{total}$) changes as a function of Hubble type (Figure 8). We can see that the observed $3.6 \mu\text{m}$ flux becomes a poorer tracer of stellar mass as the Hubble type increases, because dust emission becomes more significant. This contamination from dust increases slightly toward late-type galaxies, as shown by the running medians, and seems to decrease again for the latest Hubble types.

The reason for this final decline in contamination is probably due to the fact that very late-type galaxies tend to have less dust as they have lower metallicity. For standard spiral galaxies (Sa-Sc), the stellar component contributes $\sim 70\%$ – 80% of the flux (i.e., as much as 20%–30% is coming from dust), with

both upper and lower outliers. Moreover, these are only global estimates, and these values can be significantly higher in individual star-forming regions, as shown by Meidt et al. (2012a). To account for completeness, we include as lower limits the galaxies to which ICA was not applied due to original blue colors (compatible with old stars, which implies little dust emission): they are shown as gray arrows marking the upper limit of 15% contamination that is estimated in Appendix A (and the arrow thickness is proportional to the number of galaxies per bin).

7.2. Trends with SFR

In an attempt to investigate the main driver behind the varying flux fraction due to old stars at $3.6 \mu\text{m}$, in Figure 9 we

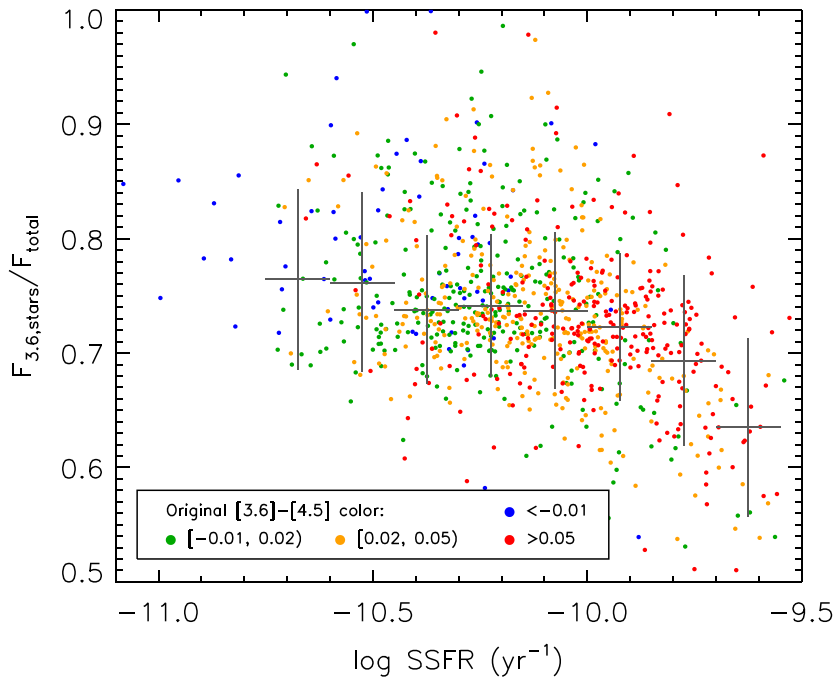


Figure 9. Fractional contribution from old stars to total $3.6 \mu\text{m}$ flux as a function of specific star formation rate: there is a clear trend between fractional $s1$ and $SSFR$, as it can be seen by the almost monotonic drop of the running mean (the width of the running median is the bin size, and height measures the standard deviation of points in each bin). The points represent all galaxies with ICA solutions compatible with old stars and SFR measurements available (a total of 819 galaxies).

plot that same quantity ($F_{3.6,stars}/F_{total}$) as a function of the specific star formation rates (SSFRs), and find a declining correlation. We calculate SSFRs as the SFRs divided by our stellar mass, which is derived from the $3.6 \mu\text{m}$ flux corrected for dust with a $M/L = 0.6$, and integrated within the $25.5 \text{ mag arcsec}^{-2}$ isophote. The SFRs come from IRAS 60 and $100 \mu\text{m}$ fluxes (the weighted average of the values reported in NED), following the recipe from Larsen & Richtler (2000). Therefore, the subsample shown in Figure 9 is all S^4G galaxies with ICA solutions compatible with old stars (within their uncertainties) and with availability of SFRs, which makes a total of 819 galaxies. Galaxies with higher SSFRs have on average higher fractional contamination from dust, which makes the fractional flux due to stars drop (see running median in Figure 9).

Finally, there is no obvious trend of dust emission fraction with SFR alone: the SFR relative to the total mass of the galaxy (SSFR) is a better first-order indicator of how much flux is arising from dust and not from old stars at $3.6 \mu\text{m}$.

7.3. Global Stellar Mass Estimates at $3.6 \mu\text{m}$

We have successfully isolated for old stellar emission the $3.6 \mu\text{m}$ images of more than 1600 galaxies in S^4G , which provides us with an unprecedentedly large sample of stellar mass estimates for nearby galaxies. This statistically powerful tool allows us to produce an empirical calibration of the M/L and its scatter as a function of observed original color of the galaxy.

Our empirical *effective* M/L as a function of $[3.6]-[4.5]$ global color is shown in Figure 10. This is the M/L required to convert the uncorrected $3.6 \mu\text{m}$ flux—including both stellar and non-stellar emission—into stellar mass, calculated by dividing the stellar mass implied by the $s1$ map for each galaxy

by the total original luminosity in the analysis area. The stellar mass is calculated by multiplying the total luminosity in the $s1$ map by a constant mass to light ratio $0.6M_{\odot}/L_{\odot}$ (Meidt et al. 2014), and divided by the total original luminosity within our area of analysis. It is important to note here that the abscissa is the original integrated color that would be available, for instance, to an observer that cannot spatially resolve a galaxy; this is different from the weighted mean color (based on the pixel-to-pixel photometric uncertainty) that we used to discriminate which galaxies to apply ICA to in the first step of our pipeline.

Overplotted in Figure 10 as a thick, continuous line is the regression to the data points in the range $-0.1 < [3.6] - [4.5] < 0.15$, which provides the calibration

$$\log(M/L) = -0.339(\pm 0.057) \times ([3.6] - [4.5]) - 0.336(\pm 0.002). \quad (7)$$

We can also express this in the following equivalent form, which provides stellar mass in terms of the measured 3.6 and $4.5 \mu\text{m}$ flux densities (expressed in Jy) and the distance (in Mpc):

$$\frac{M_*}{M_{\odot}} = 10^{8.35} \times \left(\frac{F_{3.6}}{\text{Jy}} \right)^{1.85} \times \left(\frac{F_{4.5}}{\text{Jy}} \right)^{-0.85} \times \left(\frac{D}{\text{Mpc}} \right)^2. \quad (8)$$

The decreasing trend in Figure 10 suggests that color is indeed a good first-order indicator of the level of contamination and, therefore, of the M/L for a given galaxy. The impact of contamination on the M/L is demonstrated by the color-coding based on SSFRs: since high SSFRs are typically associated with redder galaxies (see color coding in Figure 9), this provides a physical connection to the trend found in Figure 10.

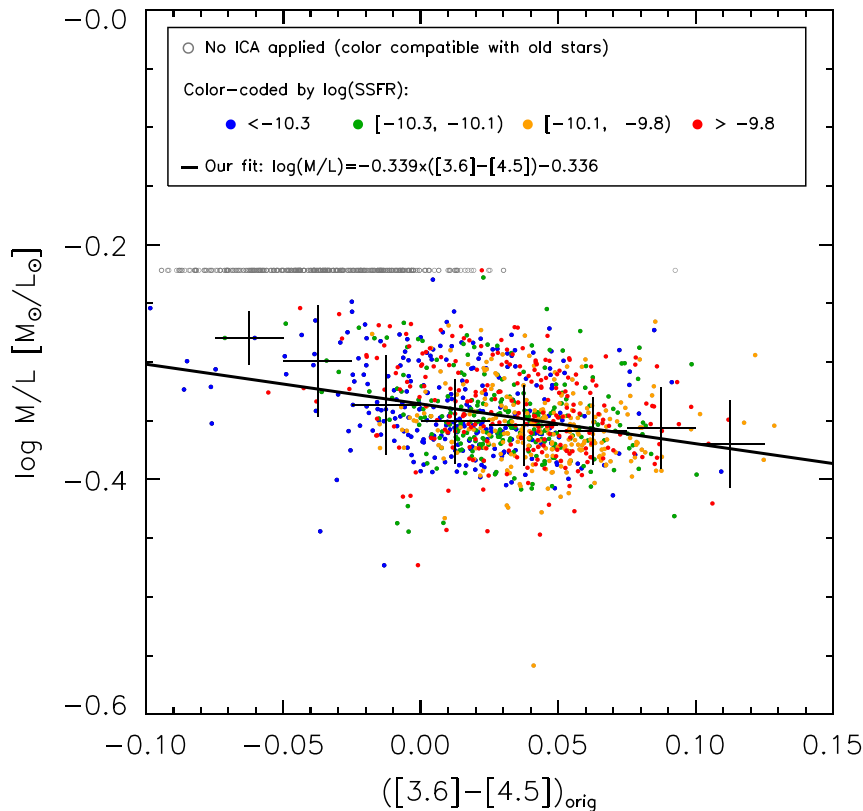


Figure 10. Our empirical mass-to-light ratio is obtained by multiplying the total flux in our dust-free maps by the $M/L_{3.6\mu\text{m}} = 0.6 (M_{\odot}/L_{\odot})$ suggested by Meidt et al. (2014), and dividing it by the total original $3.6\mu\text{m}$ flux inside the ICA solution area. This is plotted against the original $[3.6]-[4.5]$ color (obtained from the integrated 3.6 and $4.5\mu\text{m}$ fluxes within our area of analysis, which makes this differ from the weighted mean color that we used to discriminate to which galaxies we apply ICA). The galaxies with original negative weighted mean colors to which we did not apply ICA are shown with gray open circles for reference, with a constant $M/L_{3.6\mu\text{m}} = 0.6 (M_{\odot}/L_{\odot})$. The color-coding shows that there is some trend with SSFR, as it could be expected from Figure 9: it is the dustiest galaxies with highest SSFRs that most significantly diverge from the constant value of $M/L = 0.6$. Running medians are shown on top, in color intervals of 0.025 (the vertical length is the standard deviation of points in each bin). The linear fit is obtained using FITEXY in the range $-0.1 < [3.6]-[4.5] < 0.15$.

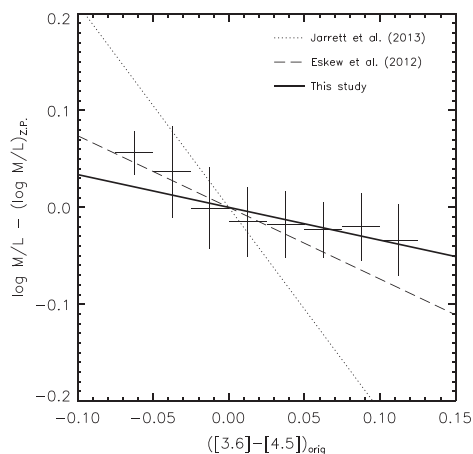


Figure 11. Linear fit to the effective M/L measured after removing dust emission from the S^4G galaxies is plotted, along with the running medians, relative to the purely stellar $M/L_{3.6\mu\text{m}} = 0.6 (M_{\odot}/L_{\odot})$ from Meidt et al. (2014). Here, we compare against the trend found by Jarrett et al. (2013), which is shown with a dotted line, and the color-dependent $M/L_{3.6\mu\text{m}}$ from Eskew et al. (2012), with a dashed line. For this comparison, all relations have been normalized so that $\log(M/L) = 0$ at $[3.6]-[4.5] = 0$.

Galaxies in which star formation is relatively more prominent (higher SSFRs) have more dust emission in these bands, leading to redder colors and thus also requiring a lower M/L to convert the light into mass.

While Figure 10 suggests that the color can be used to constrain the *effective* M/L , there is still considerable scatter at fixed $[3.6]-[4.5]$ color. We therefore recommend adopting an uncertainty of ~ 0.2 dex on our empirical relation, which also accounts for the 0.1 dex uncertainty associated with our adopted stellar M/L (see Section 5.1). (We note, however, that a method that can correctly remove dust emission, such as the one that we have presented here, should be the preferred approach for estimating stellar masses.)

Our relation between the effective M/L and $[3.6]-[4.5]$ color, calibrated using our optimal stellar mass estimates, compares well with other relations in the literature. As part of the *WISE* Enhanced Resolution Galaxy Atlas, Jarrett et al. (2013) also found a declining correlation between $W1$ and $W2$ color (the 3.4 and $4.6\mu\text{m}$ *WISE* bands) and M/L at $3.6\mu\text{m}$, based on their observational stellar mass estimates of a few (~ 15) galaxies. Figure 11 shows that the slope that we find is considerably shallower, based on a sample nearly 100 times larger. In this plot we show $\Delta M/L$ in order to highlight the IMF-independent

slopes of each relation and avoid differences in vertical offset due to choice of the IMF.

We also find good agreement with the stellar M/L estimated by Eskew et al. (2012). Using a different method, based on spatially resolved star formation histories (SFHs) in the LMC, they calibrated a conversion between 3.6 and 4.5 μm fluxes and stellar mass. This can be translated into an equivalent color-dependent M/L ($\log M/L = -0.74([3.6] - [4.5]) - 0.236$), which is overplotted on Figure 11, also normalized so that $\log(M/L) = 0$ at $[3.6] - [4.5] = 0$.

It is remarkable that, in spite of the very different method used, their declining slope is very similar to the fit to our data. Finally, it is also worth mentioning that McGaugh & Schombert (2014) recently point to a constant $M/L_{3.6\mu\text{m}} = 0.47$, with a scatter of 0.1 dex, which is also compatible with our result.

8. SUMMARY AND CONCLUSIONS

We have developed a pipeline to obtain maps of the flux from old stars for the 3.6 μm images in the *Spitzer* Survey of Stellar Structure in Galaxies (S⁴G). Following two different approaches, Meidt et al. (2014) and Norris et al. have shown that the M/L for old stars at 3.6 μm varies modestly with the age and metallicity of the population, so that a constant M/L is applicable with an uncertainty of ~ 0.1 dex. Therefore, when only old stars contribute to the flux at 3.6 μm , a simple re-scaling of the corresponding dust-free S⁴G image effectively constitutes a stellar mass map. However, this is complicated by the fact that dust emission usually contributes a significant fraction of that flux ($\sim 10\%$ – 30%); therefore, a way to automatically correct for this dust emission is highly desirable.

At the core of our method is the application of an ICA technique, first presented in Meidt et al. (2012a), to remove dust emission from these bands. We simultaneously use the information from the 3.6 and 4.5 μm images, which are uniformly available for the whole S⁴G sample. Old stars (age $\tau \sim 2$ – 12 Gyr) have colors in the range $-0.2 < [3.6] - [4.5]_{\text{stars}} < 0$, whereas dust corresponds to $[3.6] - [4.5]_{\text{dust}} > 0$, and this difference in SED allows ICA to separate both components. Our method results in an unbiased view of the flux from old stars, which can then be readily used to chart the stellar mass distribution.

Some galaxies in S⁴G have original colors which are already compatible with an old stellar population, but they are the exception rather than the rule (376, 16% of the sample). These are preferentially early-type galaxies, and they have little dust emission: we therefore do not run ICA on them. We also exclude from the ICA analysis all galaxies with average signal to noise below $S/N < 10$, to make sure that we apply our pipeline in a regime in which ICA can perform correctly.

For 1251 galaxies (54% of the overall sample), ICA is able to find a trustworthy separation into dust emission and old stars. For these galaxies, stars typically contribute 70%–90% of the flux at 3.6 μm , with dust contamination peaking at $T \sim 5$. This dust contamination shows a strong correlation with SSFRs, confirming that the dust emission that we are correcting for is mostly related to star formation.

We have also profited from the statistical power of such a large sample of accurate mass estimates to calibrate a relationship between the observed $[3.6] - [4.5]$ color and the empirical $M/L_{3.6\mu\text{m}}$ that should be applied to obtain the same stellar masses as we measure. Our regression line is $\log(M/L) =$

$-0.339(\pm 0.057) \times ([3.6] - [4.5]) - 0.336(\pm 0.002)$, for an assumed $M/L_{3.6\mu\text{m}} = 0.6 M_{\odot}/L_{\odot}$ for the old stellar population. The correlation shows a large scatter, however, which points out the necessity to apply a method like the one we have described if higher precision is required, or if one is interested in the spatial distribution of such stellar mass.

In conclusion, we have produced maps which reliably trace the old stellar flux for a large fraction of the S⁴G sample. These maps, which trace the distribution of stellar mass, will be made publicly available through IRSA (along with the S⁴G archive), providing a powerful tool for the astronomical community. Additionally, we have outlined a strategy to remove dust emission from mid-IR images, and analyzed the requirements for a successful application. This could be relevant for similar studies that aim to exploit *Spitzer* archival data, and, eventually, with the advent of the *James Webb Space Telescope*, this technique should prove very useful to push spatially resolved galaxy mass estimations further to higher redshifts.

We are grateful to the anonymous referee for very insightful comments and suggestions, which have helped us improve the quality of the paper. We acknowledge financial support to the DAGAL network from the People Programme (Marie Curie Actions) of the European Union's Seventh Framework Programme FP7/2007-2013/ under REA grant agreement number PITN-GA-2011-289313. M.Q. acknowledges the International Max Planck Research School for Astronomy and Cosmic Physics at the University of Heidelberg (IMPRS-HD). We thank Emer Brady for acting as an external classifier for assigning quality flags, and Simón Díaz-García for helpful comments. K.S., J.-C. M.-M., and T.K. acknowledge support from the National Radio Astronomy Observatory is a facility of the National Science Foundation operated under cooperative agreement by Associated Universities, Inc. E.A. and A.B. acknowledge financial support from the CNES (Centre National d'Études Spatiales). L.C.H. acknowledges support from the Kavli Foundation, Peking University, and the Chinese Academy of Science through grant No. XDB09030100 (Emergence of Cosmological Structures) from the Strategic Priority Research Program. This research has made use of the NASA/IPAC Extragalactic Database (NED) which is operated by the Jet Propulsion Laboratory, California Institute of Technology, under contract with the National Aeronautics and Space Administration.

APPENDIX A

ROBUSTNESS OF ICA SOLUTIONS FOR S⁴G IMAGES

In order to quantify the conditions under which ICA retrieves robust solutions, we have constructed a set of models representing realistic distributions of stars and dust in nearby galaxies. These models cover a range of dust colors and fractional dust flux contributions, and also allow for the inclusion of a third component that emulates hot dust in H II regions. We consider the latter of such models in order to demonstrate the improvement to solutions possible when a second ICA iteration is applied in the presence of a second non-stellar source (three sources in total; see Section 4.3).

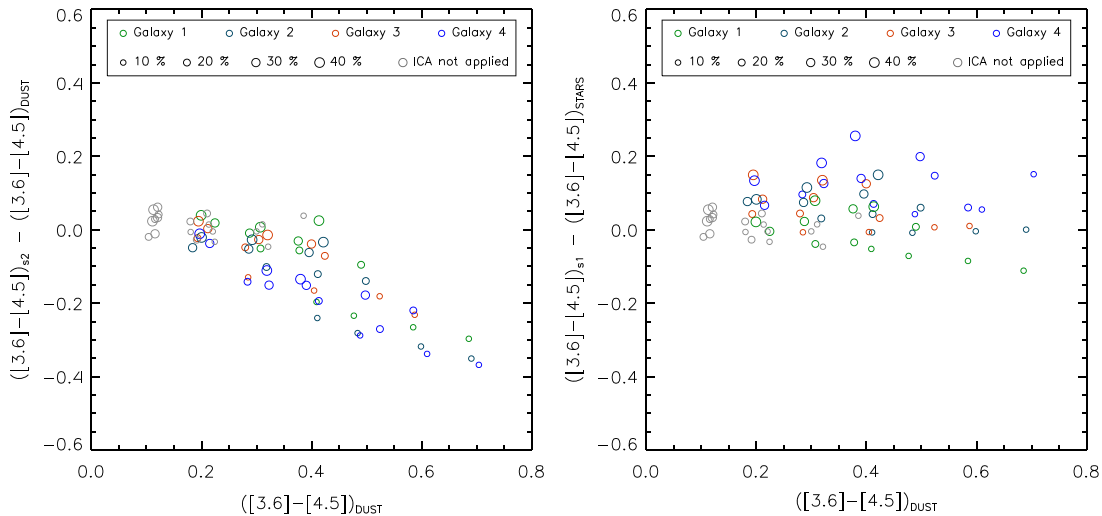


Figure 12. Difference between the $s1$ (left) and $s2$ (right) colors identified by ICA and the original color of stars and dust in the models as a function of dust input color. Models where ICA would not have been applied due to original blue colors are shown in gray.

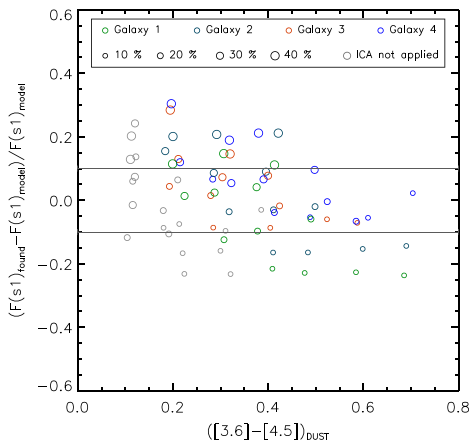


Figure 13. Difference between the corrected stellar fluxes found by ICA and the stellar flux imposed on each of model, as a function of the imposed dust color. Symbol sizes are proportional to the dust contamination fraction, and different colors correspond to models based on different galaxies. Gray circles are those models that lead to original (weighted) mean colors that are negative, which means that we would not have applied ICA to them.

A.1 Input Parameters and Models

We conduct our tests by creating two-dimensional realistic distributions of the emission from old stars and dust. As input models we utilize the spatial distributions of the components $s1$ (old stellar light) and $s2$ (dust emission) identified with ICA for four galaxies that cover a range in morphology. For these specific galaxies, the $s1$ and $s2$ components were shown to be representative of old stars and dust in Meidt et al. (2012b). Based on these, our model input maps at 3.6 and 4.5 μm are generated in the following way: (a) the color of old stars is fixed at $[3.6]-[4.5] = -0.12$; (b) the color of dust is varied between $[3.6]-[4.5] = 0$ and $[3.6]-[4.5] = 0.6$; (c) the fractional contribution of dust emission to the total flux is varied from 5% to 40%.

In each case, we verified that the resulting colors of each of the combined $s1+s2$ models are consistent with the observed colors in the S^4G sample, which cover the range

$-0.05 < [3.6]-[4.5] < 0.20$ (if we exclude the 5% tail at the upper and lower ends).

A.2 Controlling Parameters

We run a total of 60 tests per galaxy, covering the total dust color range $0.2 \leq [3.6]-[4.5] \leq 0.7$ in steps of 0.1, and varying the fractional contribution of dust by 10%, 20%, 30%, and 40%. We also explore the dependence on the dust spatial distribution by repeating each battery of experiments on four different galaxy models; for reference, models 1 through 4 are based on NGC 2976, NGC 3184, NGC 4321, and NGC 5194, respectively.

A.2.1 Relative Color Difference Between $s1$ and $s2$

As explained above, we have fixed the stellar color to $[3.6]-[4.5]_{\text{stars}} = -0.12$. In testing we have found that only the *relative* difference between the colors imposed for the dust and stars impacts the colors determined by ICA for a given model; tests with a stellar color -0.02 return identical results to those presented below when the $[3.6]-[4.5]_{\text{dust}}$ in the model is also shifted by 0.10.

A.2.2 Fractional Contribution of Dust Emission

The maximum fractional contribution of dust to the total flux that we impose, 40%, is motivated by the fact that we do not expect larger dust contributions in real galaxies. Following Bendo et al. (2008), we obtain an estimate of the PAH fluxes at 8 μm based on 160 μm measurements from Galametz et al. (2012). We then calculate the possible range corresponding to those values at 3.6 μm following Flagey et al. (2006). That provides the possible dust fluxes at 3.6 μm , and for that sample of galaxies, we also obtain the total 3.6 μm fluxes from NED (as the weighted mean of the available values, using the quoted uncertainties). This allows us to set an upper limit of 40% to the fractional contribution of dust flux for star-forming spirals (but that is a rare upper limit; the typical values range 20%–25%). Using the fact that $I_{160 \mu\text{m}}$ correlates well with the $f_{\text{dust}}/f_{\text{stars}}$ parameter, we can make use of the fractions $f_{\text{dust}}/f_{\text{stars}}$ from Skibba et al. (2010) to conclude that the fractional

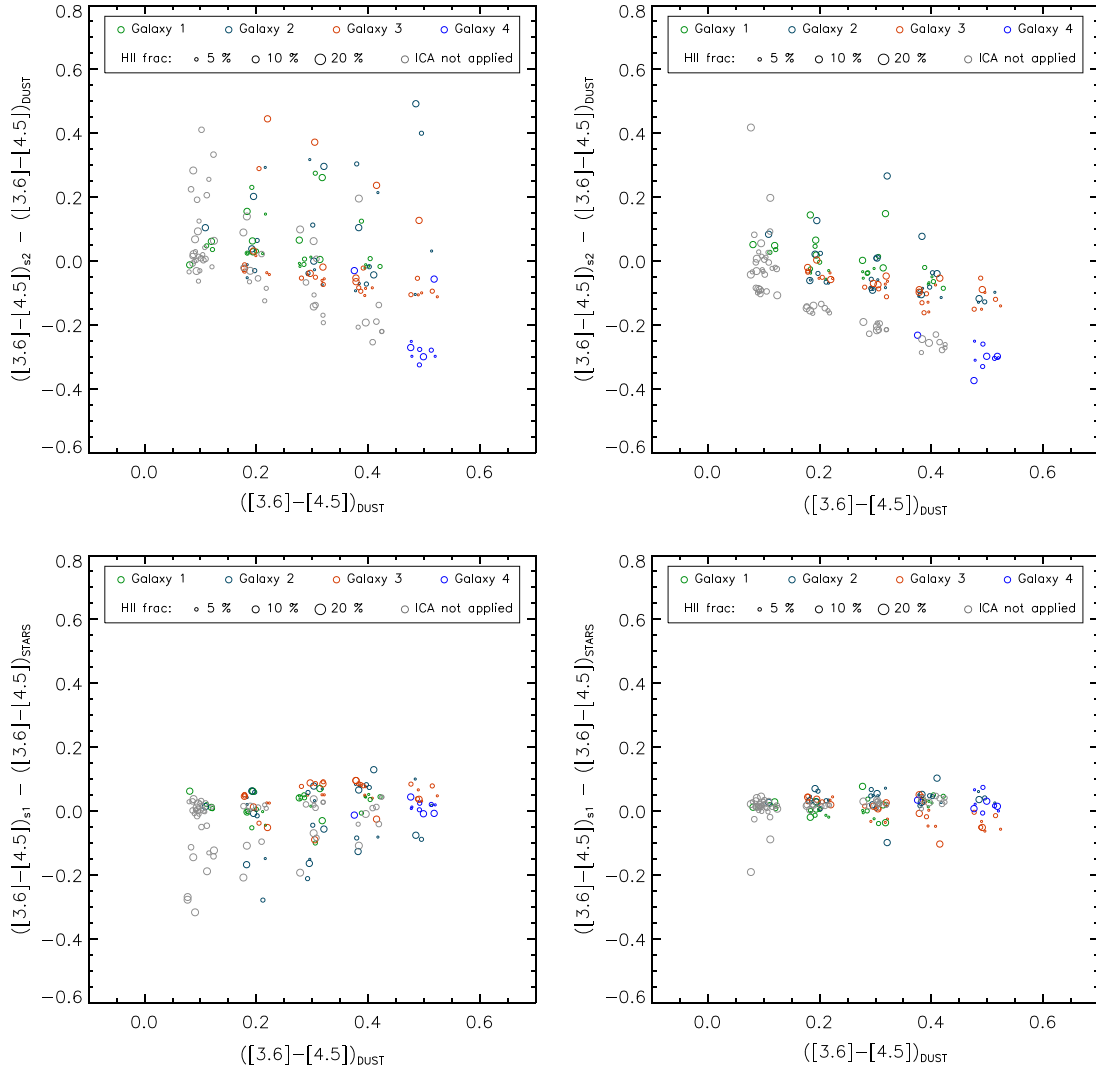


Figure 14. Plots showing the effect of including a third component of redder colors in the models, and how our second iteration of ICA alleviates that problem. Left column: first iteration, ICA₁; right column: second iteration, ICA₂. Top: difference between s_2 color and the color imposed on the spatially extended dust, as a function of the color imposed on H II regions; bottom: same difference as a function of the color imposed on the spatially extended dust.

contribution of dust flux for early-type galaxies ($T \leq 0$) is a factor of 3 lower than for late-type galaxies, which corresponds to an upper limit of $\approx 15\%$.

In addition, in Section 4.2 we introduced our criterion to exclude galaxies with original blue colors from the ICA analysis, as it is an indication that those galaxies are already compatible with an old stellar population. To account for this, in Figure 13 we identify the models in which that criterion is met with a different color.

A.3 Findings

The difference between the stellar and dust colors imposed on each model and the s_1 and s_2 colors found by ICA are shown in Figure 12, as a function of the dust color of the model. To improve the visibility of the plotted data points, we introduce a small artificial random scatter around each discrete dust color value (a random dithering within ± 0.05). The symbol size of each point is proportional to the dust fraction, while the colors denote the original galaxy on which the

models are based (highlighting the effect of two-dimensional dust distribution). Most striking is the clear trend for increased scatter in the ICA-determined dust colors (and stellar colors, although less so) when the “intrinsic” dust colors are redder. ICA underestimates the dust color more severely for low contamination fractions, and, conversely, it tends to overestimate the stellar color (but not as much) at the highest contamination fractions.

However, as shown in Figure 13, this large uncertainty in dust and stellar colors does not necessarily imply larger uncertainties in the estimation of fluxes. Plotted there is the difference between the stellar flux imposed on the model and the total flux in the s_1 map retrieved by ICA for all possible combinations of dust colors and contamination fractions in our model grids. Flux uncertainties in both components are sensitive to the relative stellar and dust fluxes (i.e., the level of dust contamination) but this tends to be balanced by an additional dependence on the actual difference between the stellar and dust colors. As we are ultimately interested in the

THE ASTROPHYSICAL JOURNAL SUPPLEMENT SERIES, 219:5 (19pp), 2015 July

QUEREJETA ET AL.

error in the corrected stellar fluxes found by ICA, Figure 13 suggests that ICA can perform quite well. We note that many of the models exhibit original (weighted) mean $[3.6]-[4.5]$ colors that are negative, so that we would not have applied ICA to them (see Section 4.2). Here we see that it is reasonable to exclude such galaxies from the analysis given that their low contamination fraction and/or very low dust colors (both of which can produce original colors $[3.6]-[4.5] < 0$) lead to the highest uncertainties.

Figure 13 also shows that most models lead to final uncertainties in flux within 10%, with some outliers covering a band up to 20% of uncertainty. However, these are mainly associated with the highest contamination fractions in our models (40%), and such extreme contamination from dust can be only very rarely expected (it is the upper limit for star-forming spirals, as argued in Section A.2.2).

Additionally, these tests confirm that the ICA uncertainties determined through the bootstrap method are reliable measures of the errors in color. This bootstrap uncertainty is obtained by running ICA based on 48 different seeds (different starting points in s_1 and s_2 colors). According to our models, in 94.6% of cases the difference in stellar color was well confined by the bootstrap uncertainty, confirming its meaningfulness.

APPENDIX B

EFFECT OF SECOND ICA ITERATION

Given the possibility that more than one emitting dust component may be present (and, in particular, for H II regions in addition to the nominal diffuse dust component), we have implemented a second iteration of ICA (Section 4.3) aimed at removing the reddest emitting regions.

Since ICA is sensitive to color outliers, a second iteration of ICA with the regions with more extreme colors masked allows us better retrieve the spatially dominant dust component, which is typically not as red. Our implementation of the second iteration is confirmed with the following tests, described below.

B.1 Input Models

To test the impact of a third component on ICA solutions assuming two components (and to confirm the usefulness of our second ICA iteration), we have included an additional component with an intrinsically redder color representative of hot dust in H II regions, i.e., $[3.6]-[4.5] = 1$. For the spatial flux distribution, we use truncated De Vaucouleurs profiles (de Vaucouleurs 1948), and place them randomly in the regions of the galaxy model where the more extended dust emission is significant (higher than the mean dust flux). We vary the total number of regions (10, 20, 30) and their relative brightness (5%, 10%, 20% of total dust flux). We also explore a range of colors, starting from the color of the spatially extended dust itself, up to a maximum color of 0.6.

B.2 Findings

When run through our pipeline, we can indeed see that our simulated H II regions get effectively masked, and the second iteration leads to a dust color closer to the nominal spatially extended “diffuse dust” in 94.7% of the experiments (see Figure 14). Moreover, the bootstrap uncertainty is effectively reduced after the second iteration (from ~ 0.8 to ~ 0.2 mag), suggesting that our measure of errors is sensitive to the problem posed by a third component of intrinsically different color,

which is relieved by the iterative ICA approach that we have constructed.

REFERENCES

- Aniano, G., Draine, B. T., Gordon, K. D., & Sandstrom, K. 2011, *PASP*, **123**, 1218
- Athanassoula, E. 1992, *MNRAS*, **259**, 328
- Athanassoula, E. 2013, in *Bars and Secular Evolution in Disk Galaxies: Theoretical Input*, ed. J. Falc3n-Barroso & J. H. Knapen (Cambridge: Cambridge Univ. Press), 305
- Bendo, G. J., Draine, B. T., Engelbracht, C. W., et al. 2008, *MNRAS*, **389**, 629
- Blain, A. W., Barnard, V. E., & Chapman, S. C. 2003, *MNRAS*, **338**, 733
- Buta, R. J., Sheth, K., Athanassoula, E., et al. 2015, *ApJS*, **217**, 32
- Buta, R. J., Sheth, K., Regan, M., et al. 2010, *ApJS*, **190**, 147
- Cappellari, M., Bacon, R., Bureau, M., et al. 2006, *MNRAS*, **366**, 1126
- Cid Fernandes, R., P3rez, E., Garc3a Benito, R., et al. 2013, *A&A*, **557**, A86
- Courteau, S., Cappellari, M., de Jong, R. S., et al. 2013, arXiv:1309.3276
- Daddi, E., Dickinson, M., Morrison, G., et al. 2007, *ApJ*, **670**, 156
- Draine, B. T., & Li, A. 2001, *ApJ*, **551**, 807
- de Vaucouleurs, G. 1948, *AnAp*, **11**, 247
- Eliche-Moral, M. C., Gonz3lez-Garc3a, A. C., Balcells, M., et al. 2011, *A&A*, **533**, A104
- Elmegreen, B. G., Elmegreen, D. M., Knapen, J. H., et al. 2007, *ApJL*, **670**, L97
- Elmegreen, B. G., Seiden, P. E., & Elmegreen, D. M. 1989, *ApJ*, **343**, 602
- Elmegreen, D. M., & Elmegreen, B. G. 1984, *ApJS*, **54**, 127
- Erwin, P., & Sparke, L. S. 2002, *AJ*, **124**, 65
- Eskew, M., Zaritsky, D., & Meidt, S. 2012, *AJ*, **143**, 139
- Falc3n-Barroso, J., Bacon, R., Bureau, M., et al. 2006, *MNRAS*, **369**, 529
- Fazio, G. G., Hora, J. L., Allen, L. E., et al. 2004, *ApJS*, **154**, 10
- Flagey, N., Boulanger, F., Verstraete, L., et al. 2006, *A&A*, **453**, 969
- Foyle, K., Rix, H.-W., & Zibetti, S. 2010, *MNRAS*, **407**, 163
- Galametz, M., Kennicutt, R. C., Albrecht, M., et al. 2012, *MNRAS*, **425**, 763
- Garc3a-Burillo, S., Combes, F., Schinnerer, E., Boone, F., & Hunt, L. K. 2005, *A&A*, **441**, 1011
- Gonz3lez, V., Labb3, I., Bouwens, R. J., et al. 2011, *ApJL*, **735**, L34
- Haan, S., Schinnerer, E., Emsellem, E., et al. 2009, *ApJ*, **692**, 1623
- Hony, S., Kemper, F., Woods, P. M., et al. 2011, *A&A*, **531**, A137
- Hunt, L. K., Combes, F., Garc3a-Burillo, S., et al. 2008, *A&A*, **482**, 133
- Hyv3rinen, A. 1999, *ISPL*, **6**, 145
- Hyv3rinen, A., & Oja, E. 2000, *NN*, **13**, 411
- Jarrett, T. H., Masci, F., Tsai, C. W., et al. 2013, *AJ*, **145**, 6
- Jogee, S., Scoville, N., & Kenney, J. D. P. 2005, *ApJ*, **630**, 837
- Knapen, J. H., Beckman, J. E., Heller, C. H., Shlosman, I., & de Jong, R. S. 1995, *ApJ*, **454**, 623
- Knapen, J. H., Shlosman, I., & Peletier, R. F. 2000, *ApJ*, **529**, 93
- Kormendy, J., & Kennicutt, R. C., Jr. 2004, *ARA&A*, **42**, 603
- Larsen, S. S., & Richtler, T. 2000, *A&A*, **354**, 836
- McGaugh, S., & Schombert, J. 2014, arXiv:1407.1839
- Meidt, S. E., Schinnerer, E., Garc3a-Burillo, S., et al. 2013, *ApJ*, **779**, 45
- Meidt, S. E., Schinnerer, E., Knapen, J. H., et al. 2012a, *ApJ*, **744**, 17
- Meidt, S. E., Schinnerer, E., Mu3oz-Mateos, J.-C., et al. 2012b, *ApJL*, **748**, L30
- Meidt, S. E., Schinnerer, E., van de Ven, G., et al. 2014, *ApJ*, **788**, 144
- Mu3oz-Mateos, J. C., Gil de Paz, A., Zamorano, J., et al. 2009, *ApJ*, **703**, 1569
- Mu3oz-Mateos, J. C., Sheth, K., Gil de Paz, A., et al. 2013, *ApJ*, **771**, 59
- Mu3oz-Mateos, J. C., Sheth, K., Regan, M., et al. 2015, *ApJS*, **219**, 3
- Noeske, K. G., Weiner, B. J., Faber, S. M., et al. 2007, *ApJL*, **660**, L43
- Norris, M. A., Meidt, S., Van de Ven, G., et al. 2014, *ApJ*, **797**, 55
- Norris, M. A., van de Ven, G., Meidt, S. E., Schinnerer, E., & Querejeta, M. 2015, *ApJ*, submitted, 000, 000
- Oh, S.-H., de Blok, W. J. G., Walter, F., Brinks, E., & Kennicutt, R. C., Jr. 2008, *AJ*, **136**, 2761
- Pahre, M. A., Ashby, M. L. N., Fazio, G. G., & Willner, S. P. 2004, *ApJS*, **154**, 235
- Peeters, E., Hony, S., van Kerckhoven, C., et al. 2002, *A&A*, **390**, 1089
- Peletier, R. F., Kutdemir, E., van der Wolk, G., et al. 2012, *MNRAS*, **419**, 2031
- Reach, W. T., Megeath, S. T., Cohen, M., et al. 2005, *PASP*, **117**, 978
- Regan, M. W., & Elmegreen, D. M. 1997, *AJ*, **114**, 965
- Rix, H.-W., & Rieke, M. J. 1993, *ApJ*, **418**, 123
- R3ock, B., Vazdekis, A., Peletier, R. F., Knapen, J. H., & Falc3n-Barroso, J. 2015, *MNRAS*, **449**, 2853
- Salo, H., Laurikainen, E., Buta, R., & Knapen, J. H. 2010, *ApJL*, **715**, L56
- Salo, H., Laurikainen, E., Laine, J., et al. 2015, *ApJS*, **219**, 4

THE ASTROPHYSICAL JOURNAL SUPPLEMENT SERIES, 219:5 (19pp), 2015 July

QUEREJETA ET AL.

Scoville, N. Z., Matthews, K., Carico, D. P., & Sanders, D. B. 1988, [ApJL](#), **327**, L61
Sheth, K., Vogel, S. N., Regan, M. W., Thornley, M. D., & Teuben, P. J. 2005, [ApJ](#), **632**, 217
Sheth, K., Regan, M., Hinz, J. L., et al. 2010, [PASP](#), **122**, 1397
Skibba, R. A., Engelbracht, C. W., Dale, D., et al. 2011, [ApJ](#), **738**, 89

Véron-Cetty, M.-P., & Véron, P. 2010, [A&A](#), **518**, A10
Whitmore, B. C., Chandar, R., Kim, H., et al. 2011, [ApJ](#), **729**, 78
Willner, S. P., Ashby, M. L. N., Bamby, P., et al. 2004, [ApJS](#), **154**, 222
Zaritsky, D., & Lo, K. Y. 1986, [ApJ](#), **303**, 66
Zibetti, S., Charlot, S., & Rix, H.-W. 2009, [MNRAS](#), **400**, 1181

Chapter 3

Molecular gas inflow in M51

In this chapter we quantify the rates of molecular gas inflow across the disc of the spiral galaxy M51. The transport of gas to the centre is important, as it can explain the feeding of the AGN, and it is intimately connected to the AGN feedback effects that will be studied in Chapter 4. This paper has been published in *Astronomy & Astrophysics*, 588, 33 (Querejeta et al. 2016).

Gravitational torques imply molecular gas inflow towards the nucleus of M51

M. Querejeta¹, S. E. Meidt¹, E. Schinnerer¹, S. García-Burillo², C. L. Dobbs³, D. Colombo⁴, G. Dumas⁵, A. Hughes^{6,7}, C. Kramer⁸, A. K. Leroy⁹, J. Pety^{5,10}, K. F. Schuster⁵, and T. A. Thompson^{9,11}

¹ Max Planck Institute for Astronomy, Königstuhl, 17, 69117 Heidelberg, Germany
 e-mail: querejeta@mpia-hd.mpg.de

² Observatorio Astronómico Nacional, Alfonso XII, 3, 28014 Madrid, Spain

³ School of Physics and Astronomy, University of Exeter, Stocker Road, Exeter EX4 4QL, UK

⁴ Department of Physics, 4-181 CCIS, University of Alberta, Edmonton, AB T6G 2E1, Canada

⁵ Institut de Radioastronomie Millimétrique, 300 rue de la piscine, 38406 Saint-Martin d'Hères, France

⁶ CNRS, IRAP, 9 avenue Colonel Roche, BP 44346, 31028 Toulouse, France

⁷ Université de Toulouse, UPS-OMP, IRAP, 31028 Toulouse, France

⁸ Instituto Radioastronomía Milimétrica, Avda. Divina Pastora 7, Núcleo Central, 18012 Granada, Spain

⁹ Department of Astronomy, The Ohio State University, 140 West 18th Avenue, Columbus, OH 43210, USA

¹⁰ Observatoire de Paris, 61 avenue de l'Observatoire, 75014 Paris, France

¹¹ Center for Cosmology and AstroParticle Physics, The Ohio State University, 191 West Woodruff Avenue, Columbus, OH 43210, USA

Received 10 October 2015 / Accepted 23 January 2016

ABSTRACT

The transport of gas towards the centre of galaxies is critical for black hole feeding and, indirectly, it can control active galactic nucleus (AGN) feedback. We have quantified the molecular gas inflow in the central $R < 1$ kpc of M51 to be $1 M_{\odot}/\text{yr}$, using a new gravitational torque map and the molecular gas traced by the Plateau de Bure Interferometer Arcsecond Whirlpool Survey (PAWS). The nuclear stellar bar is responsible for this gas inflow. We also used torque profiles to estimate the location of dynamical resonances, and the results suggest a corotation for the bar $CR_{\text{bar}} \sim 20''$, and a corotation for the spiral $CR_{\text{sp}} \sim 100''$. We demonstrate how important it is to correct $3.6 \mu\text{m}$ images for dust emission when gravitational torques are to be computed, and we examine further sources of uncertainty. Our observational measurement of gas inflow can be compared with nuclear molecular outflow rates and provide useful constraints for numerical simulations.

Key words. galaxies: individual: M 51 – galaxies: ISM – galaxies: structure – galaxies: kinematics and dynamics – galaxies: nuclei – galaxies: Seyfert

1. Introduction

The past decades have seen remarkable progress in our understanding of active galactic nuclei (AGN), which are associated with some of the most energetic phenomena in the Universe. It is now widely accepted that nuclear activity is caused by gas accretion onto a central supermassive black hole (SMBH; e.g. Antonucci 1993), and such black holes are expected to exist in all massive galaxies (Kormendy & Richstone 1995; Magorrian et al. 1998; Ferrarese & Merritt 2000; Gebhardt et al. 2000; Ferrarese & Ford 2005; Gültekin et al. 2009; McConnell & Ma 2013). However, fewer than half of the local galaxies that are massive enough to have an SMBH are currently active ($\sim 43\%$ if we include Seyferts, low-ionisation nuclear emission-line region galaxies, or LINERs, and transition objects; Ho et al. 1997b). It therefore seems natural to associate different levels of nuclear activity with changes in the availability of fuel: either there is an intrinsic dearth of gas in quiescent galaxies, or the transport of the existing gas to the centre is less efficient.

Recent efforts to try and understand gas transport towards the nuclei of nearby galaxies include the project NUClei of GALaxies (NUGA; e.g. García-Burillo et al. 2003, 2005; Combes et al. 2004; Boone et al. 2007; Hunt et al. 2008). It is well known

that asymmetries in the gravitational potential, such as those caused by bars, drive gas inwards (Mundell & Shone 1999; Combes 2003; Jogee 2006; Haan et al. 2009); simulations including large-scale bars also confirm this (Sparke & Sellwood 1987; Athanassoula 1992b; Shlosman & Noguchi 1993; Heller & Shlosman 1994; Hopkins & Quataert 2010, 2011). Vertical instabilities in the bar that result in boxy- and peanut-shaped bulges can also have a significant impact on the in-plane forces (Fragkoudi et al. 2015). Other mechanisms have also been suggested to explain inward motions of gas and AGN feeding, including secondary bars (Shlosman et al. 1989), nuclear spirals (Combes et al. 2014), $m = 1$ perturbations, and nuclear warps (Schinnerer et al. 2000). Finally, non-gravitational mechanisms such as viscous torques or dynamical friction of giant molecular clouds against stars have also been invoked to explain gas flows: these can become important near the very centre (Lynden-Bell 1969; Lynden-Bell & Kalnajs 1972; Combes 2002; Combes et al. 2004; García-Burillo et al. 2005).

If there is indeed a connection between asymmetries in the gravitational potential and AGN fuelling, and if such an effect is sustained over long enough timescales, an increase of AGN activity in barred galaxies might naturally be expected. However, from an observational perspective, no clear connection between

bars and AGN activity has been found so far (e.g. Knäpen et al. 2000; Laine et al. 2002; Cisternas et al. 2013). A possible explanation for this discrepancy would be the existence of some time delay that is still poorly understood (sometimes dubbed the timescale conspiracy). In particular, it might well be that a hierarchy of mechanisms combine, involving different timescales, which overall conceal the underlying connection (Shlosman et al. 1990; Combes 2001, 2003; Wada & Koda 2004; García-Burillo et al. 2005). Only recently have observations and simulations begun to achieve the sufficient spatial resolution to track the journey of molecular gas in its last phases of infall towards the central SMBH, showing that a cascade of possibly transient gravitational torques, dynamical friction effects, and filamentary structures can be efficient in transporting the gas to the very centre (Combes et al. 2013, 2014; García-Burillo et al. 2014; Emsellem et al. 2015).

Given the complex interplay of processes suggested so far, it is important to study the feeding of AGN in galaxies with gas imaging at high enough resolution in terms of physical scales, which constrains our targets to nearby galaxies. The grand-design spiral M51 is an ideal target in this sense because of its proximity and the low inclination of the disc (7.6 Mpc and $i \sim 22^\circ$; Ciardullo et al. 2002; Colombo et al. 2014). Additionally, as was shown by García-Burillo et al. (2009) and van der Laan et al. (2011), one of the key points that limit the accuracy in the determination of the radial gas flows is the availability of short-spacing corrections for interferometric molecular gas data. M51 is one of the few galaxies with very high spatial resolution, short-spacing corrected CO(1–0) data (the Plateau de Bure Interferometer Arcsecond Whirlpool Survey, PAWS, has a resolution of $1''$, ~ 40 pc; Schinnerer et al. 2013; Pety et al. 2013). M51 hosts an active galactic nucleus (Seyfert 2, Ho et al. 1997a) that is associated with a radio jet (Crane & van der Hulst 1992), an outflow in the ionised component (Bradley et al. 2004), and also a molecular gas outflow (Scoville et al. 1998; Matsushita et al. 2004, 2007, 2015). For the purpose of estimating planar gas flows, we here ignore the molecular gas emission that is not consistent with disc motions. This emission has a significant impact only in the central $\sim 3'' \sim 120$ pc.

A number of alternatives exist for measuring radial gas flows in nearby galaxies. Based on gas kinematics (traditionally from radio data), the velocity field can be decomposed into its Fourier components, and their radial variations can be used to search for evidence of gas inflow or outflow (e.g. Wong et al. 2004). Also based on gas kinematics, the gas streaming motions can be estimated from analytical solutions for gas orbits in a model that is fitted to the data (e.g. Boone et al. 2007). A third option is to obtain the gravitational potential from near-infrared (NIR) images, and weight the implied gravitational torques with the gas distribution to obtain a statistical estimate of gas flows (García-Burillo et al. 1993, 2005; Quillen et al. 1995; Haan et al. 2009; Meidt et al. 2013).

In practice, it is hard to extract quantitative measurements from the kinematic method (see Haan et al. 2009), and modelling tends to rely on too many assumptions and simplifications, which make it only useful for studying some specific effects (e.g. van der Laan et al. 2011). Additionally, a decomposition of the velocity field becomes increasingly degenerate at low inclinations (the line-of-sight velocities can be difficult to interpret), which is the case for M51. In our attempt to quantify gas inflow, we therefore opted for the third method. Another motivation for measuring full torque profiles based on accurate stellar mass maps is that it allows us to estimate the position of dynamical resonances; most importantly, to identify the number and

location of corotation radii in the disc, as we show in Sect. 6.2. A complementary, qualitative discussion of the streaming motions in M51, in the line of the first method, and also based on the PAWS dataset, can be found in Colombo et al. (2014).

In the upcoming ALMA and NOEMA era, high-resolution maps of molecular gas will become accessible for an increasing number of nearby galaxies. One of the most important questions to answer is whether the gas that is detected in those galaxies is losing or gaining angular momentum, possibly contributing to the feeding of AGN or nuclear star formation, which can indirectly control possible feedback effects. In this context, it is important to understand the limitations of the observational methods used to calculate gas flows and have the appropriate tools for it, including accurate stellar mass maps, whose importance is emphasised in this paper. Additionally, observational estimates of gas flows play the important role of helping theorists impose constraints on models and simulations of galaxy secular evolution, black hole growth, and AGN feedback.

With the high-resolution map of CO from PAWS and our stellar mass map (based on $3.6\mu\text{m}$ *Spitzer* IRAC imaging), we are in a position to determine the rates of gas flows in M51 with unprecedented accuracy. Our major goals are 1) to estimate the inflow rate of molecular gas towards the nucleus; 2) use the torque profiles to reassess the location of resonances in M51; and 3) provide an updated study of the uncertainties involved in the observational quantification of gravitational torques and gas flows for nearby galaxies. With these objectives in mind, the paper is organised as follows. After presenting the data in Sect. 2, we explain the steps involved in the method to calculate torques and gas flows in Sect. 3. The results on torques, inflow, and dynamical resonances are presented in Sect. 4 and discussed in Sect. 6. The dominant sources of uncertainty are examined in Sect. 5, while the details of the tests carried out to quantify them are deferred to Appendix A. We close the paper with a summary and conclusions in Sect. 7.

2. Data

Our study relies on NIR imaging from the *Spitzer* Survey of Stellar Structure in Galaxies (S^4G ; Sheth et al. 2010) and the molecular gas emission traced by PAWS (Schinnerer et al. 2013; Pety et al. 2013). For the purpose of determining the location of dynamical resonances, the information provided by PAWS is complemented with The HI Nearby Galaxy Survey (THINGS; Walter et al. 2008) and the HERA CO Line Extragalactic Survey (HERACLES; Leroy et al. 2009).

2.1. Near-infrared data: stellar mass distribution

Near-infrared emission is often exploited as a stellar mass tracer in nearby galaxies because the light at these wavelengths mainly arises from the old stars that dominate the baryonic mass budget (Rix & Rieke 1993; Quillen et al. 1994). Additionally, NIR images have the advantage that the effect of extinction is minimised, and biases in the mass-to-light ratio that are due to young O and B stars are also attenuated. For these reasons, the NIR, and, in particular, the first *Spitzer* IRAC band (centred at $3.6\mu\text{m}$) has been argued to be an optimal window to trace stellar mass (e.g. Meidt et al. 2014; Norris et al. 2014; Querejeta et al. 2015).

However, emission from dust can also contribute significantly to the NIR flux, especially locally, as shown by Meidt et al. (2012) and Querejeta et al. (2015). Specifically, for M51, the dust emission contributes as much as 34% of the total flux at

3.6 μm , and the correction is especially critical in star-forming regions (reaching $\sim 80\%$, Querejeta et al. 2015). Therefore, we used the 3.6 μm image of M51 corrected for dust emission using the independent component analysis (ICA; Querejeta et al. 2015). After the stellar flux in the 3.6 μm IRAC band is correctly identified, even a single mass-to-light ratio $M/L \equiv \Upsilon_{3.6} = 0.6$ is applicable with an uncertainty of $\lesssim 0.1$ dex (Meidt et al. 2014; Norris et al. 2014).

2.2. CO data: molecular gas distribution

We used the molecular gas amount and distribution probed by the CO(1–0) map of M51 from PAWS to perform weighted azimuthal averages of the torques and determine how much gas participates in radial flows. PAWS offers an exquisite angular resolution of $1''$ (~ 40 pc) and covers the central 9 kpc of the galaxy (with uniform azimuthal coverage out to $R = 85'' \sim 3$ kpc). The importance of performing short-spacing corrections to interferometric data for torque-based flow studies has only recently been fully recognised (e.g. van der Laan et al. 2011). Our PAWS map includes short-spacing corrections based on IRAM 30m single-dish data, which by definition recovers all the flux. We transformed the measured flux into the molecular hydrogen (H_2) gas surface density using the Galactic conversion factor $X_{\text{CO}} = 2 \times 10^{20} \text{ cm}^{-2} (\text{K km s}^{-1})^{-1}$ (Schinnerer et al. 2013); the adopted value has no consequence for the measured torque profiles (since the gas map will only serve to weight the azimuthal average of the torques), although it does affect the measured net inflow rate. For more details on the data reduction, we refer to Pety et al. (2013).

Within the PAWS field of view, the gas is predominantly molecular, and this becomes even more so towards the centre. Since we are interested mostly in the central region, where atomic HI gas is largely depleted (HI surface density lower than CO by a factor of 5–10 inside $R < 3$ kpc, Schuster et al. 2007), and for uniformity reasons, we assumed the gas distribution to be the one traced by the CO observations from PAWS. But we use the information provided by HI (from the THINGS survey, at $6''$ spatial resolution) and by CO at lower resolution (HERACLES, $13''$) in Sect. 4.4 to extend the torque analysis to the outer regions of the disc and estimate the positions of resonances.

3. Measuring gravitational torques and gas inflow rates

We focus on the gravitational torques exerted by the stellar potential on the gaseous disc. By definition, a torque is a vectorial quantity, $\boldsymbol{\tau}$, parallel to the axis of the rotation that it would tend to produce: $\boldsymbol{\tau} = \mathbf{r} \times \mathbf{F}$, the cross product of the position vector and net force acting on a given (test) particle. From this operative definition, the equivalent identity $\boldsymbol{\tau} = d\mathbf{L}/dt$ can be derived; therefore, the torque measures the derivative of the angular momentum with respect to time. Since gas needs to lose (gain) angular momentum to move inwards (outwards), torques applied on the gas distribution provide the necessary link to determine gas flows. Our strategy is to first obtain the gravitational potential using Fourier transforms of the mass distribution (3.6 μm image corrected for dust emission), and, subsequently, the torques implied by that potential are weighted with the molecular gas distribution to determine the gas inflow (outflow) rates as a function of radius. The code we use is partially based on PyPot (Haan et al. 2009).

3.1. Deprojection

Our input is the stellar mass surface density projected on the plane of the sky (the “stellar mass map” from the ICA method described in Sect. 2.1). Therefore, to obtain the gravitational potential, we first need to deproject this map into the true plane of the galaxy. We did this using the accurate inclination and position angle (PA) kinematic measurements obtained for M51 by Colombo et al. (2014). Their results constrain these values to inclination $i = (22 \pm 5)^\circ$ and PA = $(173 \pm 3)^\circ$. In Sect. 5 we examine the effect of deprojecting the image according to the extreme values of i and PA allowed by these uncertainty limits.

Another subtlety that needs to be considered is the fact that a bulge (or any departures from a disc) will become artificially elongated by the deprojection. In the case of M51, the central structure that has traditionally been called the “bulge” has a disc-like Sérsic index ($n = 0.995$, Salo et al. 2015), and it could in principle have been a pseudo-bulge (or “discy bulge”); however, it has a very similar orientation and extent (PA = 130° , $R_e = 16.2''$, Salo et al. 2015) as what we will identify as the nuclear bar, suggesting that it is the same stellar structure. Moreover, the low Sérsic index implies that it is flattened parallel to the plane of the galaxy. Therefore, provided that the deviation from a plane is very small, the size is modest, and the inclination of M51 is small, it seems justified to ignore the structure of the nuclear bar for the deprojection.

3.2. Obtaining the gravitational potential

Our technique is based on the idea that the gravitational potential, $\Phi(\mathbf{r})$, can be written as the convolution of the mass density, ρ , and the function $1/r$ (e.g. Binney & Tremaine 1987, Sect. 2.8):

$$\Phi(\mathbf{r}) = -G \int \frac{\rho(\mathbf{r}') d^3 \mathbf{r}'}{|\mathbf{r} - \mathbf{r}'|}. \quad (1)$$

However, to access the true 3D mass density distribution, it is necessary to consider the non-negligible thickness of the galaxy stellar discs. To account for this, we assumed a vertical profile of constant scale-height (in agreement with observations of edge-on galaxies, Wainscoat et al. 1989; Barnaby & Thronson 1992), which allows us to write

$$\Phi(x, y, z = 0) = -G \int \Sigma(x', y') g(x - x', y - y') dx' dy', \quad (2)$$

where $g(x, y)$ is the modified convolution function,

$$g(x, y) = \int_{-\infty}^{+\infty} \frac{\rho_z(z) dz}{\sqrt{x^2 + y^2 + z^2}}. \quad (3)$$

In particular, we expect the galaxy to have a vertical distribution similar to an isothermal disc, $\rho_z(z) = \rho_0 \text{sech}^2(z/h)$, with $h \sim 1/12 H_{\text{disc}}$ (Wainscoat et al. 1989; Barnaby & Thronson 1992). We chose $H_{\text{disc}} = 100''$, based on the Galfit photometric decomposition of M51 performed by Salo et al. (2015).

An important technical detail is that the convolution is carried out using fast Fourier transforms (FFT) that are computed on a $(2n \times 2n)$ mesh to avoid periodic images (Hohl & Hockney 1969): the original image occupies one quarter of the grid, and all remaining three quarters are invalid. This means that we initially pad the image with zeroes and eliminate those invalid areas after performing the FFTs.

A&A 588, A33 (2016)

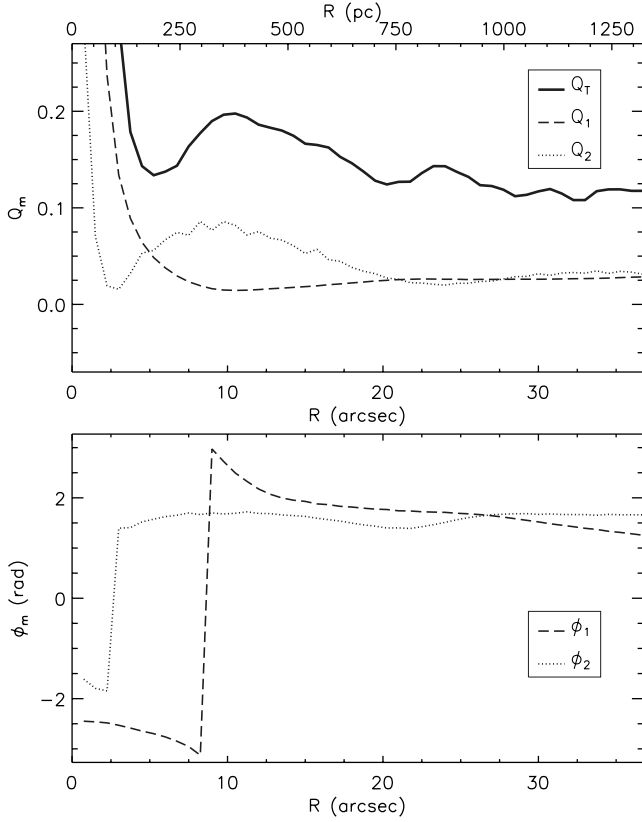


Fig. 1. *Top:* relative strength of the first two Fourier modes in the gravitational potential ($Q_{m=1,2}$) as a function of radius, compared to the total strength of the non-axisymmetric perturbation Q_T . *Bottom:* phases of the first two Fourier modes in the gravitational potential $\phi_{m=1,2}$, measured counter-clockwise from the major axis of the galaxy on the deprojected image (represented here in radians from $-\pi$ to π).

3.3. Harmonic decomposition of the gravitational potential

To assess the radial contribution of the different Fourier modes, we performed a harmonic decomposition of the potential,

$$\Phi(R, \theta) = \Phi_0(R) + \sum_m \Phi_m(R) \cos(m\theta - \phi_m(R)), \quad (4)$$

where $\Phi_m(R)$ and $\phi_m(R)$ are the amplitude and phase of the m -mode.

We followed [Combes & Sanders \(1981\)](#) and calculated the strength of the m th Fourier component, $Q_m(R)$, as

$$Q_m(R) = \frac{m\Phi_m(R)}{R|F_0(R)|}, \quad (5)$$

which is the amplitude of the m th harmonic component normalised by the mean axisymmetric radial force, $F_0(R)$. Finally, we also computed the maximum tangential force in terms of the mean radial force,

$$Q_T(R) = \frac{F_T^{\max}(R)}{F_0(R)} = \frac{\frac{1}{R} \left(\frac{\partial \Phi(R, \theta)}{\partial \theta} \right)_{\max}}{\frac{d\Phi_0(R)}{dR}}. \quad (6)$$

The top panel of Fig. 1 shows the relative strength of the first two modes ($m = 1, 2$) as a function of radius, compared to the total strength of the non-axisymmetric perturbation Q_T ; the bottom panel shows the corresponding phases, $\phi_{m=1,2}$. These results are discussed in Sect. 4.1.

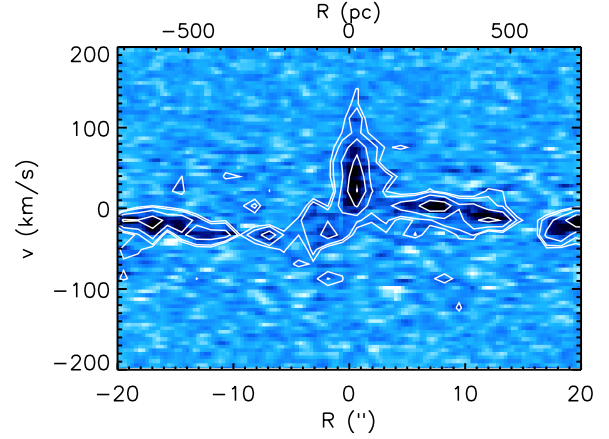


Fig. 2. Position-velocity diagram of the PAWS 1'' cube, taken along a position angle of 272° crossing the nucleus. There is highly redshifted CO emission near the nucleus ($R < 2.5''$), with velocities exceeding 100 km s^{-1} . This molecular gas is outflowing, not participating in disc motions, and it has been removed from the moment-0 map used to estimate the molecular gas distribution in the disc.

3.4. Torques from the potential

We obtained the forces per unit mass as the gradient of the potential in Cartesian coordinates,

$$F_{x,y}(x, y) = -\nabla_{x,y} \Phi(x, y), \quad (7)$$

and, subsequently, we used these forces (the components of the local force along each of the Cartesian axes) to obtain the torques,

$$\tau(x, y) = xF_y - yF_x. \quad (8)$$

It is important to emphasise that these are torques per unit mass (i.e. torques per unit gas mass, since we are interested in stellar gravitational torques on the gaseous component), and we measured them in units of $\text{km}^{-2} \text{ s}^2$. Therefore, multiplying the $\tau(x, y)$ in a given pixel by the total gas mass contained in that pixel (e.g. traced by CO) will provide the change rate of angular momentum with respect to time experienced by the gas ($\tau = dL/dt$).

Figure 3 shows the gravitational potential and the torques that stem from our ICA-corrected stellar mass map, deprojected according to the PAWS measurements of PA and ellipticity.

3.5. Gas flows

Torques applied on gas are, by definition, a measure of the change of angular momentum per unit time ($\tau = dL/dt$). Naturally, angular momentum loss of the gas is associated with inflow, whereas increasing its angular momentum corresponds to radial outflow. Multiplying the torque map by the present-day gas distribution (e.g. from PAWS) provides the instantaneous view of angular momentum loss and gain across the galaxy. However, this is not necessarily representative, overall, of the net effect experienced by a given gas cloud. We followed [García-Burillo et al. \(2005\)](#) and computed an azimuthal average of the torques, weighted with the local gas column density, $N(x, y)$,

$$\tau(R) = \frac{\int_\theta [N(x, y) \cdot (xF_y - yF_x)]}{\int_\theta N(x, y)}. \quad (9)$$

M. Querejeta et al.: Molecular gas inflow in M51

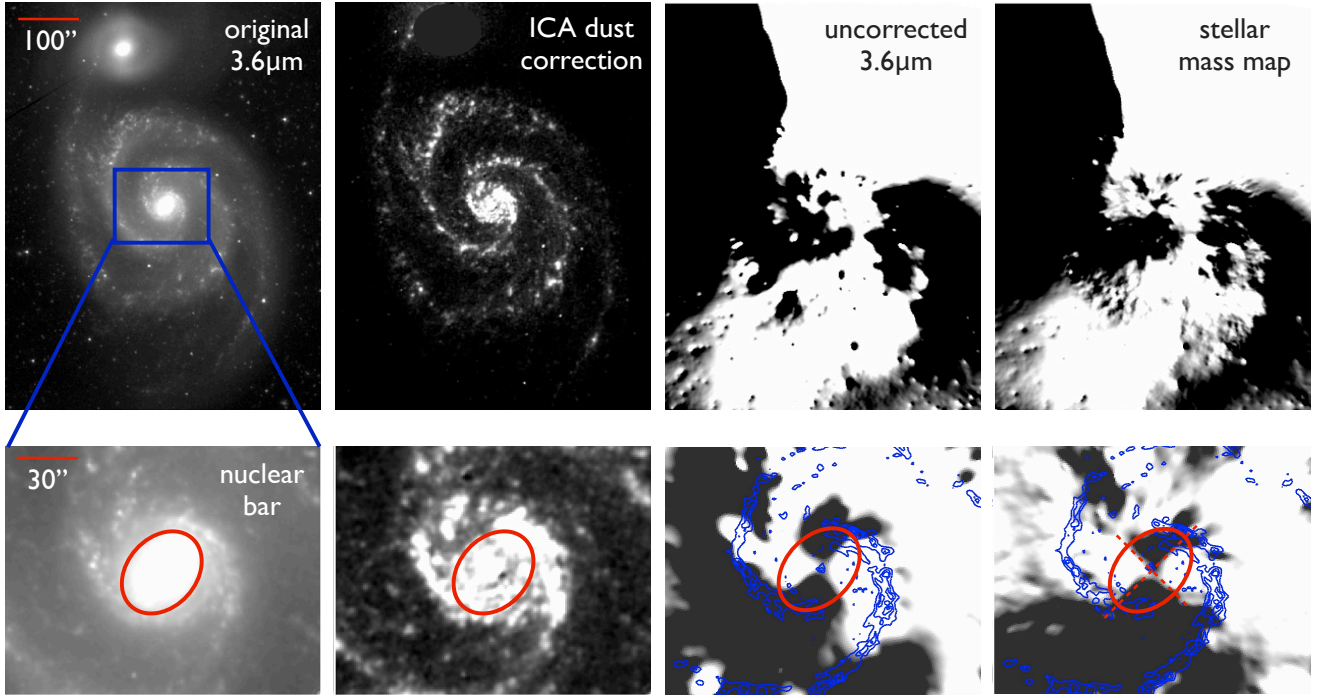


Fig. 3. *Top panel:* original $3.6\ \mu\text{m}$ image of M51; dust emission identified with ICA (subtracted from the original image to produce the stellar mass map); gravitational torques, $\tau(x, y)$, based on the uncorrected $3.6\ \mu\text{m}$ image of M51 (assuming a constant M/L); same gravitational torques, $\tau(x, y)$, based on our ICA dust-corrected stellar mass map of M51. *Bottom panel:* blow-up of the maps above, showing the area close to the nucleus. The red ellipse displays the shape of the nuclear bar, determined from the ellipticity and PA profiles measured by Muñoz-Mateos et al. (2015) at the radius where the bar ends ($R = 20''$: $\varepsilon = 0.262$, $PA = -42.6^\circ$); this agrees excellently well with an isocontour of $F = 10\ \text{MJy/sr}$ in the original $3.6\ \mu\text{m}$ image. The red dashed lines are the approximate axes of symmetry of the bar, which coincide with a change of sign in the torques, following the expected butterfly pattern. The blue contours indicate CO emission from PAWS, from 50 to $250\ \text{K km s}^{-1}$ in steps of $50\ \text{K km s}^{-1}$. All images are shown in the plane of the sky; north is up (even if, naturally, torques are calculated in the plane of the galaxy). The scale bar shown in the leftmost images applies to the whole row. (The $3.6\ \mu\text{m}$ image is shown in square-root scale to emphasise low-level structure in the range $(0, 10)\ \text{MJy/sr}$; the dust map is displayed in linear scale, $(0, 3)\ \text{MJy/sr}$; the torque maps are also shown on a linear scale, $(-1000, 1000)\ \text{km}^2\ \text{s}^{-2}$, with negative torques in black and positive torques in white.)

To weight the torques, we used the PAWS CO(1–0) map of M51 corrected for outflow motions (Sect. 2.2) and convolved to the spatial resolution of the stellar mass map ($\text{PSF}_{3.6\ \mu\text{m}} = 1.7''$). At $R = 4\ \text{kpc}$, HI starts to dominate over CO (Schuster et al. 2007), therefore we used HI traced by THINGS to extend the profiles to larger radii. We deprojected the gas maps using the same parameters as for the stellar mass map, following Sect. 3.1.

To calculate the fuelling efficiency, we normalised the azimuthally averaged torques $\tau(R)$ at each radius by the angular momentum and rotation period. This provides an estimate of the average fraction of gas specific angular momentum transferred by the stellar potential in one rotation (T_{rot}),

$$\frac{\Delta L}{L} = \frac{dL}{dt} \Big|_{\theta} \cdot \frac{1}{L} \Big|_{\theta} \cdot T_{\text{rot}} = \frac{\tau(R)}{L_{\theta}} \cdot T_{\text{rot}}, \quad (10)$$

since $\tau(R)$ is, by definition, the azimuthally averaged time-derivative of the specific angular momentum of the gas. The azimuthal average of the angular momentum was assumed to be $L_{\theta} = R \cdot v_{\text{rot}}$. The inverse of Eq. (10), $L/\Delta L$, represents the number of rotation periods needed to transfer all the angular momentum of the gas; a large $L/\Delta L$ would imply that the gas distribution and potential do not vary too much on the timescale of a rotation, which justifies the approximation introduced above. Finally, based on this, we express the gas inflow/outflow rate per

unit length as

$$\frac{d^2 M(R)}{dR dt} = \frac{dL}{dt} \Big|_{\theta} \cdot \frac{1}{L} \Big|_{\theta} \cdot 2\pi R \cdot N(x, y) \Big|_{\theta}, \quad (11)$$

which provides the result in units of $M_{\odot}\ \text{yr}^{-1}\ \text{pc}^{-1}$. This can be integrated radially, using radial bins of width Δr , to obtain a net inflow/outflow rate up to a given radius R ,

$$\frac{dM(R)}{dt} = \sum_{r=0}^R \left[\frac{d^2 M(r)}{dr dt} \cdot \Delta r \right]. \quad (12)$$

If measured close enough to the nucleus, dM/dt in Eq. (12) provides an estimate of the instantaneous AGN feeding rate. Figure 4 presents these results.

3.6. Subtracting the outflow component

Our method to estimate gas flows based on the gravitational torques assumes planar motions for the molecular gas. The regular kinematics of molecular gas in M51 and the relatively constant CO line width (Pety et al. 2013) are indicative that this assumption is reasonable. However, near the nucleus, significant molecular emission is clearly deviating from disc motions: this has been argued to be a molecular gas outflow (Scoville et al. 1998; Matsushita et al. 2004, 2007, 2015), and it becomes clear

A&A 588, A33 (2016)

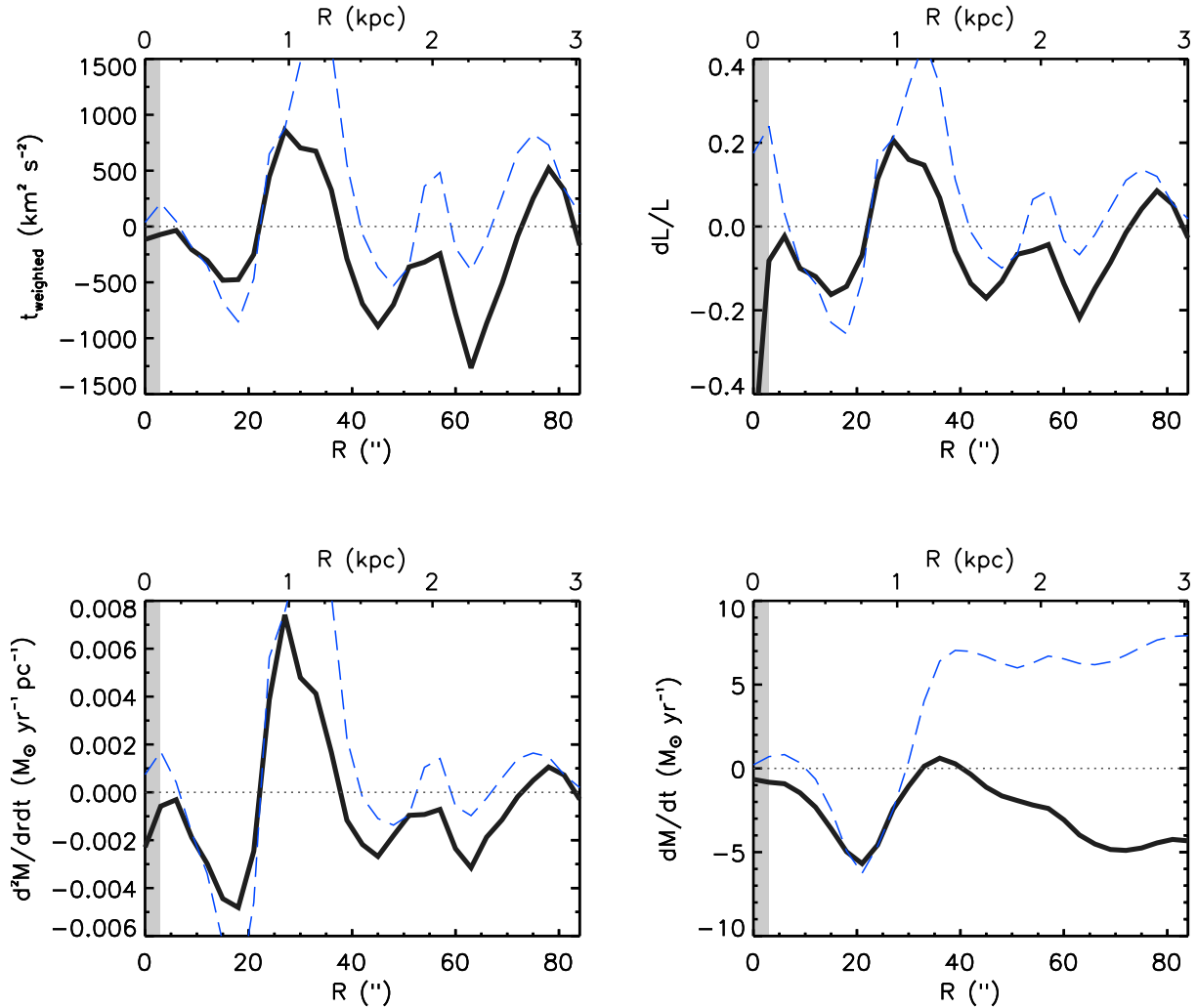


Fig. 4. Results of the gravitational torques (weighted with the molecular gas distribution), angular momentum transfer, and resulting gas flow, both in radial bins and integrated out to radius R for our ICA dust-corrected stellar mass map (solid black line) and the original $3.6\ \mu\text{m}$ image (dashed blue line). Positive values imply radial gas outflow, negative values denote an inflow. The innermost bin has been shaded to emphasise that it is subject to high uncertainties.

in the position-velocity diagram shown in Fig. 2. To correct for it, we subtracted the CO(1–0) emission that is not associated with disc motion by constructing a new moment-0 map (using 3σ clipping, Pety et al. 2013) in which we neglected the flux from pixels in the central $R = 2.5''$ in channels of velocities that correspond to the outflow ($40\text{--}180\ \text{km s}^{-1}$). We verified that the final torque profiles do not change significantly if this cut is modified by $\pm 10\ \text{km s}^{-1}$; this implies that our model is reliable.

4. Results

4.1. Stellar potential

Figure 1 shows the Q_m values for the first two Fourier modes ($m = 1, 2$) in the stellar gravitational potential of M51. These represent the strength of each mode in the potential as a function of radius (compared to the total non-axisymmetric contribution, Q_T). There is a clear dominance of the $m = 2$ mode all the way out to $R = 20''$, which can be attributed to the influence of the nuclear bar; indeed, the bar has a length of $R_{\text{bar}} \approx 20''$ (Comerón et al. 2010). The area of influence of the bar is therefore similar to its size as measured on NIR images, as expected.

The bar is considerably strong, reaching a maximum $Q_2 \sim 0.1$ at a radius of $10'' \sim 400\ \text{pc}$. In addition, the phase of the $m = 2$ bar in Fig. 1, which we find is relatively constant around $\phi_2 \sim \pi/2$ rad (oscillating between 1.5 and 1.7, with an average of 1.63 radians), corresponds to a disc-plane bar orientation¹ of 135° measured counterclockwise from the major axis of M51 or, equivalently, a sky-plane orientation of $\text{PA} = -47^\circ$ (given the projection of the disc). This agrees well with the PA value of -43° given by the profiles of Muñoz-Mateos et al. (2015) at a radius of $R = 20''$ and the bar angle of -41° measured by Menéndez-Delmestre et al. (2007) from NIR imaging.

4.2. Torque map of M51

Figure 3 shows the torques implied by the stellar mass map. In all these maps, black corresponds to negative torques and white

¹ In our Fourier expansion we assumed positive amplitudes, $\Phi_m(R) \cos[m\theta - \phi_m(R)]$ with $\Phi_m(R) > 0$, which implies that the major axis of the bar, where the potential is lowest, is given by $2\theta - \phi_2 = \pi$ (or an integer multiple of π). Therefore, $\theta = \pi/2 + \phi_2/2 \sim 3\pi/4 = 135^\circ$ on the plane of the galaxy.

implies positive torques; with our sign convention (right-hand rule), negative torques make the gas lose angular momentum (inflow), while positive torques transfer additional angular momentum to the gas (outflow). The blow-up shown in the bottom panels demonstrates the good agreement between the morphology of the nuclear bar (delineated in red) and the butterfly pattern in the torque map: torques change signs according to four quadrants that are delimited by the axes of symmetry of the bar, as expected. The nuclear bar extends out to a radius of $R = 20'' \sim 800$ pc (Comerón et al. 2010). As we show in Sect. 4.3, there is evidence for gas inflow inside $R = 22'' \sim 880$ pc, which, judging from the butterfly pattern visible in the torque map, can be clearly interpreted as the effect of the bar.

The right panels of Fig. 3 stress the difference with the torque map stemming from the uncorrected $3.6\mu\text{m}$ band (i.e. stellar mass distribution obtained multiplying the $3.6\mu\text{m}$ image with a single M/L); the change is even more evident in the radial profiles in Fig. 4. The presence of dust emission leads to a significantly different distribution of torques, which results in no consistent gas inflow in the central area (in spite of the morphological evidence for a nuclear bar). One of the side-effects of correcting the $3.6\mu\text{m}$ image for dust emission using ICA is that small oversubtractions appear in areas of very red original [3.6]–[4.5] colours, which manifest themselves as small holes or dipoles in the torque map. However, in Appendix A.1 we show that these small oversubtractions due to the ICA correction only have a weak effect when they are azimuthally averaged, while the difference with the uncorrected $3.6\mu\text{m}$ image is large.

In addition to the butterfly pattern associated with the nuclear bar, the torque maps in Fig. 3 display a second butterfly pattern at larger radii, which is tilted with respect to the nuclear butterfly pattern (especially obvious at $R \gtrsim 80'' \sim 3$ kpc). Comparison to a smooth mass model of M51 demonstrates that this is probably due to an oval distortion in the disc. For a perfectly axisymmetric (circular) disc, no butterfly pattern is expected; but in the case of M51, the disc is photometrically elongated along an axis of PA = 39° (Salo et al. 2015), while kinematics imply that the orientation of the (molecular) disc is such that PA = 172° (Colombo et al. 2014). Provided that the disc is not significantly warped inside $r \lesssim 6$ kpc (Colombo et al. 2014), the most natural interpretation for such a configuration would be that the disc is not circular, but rather oval, which might be expected as a consequence of the interaction (a global $m = 2$ mode induced by the encounter with NGC 5195; see also Meidt et al. 2013). Simulations from Dobbs et al. (2010) also support the idea that the disc is not strongly warped inside 5 kpc and that there is an oval at $r \sim 2$ kpc, with aspect ratio 2:1 (see also Shetty et al. 2007, on the possibility of a warp in M51).

4.3. Inflow rate in M51

Our best estimate of the gas flows is presented in Fig. 4. The top-left panel shows that the (gas-weighted) azimuthally averaged torques are consistently negative from the centre all the way out to $R = 22''$, which implies secular molecular gas inflow in the central ~ 1 kpc of the galaxy (down to our resolution limit of $1.7'' = 63$ pc). After this, in the range $R = (22\text{--}37)''$, torques become positive, which is indicative of radial molecular gas outflow along the plane of the galaxy; then, from $R = 37''$ to $R = 73''$, torques are again continuously negative, implying inflow. This means that there is evidence for secular transport of the gas from $R = 2.7$ kpc down to our resolution limit with the exception of the range $R = (22\text{--}37)''$, which seems to be a dynamical barrier for gas transport; precisely in this region

the molecular ring is located ($R \sim 30''$ Meidt et al. 2013), which can be explained as the accumulation of molecular gas as a consequence of these gas flows (e.g. Buta & Combes 1996; van der Laan et al. 2013). This seems to be the same structure as the inner pseudo-ring identified by Comerón et al. (2014) around $R \sim 20''$ (which is star-forming, Comerón 2013). It becomes especially obvious in the dust component separated by the ICA correction of the $3.6\mu\text{m}$ image (second panels of Fig. 3, at the end of the ellipse that delineates the bar). As a transition region between the nuclear bar and the radius where spiral arms end, the molecular ring is not as strong and dominant as rings in other galaxies; in this sense, it can be associated with the zero-crossing occurring around $R \sim 40''$ in the torque profile, which coincides with the radius at which the spiral arms terminate.

The top-right panel represents the fraction of the angular momentum of the gas at a certain radius that is lost in one rotation. The fact that dL/L takes a maximum value of the order of 0.2 (20%) justifies the assumption (implicit to azimuthal averaging) that the gas distribution does not change by much in one rotation. Out to $R = 22''$, ignoring the innermost bin, the average dL/L is $\sim 10\%$, which means that the gas will lose all of its angular momentum on a timescale of ~ 10 rotations, that is, in about 200 Myr ($T_{\text{rot}}(R = 12'') = 22$ Myr). This timescale is also relatively short compared to the dynamical timescale of the interaction of M51 with NGC 5195 (~ 1 Gyr), which allows us to assume that the gravitational potential of M51 will not have changed by much in that period.

The bottom left panel of Fig. 4 shows the instantaneous flow rates implied by the gravitational torques across the disc of the galaxy, the bottom right panel shows the “integrated” inflow rates (i.e. summing the contributions of all bins out to radius R). The “integrated” inflow rate out to $R = 22''$ is $\sim 5 M_\odot/\text{yr}$, which means that on a timescale of one year, a total of about $5 M_\odot$ of gas participates in *net* inflow motions in that particular radial extent of the galaxy. Closer to the AGN (considering only the first or first two bins, $3\text{--}6''$), this rate decreases to $\sim 1 M_\odot/\text{yr}$, with the caveat that the innermost bin is compromised by the outflow and by increasingly large systematic uncertainties (see Sect. 5). In Appendix A.6 we confirm these results using the gravitational potential computed from an HST $1.9\mu\text{m}$ image (instead of the stellar mass map). The inflow rates and resonances are basically coincident with those presented here, and significant divergencies only appear in the inner $R \lesssim 5''$, where uncertainties become increasingly large and data are becoming inconclusive as a result of the additional impact of the central AGN.

4.4. Dynamical resonances in M51

We used our new map of gravitational torques to reassess the locations of the main dynamical resonances in the disc of M51. Meidt et al. (2013) have used the technique of constructing radial profiles of the azimuthally averaged torques to assess the positions of resonances in M51 with PAWS. Here we also used a $3.6\mu\text{m}$ -based stellar mass map (distinct from the earlier version of Meidt et al. 2013, as discussed in Sect. 6), but we extended the analysis out to larger radii using the more extensive area probed by the HERACLES and THINGS maps of the molecular and atomic gas distributions (Walter et al. 2008; Leroy et al. 2009). This avoids potential biases due to the non-circular shape of the PAWS field of view, which leads to incomplete azimuthal coverage at radii $R > 85''$.

In the framework of the density wave theory, the response of gas to the gravitational potential is expected to change at corotation (CR). The torque profile obtained at highest angular

resolution using the PAWS map exhibits an abrupt change of sign (from negative to positive torques) at $R = 22''$, which can be associated with the CR of the nuclear bar ($R_{\text{CR,bar}}$; see also Meidt et al. 2013; Colombo et al. 2014). Comerón et al. (2010) obtained a bar radius of $R_{\text{bar}} = 20''$ (800 pc) based on ellipse fitting, which implies a ratio of $R_{\text{CR,bar}}/R_{\text{bar}} \approx 1.1$. This agrees with expectations for fast bars (e.g. Athanassoula 1992a) and is also well compatible with the values measured by Rautiainen et al. (2008) for galaxies of similar morphological type (SABbc). As we commented above, the inner star-forming ring identified by Comerón et al. (2014) around $R \sim 20''$ overlaps the molecular ring and is located next to the corotation of the bar, suggesting that it is indeed a resonant ring.

Inner torque variations locating the bar corotation are not as obvious in the lower resolution profiles obtained with THINGS² or HERACLES (the latter of which covers the bar with only two resolution elements). However, we expect these maps to offer a more reliable measure of gravitational torques at larger radii, where the gravitational torques can be estimated with full ($0-2\pi$) azimuthal information. A second zero-crossing from negative to positive torques is visible in the THINGS profile near $100''$ (Fig. 5, bottom panel), which we suggest is indicative of corotation for the spiral pattern; this interpretation is reinforced by a similar crossing in the HERACLES profile (with an offset of only $5''$, i.e. fully compatible given the HERACLES resolution of $13''$). The final change of sign at $R \sim 150-160''$ probably marks the outer Lindblad resonance (OLR) of the spiral.

These findings qualitatively agree with the results of the harmonic decomposition of the PAWS line-of-sight velocity field performed at $1''$ resolution by Colombo et al. (2014). These authors observed a change in dominance from the $s1$ to the $s3$ harmonic coefficients around $R \sim 100''$, which we associate with the location of corotation. As first shown by Canzian (1993), a change from $m = 1$ to $m = 3$ mode is expected at corotation, which will reflect on a change in dominance of the $s1$ and $s3$ terms of the Fourier harmonic decomposition of the velocity field (even if the behaviour of those harmonic terms is more complex in spirals than in bars; e.g. Wong et al. 2004). We strongly recommend combining the information contained in torque profiles with other (kinematic and morphological) evidence to accurately identify resonances. In particular, while corotation is expected to result in a zero-crossing in the torques, other resonances might also have an imprint in the form of a change of sign. Our estimates for the bar and spiral corotation radii in M51 are also consistent with the values independently estimated by Zhang & Buta (2012) ($R_{\text{CR1}} = 25''$ and $R_{\text{CR2}} = 110''$).

A very useful tool to interpret the results on dynamical resonances and analyse possible couplings is a so-called angular frequency plot, in which the angular frequency corresponding to circular rotation is plotted ($\Omega = V_{\text{rot}}/R$) along with the epicyclic curves (e.g. $\Omega \pm \kappa/2$, $\Omega \pm \kappa/4$). In Fig. 5, we show those curves as derived from the three-parameter rotation curve of M51 calculated in Meidt et al. (2013). For a direct comparison, the middle and bottom panels of Fig. 5 show the torque profiles (weighted by PAWS and THINGS/HERACLES, respectively) and some coloured circles indicating the corotation positions that we have inferred (red for the bar, blue for the spiral). The intersections of the zero-crossings with the angular frequency curve Ω in the top plot indicate the corresponding pattern speeds (since $\Omega(R_{\text{CR}}) = \Omega_{\text{p}}$). The dashed coloured lines show the range of possible values due to 1.5 times the resolution of each survey

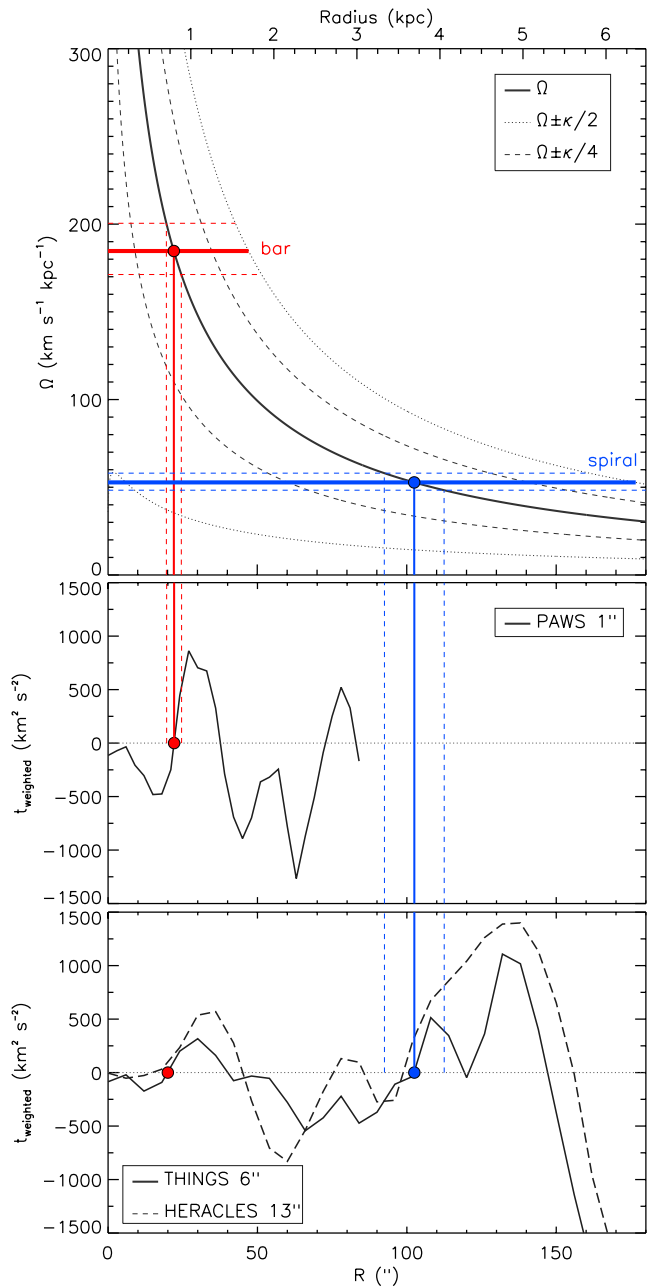


Fig. 5. *Top panel:* angular frequency plot based on the rotation curve of M51 calculated in Meidt et al. (2013): Ω (solid black), $\Omega \pm \kappa/2$ (dotted black), $\Omega \pm \kappa/4$ (dashed black). The red circle indicates the crossing of the estimated corotation radius of the bar ($\text{CR}_{\text{bar}} = (22 \pm 2.5)''$) with the angular frequency curve Ω , which implies a bar pattern speed of $\Omega_{\text{p}}^{\text{bar}} = (185 \pm 15) \text{ km s}^{-1} \text{ kpc}^{-1}$ (horizontal red line). The blue circle shows the analogous crossing of the suggested corotation radius of the spiral ($\text{CR}_{\text{sp}} = (102 \pm 10)''$), implying a pattern speed for the spiral of $\Omega_{\text{p}}^{\text{spiral}} = (53 \pm 5) \text{ km s}^{-1} \text{ kpc}^{-1}$ (horizontal blue line). *Middle panel:* torque profile weighted by the PAWS gas distribution (same as Fig. 4, reproduced here for comparison). As a result of the smaller field of view of PAWS, the profile stops at $R = 85''$. *Bottom panel:* torque profile weighted by the gas emission traced by THINGS (solid line) and HERACLES (dashed line).

($2.5''$ for PAWS; $10''$ for THINGS), in an attempt to give an idea of how those observational uncertainties translate into a range of possible pattern speeds and overlapping resonances.

² Additionally, HI is almost completely depleted in the inner regions.

Table 1. Dynamical resonances of M51 from our torque analysis.

Resonance	Radius (")	Radius (pc)
Bar corotation	22 ± 2.5	830 ± 90
Bar outer Lindblad resonance	50 ± 5	1800 ± 180
Spiral corotation	102 ± 10	3800 ± 370
Spiral ultra-harmonic resonance	55 ± 5	2000 ± 180
Spiral outer Lindblad resonance	165 ± 15	6100 ± 550

The pattern speed of the bar (for a $CR_{\text{bar}} = (22 \pm 2.5)''$) would be $\Omega_{\text{p}}^{\text{bar}} = (185 \pm 15) \text{ km s}^{-1} \text{ kpc}^{-1}$ (horizontal red line). Analogously, for our suggested corotation radius of the spiral ($CR_{\text{sp}} = (102 \pm 10)''$), the spiral pattern would rotate with an angular frequency of $\Omega_{\text{p}}^{\text{spiral}} = (53 \pm 5) \text{ km s}^{-1} \text{ kpc}^{-1}$ (horizontal blue line). Placing the main corotation of the spiral around $R \sim 100''$, as suggested by our torque analysis, has interesting implications in terms of coupled resonance patterns. On the one hand, if a single (or dominant) pattern speed applies to the whole spiral, the crossing of $\Omega_{\text{p}}^{\text{spiral}} = (53 \pm 5) \text{ km s}^{-1} \text{ kpc}^{-1}$ with the $\Omega + \kappa/2$ curve would imply an OLR_{sp} $\sim (150\text{--}180)''$, in agreement with torques (last zero-crossing around $(150\text{--}160)''$). The inner ultraharmonic resonance of the spiral (UHR, or 4:1) is given by the crossing of that same pattern speed with the $\Omega - \kappa/4$ curve, which results in UHR_{sp} $\sim (50\text{--}60)''$; this is compatible with the OLR of the bar ($\Omega + \kappa/2$ curve crossing with $\Omega_{\text{p}}^{\text{bar}} \sim 185 \text{ km s}^{-1} \text{ kpc}^{-1}$), which points to a possible dynamical coupling of the two structures (on resonance coupling, see e.g. Tagger et al. 1987; Font et al. 2014). These measurements are summarised in Table 1.

Determining the location of the ILR is often more challenging in the discs of spiral galaxies, given the characteristic rapid changes in the shape of the innermost parts of rotation curves. In M51, the shape of the $\Omega - \kappa/2$ curve at radii $r \lesssim 30''$ is very sensitive to the exact parameterisation of the rotation curve we adopt. Given this uncertainty in the inner shape of the $\Omega - \kappa/2$ curve, we note that the resonant overlap of the bar CR and spiral ILR might be possible (although this is difficult to claim with great certainty); this would further support the resonant nature of the inner pseudo-ring around $R \sim 20''$.

Based on all this, we propose a scenario in which M51 has two main corotations: one associated with the nuclear bar, approximately at $CR_{\text{bar}} \sim 20''$, and one for the spiral around $CR_{\text{sp}} \sim 100''$. There are only two clear zero-crossings (from negative to positive) in the extended torque profiles using THINGS and HERACLES. These are consistent with the $s1/s3$ radial profiles from the harmonic decomposition of the PAWS and THINGS velocity fields.

4.5. Use of a dust correction map to estimate flows and resonances

In Sect. 2.1 we outlined the interest of correcting the $3.6 \mu\text{m}$ image for dust emission using an ICA technique. Here, we briefly examine the possibility of using the dust correction map ($s2$) produced by the ICA separation as a tracer of the ISM. The $s2$ map is uniformly available for more than 1500 nearby galaxies, whereas obtaining interferometric observations of the gas at equivalent resolution remains prohibitively expensive. Therefore, while speculative, the dust correction map $s2$ is potentially a very powerful alternative.

As discussed in detail in Querejeta et al. (2015), the $s2$ map contains all the non-stellar emission present at $3.6 \mu\text{m}$, which is essentially a diffuse mixture of PAH and continuum dust

emission. Therefore, it indirectly traces star formation (by hot dust and PAH emission), which is expected to correlate to some degree with the presence of molecular gas. In M51, we can test how good this correlation is by directly dividing the $s2$ map by the CO map from PAWS. The ratio of $s2$ to CO is fairly uniform in the spiral arms and star-forming ring (0.009–0.033), while in the area of the bar it suddenly rises to 0.1–0.3, which means that it is a factor of 10 higher. This large difference provides a first clue that the dust map $s2$ may not be a reliable tracer of molecular gas in the central region of M51.

Figure 6 confirms that the discrepancy between the torque profiles weighted by CO (PAWS) and by the map $s2$ is especially large towards the area of the nuclear bar. However, even without a one-to-one agreement, the correspondence with HI is considerably better (the resulting torque profiles are good to about a factor of $\lesssim 2$). This suggests that the dust map $s2$ provided by the ICA separation can be used in a first-order approximation as a tracer of the ISM to weight the torques with, but this needs to be done with caution. In areas where the interstellar radiation field is strong (like the nuclear bar of M51), the $s2$ map can display significant flux even if CO emission is minimal, which could account for the differences we see between CO and $s2$ in the central region of M51. Additionally, we recommend using $s2$ as a tracer of the gas distribution only at low resolution; at high resolution it is less reliable because spatial offsets between tracers of the gas and star formation start to become evident.

5. Dominant sources of uncertainty

We note that some sources of uncertainty have been considered previously (most notably, by Haan et al. 2009), but many have not, including uncertainties intrinsic to the determination of the stellar mass distribution. We start by summarising the main sources of uncertainty involved in the torque and gas flow calculation and then consider their relative importance.

1. Projected stellar mass distribution:
 - Importance of ICA dust correction: bias due to dust emission in $3.6 \mu\text{m}$ image.
 - Effectiveness of ICA dust correction: imperfections in the stellar map introduced by ICA.
 - Variations in stellar M/L .
2. 3D mass distribution and torques:
 - Deprojection: accuracy in PA, inclination.
 - Vertical disc structure: implications of assuming an isothermal disc and variations in disc scaleheight.
 - Centring of stellar mass map.
 - Centring of gas map.
3. Choice of ISM tracer:
 - Implications of neglecting HI in the central region.
 - Large-scale smooth component (short spacings).
 - Variations in X_{CO} .
 - Effect of resolution ($1''$, $3''$, $6''$).
 - Use of dust correction map to estimate radial gas flows.

In the next subsections and in Appendix A, we present a number of tests to quantitatively assess the impact of these uncertainties on torques and inflow estimates. The results of these tests are summarised in Table 2. We used the torques derived from our best ICA dust-corrected stellar mass map and the molecular gas distribution traced by PAWS as our fiducial result. For the various tests, we computed the relative difference with respect to the fiducial result, and the weighted mean is presented as an estimate of the relative uncertainty. We used the weighted average

A&A 588, A33 (2016)

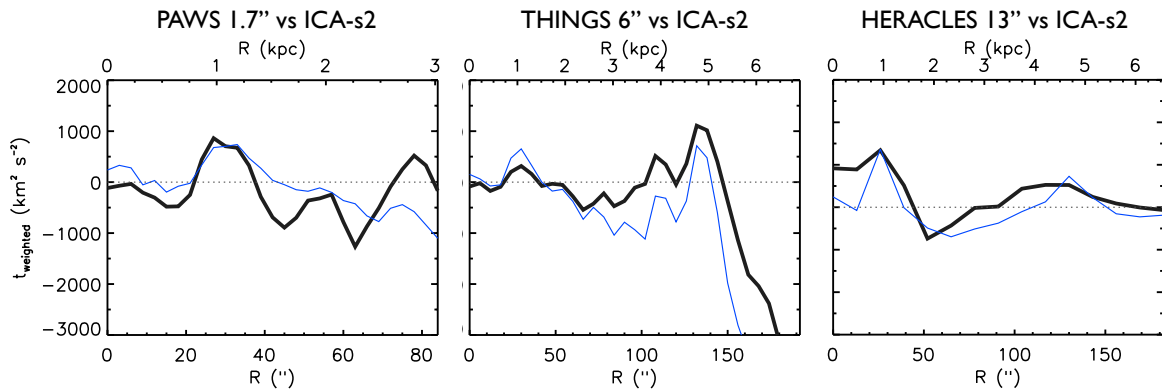


Fig. 6. Torque profiles using PAWS (1.7'' resolution), THINGS (6''), and HERACLES (13'') compared to the equivalent profiles using the ICA s_2 component (dust map) at matched resolution. The thick black line is the fiducial profile (using the actual gas distribution), the thin blue line corresponds to s_2 . The agreement is not one-to-one, but s_2 can be used as a first-order approximation in the absence of gas information at high enough resolution.

Table 2. Effect of the uncertainties in different input parameters on gravitational torques and inflow rates for M51.

Uncertainty due to...	Δt (%)	Δt for $R < 22''$ (%)	$\Delta(d^2M/dr dt)$ (%)	$\Delta(d^2M/dr dt)$ for $R < 22''$ (%)
Uncorrected, original $3.6\mu\text{m}$ image	101.3	70.7	93.2	73.0
Inclination ($\pm 5^\circ$)	51.7	39.3	45.3	50.1
Position angle ($\pm 3^\circ$)	34.6	6.7	21.0	19.0
Radially varying M/L	21.4	27.8	20.5	27.5
Shift of stellar mass map (0.75'')	20.3	71.2	34.3	80.6
Shift of gas image (0.75'')	12.6	27.2	17.5	33.7
Stellar disc scale-height ($\pm 20\%$)	5.1	10.8	6.4	11.0
Stellar disc vertical function (sech^2 vs. sech)	2.4	5.4	3.1	5.6
PAWS: 1.7'' vs. 3''	38.3	32.6	26.1	22.2
PAWS: 1.7'' vs. 6''	43.9	32.0	64.0	72.0
PAWS: 1.7'' vs. 13''	84.5	111.2	90.1	103.3
PAWS 6'' vs. THINGS 6''	79.7	65.6	85.8	85.1
PAWS 13'' vs. HERACLES 13''	32.2	40.0	41.0	34.0

to avoid divergencies associated with values close to zero, which would unrealistically bias the mean difference; for this reason, the corresponding fiducial profiles, $\tau(r)$ or $d^2M/dr dt$ were used to provide those radial weights.

As shown by Meidt et al. (2014) and Norris et al. (2014), the $3.6\mu\text{m}$ band minimises to a large extent the uncertainties in mass estimation, in the sense that it minimises extinction problems and allows for a single M/L to be applicable (with an uncertainty of 0.1 dex, smaller than the 0.2–0.3 dex associated with prescriptions based on optical colours, which are often used to calibrate other NIR bands, e.g. Zibetti et al. 2009). However, mass estimates based on $3.6\mu\text{m}$ require proper accounting for dust emission, which can contribute as much as $\sim 30\%$ of the flux globally in star-forming spirals. We assess the relevance of that critical correction for dust emission when the stellar mass distribution is calculated using a $3.6\mu\text{m}$ image in Sect. 5.1. This is the most critical uncertainty that had not been considered before, along with the resolution of the gas tracer, which we study in Sect. 5.2. The former has an impact of the order of $\sim 100\%$ in the case of M51 (a factor of 2), while the latter acts to “wash out” the signatures of the torque profiles, leading to much flatter profiles, and resulting in a difference of also $\sim 100\%$ when the resolution is degraded from 1'' to 13''.

The uncertainties on the position angle of the disc (PA), its inclination (i), and the correct centring of the stellar mass map and the gas map are likewise important, as has been shown by Haan et al. (2009). In Appendix A we confirm that these effects

are significant for the configuration of M51 and that they show a radial dependence that causes the inner bins to be more strongly subject to centring errors and bins at large radii more uncertain because of errors in the deprojection parameters (PA, i). Fortunately, we have access to precise measurements of the i and PA (Colombo et al. 2014), and the astrometry of our images (stellar mass map and gas map) was carefully calibrated to $< 1''$ (Schinnerer et al. 2013). The relevance of short spacing corrections on the interferometric gas maps was also stressed by García-Burillo et al. (2009, see their Fig. 20) and van der Laan et al. (2011, see their Fig. 12). Errors can be as high as a factor of 2 for some radii in the case of missing short spacings; this study, however, did not suffer from this problem because our PAWS map includes short spacing information that ensures the recovery of all the flux (see Pety et al. 2013).

For completeness, we also show in Appendix A that other possible uncertainties listed in Table 2, such as the vertical disc structure (function and scaleheight) or the radial variation of M/L , are clearly subdominant, with an impact $\leq 10\%$. In principle, a radially varying M/L could have an impact of as much as ~ 20 – 30% (as listed in Table 2), but this is an upper limit for galaxies with strong abundance gradients; for M51, the measured metallicity gradient is very shallow (0.02 ± 0.01 dex kpc^{-1} , Bresolin et al. 2004). We can therefore safely conclude that M/L variations within its disc will not pose a large problem for measuring torques and gas flows.

M. Querejeta et al.: Molecular gas inflow in M51

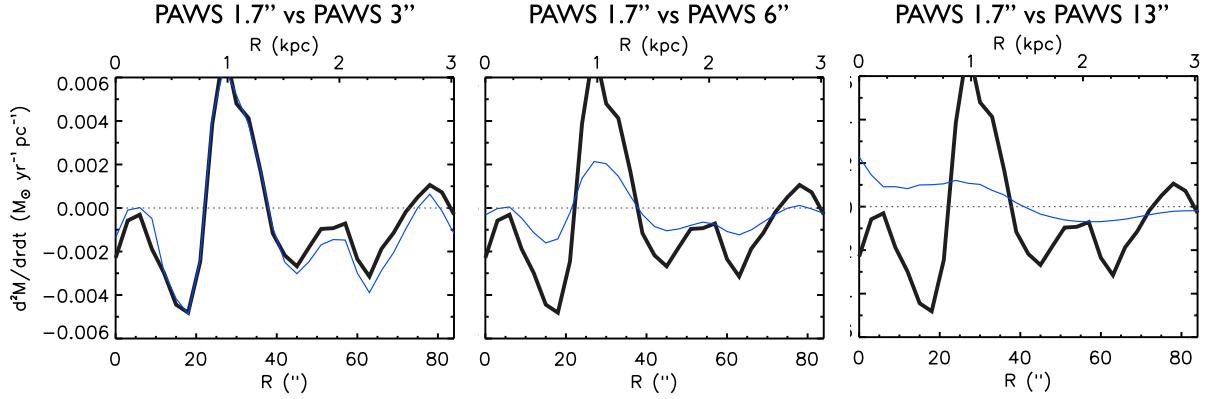


Fig. 7. Change in the torques that is due to the use of a gas map with different spatial resolutions. The thick blue line corresponds to the PAWS CO(1–0) intensity map at the resolution of the stellar mass map (1.7''), the blue line in the profiles from left to right correspond to the same PAWS map smoothed to 3'', 6'' and 13''.

Finally, we also demonstrate in Appendix A.1 that the uncertainty introduced by oversubtractions in the stellar mass map (a drawback of assuming only two sources with ICA) is modest. In fact, these oversubtractions are not a concern in the area of the nuclear bar, while the ICA correction clearly is important in that region because a considerable amount of dust emission needs to be accounted for. In Appendix A.6 we double-check the validity of the ICA-corrected stellar mass map by comparing it with the gravitational potential obtained from an independent band (HST 1.9 μm).

5.1. Importance of ICA dust correction

Querejeta et al. (2015) showed that the difference between the uncorrected 3.6 μm images and our ICA dust-corrected stellar mass maps is not only caused by hot dust in HII regions, but also by diffuse dust heated by the interstellar radiation field. Specifically, we identified considerable dust emission with ICA for M51 in the area of the nuclear bar (within $R < 22'' \sim 1 \text{ kpc}$). As much as 26% of the 3.6 μm light is due to dust emission within the central $R < 22''$ covered by the nuclear bar (see Fig. 3), and the ratio of dust emission (as identified with ICA) to CO (via PAWS 1'') increases from an average of ~ 0.02 in the PAWS field of view to ~ 0.2 in the area of the nuclear bar (a factor of 10).

The average change in the torque profile is a factor of 2 when the dust correction is not taken into account (100%, over the whole extent of the profile; 70% if we only consider the area of the nuclear bar, within $R < 22''$). Moreover, while the calculation based on the original, uncorrected 3.6 μm image led to positive profile values in the inner region ($r < 7'' = 250 \text{ pc}$; see Fig. 4), suggesting a radial outflow that would impede the flow of gas to the AGN, the ICA dust-corrected stellar mass map implies molecular gas inflow down to our resolution limit, leading to a qualitatively different interpretation. This stresses the importance of correcting 3.6 μm images for dust emission when the images are used to trace the distribution of stellar mass and gravitational torques are to be calculated.

5.2. Effect of the gas tracer resolution (1'', 3'', 6'', 13'')

In Fig. 7 we analyse the impact of spatial resolution on the profiles. Changing the resolution of the gas tracer will have an effect on the $\tau(r)$ torque profiles because the torques are weighted

by the gas distribution when computing the azimuthal averages. However, the effect becomes even stronger when measuring gas flows because in this case the gas column density is directly part of the equation; this is why we show the profile $d^2M/drdt$ instead of $\tau(r)$ in Fig. 7.

To determine the resolution effect, we compared the different versions of the PAWS map, 1'' = 40 pc, 3'' = 120 pc and 6'' = 240 pc (tapered), and 13'' = 520 pc (smoothed), corrected for the nuclear outflow component as described in Sect. 3.6. For reference, we recall that the nuclear bar has a radius of $R_{\text{bar}} \approx 20''$ and the spirals arms traced by CO have a typical width of around $\sim 10''$. We verified that the results do not change if (instead of tapering) we smooth the PAWS moment-0 map with the corresponding Gaussian kernel ($FWHM = 3''$, 6'', 13''). We note that 6'' and 13'' are the angular resolutions provided by the THINGS HI and HERACLES CO surveys. For consistency in terms of resolution, we also smoothed our stellar mass map to match these resolutions following an analogous procedure.

Degrading the resolution from 1.7'' to 3'' is associated with only a modest change of the gas flow rates (26%). However, the average change is large when we move to 6'' (64%) and becomes even more so at a resolution of 13'' (90%). This stresses that a map of the gas distribution is necessary that probes the adequate spatial scales; if the resolution of the gas tracer is too low ($\geq 200 \text{ pc}$), the torque profiles are artificially smoothed and important structure becomes lost.

5.3. Typical final uncertainty

As we have seen, the factors that would most severely hamper the analysis of gravitational torques are the absence of dust correction in the 3.6 μm images and using a gas map with poor resolution; these two are not a concern for our analysis. The next most significant sources of error are the uncertainty in the de-projection parameters (PA, i), which can introduce an error of as much as $\sim 30\text{--}50\%$. Similarly, the incorrect centring of the NIR image can have a very strong effect on the torques, but we confirmed our astrometry to an accuracy better than 1'', therefore the error should typically be smaller than $\sim 20\%$ (the innermost bin is a special case discussed below). The centring of the gas image is even less problematic because the associated uncertainty is smaller and our astrometry is even more accurate.

As shown in Appendix A (Fig. A.2), the uncertainty introduced by an error in the determination of deprojection parameters (PA, i) has a clear radial dependence, becoming particularly important in the outer regions of the galaxy ($\sim 100\%$ at a radius of 3 kpc). In the inner 1 kpc, only the uncertainty due to errors in i could be significant, $\sim 40\%$ (the uncertainty due to errors in PA is below $\sim 10\%$). Conversely, for the centring of the NIR image, the radial dependence of the uncertainty is reversed, with larger errors for smaller radii (up to $\sim 50\%$ in the first bin). As a consequence of this, the innermost bin is subject to considerably high uncertainties, which add to potential complications associated with the outflow component that we subtracted in Sect. 3.6. Appendix A.6 also suggests divergencies in the inner $R \lesssim 5''$ when using an independent band to compute the gravitational potential (HST $1.9\mu\text{m}$). Therefore, the innermost bin has to be treated with caution, and we have shaded it in Fig. 4.

6. Discussion

The feedback from AGN plays a critical role in reconciling observations with cosmological simulations of galaxy evolution, prevents galaxies from over-growing, and it might hold the key to the tight scaling relations observed between the mass of supermassive black holes and their host galaxies. However, this important process is ultimately regulated by the availability of fuel in the nucleus, and consequently, the transport of gas across the galaxy is a crucial process. The gas might be accreted and continuously replenished from the circumgalactic medium, but in the absence of effective mechanisms to transport it to the centre, the fuel will never reach the AGN.

In this context, we have studied the gas transport in the disc of M51, making use of our stellar mass map (based on $3.6\mu\text{m}$ imaging and corrected for dust emission with ICA). We have shown that the use of a proper stellar mass map is critical, as is the use of a gas tracer at sufficiently high spatial resolution (see Table 2, which summarises the tests that we have presented in Sect. 5). Even if the analysis of all the possible sources of uncertainty might sound pessimistic, the radical improvement of instrumental capabilities and the advancement of techniques allow us to enter a regime where this can be overcome. With ALMA and NOEMA, maps of the molecular gas distribution at sufficiently high spatial resolution are expected to be easily achievable. Moreover, in the mid-term future, the advent of JWST should make it possible to obtain proper stellar mass maps using our technique or others with even higher resolutions and for more galaxies.

6.1. Inflow rates

The main result of the paper is that torques imply consistent molecular gas inflow from $R = 22'' \sim 1$ kpc down to our resolution limit when the ICA-corrected stellar mass map of M51 is used (but we note that the inner bin, $R < 3''$, is subject to large uncertainties; see also Appendix A.6). Torques become positive after $R = 22''$, implying radial outflow, and become negative again at a radius of $R = 37''$. This agrees with the presence of a nuclear molecular ring, which could have formed through the accumulation of molecular gas as a consequence of the flow pattern that we have discussed, and which would imply a dynamical barrier for gas transport. There must be other mechanisms (viscous torques, instabilities, etc.) that allow the gas to overcome this barrier and access the area of the nuclear bar, but they probably operate over longer timescales, and that is the reason for the formation of the overdense molecular gas in the shape of a ring.

We find that as much as $\sim 5 M_{\odot}/\text{yr}$ of molecular gas are involved in net inflow motions in the central 1 kpc of M51. In its way towards the centre, part of this amount of gas will form stars and never reach the nucleus; for reference, the integrated star formation rate within the central $20''$ is around $0.5 M_{\odot}/\text{yr}$ (Kennicutt et al. 2007). At the smallest scales accessible to us ($R \sim 3'' \sim 110$ pc), the inflow rate is $\sim 1 M_{\odot}/\text{yr}$. Even if we ignore this innermost bin because of the increasingly large uncertainties, the second and third bins imply virtually the same inflow value, which suggests that the result is robust. These net inflow rates should be regarded as a lower limit, since we did not attempt to account for viscous torques or other dissipative effects (cloud-cloud collisions, shocks, etc.). However, these effects usually operate on much longer timescales, therefore the global value is expected to be close to the value that we have derived using torques. After gas has reached a radius of 100 pc (the outer edge of our innermost bin), dynamical friction effects are expected to quickly bring the gas close enough to the SMBH (Combes 2002).

This observationally estimated inflow rate is an important number, for instance, to compare with the rates obtained using simulations of M51 or other grand-design spiral galaxies. In particular, the simulation of the M51 system presented in Dobbs et al. (2010) allows us to measure the flow of molecular gas and compare this to our observations. As we show in Appendix B, the interacting system evolves towards a more centrally concentrated molecular gas distribution, while an analogous model in isolation does not show such a trend. The change in H_2 surface density in the simulation implies molecular gas inflow at a rate of $\sim 2 M_{\odot}/\text{yr}$, which is similar to our observational findings. From a future perspective, gathering similar inflow rates for more galaxies will permit accessing valuable statistics, which might help to impose constraints on cosmological simulations.

6.2. Dynamical resonances

Our analysis of the new gravitational torque profiles for M51 has led us to suggest that the galaxy has two main corotations: one associated with the nuclear bar, approximately at $\text{CR}_{\text{bar}} \sim 20''$, with a pattern speed of $\Omega_{\text{p}}^{\text{bar}} = (185 \pm 15) \text{ km s}^{-1} \text{ kpc}^{-1}$, and one for the spiral pattern near $\text{CR}_{\text{sp}} \sim 100''$, implying a pattern speed of $\Omega_{\text{p}}^{\text{spiral}} = (53 \pm 5) \text{ km s}^{-1} \text{ kpc}^{-1}$. The other resonances associated with these two corotations are summarised in Table 1.

The corotation of the spiral occurs much farther out than the crossing near $R = 60''$ suggested by Meidt et al. (2013) as a potential location for the spiral corotation, which should be considered superceded by our more robust determination at $100''$. Meidt et al. (2013) also used the technique of constructing radial torque profiles to assess the positions of resonances, but there are a number of factors that account for the difference between both results. First, the torque map of Meidt et al. (2013) was compromised by remaining non-stellar emission, which only our improved strategy has been able to identify (through an iterative implementation of ICA, see Querejeta et al. 2015). The difference in the dust fraction identified with ICA is from 8% (Meidt et al. 2013) to 34% (Querejeta et al. 2015). We note that, specifically, the region from $40\text{--}80''$ is characterised by a high incidence of HII regions along the spiral arms (hence the large change of the torque profile in that area given our second iteration of ICA, which is designed to better accommodate for the multi-source mix of hot dust and PAHs).

Secondly, the new tests that we performed here have shown that the torque profiles based on PAWS are not meaningful

outside $85''$; even if PAWS provides information out to a radius of $R \sim 120''$, the coverage is not uniform in the range $R \sim 85\text{--}120''$ because of the rectangular field of view of the survey. Even at a radius of $R \sim 90''$ (only $5''$ beyond the last possible circular aperture) the difference between the two profiles can be as much as a factor 2, and this only deteriorates as the radius increases and the sampling is more incomplete. We therefore opted to limit our measurements with the PAWS data to within $R < 85''$ and extracted measurements of torques at larger radii with THINGS, which covers a full $0\text{--}2\pi$ radians out to $R \sim 20$ kpc, albeit with lower spatial resolution.

We also used HERACLES, which traces molecular gas (as opposed to THINGS, tracing atomic gas) to confirm the analysis out to larger radii; this should allow us to avoid the biases that we just discussed that are due to the non-circular shape of the PAWS field of view. In principle, there might be important differences between THINGS and HERACLES, not only because of the different spatial resolution, but also because HI and CO emission are not exactly co-spatial (see Schinnerer et al. 2013), and they also have significant kinematic differences (Colombo et al. 2014). However, despite tracing different phases of the ISM and having different resolutions, the bottom panel of Fig. 5 shows that the corresponding torque profiles are reasonably similar, and they have major negative–positive zero-crossings at similar positions ($R \sim 20''$, the CR of the nuclear bar; $R \sim 100''$, the proposed CR of the spiral). The qualitative agreement between both profiles (and the analysis of $s1/s3$ terms) reinforces the scenario that we proposed here.

Additionally, our estimates for the two (bar and spiral) corotation radii in M51 are consistent with the values independently estimated by Zhang & Buta (2012) ($R_{\text{CR1}} = 25''$ and $R_{\text{CR2}} = 110''$). The corotation of the bar also agrees with Colombo et al. (2014), who suggested a radius of $R_{\text{CR}}^{\text{bar}} = 20''$ that was confirmed visually and analytically with a clear change from $m - 1$ to $m + 1$ modes in the residual velocity field (Canzian 1993). Their proposed resonances for the spiral, however, mostly relied on the torque result from Meidt et al. (2013), which suffered from the problems mentioned above. It is interesting to note that their proposed $m = 3$ mode could play the role of dynamically coupling the bar with the spiral structure, explaining the position of the inner pseudo-ring around $R \sim 20''$.

From a broader perspective, these results raise interesting questions about the nature of spiral structure. The interaction with the companion NGC 5195 has been suggested to drive dynamical changes over relatively short timescales (~ 100 Myr – 1 Gyr), which might contradict the naïve picture of a long-lasting density-wave spiral. For example, Dobbs et al. (2010) did not find a single global pattern speed for M51 in their numerical simulation and instead suggested a picture in which the spiral arms are the result of tidally induced local kinematic density patterns that wind up (i.e. the pattern speed varies with radius). In their simulation, corotation can only exist beyond a radius of 7 kpc (probably around 10 kpc, close to the satellite NGC 5195). Salo and Laurikainen (2000) also used numerical simulations to show that the close passage of the companion removes any previous hints of spiral structure, suggesting that the spiral appearance that we see today is relatively new and might not persist very long.

In this context, we need to be very cautious when interpreting the observational torque profiles in terms of resonances because ILR, OLR and other resonances can also have an imprint in the form of a change of sign. The fact that the THINGS profile only shows two crossings from negative to positive is reassuring, but it could be that the second one is not corotation, but rather an

inner resonance of the spiral that might have corotation much farther out, even outside our fields of view. This possibility cannot be ruled out with our data.

7. Summary and conclusions

We have used the new $3.6\mu\text{m}$ dust-corrected stellar mass map from Querejeta et al. (2015) to construct a gravitational torque map for M51, which, in conjunction with the PAWS dataset, has allowed us to estimate radial gas flows in this galaxy.

1. There is plenty of molecular gas inflow in the central area of M51: $\sim 5 M_{\odot}/\text{yr}$ in the central $20'' \sim 1$ kpc, $\sim 1 M_{\odot}/\text{yr}$ as we approach our resolution limit (60 pc from the nucleus). This inflow is driven by the nuclear bar.
2. Torques suggest a corotation of the bar at $R \sim 20''$ and corotation of the spiral at $R \sim 100''$.
3. We demonstrated the importance of correcting $3.6\mu\text{m}$ images for dust emission when estimating torques. For these purposes, differences can reach a factor of 2. In the case of M51, even the qualitative result of whether or not there is inflow in the central kpc changes as a consequence of the dust correction in the central area.
4. We also assessed the difference due to varying M/L and uncertainties in inclination, PA, etc., showing that the effect of M/L is modest, and confirming the results from Hopkins et al. (2009) for the other parameters (largest uncertainty due to centring of NIR image and deprojection parameters).
5. We considered different ISM tracers for the azimuthal weighing of the torques. We showed that the spatial resolution of the molecular gas is critical (better than ~ 100 pc needed), and the contaminant map $s2$ can be used at most as a first-order approximation to identify the presence of dynamical resonances and gas flows.

In conclusion, this study provides the first estimation of radial gas flows in M51, with an inflow rate that can be checked against simulations and can be compared with outflow rates. We also carefully analysed the limitations in the calculation of gravitational torques, which should be useful when planning similar studies in other galaxies; this will be especially relevant as ALMA and NOEMA become fully operative. In particular, we stressed the importance of using proper stellar mass maps when estimating radial gas flows in nearby galaxies, in addition to the strong limitation imposed by the resolution of the available molecular gas observations. Thanks to the efforts of S⁴G and the public data release of accurate stellar mass maps through IRSA for more than 1500 nearby galaxies, with the spatial resolutions achieved with ALMA and NOEMA, these estimations should be feasible in the opening ALMA and NOEMA era.

Acknowledgements. The authors would like to thank the anonymous referee for a helpful report, as well as Daniela Calzetti, Nick Z. Scoville and Mari Polletta for making the HST/F190N mosaic available to us. We also appreciate valuable comments from Françoise Combes and Sebastian Haan. We acknowledge financial support from the DAGAL network from the People Programme (Marie Curie Actions) of the European Union’s Seventh Framework Programme FP7/2007-2013/ under REA grant agreement number PITN-GA-2011-289313. M.Q. acknowledges the International Max Planck Research School for Astronomy and Cosmic Physics at the University of Heidelberg (IMPRS-HD). S.G.B. thanks support from Spanish grant AYA2012-32295. J.P. acknowledges support from the CNRS programme “Physique et Chimie du Milieu Interstellaire” (PCMI). M.Q., S.E.M., D.C. and A.H. acknowledge funding from the Deutsche Forschungsgemeinschaft (DFG) via grants SCHI 536/7-2, SCHI 536/5-1, and SCHI 536/7-1 as part of the priority program SPP 1573 “ISM-SPP: Physics of the Interstellar Medium”.

References

- Antonucci, R. 1993, *ARA&A*, 31, 473
- Athanassoula, E. 1992a, *MNRAS*, 259, 328
- Athanassoula, E. 1992b, *MNRAS*, 259, 345
- Barnaby, D., & Thronson, Jr., H. A. 1992, *AJ*, 103, 41
- Binney, J., & Tremaine, S. 1987, in *Galactic dynamics* (Princeton, NJ, Princeton University Press), 747
- Boone, F., Baker, A. J., Schinnerer, E., et al. 2007, *A&A*, 471, 113
- Bradley, L. D., Kaiser, M. E., & Baan, W. A. 2004, *ApJ*, 603, 463
- Bresolin, F., Garnett, D. R., & Kennicutt, Jr., R. C. 2004, *ApJ*, 615, 228
- Buta, R., & Combes, F. 1996, *Fund. Cosm. Phys.*, 17, 95
- Canzian, B. 1993, *ApJ*, 414, 487
- Ciardullo, R., Feldmeier, J. J., Jacoby, G. H., et al. 2002, *ApJ*, 577, 31
- Cisternas, M., Gadotti, D. A., Knapen, J. H., et al. 2013, *ApJ*, 776, 50
- Colombo, D., Meidt, S. E., Schinnerer, E., et al. 2014, *ApJ*, 784, 4
- Combes, F. 2001, in *Advanced Lectures on the Starburst-AGN*, eds. I. Aretxaga, D. Kunth, & R. Mújica, 223
- Combes, F. 2002, ArXiv e-prints [arXiv:astro-ph/0208113]
- Combes, F. 2003, in *Active Galactic Nuclei: From Central Engine to Host Galaxy*, eds. S. Collin, F. Combes, & I. Shlosman, *ASP Conf. Ser.*, 290, 411
- Combes, F., & Sanders, R. H. 1981, *A&A*, 96, 164
- Combes, F., García-Burillo, S., Boone, F., et al. 2004, *A&A*, 414, 857
- Combes, F., García-Burillo, S., Casasola, V., et al. 2013, *A&A*, 558, A124
- Combes, F., García-Burillo, S., Casasola, V., et al. 2014, *A&A*, 565, A97
- Comerón, S. 2013, *A&A*, 555, L4
- Comerón, S., Knapen, J. H., Beckman, J. E., et al. 2010, *MNRAS*, 402, 2462
- Comerón, S., Salo, H., Laurikainen, E., et al. 2014, *A&A*, 562, A121
- Crane, P. C., & van der Hulst, J. M. 1992, *AJ*, 103, 1146
- Dobbs, C. L., Glover, S. C. O., Clark, P. C., & Klessen, R. S. 2008, *MNRAS*, 389, 1097
- Dobbs, C. L., Theis, C., Pringle, J. E., & Bate, M. R. 2010, *MNRAS*, 403, 625
- Emsellem, E., Renaud, F., Bournaud, F., et al. 2015, *MNRAS*, 446, 2468
- Ferrarese, L., & Ford, H. 2005, *Space Sci. Rev.*, 116, 523
- Ferrarese, L., & Merritt, D. 2000, *ApJ*, 539, L9
- Font, J., Beckman, J. E., Querejeta, M., et al. 2014, *ApJS*, 210, 2
- Fragkoudi, F., Athanassoula, E., Bosma, A., & Iannuzzi, F. 2015, *MNRAS*, 450, 229
- García-Burillo, S., Combes, F., & Gerin, M. 1993, *A&A*, 274, 148
- García-Burillo, S., Combes, F., Hunt, L. K., et al. 2003, *A&A*, 407, 485
- García-Burillo, S., Combes, F., Schinnerer, E., Boone, F., & Hunt, L. K. 2005, *A&A*, 441, 1011
- García-Burillo, S., Fernández-García, S., Combes, F., et al. 2009, *A&A*, 496, 85
- García-Burillo, S., Combes, F., Usero, A., et al. 2014, *A&A*, 567, A125
- Gebhardt, K., Bender, R., Bower, G., et al. 2000, *ApJ*, 539, L13
- Glover, S. C. O., & Mac Low, M.-M. 2007, *ApJS*, 169, 239
- Gültekin, K., Richstone, D. O., Gebhardt, K., et al. 2009, *ApJ*, 698, 198
- Haan, S., Schinnerer, E., Emsellem, E., et al. 2009, *ApJ*, 692, 1623
- Heller, C. H., & Shlosman, I. 1994, *ApJ*, 424, 84
- Ho, L. C., Filippenko, A. V., & Sargent, W. L. W. 1997a, *ApJS*, 112, 315
- Ho, L. C., Filippenko, A. V., & Sargent, W. L. W. 1997b, *ApJ*, 487, 568
- Hohl, F., & Hockney, R. W. 1969, *J. Comput. Phys.*, 4, 306
- Hopkins, P. F., & Quataert, E. 2010, *MNRAS*, 407, 1529
- Hopkins, P. F., & Quataert, E. 2011, *MNRAS*, 415, 1027
- Hopkins, P. F., Cox, T. J., Younger, J. D., & Hernquist, L. 2009, *ApJ*, 691, 1168
- Hunt, L. K., Combes, F., García-Burillo, S., et al. 2008, *A&A*, 482, 133
- Jogee, S. 2006, in *Physics of Active Galactic Nuclei at all Scales*, ed. D. Alloin, (Berlin Springer Verlag), *Lect. Notes Phys.*, 693, 143
- Kennicutt, Jr., R. C., Calzetti, D., Walter, F., et al. 2007, *ApJ*, 671, 333
- Knapen, J. H., Shlosman, I., & Peletier, R. F. 2000, *ApJ*, 529, 93
- Kormendy, J., & Richstone, D. 1995, *ARA&A*, 33, 581
- Laine, S., Shlosman, I., Knapen, J. H., & Peletier, R. F. 2002, *ApJ*, 567, 97
- Leroy, A. K., Walter, F., Brinks, E., et al. 2008, *AJ*, 136, 2782
- Leroy, A. K., Walter, F., Bigiel, F., et al. 2009, *AJ*, 137, 4670
- Lynden-Bell, D. 1969, *Nature*, 223, 690
- Lynden-Bell, D., & Kalnajs, A. J. 1972, *MNRAS*, 157, 1
- MacArthur, L. A., Courteau, S., Bell, E., & Holtzman, J. A. 2004, *ApJS*, 152, 175
- Magorrian, J., Tremaine, S., Richstone, D., et al. 1998, *AJ*, 115, 2285
- Matsushita, S., Sakamoto, K., Kuo, C.-Y., et al. 2004, *ApJ*, 616, L55
- Matsushita, S., Muller, S., & Lim, J. 2007, *A&A*, 468, L49
- Matsushita, S., Trung, D.-V., Boone, F., et al. 2015, *ApJ*, 799, 26
- McConnell, N. J., & Ma, C.-P. 2013, *ApJ*, 764, 184
- Meidt, S. E., Schinnerer, E., Knapen, J. H., et al. 2012, *ApJ*, 744, 17
- Meidt, S. E., Schinnerer, E., García-Burillo, S., et al. 2013, *ApJ*, 779, 45
- Meidt, S. E., Schinnerer, E., van de Ven, G., et al. 2014, *ApJ*, 788, 144
- Menéndez-Delmestre, K., Sheth, K., Schinnerer, E., Jarrett, T. H., & Scoville, N. Z. 2007, *ApJ*, 657, 790
- Muñoz-Mateos, J. C., Sheth, K., Regan, M., et al. 2015, *ApJS*, 219, 3
- Mundell, C. G., & Shone, D. L. 1999, *MNRAS*, 304, 475
- Norris, M. A., Meidt, S., Van de Ven, G., et al. 2014, *ApJ*, 797, 55
- Peng, C. Y., Ho, L. C., Impy, C. D., & Rix, H.-W. 2010, *AJ*, 139, 2097
- Pety, J., Schinnerer, E., Leroy, A. K., et al. 2013, *ApJ*, 779, 43
- Querejeta, M., Meidt, S. E., Schinnerer, E., et al. 2015, *ApJS*, 219, 5
- Quillen, A. C., Frogel, J. A., & Gonzalez, R. A. 1994, *ApJ*, 437, 162
- Quillen, A. C., Frogel, J. A., Kenney, J. D. P., Pogge, R. W., & Depoy, D. L. 1995, *ApJ*, 441, 549
- Rautiainen, P., Salo, H., & Laurikainen, E. 2008, *MNRAS*, 388, 1803
- Rix, H.-W., & Rieke, M. J. 1993, *ApJ*, 418, 123
- Salo, H., Laurikainen, E., Laine, J., et al. 2015, *ApJS*, 219, 4
- Schinnerer, E., Eckart, A., Tacconi, L. J., Genzel, R., & Downes, D. 2000, *ApJ*, 533, 850
- Schinnerer, E., Meidt, S. E., Pety, J., et al. 2013, *ApJ*, 779, 42
- Schuster, K. F., Kramer, C., Hitschfeld, M., García-Burillo, S., & Mookerjee, B. 2007, *A&A*, 461, 143
- Scoville, N. Z., Yun, M. S., Armus, L., & Ford, H. 1998, *ApJ*, 493, L63
- Scoville, N. Z., Polletta, M., Ewald, S., et al. 2001, *AJ*, 122, 3017
- Sheth, K., Regan, M., Hinz, J. L., et al. 2010, *PASP*, 122, 1397
- Shetty, R., Vogel, S. N., Ostriker, E. C., & Teuben, P. J. 2007, *ApJ*, 665, 1138
- Shlosman, I., & Noguchi, M. 1993, *ApJ*, 414, 474
- Shlosman, I., Frank, J., & Begelman, M. C. 1989, *Nature*, 338, 45
- Shlosman, I., Begelman, M. C., & Frank, J. 1990, *Nature*, 345, 679
- Sparke, L. S., & Sellwood, J. A. 1987, *MNRAS*, 225, 653
- Tagger, M., Sygnet, J. F., Athanassoula, E., & Pellat, R. 1987, *ApJ*, 318, L43
- Theis, C., & Spinneker, C. 2003, *Ap&SS*, 284, 495
- van der Laan, T. P. R., Schinnerer, E., Boone, F., et al. 2011, *A&A*, 529, A45
- van der Laan, T. P. R., Schinnerer, E., Emsellem, E., et al. 2013, *A&A*, 556, A98
- Wada, K., & Koda, J. 2004, *MNRAS*, 349, 270
- Wainscoat, R. J., Freeman, K. C., & Hyland, A. R. 1989, *ApJ*, 337, 163
- Walter, F., Brinks, E., de Blok, W. J. G., et al. 2008, *AJ*, 136, 2563
- Wong, T., Blitz, L., & Bosma, A. 2004, *ApJ*, 605, 183
- Zhang, X., & Buta, R. J. 2012, ArXiv e-prints [arXiv:1203.5334]
- Zibetti, S., Charlot, S., & Rix, H.-W. 2009, *MNRAS*, 400, 1181

Appendix A: Sources of uncertainty involved in torque and gas flow estimations

A.1. Imperfections introduced by the ICA dust correction

As commented in Meidt et al. (2012) and Querejeta et al. (2015), the choice of only two components for the ICA separation can introduce some imperfections in the output stellar mass map. These come mostly in the form of oversubtractions corresponding to HII regions, where the [3.6]–[4.5] colour of the hot dust is considerably redder than the average dust colour found by ICA; when the $3.6\mu\text{m}$ image is separated into two components using the scaling given by the stellar and dust colours solved for by ICA, the regions of intrinsically redder colour than average will be overestimated in terms of dust, leading to an oversubtraction in the stellar component. The problem can be alleviated by a sophisticated interpolation technique or by masking these regions. However, here we show that for the purpose of estimating gas flows based on the corresponding gravitational torque map, the impact of leaving these imperfections in the stellar mass map is not very large. Moreover, as becomes evident from Fig. A.1, the oversubtractions are completely absent from the region of the bar, which means that they would not affect the inflow claim that we have made for the central $R < 1$ kpc.

An inspection of our M51 stellar mass map with attention to the areas of very red colours ($[3.6] - [4.5] > 0.2$, which is similar to imposing a sufficiently high $H\alpha$ flux) shows that the ‘oversubtractions’ have average sizes of ~ 6 px in diameter (minimum ~ 3 px, maximum ~ 12 px in diameter; i.e. $\sim 2 - 9'' \sim 80 - 320$ pc; see Fig. A.1). The contrast of these oversubtractions, measured as the minimum value in the centre of the oversubtraction divided by the average value in the immediate surroundings, is typically ~ 0.7 (a contrast value of 1 would indicate no oversubtraction at all; the contrast of 0.7 means that the oversubtractions typically involve a $\sim 30\%$ depression with respect to the local flux); we have also confirmed that the standard deviation of the contrast from one region to another is small (≤ 0.1).

In an attempt to quantify the impact of these oversubtractions, we used a smooth, multi-component Galfit model of M51 (Peng et al. 2010) and imposed a random distribution of oversubtractions that scale to the local flux (one of these realisations is also illustrated in the right panel of Fig. A.1). The imperfections were modelled as de Vaucouleurs profiles that were subtracted from the smooth model, with the central peak brightness of each oversubtraction being a fraction of the local flux (contrast of 0.7), and with a scale length that reflects the typical range of scale lengths covered by the oversubtractions in the ICA dust-corrected stellar mass map (we assumed a normal distribution for the sizes, with a mean of 6 px and a standard deviation of 2 px). We performed a battery of 40 such experiments, in which the oversubtractions are placed randomly in the disc, wherever the model shows significant flux (> 0.6 MJy/sr). This leads to a typical change in the torque profile of $\sim 10\%$ (0.13 ± 0.06). We also checked that forcing the positions of the oversubtractions to “cluster” by allowing them only to be placed where the colour map $[3.6] - [4.5] > 0.2$ (or, equivalently, very high $H\alpha$ flux) does not have a dramatic effect on the torque profiles: the final uncertainty in the torque profile increases, but is still below 25%. We imposed a total of 20 oversubtractions, but we checked that doubling this amount (40 oversubtractions) also keeps the final errors below 20%.

Therefore, the uncertainty introduced on the final torque profiles by the imperfections associated with the ICA correction is of the order of $\sim 10\%$ and is reasonably bound to be below

20% even under the most unfavourable conditions. This is much smaller than the change implied by the ICA correction itself ($> 80\%$), which shows that the benefit and importance of using the dust-corrected stellar mass map clearly outweighs the drawback associated with these oversubtractions.

A.2. Variations in stellar M/L

As identified by MacArthur et al. (2004), the most significant changes in ages and metallicity within spiral galaxies are radial, with a fairly smooth variation as a function of radius. The change is such that the inner regions are older and more metal-rich, while the outer regions are younger and more metal-poor. Even if we assume that the radial change in M/L that is due to these age and metallicity gradients is the maximum variation allowed by the Meidt et al. (2014) conversion value (from 0.48 at $R = 0$ to 0.75 at $R = R_{\text{max}}$, spanning the 0.6 ± 0.1 dex uncertainty), this introduces only a modest change in the final torque profile ($\sim 20\%$), as is also visible in the bottom right panel of Fig. A.3.

We note that our assumption is very conservative because the age and metallicity gradients within a given galaxy are in general much smaller than the changes from galaxy to galaxy, for which the Meidt et al. (2014) uncertainty accounts. Moreover, the measured metallicity abundance gradient in M51 is very shallow (0.02 ± 0.01 dex kpc^{-1} Bresolin et al. 2004). Therefore, we can safely conclude that M/L variations within the disc of a galaxy will not pose a large problem for measuring torques and gas flows, and even less so for M51.

A.3. Deprojection: accuracy in PA and inclination

Figure A.3 shows the effect of varying the deprojection parameters, inclination, and PA of the disc within the range covered by the error bars of the observational measurements ($i = 22 \pm 5$, $\text{PA} = 173 \pm 3$; Colombo et al. 2014). Our underlying assumption is that the molecular gas disc traced by CO is coplanar with the stellar disc, which seems to be a justified assumption; this leads to a considerable reduction of the uncertainties in these parameters (derived from kinematics) with respect to what could be obtained from photometry. For the particular configuration of M51, the change implied by the uncertainty in inclination and PA is significant, $\sim 50\%$ and $\sim 35\%$, respectively, when the whole extent of the profiles is considered. We note, like Haan et al. (2009) have pointed out, that there is a radial dependence of the resulting errors. Specifically, for the deprojection parameters (PA, i), the impact of the uncertainties becomes larger for larger radii; in the area of the nuclear bar, the uncertainties decrease to 39% and 7% for i and PA, respectively. However, the errors in PA and i can become dominant at large radii ($> 2 - 3$ kpc): this radial dependence of the errors is demonstrated in Fig. A.2.

A.4. Vertical disc structure

We assumed that the vertical structure of the stellar disc corresponds to an isothermal disc with constant scale height; this is confirmed by observations (Wainscoat et al. 1989; Barnaby & Thronson 1992) and expected theoretically if the disc is in equilibrium. The vertical distribution of mass can be described by the following function:

$$\rho_z(z) = \rho_0 \text{sech}^2(z/h). \quad (\text{A.1})$$

We also checked that using other functions, such as sech instead of sech^2 , provides almost exactly the same answer; the

A&A 588, A33 (2016)

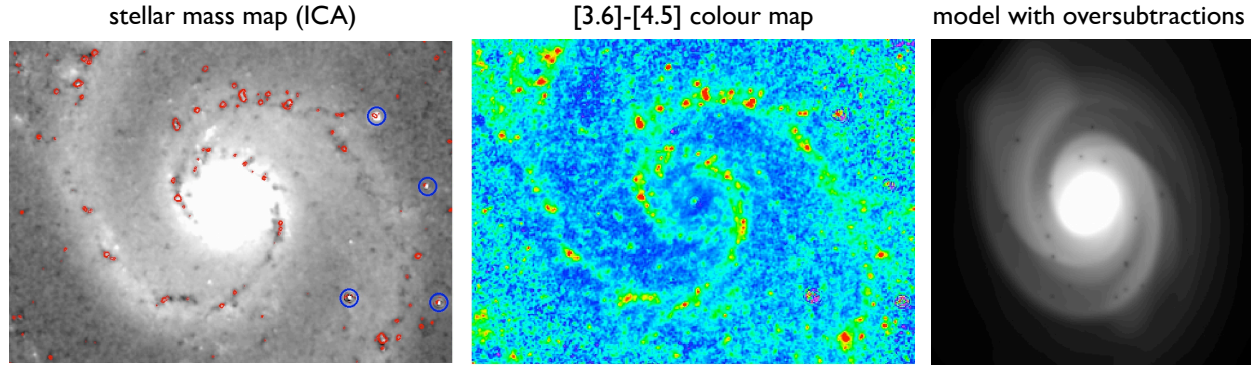


Fig. A.1. *Left:* stellar mass map of M51, shown on a scale that emphasises the oversubtractions associated with the ICA dust correction; the red contours are the regions of M51 where the [3.6]–[4.5] colour is very red, basically corresponding to HII regions ([3.6]–[4.5] > 0.2). The blue circles mark the positions of field stars, with the clear signature of concentric circles in the colour map due to a saturated PSF. *Middle:* [3.6]–[4.5] colour map of M51; compare the lack of very red regions in the central $R < 22'' \sim 1$ kpc with their presence in the spiral arms. *Right:* one of the 40 random realisations of the model with oversubtractions as described in the text (Sect. A.1), which we use to assess the effect of these imperfections on gravitational torques.

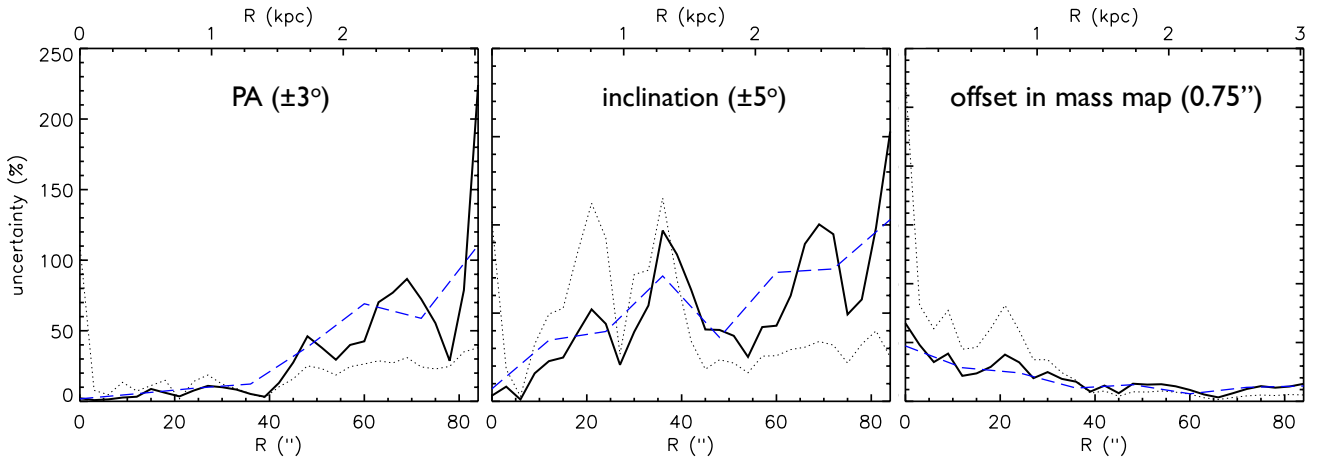


Fig. A.2. Radial dependence of uncertainties associated with PA ($\pm 3^\circ$), inclination ($\pm 5^\circ$) and an offset of 1px in the centring of the NIR image. The continuous black line shows the effect on torques, the dotted line corresponds to the effect on the local flow rates, and the dashed blue line is the average tendency (effect on torques averaged over regions of ~ 400 pc).

changes are $\leq 10\%$ in any case. The scale height is estimated as $h \sim 1/12H_{\text{disc}}$ (Wainscoat et al. 1989; Barnaby & Thronson 1992), for which $H_{\text{disc}} = 100''$ from the Galfit photometric decomposition of M51 (Salo et al. 2015). We also considered possible variations in the disc scale-height: as long as the variation in the scale height is kept below 20%, the effect is negligible (average change of 5% on the torque profile). Even a very large change in the scale height, of the order of 50%, would only have an effect of $\sim 30\%$ on the torques.

A.5. Centring of gas and stellar mass maps

As has discussed by Haan et al. (2009), one of the most critical points limiting the accuracy of the torques is the proper centring of the NIR image. Figure A.3 shows the difference introduced by an offset of $0.75''$ and demonstrates the clear radial dependence of the error: it decreases with distance. The implied difference in the central $22''$ (880 pc) is 71%, while it drops to only 20% if we consider all radii out to $90''$ (3 kpc). This is also illustrated

by Fig. A.2, in which the average radial dependence of the uncertainties is made explicit.

For the $3.6\mu\text{m}$ image and the stellar mass map based on it, the astrometric accuracy is lower than $1''$, as inferred from a comparison with the shifted SINGS $3.6\mu\text{m}$ image (Schinnerer et al. 2013) using foreground point sources as the matching reference. This is reassuring because even if offsets in the stellar mass map are one of the main sources of uncertainty, in our case this uncertainty should be clearly below $1''$, which involves a maximum average effect of $\sim 20\%$. However, as a result of the radial dependence that we have already noted, the inner bins will be subject to a larger uncertainty.

As also pointed out by Hopkins et al. (2009), the centring of the gas map (e.g. moment-0 map of molecular gas intensity distribution) is not as crucial as the centring of the NIR image. This is because an error in the gas centring will only slightly modify the weights of the azimuthal average, while an incorrect centring of the stellar mass map will result in artificial torques. We confirm for the case of M51 that the uncertainty introduced

M. Querejeta et al.: Molecular gas inflow in M51

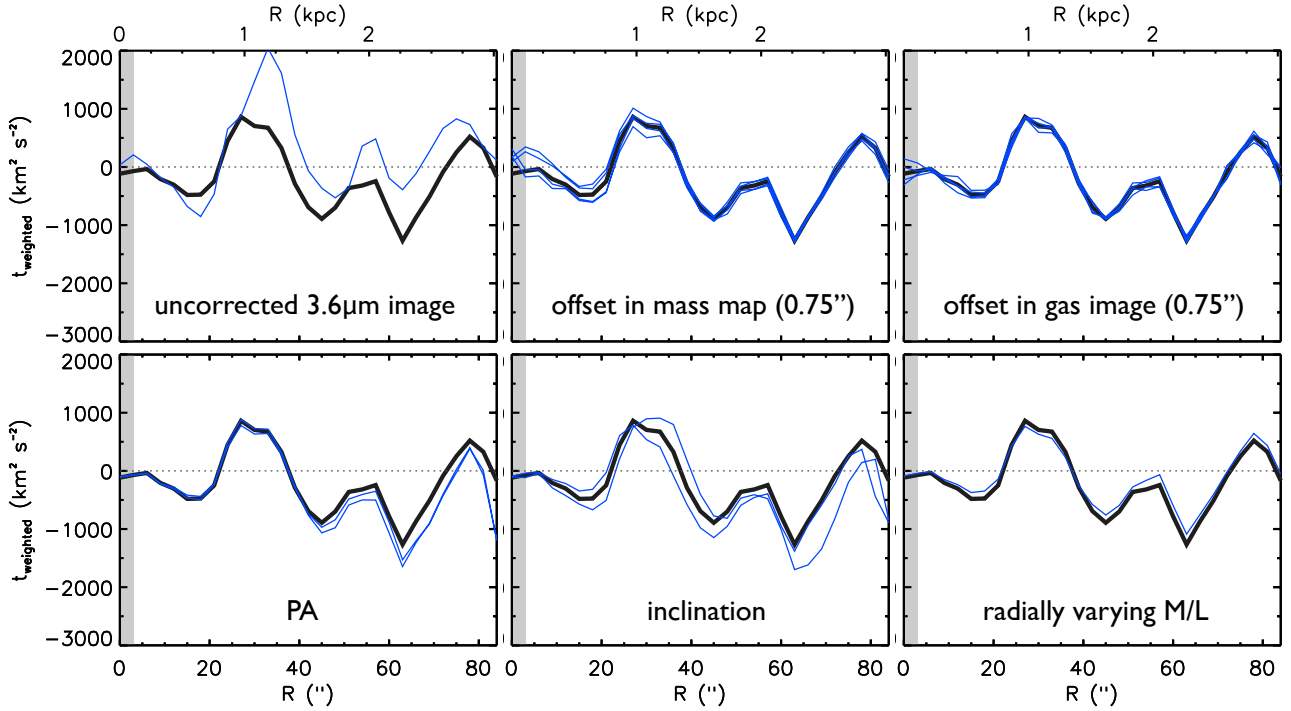


Fig. A.3. Change in the torque profiles due to a number of systematic uncertainties. The thick black line is our fiducial profile, based on the ICA dust-corrected $3.6\mu\text{m}$ image. *From top left to bottom right*, the thin blue lines are the profiles based on the uncorrected $3.6\mu\text{m}$ image (i.e. difference due to dust emission at $3.6\mu\text{m}$); an offset in the centring of the stellar mass map of $0.75''$; an offset in the centring of the gas map (CO traced by PAWS) of $0.75''$; a variation in the position angle of the disc corresponding to the extremes of the error bars given by Colombo et al. (2014); a variation in the inclination of the disc corresponding to the extremes of the error bars given by Colombo et al. (2014); and the difference in mass distribution associated with the maximum possible radially varying M/L .

by an offset of 1 px ($0.75''$) in the centring of the gas map is $\sim 10\%$. Given the accuracy of the astrometry in the PAWS map ($< 1''$), this should not be a problem.

A.6. Confirming torques with $1.9\mu\text{m}$ imaging

As an additional sanity check, here we employ a $1.9\mu\text{m}$ image to re-assess the gravitational potential and the inflow rates. We used the HST $1.9\mu\text{m}$ continuum narrow-band image from Scoville et al. (2001), a 3×3 mosaic of the central region of M51 (uniformly sampled only out to $R \sim 50''$) obtained with the F190N filter on the NICMOS 3 camera (continuum next to the Pa α line); for details on data reduction see Scoville et al. (2001). The inflow rates and resonances are essentially identical as those presented in Sect. 4.3. Only in the central $R \lesssim 5''$ do the results using this HST image differ, but this has already been flagged as a problematic region associated with very high uncertainties.

Given the importance of image centring for torque computations (Appendix A.5), we corrected the HST/F190N mosaic to an absolute astrometric frame of reference following the technique described in Schinnerer et al. (2013), Sect. 7.3; this results in an astrometric offset of $1.3''$ ($\Delta x = +0.729''$, $\Delta y = -1.08''$). We assumed a constant mass-to-light ratio, $M/L_{1.9\mu\text{m}} = 0.2 M_{\odot}/L_{\odot}$, chosen so that the stellar mass radially matches our stellar mass map in the range $5\text{--}20''$. In Fig. A.4 (left) we show the radial surface brightness profile for HST/F190N, compared with the uncorrected $3.6\mu\text{m}$, and the ICA-corrected $3.6\mu\text{m}$ (stellar mass map). The slopes of the stellar mass map and the HST/F190N image are basically

identical (-0.044 and -0.045), while the slope of the $3.6\mu\text{m}$ image differs significantly (-0.032). The vertical offset determines the $M/L_{1.9\mu\text{m}}$ necessary to match both profiles, $M/L_{1.9\mu\text{m}} = 0.2 M_{\odot}/L_{\odot}$ (a factor of 3 lower than $M/L_{3.6\mu\text{m}} = 0.6 M_{\odot}/L_{\odot}$); equivalently, this can be obtained as the ratio of the magnitude zero points, since the HST/F190N and ICA-corrected $M/L_{3.6\mu\text{m}}$ profiles expressed in magnitudes clearly overlap ($ZP_{3.6\mu\text{m}} = 280.9\text{ Jy}$, $ZP_{F190N} = 835.6\text{ Jy}$, leading also to a factor 3 difference).

Figure A.4 (left) highlights a clear excess of emission in the centre, especially large in the case of the HST/F190N band, with respect to a simple Sérsic profile (which shows as a straight line, given that the vertical axis is logarithmic). This excess could be associated with a young stellar population, or it might be contamination from the AGN. The fact that we find $[3.6\text{--}4.5] > 0$ for this region rules out the possibility of a massive central “bulge” or other old inner components. In either case, this will bring the results closer to what we measure with the stellar mass map because for young stars the M/L would be considerably lower in the central region and, for an AGN, the excess emission should be ignored.

We recomputed the torques and inflow rates assuming that all emission seen at $1.9\mu\text{m}$ arises from an old stellar population (which would provide a very conservative upper limit, as just argued), and we present the main plots in Fig. A.4 (right). The agreement between the two profiles is very good, except in the region where the HST image displays the “bump”. In principle, the higher spatial resolution afforded by HST ($0.2''$) should allow us to confirm whether inflow persists down to $R = 1''$ (limited by the resolution of PAWS), instead of $R = 1.7''$

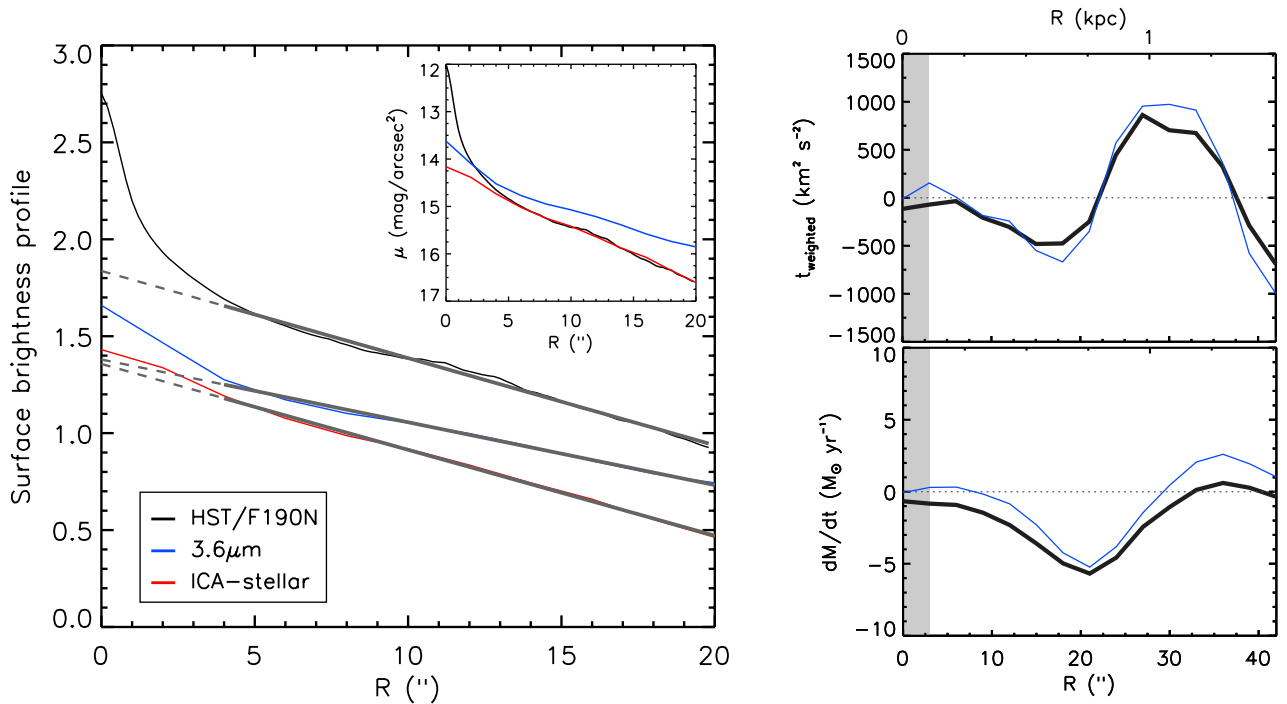


Fig. A.4. *Left:* radial surface brightness profiles for the HST/*F190N* narrow-band image of M 51, the uncorrected $3.6\mu\text{m}$, and the ICA-corrected $3.6\mu\text{m}$ (stellar mass map) in units of $\log(F_\nu/[\text{MJy}/\text{sr}])$. The linear fits in the range $5\text{--}20''$ highlight the good agreement with the expectation from a simple Sérsic profile in this region and show that *F190N* and the stellar mass map have basically identical slopes. The small inset panel shows the equivalent surface brightness profiles in magnitude units (Vega): after accounting for the different zero points, the HST/*F190N* profile perfectly matches the levels of the stellar mass map. *Right:* radial torque profile (*top*) and accumulated inflow rates (*bottom*) for the gravitational potential based on HST/*F190N* (blue), compared with our fiducial stellar mass map (black). The blue profile should be regarded as an (extreme) upper limit, in which the “bump” in the central region of HST/*F190N* is entirely attributed to old stars (which is highly unlikely, as argued in the text). The reason for divergencies out to $R \lesssim 5''$ in the top plot (torques) to propagate farther out in the bottom plot (inflow) is that the bottom profile displays cumulative flow rates, and an offset in the inner bin will shift the whole profile up or down.

(current resolution limit with *Spitzer*). However, as we have emphasised in Sect. 5.3, we would be approaching the dangerous regime where uncertainties become extremely large. Therefore, we highlight again the point that we made before, and consider the inflow measurements highly uncertain in the very central region ($R \lesssim 5''$).

Appendix B: Hydrodynamical simulations of gas inflow in M51

Dobbs et al. (2010) performed N-body and gas simulations of the interaction of M 51 and its companion NGC 5195 and demonstrated that the interaction leads to spiral structure that is remarkably similar to the actual M 51. Here we repeat a similar calculation to examine the radial variation of H_2 during the encounter, and whether the model predicts a molecular inflow comparable to that observed.

We show here a simulation similar to that shown in Dobbs et al. (2010), but with some important differences. We used the same orbit for the two galaxies, taken originally from Theis & Spinneker (2003), and again fully modelled the gas, stars, and dark matter halo using the sphNG code. We used one million particles for the gas, 100 000 particles each for the halo and stellar disc, and 40 000 for the bulge. However, we included a much more massive gas disc (with total gas mass $\sim 5 \times 10^9 M_\odot$) to better represent the high surface densities in M 51. We did not include gas self-gravity, however, so the gas does not undertake

gravitational collapse, and the simulation is much easier to run. This also means that we were able to fully model the cold phase of the ISM, including H_2 chemistry, effectively. Self-gravity was of course included for the stellar and dark matter components of the simulations. Also, unlike Dobbs et al. (2010), the simulation here is not isothermal, but includes cooling down to a temperature of 10 K and heating (following Glover & Mac Low 2007 and Dobbs et al. 2008), so that the molecular cold HI and warm HI phases of the ISM are modelled. The formation of H_2 (Dobbs et al. 2008) was also included. The final difference between the simulation here and that of Dobbs et al. (2010) is that the companion galaxy was modelled fully with smooth particle hydrodynamics and not with a point mass. However, the companion galaxy is not well resolved, with only 150 000 particles in total. Modelling the companion galaxy has little effect, apart from the fact that the time of the simulation that best matches the current day is slightly earlier. For comparison we also ran a simulation of an isolated galaxy with the same initial conditions as our M 51 galaxy.

In Fig. B.1 we show the structure of the M 51 galaxy at a time of 292 Myr, corresponding roughly to the present day. The companion is also shown in the figure. The structure is fairly similar to that in Dobbs et al. (2010). The gas shows slightly more structure because it can cool to lower values. Figure B.2 shows radial profiles of the atomic, molecular, and total gas for the isolated example (top panel) and the interacting galaxy (middle and lower panels). For the isolated galaxy, the profiles are relatively similar after the first 80 Myr of evolution until the end

M. Querejeta et al.: Molecular gas inflow in M51

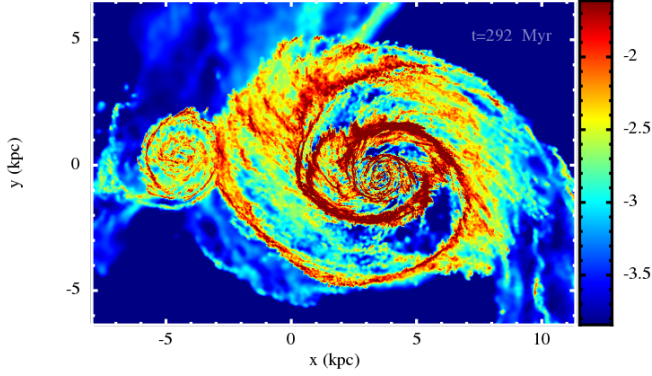


Fig. B.1. Column density for a simulation of the M51 galaxy interacting with its companion (NGC 5195). The colour bar is in logarithmic scale, with units of g cm^{-2} . The time shown is 292 Myr, corresponding roughly to the present day.

of the simulation. The disc is predominantly molecular within 6 kpc, and atomic outside 6 kpc. For the first 150 Myr, the radial profiles of the interacting galaxy evolve similarly to the isolated case, although the molecular gas tends to always be more concentrated. For the time between 150 and 300 Myr, the molecular radial profile is notably more concentrated, with molecular surface densities in excess of $100 M_{\odot} \text{pc}^{-2}$ in the central region (where all the gas is molecular). The molecular surface density profile is consistent with observations by Leroy et al. (2008).

The interaction of the simulated M51 clearly makes the gas, in particular the molecular gas, more concentrated, which means that effectively there is inflow towards the centre. We can compare the increase in gas in the centre with the observed inflow rates by making a rough estimate of the change in gas mass in the central 2 kpc. The change in gas mass for a given radial ring is

$$\text{inflow} = \frac{(\hat{\Sigma}_2 - \hat{\Sigma}_1)A}{(T_2 - T_1)}, \quad (\text{B.1})$$

where $\hat{\Sigma}_2$ is the mean surface density at T_2 , $\hat{\Sigma}_1$ is the mean surface density at T_1 , and A is the area of the ring. Here we consider that the area is that of a circle of radius 2 kpc. The timescale for the interaction is somewhat difficult to judge, but the profiles show evident deviations between the isolated and interacting galaxies from 150 to 300 Myr, therefore we took $T_2 = 300$ Myr and $T_1 = 150$ Myr. This yields an inflow rate for H_2 of $2.1 \pm 0.5 M_{\odot} \text{yr}^{-1}$. This value agrees very well with the observed inflow of M51, suggesting that the interaction of M51 might be responsible for the observed CO inflow.

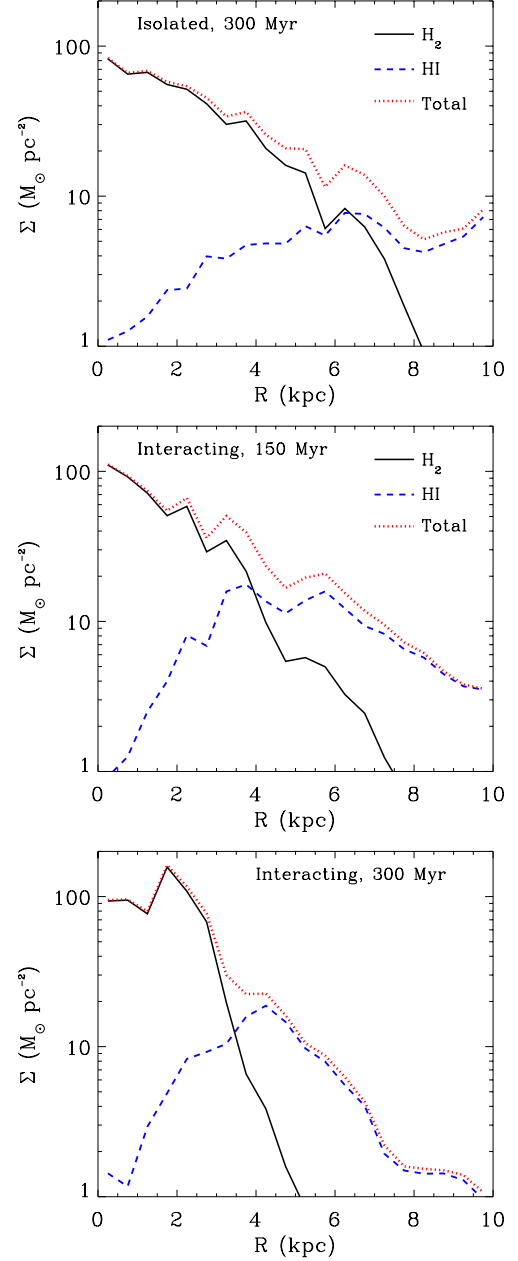


Fig. B.2. Radial profiles are shown for the molecular, atomic, and total gas surface densities. *The top panel* shows the profiles for an isolated galaxy example (set up otherwise in the same way as our model M51 galaxy), and *the middle and lower panels* show the profiles when our M51 galaxy interacts with a companion.

Chapter 4

AGN feedback in M51

In this chapter we address the role of AGN feedback on molecular gas in the spiral galaxy M51. These feedback effects are indirectly controlled by the gas inflow rates that we determined in Chapter 3; feedback has strong implications in terms of regulating star formation. This paper is currently under revision from the co-authors, and will be submitted to *Astronomy & Astrophysics* soon.

AGN feedback in the nucleus of M51

M. Querejeta¹, E. Schinnerer¹, S. García-Burillo², F. Bigiel³, G. A. Blanc^{4,5,6}, D. Colombo⁷, A. Hughes^{8,9},
K. Kreckel¹, A. K. Leroy¹⁰, S. E. Meidt¹, D. S. Meier¹¹, J. Pety^{12,13}, and K. Sliwa¹

¹ Max Planck Institute for Astronomy, Königstuhl, 17, 69117 Heidelberg, Germany, e-mail: querejeta@mpia-hd.mpg.de

² Observatorio Astronómico Nacional, Alfonso XII, 3, 28014 Madrid, Spain

³ Institut für theoretische Astrophysik, Zentrum für Astronomie der Universität Heidelberg, Albert-Ueberle-Str. 2, 69120 Heidelberg, Germany

⁴ Departamento de Astronomía, Universidad de Chile, Camino del Observatorio 1515, Las Condes, Santiago, Chile

⁵ Centro de Astrofísica y Tecnologías Afines (CATA), Camino del Observatorio 1515, Las Condes, Santiago, Chile

⁶ Visiting Astronomer, Observatories of the Carnegie Institution for Science, 813 Santa Barbara St, Pasadena, CA 91101, USA

⁷ Max Planck Institute for Radioastronomy, Auf dem Hügel 69, 53121 Bonn, Germany

⁸ CNRS, IRAP, 9 Av. Colonel Roche, BP 44346, 31028 Toulouse, France

⁹ Université de Toulouse, UPS-OMP, IRAP, 31028 Toulouse, France

¹⁰ Department of Astronomy, The Ohio State University, 140 West 18th Avenue, Columbus, OH 43210, USA

¹¹ Physics Department, New Mexico Tech, 801 Leroy Place, Socorro, NM 87801, USA

¹² Institut de Radioastronomie Millimétrique, 300 Rue de la Piscine, 38406 Saint Martin d'Hères, France

¹³ Observatoire de Paris, 61 Avenue de l'Observatoire, 75014 Paris, France

Received / Accepted

ABSTRACT

AGN feedback is invoked as one of the most relevant mechanisms that shape the evolution of galaxies. Our goal is to understand the interplay between AGN feedback and the interstellar medium in M51, a nearby spiral with a modest AGN and a kpc-scale radio jet expanding through the disc of the galaxy. For that purpose, we combine molecular gas observations in the CO(1-0) and HCN(1-0) lines from the Plateau de Bure interferometer with archival radio, X-ray, and optical data. We show that there is a significant scarcity of CO emission in the ionisation cone, while molecular gas emission tends to accumulate towards the edges of the cone. The distribution and kinematics of CO and HCN line emission reveal AGN feedback effects out to $r \sim 500$ pc, covering the whole extent of the radio jet, with complex kinematics in the molecular gas which displays strong local variations. We propose that this is the result of the almost coplanar jet pushing on molecular gas in different directions as it expands; the effects are more pronounced in HCN than in CO emission, probably as the result of radiative shocks. Following previous interpretation of the redshifted molecular line in the central 5'' as caused by a molecular outflow, we estimate the outflow rates to be $\dot{M}_{\text{H}_2} \sim 0.9 M_{\odot}/\text{yr}$ and $\dot{M}_{\text{dense}} \sim 0.6 M_{\odot}/\text{yr}$, which are comparable to the molecular inflow rates ($\sim 1 M_{\odot}/\text{yr}$); gas inflow and AGN feedback could be mutually regulated processes. The agreement with findings in other nearby radio galaxies suggests that this is not an isolated case, and probably the paradigm of AGN feedback through radio jets, at least for galaxies hosting low-luminosity active nuclei.

Key words. galaxies: individual: NGC 5194 – galaxies: ISM – galaxies: structure – galaxies: nuclei – galaxies: Seyfert – galaxies: jets

1. Introduction

1.1. AGN feedback

Feedback from star formation (SF) and active galactic nuclei (AGN) plays a key role in reconciling cosmological simulations of galaxy formation and evolution with observations across different redshifts (Somerville & Davé 2015). It is often invoked to explain the co-evolution of black holes and their host galaxies (Kormendy & Ho 2013), the mass-metallicity relation (Tremonti et al. 2004; Kewley & Ellison 2008), the bimodality in the colours of galaxies (Schawinski et al. 2015), the enrichment of the intergalactic medium (Martin et al. 2010), and it can prevent galaxies from over-growing in stellar mass (e.g. Croton et al. 2006). By expelling molecular gas from the host galaxy, or by changing its ability to form stars, AGN feedback can also regulate star formation; it can either result in the suppression of star formation (Alatalo et al. 2014), or in its local enhancement (Silk 2013).

AGN feedback is necessary to alleviate the tension between simulations and observations for the most massive galaxies: for $M_* \gtrsim 10^{10} M_{\odot}$ cosmological simulations start to overpredict the stellar mass content of galaxies relative to the mass in their dark matter haloes (Moster et al. 2010). However, feedback is implemented in numerical models in a relatively *ad hoc* way, adjusting its intensity so that the output stellar masses match observations; it remains to be confirmed to what extent these feedback levels are realistic. There is also some observational evidence for the relevance of AGN feedback in quenching star formation in massive $M_* > 10^{10} M_{\odot}$ galaxies (e.g. Leslie et al. 2016). We note that the stellar mass of M51, the galaxy that we study here, is $\sim 7 \times 10^{10} M_{\odot}$ (Querejeta et al. 2015), and therefore it is already in the regime where AGN feedback is expected to be relevant. The strongest feedback effects are found in high-redshift galaxies, but studying more modest local counterparts such as M51 is important, as it permits to reveal the physics involved.

In a cosmological context, a number of studies have recently brought attention to the relevance of AGN-powered outflows

(see Fabian 2012, for a review); specifically, the last years have seen a plethora of detections of ionised “winds” driven by AGN activity, including valuable statistics based on large samples (e.g. Bae & Woo 2014; Cicone et al. 2016). There is also ample observational evidence of AGN-driven massive molecular outflows in relatively distant sources (e.g. Cicone et al. 2012, 2014; Feruglio et al. 2013; Dasyra et al. 2014; García-Burillo et al. 2015); however, few nearby counterparts have been studied, and the details of feedback are still poorly understood. Notable exceptions AGN-driven include M51 (Matsushita et al. 2004, 2007, 2015b), NGC 4258 (Krause et al. 2007), and since the advent of ALMA, IC 5063 (Morganti et al. 2015) and NGC 1068 (García-Burillo et al. 2014).

Careful analysis of the ALMA 0.5'' (100 pc) resolution CO(2-1) data of the radio galaxy IC 5063 (Morganti et al. 2015) favours a scenario of a cold molecular gas outflow driven by an expanding radio plasma jet; this results in a high degree of *lateral expansion*, in agreement with numerical simulations of radio jets expanding through a dense clumpy medium (e.g. Wagner & Bicknell 2011; Wagner et al. 2012). However, the high inclination of the disc of IC 5063 ($i \sim 80^\circ$) complicates the analysis, and does not allow one to directly map the distribution of molecular gas relative to the jet.

A massive ($M_{\text{gas}} \sim 3 \times 10^7 M_\odot$) AGN-driven outflow of dense molecular gas has also been detected by ALMA using high density tracers in the inner 400 pc of NGC 1068, revealing a very complex scenario (García-Burillo et al. 2014). These observations suggest that the outflow is efficiently regulating gas accretion in the circumnuclear disc ($r \lesssim 200$ pc), and they emphasise the importance of characterising the amount of dense ($n(\text{H}_2) > 10^{4-5} \text{ cm}^{-3}$) molecular gas that is expelled through this process in order to obtain a complete multiphase picture of AGN feedback.

From a theoretical perspective, the mere existence of fast molecular outflows is problematic, as large velocities are expected to result in the dissociation of the molecular gas. Cooling into a two-phase medium has been proposed as a mechanism to explain how molecular gas survives outflows (Zubovas & King 2012, 2014). The numerical simulations from Wagner & Bicknell (2011) and Wagner et al. (2012) also demonstrate the possibility of AGN feedback via radio plasma jets impinging on a clumpy ISM, showing how the interaction between jet and gas can result in significant lateral expansion, away from the purely radial outflow that one would naïvely expect if gas is entrained by the jet.

1.2. The nucleus of M51

The grand-design spiral galaxy M51 constitutes a unique setup due to its proximity (7.6 Mpc; Ciardullo et al. 2002) and the low inclination of the disc ($i \sim 22^\circ$; Colombo et al. 2014b). Its well-studied Seyfert 2 nucleus (Ho et al. 1997; Dumas et al. 2011) is seen as two radio lobes that are filled with hot X-ray gas (Terashima & Wilson 2001) and an outflow of ionised gas (Bradley et al. 2004). In the context of the AGN unification picture from Antonucci (1993), the fact that only narrow lines are visible (and no broad lines), which determines the Seyfert 2 nature of M51, would be explained by obscuration from a dusty torus almost perpendicular to our line of sight; the orientation of the radio jet (inclined 15° with respect to the plane of the disc; Cecil 1988), if perpendicular to the torus, as expected, supports this idea. We assume that the AGN location is given by the nuclear maser emission position determined by Hagiwara & Edwards (2015), RA=13:29:52.708, Dec=+47:11:42.810, which is

less than $\sim 0.1''$ away from the radio continuum peak (Turner & Ho 1994; Hagiwara 2007; Dumas et al. 2011).

Even if the potential impact of the AGN on the surrounding molecular material has been a matter of debate, high-resolution observations have demonstrated that both CO and HCN are participating in an outflow (Scoville et al. 1998; Matsushita et al. 2007), with an extraordinarily high HCN/CO ratio (> 2) in the immediate vicinity of the AGN (Matsushita et al. 2015b).

In Querejeta et al. (2016), we have studied the molecular gas flows across the full disc of M51, probing the transport of gas to the nucleus. Combining our stellar mass map (Querejeta et al. 2015) with the high-resolution CO gas distribution mapped by PAWS (Schinnerer et al. 2013; Pety et al. 2013), we have found evidence for gas inflow, with rates which are comparable to the amount of outflowing gas ($\sim 1 M_\odot/\text{yr}$), as we will show.

Our goal is to understand the interplay between nuclear activity and the ISM in the nucleus of M51, relating it to the molecular gas inflow rates that we have already measured. Thus, we present a multi-wavelength study of the inner ~ 1 kpc of M51, the region affected by the radio plasma jet. In order to study the stratification in the response of the molecular gas to AGN feedback in M51, we have obtained new Plateau de Bure interferometric observations of dense gas tracers for the central $60''$ (2 kpc) of the galaxy. We have detected and imaged three lines (HCN, HCO^+ , HNC), but here we will focus on the brightest one, HCN, and compare it to the bulk molecular gas traced by CO from PAWS. HCO^+ and HNC will be analysed in a forthcoming publication.

The paper is structured as follows. We describe the new and archival data used in the analysis in Sect. 2. The main results are presented in Sect. 3, and discussed in Sect. 4. Finally, Sect. 5 consists of a summary, conclusions, and some open questions.

2. Observations and data reduction

2.1. Dense molecular gas tracers

We have observed the HCN(1–0), $\text{HCO}^+(1-0)$, and HNC(1–0) lines in the central ~ 2 kpc of M51 with the IRAM Plateau de Bure Interferometer (PdBI) in C and D configurations, and corrected for missing short spacings with single dish observations from the IRAM 30m telescope (Bigiel et al. submitted). The PdBI observations in D configuration were carried out between 20th August and 13th September 2011 using 5 antennas, with system temperatures between 70 and 130 K, and precipitable water vapour between 4 and 8 mm. The PdBI observations in C configuration were performed on 1st and 20th November 2011, and 21st November 2014 with 6 antennas, yielding system temperatures between 60 and 250 K, and precipitable water vapour between 5 and 8 mm. During our observations, the wide-band correlator (WideX) operated in parallel to the narrow-band correlator, simultaneously recording a bandwidth of 3.6 GHz with a native spectral resolution of 1.95 MHz (6.6 km/s), and allowing us to access all of our lines of interest simultaneously. MWC349 was used as the flux calibrator (except for 1st and 20th November 2011, when 1415+463 was used instead). Various quasars were used as the bandpass calibrators for the different sessions (3C84, 3C273, 3C279, 3C345, 3C454.3, 0923+392, 2013+370), and the quasars 1415+463 and J1259+516 were used as amplitude and phase calibrators (except for 20th November 2011, when 1418+546 and 1150+497 were used). The observations were reduced using GILDAS (calibrated with CLIC, and mapped with MAPPING; Pety 2005).

Single-dish observations for the central $4.2' \times 5.7'$ field of view (9×13 kpc) were obtained with the IRAM 30m telescope in July and August 2012 (integrating a total of 75 hours). The observations were carried out under typical summer conditions with the 3mm-band EMIR receiver, with a bandwidth of 15.6 GHz and a spectral resolution of 195 kHz, and reduced following the standard procedures in CLASS (Bigiel et al. submitted). We carried out short spacings correction (SSC) of our interferometric data with the single-dish observations from the 30m telescope, which were reprojected to the centre and channel width of the PdBI observations. The single-dish data were combined with the PdBI observations applying the task UV-short in GILDAS.

CLEANing was performed using the Hogbom algorithm within MAPPING, with natural weighting. This leads to a final HCN(1-0) datacube with a synthesised beam (spatial resolution) of $4.81'' \times 3.94''$ (PA = 71°), which corresponds to 178×146 pc, and a 1σ noise level of 0.431 mJy/beam. We have also performed an alternative cleaning with ROBUST weighting, and we obtain a resolution of $3.66'' \times 3.25''$ (PA = 68°), with a 1σ noise level of 0.460 mJy/beam. We have chosen a pixel size of $1''$, which produces a cube of 256×256 pixels and 120 frequency channels of 2.07 MHz (~ 7 km/s) each.

2.2. CO data from PAWS

We make use of the bulk molecular gas emission probed by the CO(1-0) map of M51 from PAWS (Schinnerer et al. 2013; Pety et al. 2013). The spatial resolution is $1''$ (37 pc) and covers the central 9 kpc of the galaxy, reaching a brightness sensitivity of 0.4 K (1σ rms), over 5 km/s channels. Our PAWS map includes short-spacing corrections based on IRAM 30m single-dish data, which by definition recovers all the flux. For more details on the data reduction, the reader is referred to Pety et al. (2013). We note that, for the central region that we are interested in, gas is clearly predominantly molecular (HI surface density lower than CO by a factor of more than 10 inside $r < 1$ kpc; Schuster et al. 2007).

2.3. HST archival data

We complement the information provided by the molecular gas emission with a number of archival datasets. We make use of *Hubble* Space Telescope (HST) observations from Bradley et al. (2004), kindly provided to us by the author. This includes a continuum-subtracted [OIII] image from WFPC2/F502N, and a [NII] + H α image from WFPC2/F656N. We note that the WFPC2/F547M image has been subtracted from both images (see Bradley et al. 2004, for details).

We also utilise HST *Advanced Camera for Surveys* (ACS) mosaics in the F435W (B-band), F555W (V-band), F658N (H α narrow-band), and F814W (I-band), from Mutchler et al. (2005). These have been corrected to an absolute astrometric frame of reference as described in Schinnerer et al. (2013), and we refer the interested reader there for more details.

2.4. Radio and X-ray archival data

The ancillary data that we use also include radio observations with the Very Large Array (VLA), already described in Dumas et al. (2011). The whole disc of M51 was mapped at 3.6, 6, and 20 cm, combining multiple configurations of the interferometer (ABCD for 20 cm). The map at 20 cm provides the highest res-

olution ($1.4'' \times 1.3''$, with a 1σ rms sensitivity of 11 μ Jy/beam), and we will primarily focus on that image. For comparison, we will also show an X-ray map, for the integrated emission in the 0.3-1 keV band. The final image is a coadded version of all archival datasets available through the Chandra archive prior to 2011, using CIAO (Fruscione et al. 2006), and post-processed using adaptive smoothing.

3. Results

3.1. Impact of the kpc-scale radio jet on the molecular gas distribution

3.1.1. The jet geometry in M51

The radio continuum image of M51 (Fig. 2) shows a number of structures in the inner 1 kpc, all of them visible at 3.6 cm, 6 cm, and 20 cm (Dumas et al. 2011). The radio continuum peaks very close to the inferred position of the AGN (RA=13:29:52.708, Dec=+47:11:42.810; Hagiwara & Edwards 2015). High-resolution VLA imaging by Crane & van der Hulst (1992) detected the presence of a nuclear radio jet, which extends $2.3''$ (85 pc) from the nucleus towards the south, with a projected width of $\sim 0.3''$ (11 pc); the jet connects to a bright extra-nuclear cloud (XNC) in the south, of $\sim 5''$ in diameter, which also shows strong optical ionised line emission. This has been confirmed by Bradley et al. (2004), who also detected a counter-jet in the north, which is curved and shorter ($1.5''$, 55 pc), and thus is probably the relic of previous nuclear activity. Interestingly, this potential counter-jet points in the approximate direction (Δ PA $\lesssim 10^\circ$) of a bright radio component $27.8''$ towards the north. This “N-component” is also elongated in the direction of the nucleus, and using a statistical approach, Rampadarath et al. (2015) have shown that this component is most likely associated with past nuclear activity (and not the chance alignment of a background radio galaxy). A large loop of radio emission is also detected $\sim 9''$ north of the nucleus (a ring or “C”-shaped structure), with a diameter of $\sim 10''$; this structure is in the direction of, but not directly connected to, the northern counter-jet. The radio images from Dumas et al. (2011) also show a faint southern radio loop that connects to the XNC ($\sim 8''$ in diameter); to our best knowledge, this southern loop has not been described so far in the literature. On larger scales, the radio continuum emission traces the spiral arms of the galaxy. In the following, we will loosely use the expression *radio jet* to refer to the radio plasma emission that stems from the nuclear area, which includes the northern loop and the southern XNC, and not only the inner collimated $\sim 4''$ jet structure. Fig. 14, in which we summarise the main results from this paper, shows an idealised version of the radio plasma structures that we have just described.

From sophisticated modelling of the superposed ionised gas kinematic components in the XNC, Cecil (1988) suggested that the (southern) jet forms an angle of 15° with respect to the disc of M51 (see Appendix C). This inclination of the jet is consistent with the Seyfert 2 nature of the AGN. Therefore, due to the low inclination of the jet, extended interaction with the ISM is possible. Fig. 1 illustrates the orientation of the jet and the disc. We note that, even though it has been assumed so far that the southern jet must be closer to us than the northern counterpart (e.g. Bradley et al. 2004), we think that this is not necessarily true. The fact that the ionised region is more luminous and extended in the south could seem, at first sight, indicative of the southern ionisation cone being closer to us (and therefore, less susceptible to extinction from the optically thick disc). However,

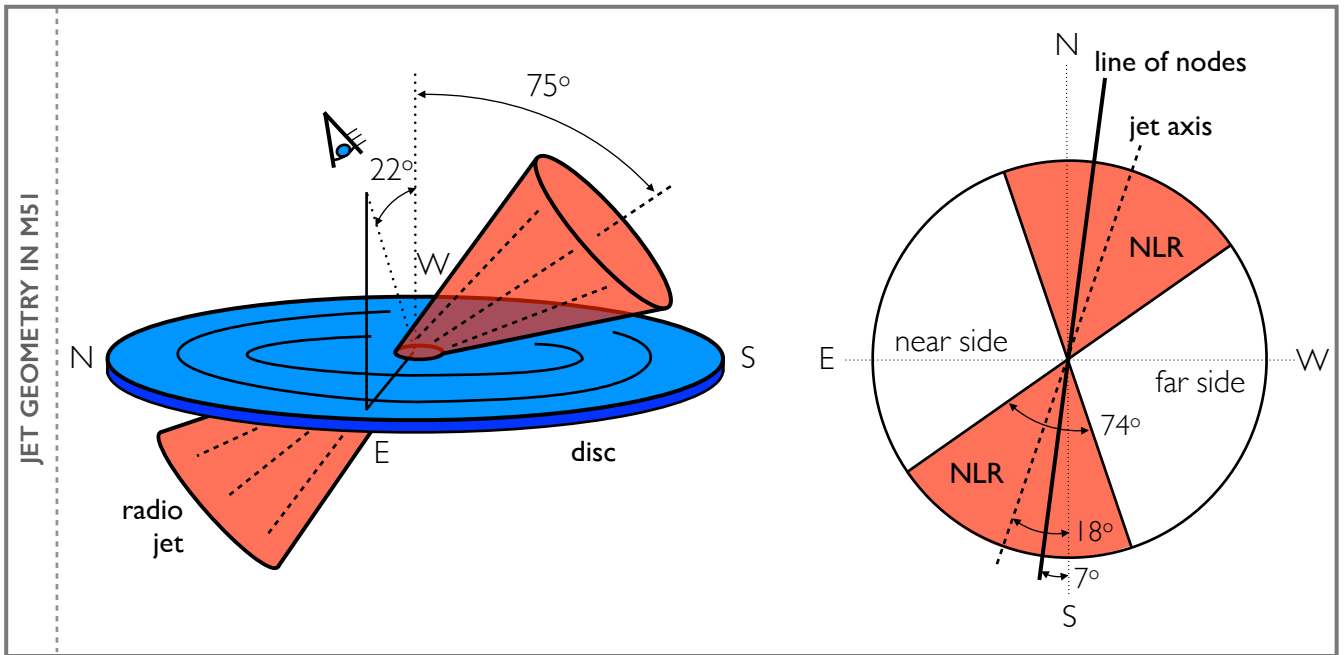


Fig. 1. *Left:* geometry of the kpc-scale radio jet in M51 relative to the disc and to the observer (the inclination of the jet is inferred from Cecil 1988, and the inclination of the disc, from Colombo et al. 2014). *Right:* orientation and opening angle of the narrow-line region (NLR) from Bradley et al. (2004), assuming that it is aligned with the jet. We follow Cecil (1988) and Bradley et al. (2004) in placing the southern jet closer to us; however, while the inclination of the jet with respect to the disc is well constrained to be low, in the text we discuss the possibility of the northern side of the jet being the one that is closer to us.

the collimated radio jet is longer and brighter in the southern direction (including the southern XNC, which is much brighter at 20 cm radio continuum than the northern loop); this is probably the consequence of an alternating one-side nuclear activity cycle, perhaps because dense clumps are currently blocking the plasma ejection towards the north of the AGN (Rampadarath et al. 2015). This could explain why the optical ionised emission lines are stronger in the south, and it does not necessarily imply that the southern jet is closer to us (in fact, if spherical, the XNC would “block” the whole molecular thin disc; see Fig. 14).

In Fig. 2, the radio emission is compared to X-rays. Radio and X-rays trace, to first order, the same structures (see also Terashima & Wilson 2001). The ionised emission mapped through the [OIII] line corresponds to the brightest structures in $H\alpha$, namely those next to the nucleus (inner $\sim 3''$) and the point of contact of the jet with the XNC, shown to be undergoing an oblique shock (Cecil 1988). Bradley et al. (2004) showed that the ionised gas along the jet, in the central $\lesssim 3''$, is probably involved in an outflow (although there are important outliers in velocity, which they interpret as gas that is possibly behind the jet, and participating in a lateral flow away from the jet axis).

3.1.2. Molecular gas in the vicinity of the radio jet

When we superpose our PAWS CO(1-0) intensity map at our best resolution ($1''$, Fig. 3) on top of the radio emission, an interesting spatial correlation between radio and molecular emission becomes apparent. We highlight as red shaded areas the contiguous regions with CO(1-0) fluxes above 60 K km/s (in the PAWS moment-0 map at $1''$ resolution). The curvature of the molecular gas features labelled as A, B, and E agree surprisingly well with the iso-intensity contours from the radio emission tracing

the jet. The blobs D, G, and H also seem to accumulate towards the edges of the jet, while C and F overlap with the jet (at least in projection). Overall, this gives the impression of CO gas being “blocked” by the jet, or alternatively, that the jet is adapting its shape according to the molecular gas distribution, which prevents it from expanding in certain directions. A simple argument of timescales shows that galactic rotation is much slower than the propagation of the jet, supporting the picture where the molecular gas distribution is modulating the appearance of the jet, and not the way around. This agrees with numerical simulations of radio jets propagating through a clumpy molecular medium, in which the jet deforms in an attempt to find the path of minimum resistance (Wagner & Bicknell 2011; Wagner et al. 2012). However, this does not mean that the molecular gas is insensitive to the interaction with the jet, as we will show in Sect 3.2; there is probably *reciprocal* interaction between the jet and the molecular gas distribution.

Now, we briefly consider the timescales involved in the AGN feedback process. We can assume that the collimated jet propagates at a velocity close to the speed of light (around $\sim 0.9c$ or even higher, as inferred from observations of other jets and comparison to simulations, e.g. Fendt & Sheikhnezami 2013). However, the bubbles and other features of radio plasma that are connected to radio jets expand and dissipate over timescales which are still unclear, or at least largely depend on local conditions (Braithwaite 2010).

At $R = 9''$ (the location of the northern radio loop), the rotation velocity of the molecular gas is 107 km/s (Meidt et al. 2013), which implies an approximate rotation period of $T_{\text{rot}}(R = 9'') = 19$ Myr; at $2.5''$, where the southern collimated jet hits the XNC, the rotational velocity is 53 km/s, leading to $T_{\text{rot}}(R = 2.5'') = 11$ Myr. Therefore, even if we assume that the southern radio XNC and the northern loop expand at a mod-

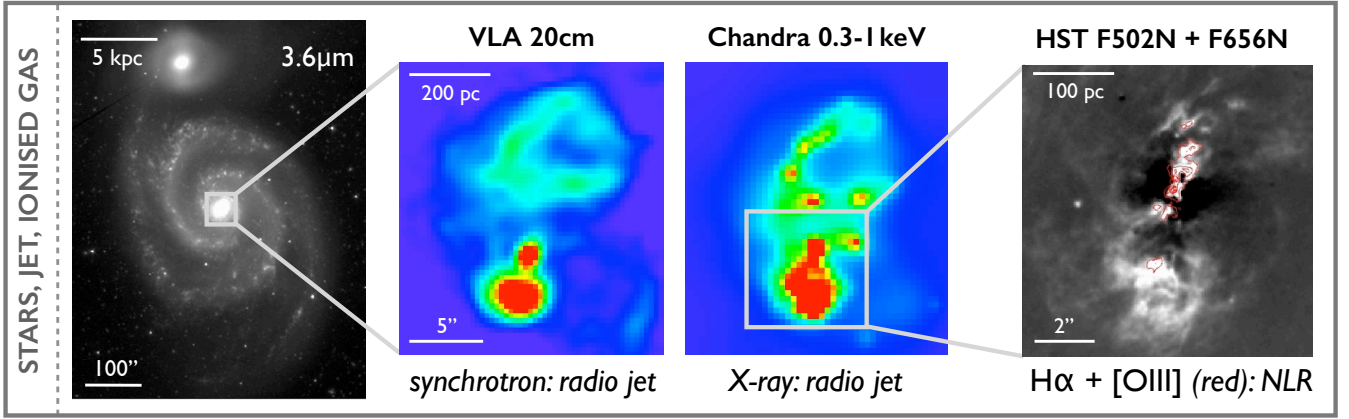


Fig. 2. From left to right: near-infrared image of M51 (*Spitzer* 3.6 μm), highlighting the region of interest; VLA 20 cm continuum image showing the kpc-scale radio jet (Dumas et al. 2011); X-ray emission in the nucleus, from Chandra, integrating emission within 0.3-1 keV; narrow-line region from Bradley et al. (2004), traced by $\text{H}\alpha$ (greyscale image) and $[\text{OIII}]$ (red contours).

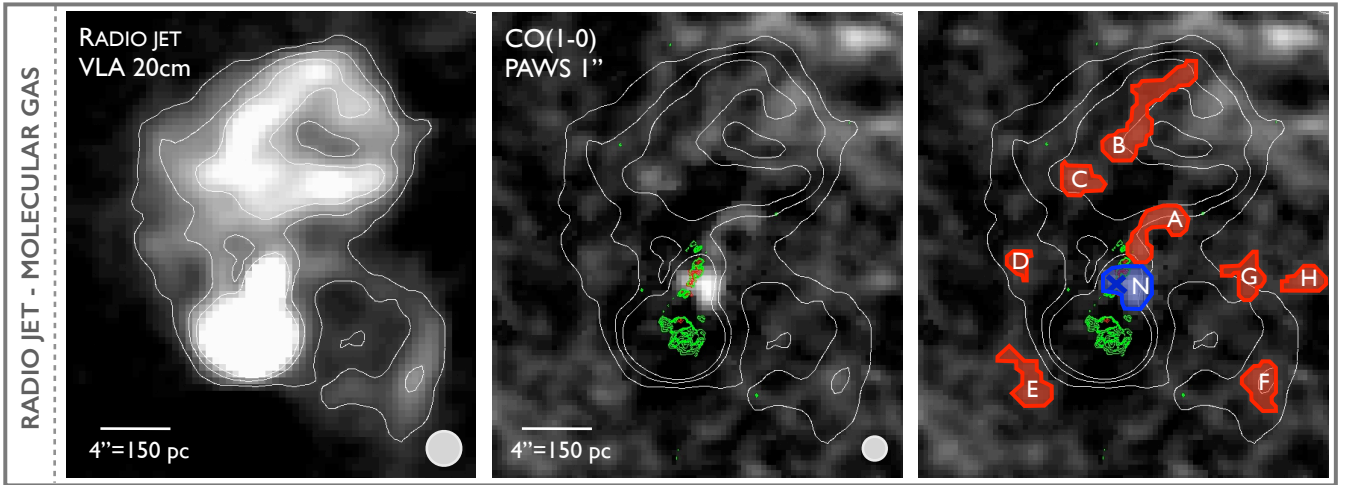


Fig. 3. From left to right: VLA 20 cm continuum image showing the kpc-scale radio jet in M51; molecular emission in the same region, traced by the CO(1-0) line imaged by PAWS at 1'' resolution, with green and red contours delineating the NLR (see Fig. 2); same image of molecular emission with some regions identified (quantitatively defined as contiguous regions with CO fluxes above 60 K km/s). The radio image is shown in linear scale from 5×10^{-5} to 5×10^{-4} Jy/beam, with three contours at levels 1.5, 3.0, and 4.5×10^{-4} Jy/beam (also reproduced on the maps of molecular emission). The CO(1-0) image is shown in linear scale between 0 and 300 K km/s.

erate speed of $\sim 0.1c$, their propagation timescales would be of the order of $\sim 10\,000$ yr, three orders of magnitude shorter than the rotation timescales. Therefore, it seems appropriate to consider the picture of a static distribution of molecular gas relative to which the jet and the plasma structures expand; only in the case of very slow plasma propagation ($\ll 0.01c$) would galactic rotation start to become relevant.

In Table 1, we quantify the velocity dispersions in the different phases of molecular gas for some regions labelled on Fig. 3. We did this by establishing some masks, defined as the positions with CO flux values above 60 K km/s on the 1''-resolution intensity map (the red shaded regions from Fig. 3), and we calculated the average of the moment-2 map¹ for CO and HCN in those positions. We confirmed that computing luminosity-weighted

¹ The moment-2 maps are the luminosity-weighted standard deviation of the velocity values in each pixel; to avoid being biased by outliers in velocity due to noise, we previously imposed a flux threshold of 5σ for each velocity channel.

Table 1. Average velocity dispersion in the different phases of molecular gas for the regions labelled on Fig. 3.

	FWHM = 2.35σ (km/s)						
	Jet ^a	No jet ^b	Disc ^c	N	A	B	E
CO(1-0) 1''	28	18	15	68	39	22	21
CO(1-0) 4''	46	24	17	90	57	29	34
HCN(1-0) 4''	84	44	22	125	82	44	46

Notes. (a) Jet area defined based on 20 cm VLA image, as the continuous region inside $r < 16''$ with fluxes $F > 0.3$ mJy/beam.

(b) Defined as the complementary region to the jet, out to $r < 16''$.

(c) Region out to $r < 40''$, excluding the jet.

mean values instead of simple averages leads to very similar results. We also define a *jet* region (fluxes $F > 0.3$ mJy/beam on the 20 cm VLA image out to $r < 16''$, before spiral arms start),

and the complementary region (*no jet*, $F \leq 0.3$ mJy/beam on the 20 cm map). For reference, we also calculated a control value as the average velocity dispersion out to $r < 40''$, the limit of the HCN field of view (excluding the jet).

The velocity dispersions of the molecular gas are clearly higher in the area of the jet than in the same radial range outside the jet (an average of $1.5 - 2\times$ higher; $2 - 4\times$ higher when compared to the mean dispersion in the disc out to $r < 40''$). Another important conclusion is that the dense gas traced by HCN shows the largest dispersions, as much as $1.5 - 2\times$ larger than CO at matched resolution ($4''$); this difference becomes less extreme (only $1.2\times$) when we consider the whole extent of the disc mapped in HCN ($r < 40''$). This is probably indicative of shocks playing a relevant role in the area of the jet and its immediate surroundings. Focusing on the specific regions labelled on Fig. 3, the nucleus (*N*) is the area with the largest line widths (as much as ~ 100 km/s at $4''$ resolution). The ridge labelled *A*, which extends north-west from the nucleus, is the second region with largest velocity dispersions; it is located next to the ionisation region, as we will show in Sect. 3.1.3. Regions *B* and *E* have similar dispersion values, but still considerably higher than the average disc values (especially in HCN, a factor of $2\times$ higher). The other regions (*C*, *D*, *F*, *G*, *H*), not listed in the table, have dispersions comparable to *B* and *E*, and follow the same trend in terms of HCN being always the broadest line.

3.1.3. Quantifying the lack of CO in the ionisation cone

In Fig. 4, we show a number of contours overlaid on the CO(1-0) intensity map from PAWS (moment-0) at $1''$ resolution. Red and green contours delimit the narrow-line region (NLR), which has an approximate projected biconical shape: in green, $\text{H}\alpha + [\text{NII}]$, and, in red, the $[\text{OIII}]$ line (Bradley et al. 2004). In white, the radio jet is shown (20 cm from VLA; Dumas et al. 2011), surrounding the XNC that forms part of the ionisation cone ($\sim 5''$ south from the nucleus), and with the characteristic loop in the north ($\sim 9''$). This ionisation cone is aligned with the axis of the radio jet, as expected from the AGN unification picture (Antonucci 1993).

We find a relative depression in CO emission coinciding with the ionisation region (Fig. 4). While the outflowing ionised gas resembles approximately a bicone, this is not the case for CO (as often assumed for distant unresolved sources); at least in M51, CO accumulates *along the edges of the jet*. Furthermore, we can quantify this scarcity: in the area shaded in blue the mean CO flux is 11 K km/s, whereas the over-concentration of CO emission towards the edge of the ionised region (shaded in red) is 114 K km/s, a factor of $10\times$ higher. Even when comparing to the average flux within the starburst ring (44 K km/s) the blue area is under-luminous by a factor of 4. This supports the new scenario proposed by Morganti et al. (2015) for jet-ISM interaction, in which the jet impinging on a clumpy molecular medium pushes the molecular gas, not only radially, but also laterally. This important result gets diluted when we consider the PAWS cube at the current resolution of our dense gas tracers ($4''$; Fig. 5). With that lower spatial resolution, the difference in CO emission between the jet area and the surroundings is only 41 to 68 K km/s. In fact, a similar mean flux ratio is measured in HCN at $4''$ resolution (12 vs 22 K km/s), so an equivalent scarcity of dense gas might exist in the ionisation region.

There are a number of reasons that could explain the relative dearth of CO emission in the ionisation cone, including photodissociation by the intense radiation field from the AGN, mechanical evacuation through the expanding plasma, or differ-

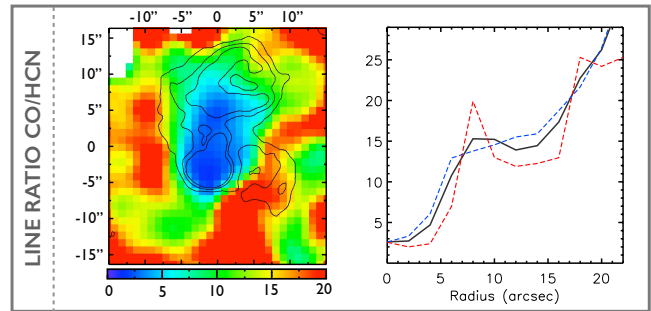


Fig. 6. Map and radial profiles of the ratio of CO/HCN fluxes. The profile shows the median values of the CO/HCN in radial bins (black line), while the blue dashed line is the ratio of fluxes in the first Gaussian (disc), and the red dashed line is the ratio of fluxes in the second Gaussian (peculiar component); see Sect. 3.2.2.

ent excitation conditions. We will discuss these in more detail in Sect. 4.

3.1.4. Dense and bulk molecular gas distribution

To investigate the dense versus bulk molecular gas distribution in the jet region, we construct a map with the line ratios of the corresponding tracers: HCN(1-0) and CO(1-0). Fig. 6 shows the map of CO/HCN ratio and its radial profile. The line ratio map is calculated by dividing the intensity maps (moment-0) of CO and HCN smoothed to the same spatial resolution ($4''$), as shown in Fig. 5, and expressing them in units of brightness temperature (K). In agreement with Matsushita et al. (2015b), we find that the CO/HCN ratio decreases significantly towards the nucleus, reaching values as low as ~ 1 . Matsushita et al. suggest shocks and infrared-pumping as the most probable causes of the abnormally high HCN brightness near the AGN position. We probe a much larger area than Matsushita et al. (2015b), and we find that the line ratio increases almost monotonically as we move towards the edge of our field of view, as expected from the gravitational potential (higher stellar surface density in the centre leads to more dense gas); however, it is interesting to note that there is a plateau and a change in the slope of CO/HCN as a function of radius around $r \sim 8''$ (300 pc), which could be reflecting a change in the excitation conditions. This suggests that the radiative effects proposed by Matsushita et al. (2015b) are not restricted to the immediate area connected with the molecular outflow ($r \lesssim 3''$), but might be relevant in the entire region affected by the radio jet. The geometry of the line ratio map also reveals a connection between the HCN/CO spatial distribution and the radio jet, although beam smearing effects do not allow us to analyse this in detail.

The dashed lines in Fig. 6 correspond to the separation into disc and peculiar kinematic components that we describe in Sect. 3.2.2. Indeed, as expected, the lowest CO/HCN line ratios are associated with the kinematically peculiar component (red dashed line), while the regularly-rotating disc component typically shows higher line ratios for a given radius. More molecular transitions are needed to further constrain the mechanisms involved, ideally including isotopologues of CO and other dense gas tracers (for instance, if photodissociation is significant, ^{13}CO should be even more under-luminous).

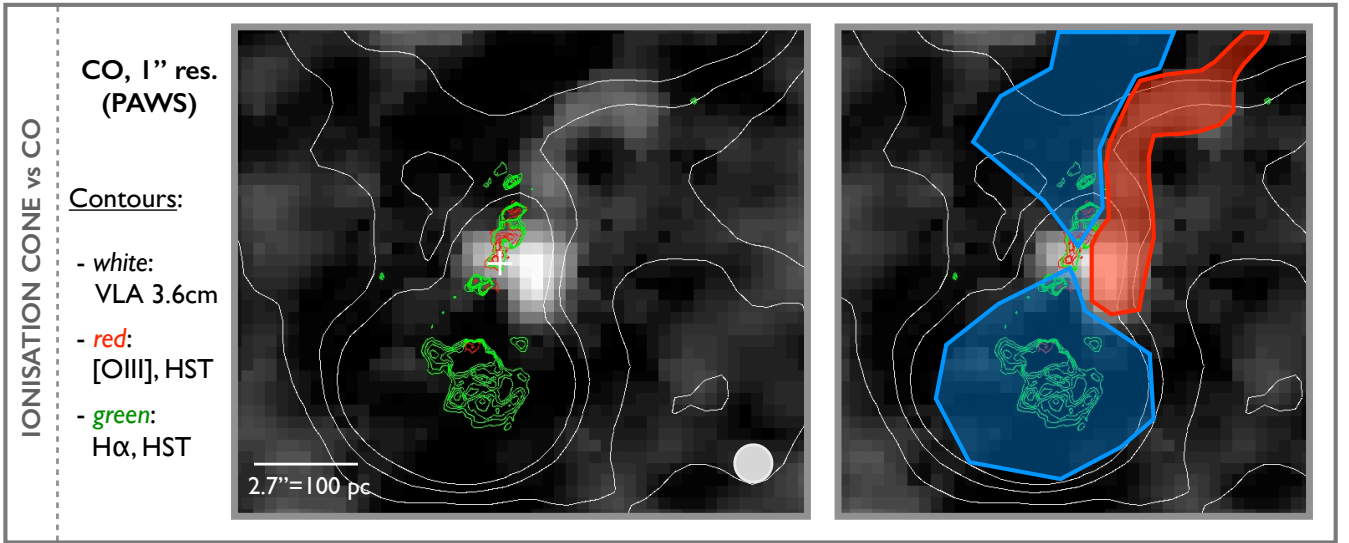


Fig. 4. Zoom on the central 500 pc of the PAWS CO(1-0) intensity map (moment-0) at 1'' resolution, with VLA 20 cm contours (Dumas et al. 2011), as well as [OIII] and [NII] + H α from HST, indicating the ionisation region (Bradley et al. 2004); the panel on the right highlights how the ionisation region is associated with under-luminous CO emission (blue shaded area), while CO seems to accumulate towards the edge of the jet (red shaded area), supporting and expanding recent findings by Morganti et al. (2015).

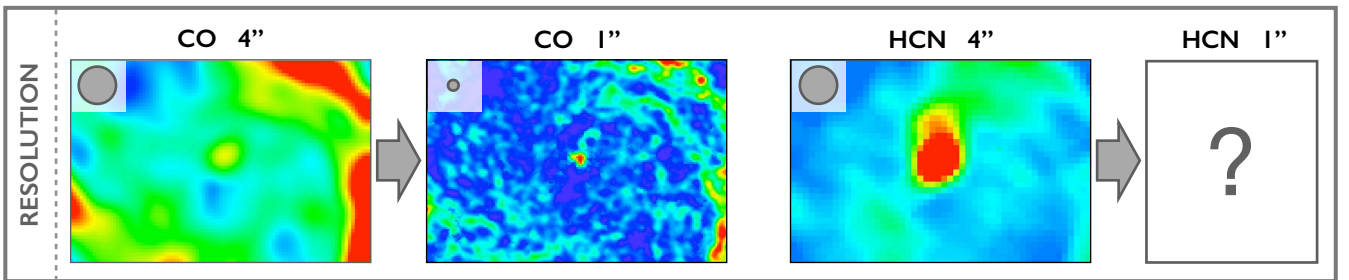


Fig. 5. Comparison of our PAWS CO intensity maps at 4'' and 1'' resolution, and our current best map of HCN at 4''. This stresses how much the analysis could be hampered by the lower resolution.

3.2. Kinematics of the molecular gas affected by the radio jet

In Sect. 3.1 we demonstrated that there is a spatial anticorrelation between CO emission and the ionisation cone, and also that HCN emission seems to be enhanced in the area covered by the radio jet. This constitutes tantalising evidence of the impact of the radio plasma jet on molecular gas. Here we look for kinematic signatures of this impact in both the CO and HCN line profiles.

Differences between the profiles of CO and HCN for a given position can be used as a diagnostic tool to identify the areas that are affected by mechanical or radiative feedback from the AGN. Some examples are given in Fig. 7. As we show next in Sect. 3.2.1, these relative differences in the CO versus HCN profile shapes become important in the area covered by the radio plasma jet, with a superposition of complex velocity components.

In addition, contrary to the simple profile found across the disc of M51 (FWHM \sim 25 km/s), secondary CO and HCN peaks are detected up to \sim 500 pc away from the nucleus, and a very broad line (FWHM \sim 150 km/s) in the area encompassing the actual AGN (Fig. 7). These multiple components, identified and discussed in Sect. 3.2.2, also point to a complex kinematic interplay with the AGN.

3.2.1. Differences in HCN-CO line profiles

In addition to significant local variations in terms of flux (Fig. 6), the CO and HCN emission lines also show very important local variations with respect to each other in their line shapes. Even if we scale the CO cube to match the peak brightness temperature of HCN in each pixel, the profiles often diverge. The HCN line is always broader and often skewed with respect to CO in those divergent positions (see Fig. 7 for some examples). Given that HCN traces a denser phase of the molecular gas, and it is more easily excited by shocks and other radiative transfer effects, it is tempting to hypothesise that these divergencies between the CO and HCN lines are revealing a non-linear response of the different molecular gas phases to the feedback from the AGN.

To test this hypothesis, we quantified the difference in the profile shape between the CO and HCN lines as a function of position. For that, we first rescaled the CO intensity map to match the peak brightness temperature of HCN on a pixel-by-pixel basis (at matched resolution, 4''); then, we obtained a cube with the difference of both profiles, and calculated the moment maps for that HCN-CO cube. To ensure that the moment maps are not driven by noise, we first implemented a threshold cutoff to the HCN and CO cubes, establishing a limit of 5σ on each channel in each pixel to identify significant emission. Scaling

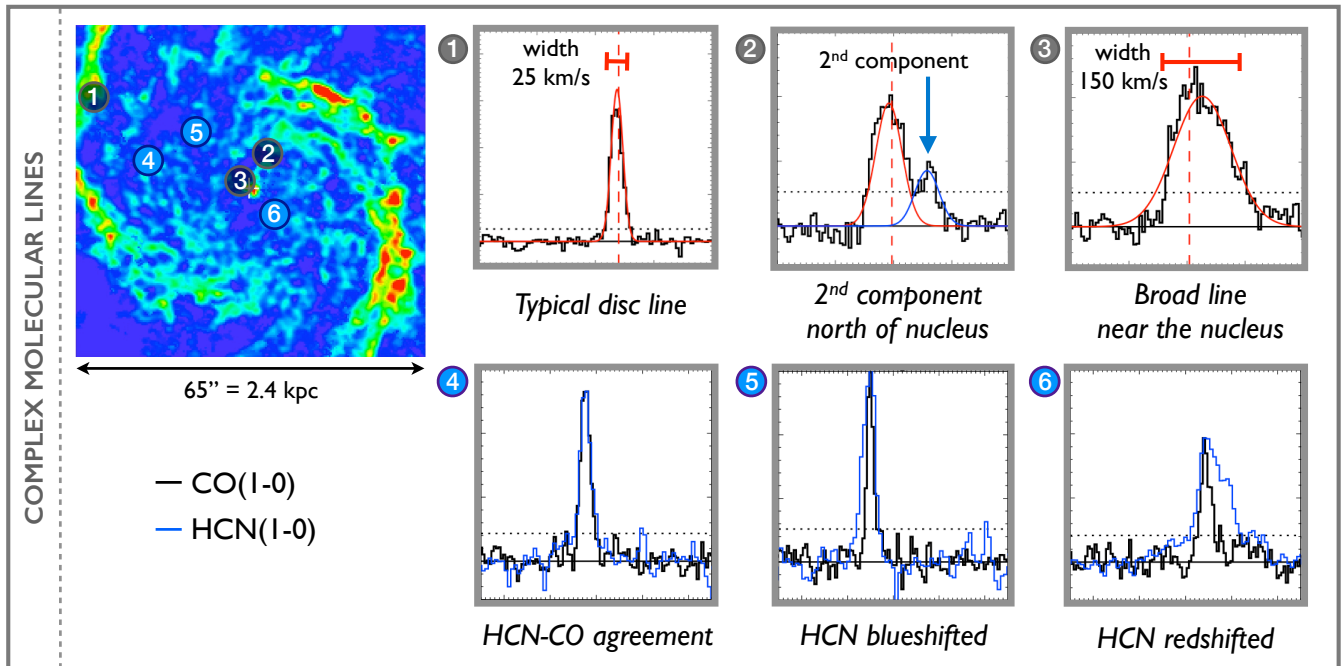


Fig. 7. PAWS moment-0 map at $1''$ resolution with an indication of the positions where different spectra have been taken. The top row highlights some peculiar components in CO: contrary to the typical CO line of 20-30 km/s (①), important secondary components appear as we approach the nucleus (②) and a very broad line (≥ 100 km/s, ③) in the immediate surroundings of the AGN. The agreement of the main line with the expectation from a TiRiFiC model is remarkable (vertical red dashed line, implementing a Spekkens & Sellwood bar); the distinction between disc and outflow contribution is robust. The bottom row shows some differences between the CO and HCN profiles for three positions: while the agreement is excellent far from the radio jet (④), there are significant departures as we approach the outer envelope of the jet (⑤), and the differences can become extreme as we approach the nucleus (⑥). We note that in these line profiles the velocity axes span the range (-250, 250) km/s, with major tickmarks separated by 100 km/s and minor tickmarks every 10 km/s; the fluxes are in arbitrary units.

CO to the peak of HCN or the other way around should lead to exactly the same velocity offsets; however, the relative “offset intensities” could in principle change. We have confirmed that scaling HCN to the peak brightness temperature of CO in each pixel, and even rescaling both cubes to an arbitrary peak temperature of 1 K everywhere, leads to exactly the same velocity (as expected by construction), and very similar “offset flux” distribution, with the maximum flux clearly occurring across the jet and leading to an analogous qualitative interpretation. We have also checked against an alternative HCN cube cleaned using robust weighting; in spite of the slightly better resolution ($3.5''$, at the expense of non-uniform noise), the offset maps are virtually identical.

The resulting intensity map (Fig. 8 left, moment-0) captures the extra emission in the HCN line with respect to CO; it will be zero wherever the HCN profile is a scaled replica of the CO line (same velocity centroid, width, and shape), and non-zero in those positions where HCN diverges from CO, typically because the HCN line is broader and/or skewed. While, in principle, it could happen that negative flux is obtained for some positions (as the CO line could be broader than HCN), we note that this is not significant in the inner $25'' \sim 1$ kpc.

The velocity map shown in Fig. 8 (right, moment-1) represents the intensity-weighted average velocity in the scaled CO cube subtracted from HCN. Therefore, this will only diverge from the original CO velocity centroid if the extra emission in HCN is kinematically asymmetric, or in other words, *if the HCN line profile is skewed with respect to that of CO*. This can be expected if the dense gas emission traced by HCN is pref-

erentially associated with energetic and dissipative phenomena such as shocks. However, due to our limited resolution, it can also happen that multiple kinematic components blend along the same line of sight (by the $\sim 4''$ beam), and this could result in zero bulk velocity offset with respect to CO due to mere superposition; however, even in this situation, the HCN profile will show wings with respect to CO on both sides (the HCN line will have overall larger line width), which will result in detectable extra emission in the HCN-CO intensity map (Fig. 8 left). For clarity, in the final velocity map we blank all pixels where this integrated extra emission is less than 1 K km/s (referred to the HCN flux scale).

At first glance, what is most remarkable about the HCN-CO line profile differences in Fig. 8 is that the highest extra flux in the central area closely follows the structure of the radio plasma jet. While there are holes near the very centre (because CO is extremely under-luminous in the ionisation cone, see Sect. 3.1.3), the areas of large HCN-CO offsets coincide with strong radio continuum emission, particularly towards the edges of the northern loop, the sides of the radio continuum peak (AGN position), and the edges of the southern XNC. Overall, this is indicative of HCN emission being affected by the radio jet out to distances of $\sim 12'' \sim 450$ pc.

In spite of this strong spatial agreement, kinematically the situation is more complex. The right panel of Fig. 8 shows very strong local variations, typically covering the range (-30, 30) km/s. Even though these velocities are not extremely high, we note that they could be reflecting much larger underlying velocity components, because: (a) the moment-1 map shows

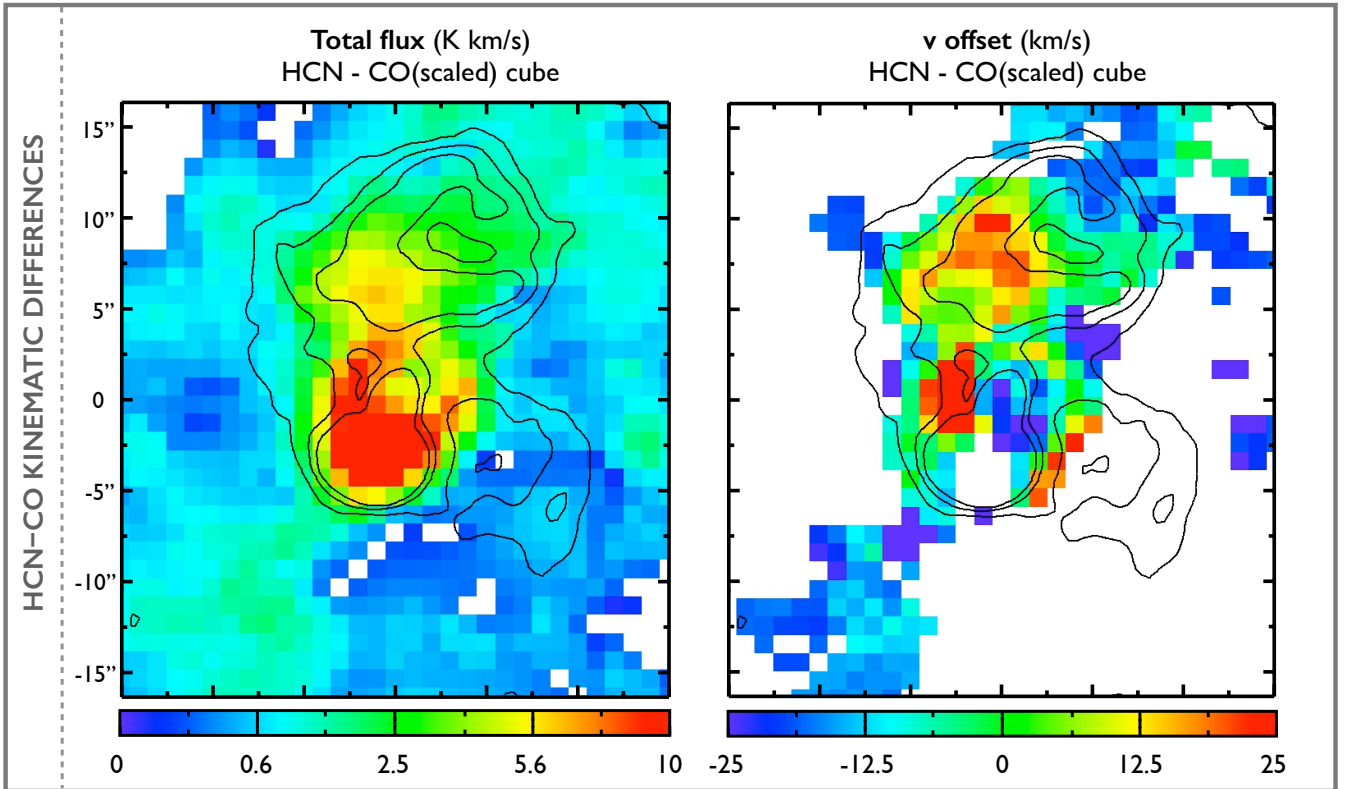


Fig. 8. Maps showing the relative differences between HCN and CO profiles (when they are scaled to match the same peak brightness temperature). *Left:* total intensity in the HCN-CO scaled cube (moment-0). *Right:* intensity-weighted velocity offset in the HCN-CO scaled cube (moment-1), expressed relative to the CO velocity centroid in each position. The contours show the radio jet from Fig 3, for reference. Both maps show the same field of view, $30'' \times 33''$, with large tickmarks indicating a separation of $5''$.

the intensity-weighted average of the velocities, to the point that negative and positive velocity offsets can cancel each other; and (b) since M51 is seen almost face-on, any lateral planar motions will project to the line of sight as small velocity components. For example, typical moment-1 values around 20 km/s in the northern loop correspond to HCN profiles which have significant emission kinematically offset by more than 50 km/s , which accounting for projection effects could translate into intrinsic velocities above 100 km/s .

In M51, the line of nodes coincides approximately with the north-south axis ($PA = -7^\circ$), and the radio jet axis is also not far from the line of nodes ($PA = -18^\circ$). Even though the inclination of M51 is not very large ($i = 22^\circ$), the near side of the galaxy is the *east side* (left in our figures; Colombo et al. 2014b). Any motions parallel to the line of nodes will have no projected components along our line of sight; therefore, we are essentially insensitive to radial propagation along the jet from the perspective of kinematics. On the other hand, any motions of lateral expansion associated with the jet will result in detectable projected velocity components. Assuming that the jet propagation is coplanar with the disc of M51, we would expect preferentially blueshifted components in the east (the near side, pointing towards us), and redshifted in the west (the far side, directed away from us). However, this is not what we see in the right panel of Fig. 8, at least in the northern loop; we find preferentially redshifted velocities in the east, and blueshifted in the west. This apparent contradiction can easily be explained if the plane of the jet is tilted with respect to the midplane of the molecular disc;

this could easily result in the observed kinematics as the consequence of lateral expansion, as illustrated by Fig. 9.

Assuming that the northern loop is a relatively flat structure, the complex kinematics could also be partially explained as the result of motions *perpendicular* to the plane of the galaxy: the loop could be pushing the molecular gas *up and down* in the galactic disc, and not only laterally in the plane of the galaxy. In any case, the resulting projected velocities will largely depend on the relative position of the affected molecular clouds or clumps vertically, relative to the galaxy midplane, which can contribute to the observed HCN-CO velocity distribution.

In general, the kinematics of HCN-CO could be reflecting at least two different possibilities: (a) the response to the radio jet traced by the difference between HCN and CO line shapes is highly stochastic, with intrinsically large variability with position; (b) we see different red- and blueshifted components superposed in the same line of sight due to our limited resolution ($\sim 4''$), because the (possibly coherent) structures involved are close to each other in projection, and are blended by the beam. Even though our limited resolution does not allow us to distinguish between (a) and (b), in both cases the data would imply significant lateral expansion. The data conclusively proves that the molecular gas is affected by the AGN through the radio jet to distances of at least $\sim 12''$ (450 pc) in the north, and $\sim 7''$ (260 pc) in the south, with rapid phase changes or different excitation conditions, which involve deprojected velocity offsets between HCN and CO of $\geq 100 \text{ km/s}$.

Even though we cannot resolve HCN into small structures ($< 4''$) with our current dataset, the rapid local variations in the

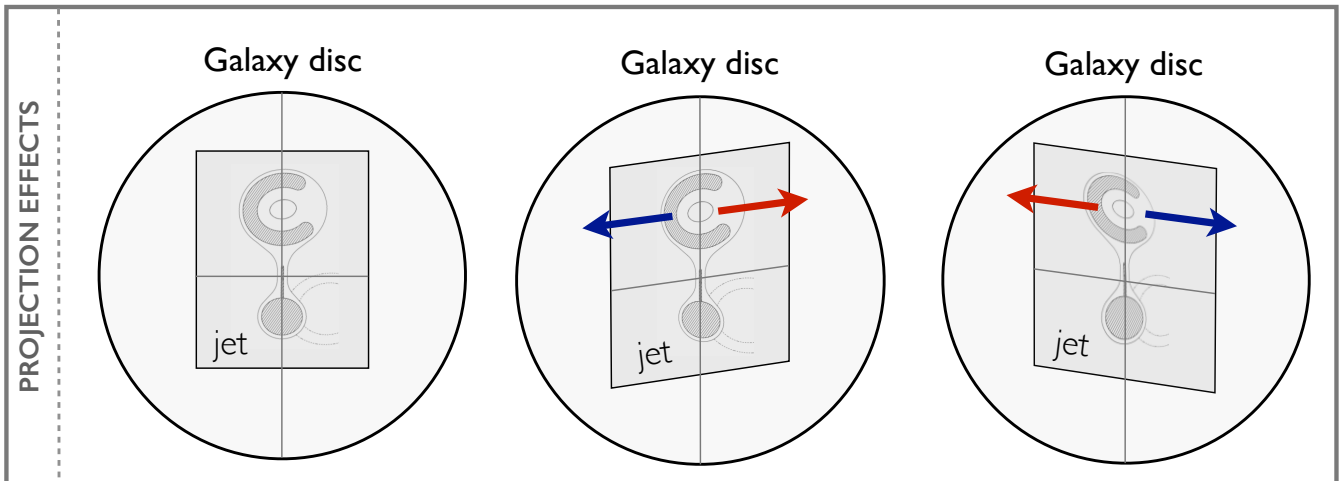


Fig. 9. Cartoon illustrating how a relatively small tilt between the plane of the jet-loop structure and the disc of M51 can result in net redshifted or blueshifted velocities on alternating sides of the galaxy (because M51 is almost face-on). The differences between HCN and CO kinematics in Fig. 8, with hints of redshifted material in the east of the northern loop and blueshifted in the west, could be indicative of the situation suggested by the right panel of this cartoon.

velocity offset with respect to CO make us hypothesise that the HCN emission comes from a clumpy medium (at least as clumpy as the bulk molecular gas traced by CO). This possibility should be confirmed with data at higher resolution.

3.2.2. Identification of multiple Gaussian components in molecular line profiles

In Fig. 7 we show some examples of the differences in CO line shape for three different positions in the central area of M51. In addition to significant offsets between HCN and CO, many positions show evidence for multiple components. With the goal of characterising those multiple components, we perform a kinematic separation of different Gaussian contributions, on a pixel-by-pixel basis, for each of the cubes (CO, HCN). For each line profile (i.e. each pixel), we iteratively fit 1, 2, or 3 Gaussians, minimising χ^2 . In the fitting process, we use the peak velocity as the starting fitting point for the first Gaussian, whereas for the second and third, we allow the fits to start from a number of equispaced spectral positions (a total of 20 starting points) that cover the whole velocity axis.

To determine which Gaussian fits are significant, we rule out *a posteriori* any fitted Gaussians which correspond to a region of the profile which does not have *at least* three adjacent channels above $5\sigma^2$. This is to avoid spurious fits to noise (since noise is spatially correlated, but fully uncorrelated among adjacent channels). This is an extreme threshold, and it is chosen to avoid potential degeneracies due to fitting multiple Gaussians when we are dominated by noise (Sect. 4), and to highlight the most significant components. Even when the emission itself follows a perfect normal distribution, if noise is not negligible compared to the peak of the Gaussian, it can happen that a random dip in the profile which originates from abrupt channel-to-channel noise variations will result in χ^2 being minimised by fitting two Gaussians instead of one; therefore, the kinematic decompositions performed this way face some practical difficulties, and

that is why we prefer to show maps with a very high threshold. We verified that lowering this threshold does not qualitatively change our conclusions.

About 30% of the pixels with significant CO emission at $r \lesssim 1$ kpc are better described by multiple Gaussian components than a single Gaussian profile. The equivalent fraction for the HCN cube is 22%. We make the conservative assumption that the Gaussian that carries most flux is the one associated with the disc. We confirm that this is a reasonable hypothesis with a TiRiFiC synthetic kinematic model that implements a rotating disc and a Spekkens & Sellwood (2007) bar for M51 (see Appendix A); only in the very centre ($r \lesssim 5'' = 200$ pc) do significant divergencies ($\Delta v > 10$ km/s) appear between the centre of the first Gaussian and the velocity centroid from TiRiFiC. The divergencies in the inner $r \lesssim 5''$ are expected, as this is the region where the line profile becomes extremely broad, and it starts to become impossible to kinematically separate disc from outflow (Fig. 7). In Appendix B, we estimate the maximum possible contribution from a hypothetical disc component in this central region, and we will include this upper limit for $r \lesssim 5''$ in the maps and analysis from now on.

3.2.3. Results of the decomposition into Gaussians

As demonstrated by Fig. 10, the main CO line associated with the disc has a very restricted range of widths, typically $20 \text{ km/s} \lesssim \text{FWHM} \lesssim 30 \text{ km/s}$; this line is in agreement with the idealised model we constructed with TiRiFiC, presented in Appendix A. When we look at the width of the main line (the one that carries most flux) we observe a very strong bimodality: in the central $\sim 5''$, we find an extremely broad line ($\text{FWHM} \lesssim 150 \text{ km/s}$), whereas outside that region, its width is more moderate (but still larger than the typical disc line). Additionally, for many positions, we identify multiple Gaussian kinematic components, following the technique described in the previous section. The width of these second components typically ranges from $\sim 10 \text{ km/s}$ to $\sim 40 \text{ km/s}$ in CO, with many more high-dispersion outliers than in the first Gaussian; the widths in HCN show an even more even distribution, covering the whole range $20 - 140 \text{ km/s}$ almost uniformly (see Fig. 10).

² We calculate σ as the standard deviation of the signal in line-free channels: channels 5–29 for PAWS-CO ($195 \text{ km/s} < v < 315 \text{ km/s}$); channels 5–38 for HCN ($84 \text{ km/s} < v < 315 \text{ km/s}$).

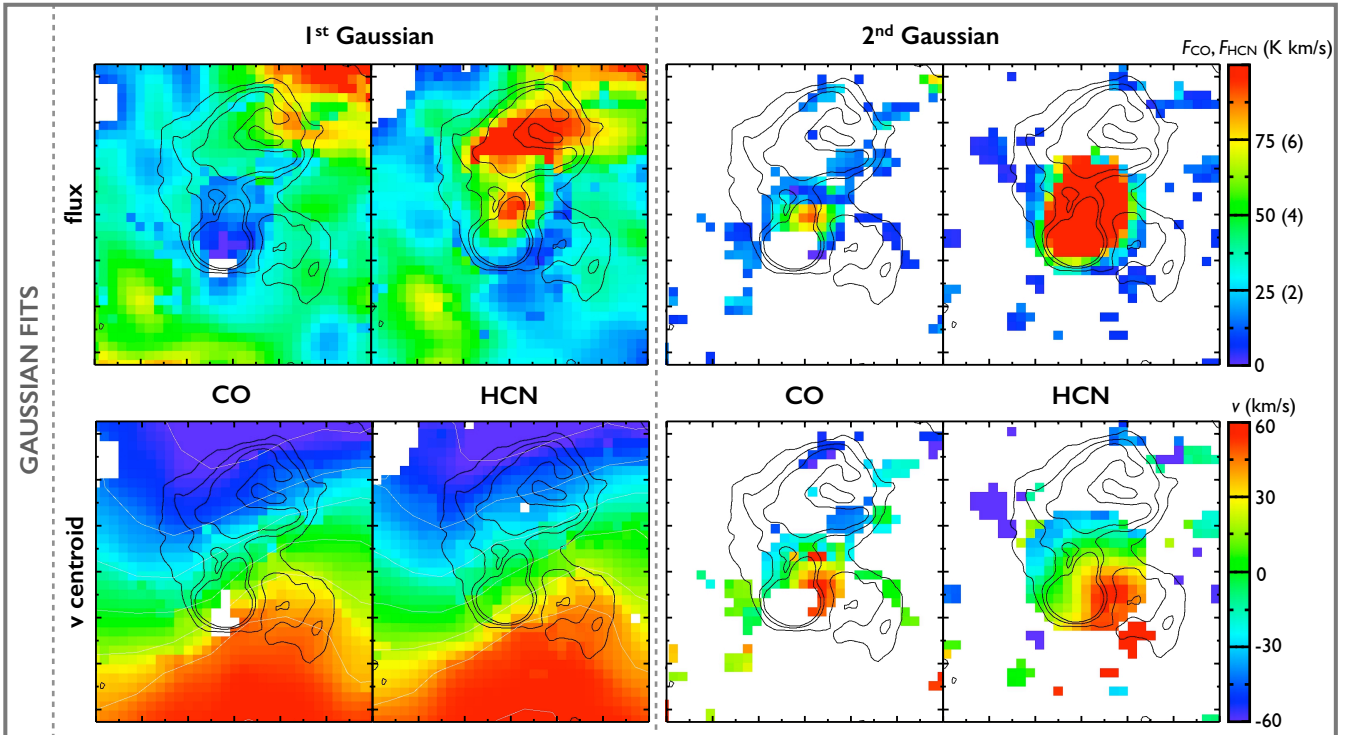


Fig. 11. Flux and velocity centroid of the Gaussians fitted on a pixel-by-pixel basis to the CO and HCN profiles (Sect. 3.2.2). The top row shows the integrated flux of the first (main) and second Gaussians, while the bottom row shows the corresponding velocity centroids. The white isovelocity contours displayed on the velocity maps cover the range $[-60, 60]$ km/s, in intervals of 20 km/s. The colourbar and scales covered are shown in the right (in parenthesis for HCN). All maps show the same field of view, $30'' \times 33''$, with large tickmarks indicating a separation of $5''$.

For the molecular emission that departs from the disc expectations, there is also a clear dichotomy in terms of flux: out to $5''$, the second component, presumably associated with the outflow, clearly dominates in flux ($> 5\times$ larger than the upper limit for the disc contribution), and it shows up as a coherent, continuous structure (Fig. 11). Outside $5''$, however, the peculiar components appear as small islands, probably associated with specific molecular clouds or cloud complexes. This is not too surprising if, instead of a coherent entrainment of the molecular material by the AGN, the effects we detect result from the radio jet pushing the gas in the disc laterally as it expands. In that case, due to projection, we will find different kinematic components (in some parts blueshifted, in others, redshifted) much more patchy in nature. This reflects a similar situation to what we interpreted from the HCN-CO velocity differences (Sect. 3.2.1).

Specifically, in the areas where gas seems to accumulate next to the ionised region (for instance, those shaded in red in Fig. 4), we find multiple peculiar components, which change very rapidly with position (this becomes visible in the CO cube at $1''$ resolution, where changes are of the order of $1''$, potentially indicative of shocks). For example, the faint radio loop in the south, which connects to the XNC on its western side, seems to be associated with a coherent secondary component in CO, which extends $\sim 5''$ parallel to the northern limit of the loop. This region does not correspond to a significant HCN-CO profile difference, though, and does not appear in the maps of Fig. 8 (this is because, in fact, HCN also shows this secondary blueshifted component, but it is not above the high S/N threshold imposed on the maps of Fig. 11).

Overall, this also allows us to refine our calculation of the amount of gas that shows significant departures from planar disc

motions. By adding up the contributions from the second and third Gaussians over each of the pixels, we arrive at a fraction of 95.5% for CO in the inner $20''$ due to peculiar kinematic components, and as much as 99.9% in the inner $5''$ (for HCN, these values are 29.7% and 79.6%, respectively). This is mostly driven by the large amount of flux that deviates from the expectations for regular rotation in the inner $\sim 5''$.

3.3. Complex structures at the base of the jet

Now we focus on the central $3''$ (110 pc) of M51 to probe the effects of feedback in the immediate vicinity of the AGN. We use position-velocity diagrams for CO and HCN (Sect. 3.3.1) to verify that our data are consistent with the molecular gas outflow proposed by Matsushita et al. (2007), and to estimate the molecular gas and dense gas outflow rates. We also present evidence for an intriguing structure with very blue optical colours in the central $1''$.

3.3.1. Dense and bulk molecular gas outflow rates

Position-velocity diagrams are one of the most straight-forward tools to probe departures from regular motions in galaxies; when taken along the kinematic minor axis, an approximately flat profile is expected (constant projected velocity), while any orthogonal velocity components will stand out as outliers in the profile (e.g. outflows). In M51, such departures from regular rotation in the molecular gas become clear in the position-velocity plots of Fig. 12, with redshifted components reaching $v \sim 150$ km/s in

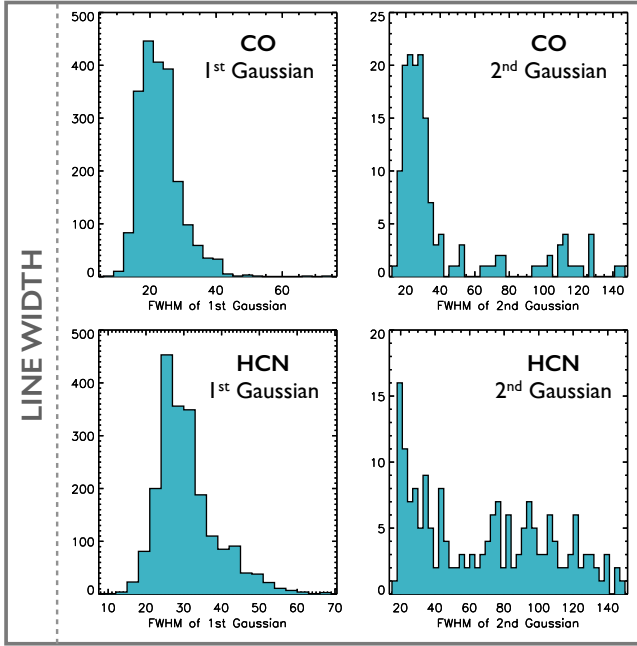


Fig. 10. Histograms showing the width of the fitted Gaussians, for CO (top) and HCN (bottom). The left histograms show the distribution of widths for the first Gaussian, which follows regular motions as expected for a rotating disc, while the right histograms display the width distributions for the second Gaussian, which show significant departures from the velocity expectations for the disc.

both the bulk molecular gas identified through CO emission and the dense gas traced by HCN.

Under the simplistic assumption of a biconical outflow (see Sect. 3.1 for details on the geometry), we can follow Feruglio et al. (2010) and Maiolino et al. (2012) to obtain an estimate of the outflow rates. In the case of a uniformly filled multi-conical outflow:

$$\frac{dM}{dt} = 3 \times V_{\text{out}} \times M_{\text{gas}}/R_{\text{out}} \times \tan(\alpha), \quad (1)$$

where M_{gas} is the total molecular gas involved in the outflow, V_{out} and R_{out} are characteristic values of the velocity and radius of the outflow, and α is the inclination angle of the outflow with respect to the disc. This is more conservative (it results in lower outflow rates) than assuming a biconical shell-like geometry, which would correspond to:

$$\frac{dM}{dt} = V_{\text{out}} \times M_{\text{gas}}/dR_{\text{out}} \times \tan(\alpha), \quad (2)$$

where dR_{out} is the thinness of the shell instead of the characteristic radius (and, in general, $dR_{\text{out}} \ll R_{\text{out}}$; Maiolino et al. 2012).

We estimate the outflowing gas mass based on the molecular emission that shows clear departures from the disc kinematics in Fig. 12; we add up the emission from the central $r \lesssim 2.5''$ over channels associated with outflow velocities (more than 30 km/s apart from the systemic velocity). We assume a conversion factor $\alpha_{\text{CO}} \sim \frac{1}{2} \times \alpha_{\text{CO,MW}} = 2.2 M_{\odot} (\text{K km s}^{-1} \text{pc}^2)^{-1}$, following the careful LVG analysis from Matsushita et al. (2007) for the centre of M51. We assume a similar reduction relative to the

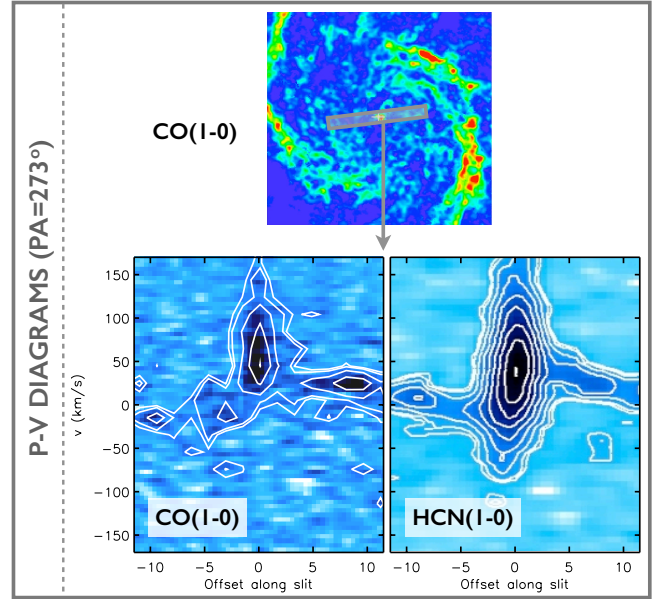


Fig. 12. Integrated intensity map of our PAWS (PdBI Arcsecond Whirlpool Survey) CO(1-0) cube at $1''$ resolution, with an indication of the slit used for the p-v diagrams shown next. Position-velocity diagrams extracted along a PA= 273° , for CO ($1''$ resolution) and HCN ($4''$), in which the redshifted wings of the outflow become manifest (with a blueshifted counterpart hinting in HCN).

Galactic value for the factor that converts HCN luminosity to dense gas mass, $\alpha_{\text{HCN}} \sim \frac{1}{2} \times \alpha_{\text{HCN,MW}} = 5 M_{\odot} (\text{K km s}^{-1} \text{pc}^2)^{-1}$, based on the Milky Way measurement from Gao & Solomon (2004). The CO conversion factor is in agreement with Israel (2009a,b), Blanc et al. (2013) and Sandstrom et al. (2013), who found that X_{CO} can be up to a factor 2 – $10\times$ lower than $X_{\text{CO}}^{\text{MW}}$ in the central ~ 1 kpc of a set of nearby galaxies with solar metallicity. The HCN conversion factor is compatible with the measurements from Garcıa-Burillo et al. (2012) for other active galaxies, and the reduction of α_{HCN} with respect to the Milky Way value is also necessary to prevent the dense gas mass from exceeding the total gas mass. This results in a total outflowing molecular gas mass of $M_{\text{CO}} = 4.1 \times 10^6 M_{\odot}$, and a dense gas mass of $M_{\text{HCN}} = 2.7 \times 10^6 M_{\odot}$.

We choose $R_{\text{out}} \sim 1'' = 37$ pc as the typical outflow radius (calculated as the luminosity-weighted average); $V_{\text{out}} \sim 100$ km/s is the characteristic velocity of the material that shows departures from the disc. The angle α is largely unconstrained, as the central area is mostly unresolved and we cannot determine the exact geometry. However, if we make the assumption that the outflow is parallel to the radio jet, we can constrain $\alpha = 15^\circ$ (based on Cecil 1988, as described in detail in Appendix C). This results in the following estimate for the outflow rate of bulk molecular gas, under the conservative assumption that it fills the cone:

$$\frac{dM(\text{H}_2)}{dt} = 0.9 M_{\odot}/\text{yr}, \quad (3)$$

and the following value for the outflow of dense gas:

$$\frac{dM(\text{HCN})}{dt} = 0.6 M_{\odot}/\text{yr}. \quad (4)$$

This suggests that the molecular outflow is predominantly made up of dense gas. The values expressed as a function of α are $\dot{M}_{\text{H}_2} = 0.3 M_{\odot}/\text{yr} \times \tan(\alpha)$ and $\dot{M}_{\text{HCN}} = 0.2 M_{\odot}/\text{yr} \times \tan(\alpha)$. In Sect. 4 we discuss how these values compare to those found for other nearby and distant molecular outflows.

The p-v diagrams that we have just presented show, overall, a lack of blueshifted counterpart to the observed redshifted velocities. There are different reasons that could explain this, but the most simple one is to assume that it is associated with asymmetric AGN activity (a hypothetical one-side activity cycle that would explain why the jet is stronger in the south). Indeed, the structure that Matsushita et al. (2007, 2015b) resolve near the nucleus, and argue that it is undergoing an outflow, is elongated towards the south, where the jet is stronger, and corresponds to redshifted velocities. In this dynamical picture, it is conceivable that, while only the redshifted component is seen now, a blueshifted counterpart might have existed in the past. We note that there are hints of a blueshifted component in HCN; examining the HCN profiles in the central area we have confirmed that this is real emission, and the fairly Gaussian HCN line shows a longer blue tail near the nucleus (this is also seen in the gradient in the velocity field of Fig. 11). However, higher angular resolution data is required to unambiguously address this issue.

3.3.2. Dust extinction and nebular emission in the nucleus: the central “bump”

Figure 13 shows the radial surface brightness profile of the central $r < 20''$ of M51 for different optical bands (HST V-band and I-band). The central $r \lesssim 5''$ cannot be fitted with the same Sérsic profile as the rest of the disc, and the central excess of light with respect to the Sérsic component is ~ 1 mag. We propose that this excess of light probably stems from a combination of two effects: (a) unobscured stellar continuum relative to the surroundings because dust has been largely evacuated in $r \lesssim 5''$; and (b) in the centremost $r \lesssim 2''$, nebular emission likely has a significant contribution in the optical bands, reflecting on a feature of distinct blue optical $B - V$ and $V - I$ colours (Fig. 13). This structure is responsible for the bump that the optical surface brightness profiles show close to the nucleus.

The very blue optical colours ($B - V = 0.3$, $V - I = 0.9$) could be indicative of a young stellar population. The excess of light was already attributed to a nuclear star cluster by Grillmair et al. (1997), who showed that an east-west dust lane is crossing the centre (the position of the excess light). Fitting a King profile they estimate an upper limit to the core radius of this alleged stellar cluster, $r_c = 0.3''$ (14 pc). According to Lee et al. (2011), the $V - I$ and $B - V$ colours can indeed be explained by a (very) young stellar population ($\lesssim 10$ Myr, labelled “P2” in their paper); therefore, if the cluster hypothesis is true, this is likely a stellar cluster in the process of getting born. This is slightly contradictory with the fact that star formation tracers do not show evidence for a significant amount of recent star formation in the centre of M51 (Kennicutt et al. 2007; Fang et al. 2015), and also the fact that the centre shows [3.6]-[4.5] near-infrared colours characteristic of non-stellar emission (see Querejeta et al. 2016). Additionally, when inspected carefully, the shape of the colour maps is not consistent with the expectations for a relaxed stellar system (even though the partial obscuration due to the central dust lane and the finite resolution of the HST images can contribute to the observed appearance, at least partially). We have extracted a central spectrum from the VIRUS-P IFU dataset of M51 presented in Blanc et al. (2009) and run Gandalf to identify the stellar populations that best explain the spectrum in the cen-

tral IFU pointing (RA=13:29:52.673, Dec=+47:11:43.62). We find no significant evidence for young stars, with an overall luminosity weighted age of 8.9 Gyr; however, the spatial resolution of this dataset (5.5'') is insufficient to conclusively rule out a small young stellar population in the very centre (1'').

Alternatively, the inner bump could be due to scattered light from the AGN (e.g. Obied et al. 2016). If scattered light is the reason, one would in principle expect (bi)conical geometry, and not the arc-like structure that we see $\sim 1''$ north of the AGN position; however, scattering cones often show significant asymmetries (Obied et al. 2016). This hypothesis was already suggested by Lee et al. (2011). If indeed due to scattered light, the reason why we see this emission only in the north of the AGN, and with such an peculiar shape, could be because the radiation is scattered by a gas cloud of higher density which has that specific shape; this would also help explain why the ionisation region in the north is not as extended as in the south of the AGN (an important part of the ionising optical radiation would be scattered by this structure, preventing ionisation further north). Polarisation studies would be useful to confirm whether the excess optical emission in the centre of M51 is indeed due to scattered light from the AGN. Probing the true nature of this structure is beyond the possibilities of our current data, but this intriguing structure reinforces the idea that the processes taking place near the nucleus of M51 are many and complex.

4. Discussion

We have presented a number of results related to the active nucleus of M51. Overall, these pieces of information delineate a complex situation, in which processes that operate on different spatial scales are interconnected. In the central $\lesssim 3''$ (110 pc) next to the AGN, molecular gas has been suggested to be entrained by the nuclear radio jet (Matsushita et al. 2007), which is collimated out to a distance of $r \lesssim 2.3''$ (85 pc) in the south ($r \lesssim 1.5'' = 60$ pc in the north). Both in CO(1-0) and HCN(1-0) emission we find extremely broadened lines in this central area, preferentially redshifted ($\Delta v \sim 100$ km/s, $\sigma \sim 150$ km/s), and with increasing HCN/CO line ratios which approach unity near the centre. In the optical, a very bright and blue structure $\sim 1''$ (37 pc) north of the AGN becomes apparent through HST imaging, but its nature and potential interplay with the outflowing (or inflowing) gas remains elusive. At the scales spanned by the ionised optical emission lines ($\text{H}\alpha$, [NII], [OIII]), out to $\sim 1''$ (37 pc), we find a clear scarcity of CO emission ($\times 10$ lower flux), which we probe down to $1''$ scales; the ionisation cone seems to be associated with a dearth of bulk molecular gas, whereas clouds of CO accumulate towards the edges of this ionisation cone. At larger spatial scales, including the northern radio-emitting loop, and the boundaries of the southern XNC, we find evidence of the radio jet impacting the surrounding molecular material. This manifests itself in the form of multiple kinematic components, an enhanced HCN/CO ratio, and strong deviations between the HCN and CO line profiles; the HCN line is typically broader and more skewed (even at matched resolution). We recall that in this paper we refer by *radio jet* to all the structures involved in the presumably expanding plasma, which produce synchrotron emission and are detected at radio wavelengths (3.6, 6, 20 cm); the collimated radio jet itself is $\sim 4''$ (150 pc) long, and $\sim 0.3''$ (12 pc) wide: it connects to the XNC in the south, and points towards the “C”-shaped loop in the north (but is not directly connected to it). The cartoon in Fig. 14 shows the different components that we will discuss and their relative sizes, in an attempt to illustrate the geometry and the scales involved.

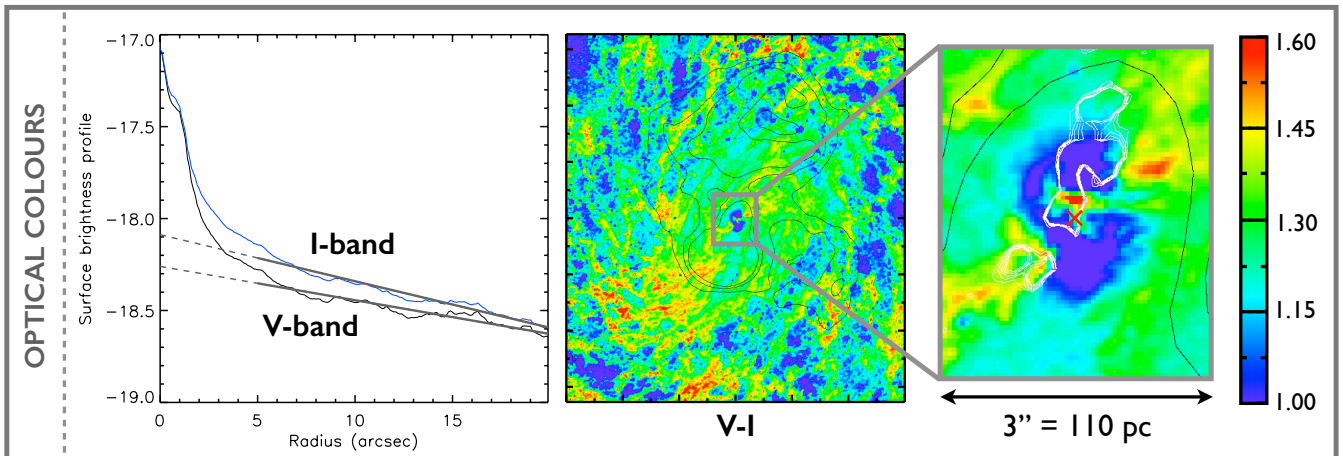


Fig. 13. From left to right: radial profile of surface brightness in the HST *I*-band and *V*-band, in units of mag/arcsec²; *V* – *I* colour map of the same field of view shown before, 30'' × 33'', with large tickmarks indicating a separation of 5'' (in linear scale from 1.0 to 1.6); blowup of the central area, where the “bump” is originating from (overlaid with *H*α contours in white; the black contours correspond to the radio jet traced by 20 cm continuum).

4.1. Under-luminous CO in the ionisation cone

There are several possibilities to explain the scarcity of CO emission in the area covered by the jet relative to the edges. First, CO gas could simply be photodissociated by the strong radiation from the non-stellar nuclear source, the AGN, as it enters the ionisation cone; this seems plausible, as energetic arguments also point to the radiation field from the AGN as the most likely source of ionisation leading to the *H*α, [OIII], and [NII] optical emission (Bradley et al. 2004). Another possibility that is compatible with our observations is that the CO-emitting clouds have been mechanically evacuated by the expanding radio plasma jet. The fact that the southern side is presently more active (the collimated radio jet is longer towards the south, brighter, and more straight) is probably the consequence of an alternating one-side activity cycle (Rampadarath et al. 2015). It is also possible that radiative transfer mechanisms are leading to reduced CO(1-0) emission in that ionised area or, conversely, radiative transfer effects that result in enhanced emission at the edge of the cone. Having said that, the masing effects identified by Matsushita et al. (2015b) are only expected to be relevant sufficiently close to the AGN (García-Burillo et al. 2014). In any case, all three hypotheses (photoionisation, mechanical evacuation, or radiative transfer effects) would explain why there is more ionised optical emission in the south, and also why the scarcity of CO(1-0) is more severe on that side. Finally, it is also possible that the magnetic field created by the expanding, probably relativistic jet plays a role in accumulating molecular clouds towards its edges (e.g. by ambipolar diffusion, as proposed by Krause et al. 2007 for NGC 4258).

The sharp picture that PAWS provides at 1'' (Fig. 4) rules out a possible chance alignment of ionised gas, radio jet, and lack of CO emission. Of course, in other galaxies projection effects could conceal this effect, even if the ionisation cone or jet has indeed evacuated or photo-dissociated the bulk molecular gas: if the cone is narrow enough, or if it is more inclined than in M51, it can well be that molecular clouds are detected flowing in front or behind the ionisation cone, and being unable to tell their relative height in the disc when seen in projection. M51 offers the unique setting of being seen almost face-on, with the jet almost exactly coplanar with the disc, and a wide opening-

angle ionisation cone (74°; Bradley et al. 2004) which blocks most of the molecular (thin) disc, and it is thus ideal to test the relative distribution of molecular gas, ionisation cone, and radio jet. What we have shown is that, at least in the area with strong ionised optical line emission, which overlaps with the radio jet, M51 is largely depleted of CO(1-0) emission.

Naturally, from our result on a single galaxy, one cannot claim that this is a typical behaviour: the current situation in M51 can certainly be special. However, the other few cases where it was possible to spatially resolve the interplay between radio jets and molecular gas also point in the same direction. Krause et al. (2007) showed that in NGC 4258 a funnel almost completely devoid of CO(1-0) exists along the radio jet, with molecular gas accumulating at the edge of the jet in two parallel CO ridges (2.8 kpc in length, and separated by 175 pc from each other). Similarly to M51, the jet has a low (15 – 30°) inclination to the disc. Interestingly, in NGC 4258, ionised gas emission traced by *H*α also peaks in the centre of the funnel, where CO is lacking; the same situation as we find in M51. From their careful analysis of the position-velocity diagram of IC 5063 obtained with ALMA, Morganti et al. (2015) propose a scenario which would also go in the same direction. They detect signatures of lateral expansion in this edge-on galaxy, and through comparison with numerical simulations by Wagner & Bicknell (2011) and Wagner et al. (2012), they suggest that a radio jet expanding through a porous medium is responsible for their observations; as it expands, the jet would look for paths of least resistance, and clear molecular gas from its way. Finally, García-Burillo et al. (2014), who study NGC 1068 with ALMA using multiple molecular transitions, also find a “hole” in the molecular emission next to the AGN, which could be indicative of gas having been evacuated; however, this cannot be claimed robustly in NGC 1068 due to the geometry of the system and projection effects.

It would be extremely interesting to confirm whether HCN emission also shows the same behaviour and equally avoids the ionisation cone in M51. Unfortunately, we cannot conclusively prove this with our current 3 – 4'' HCN dataset (Fig. 5). In fact, we find similar HCN flux levels between the ionisation cone and surroundings as we do for CO when matched to 4'' resolution. Therefore, it is possible that a similar spatial distribution applies

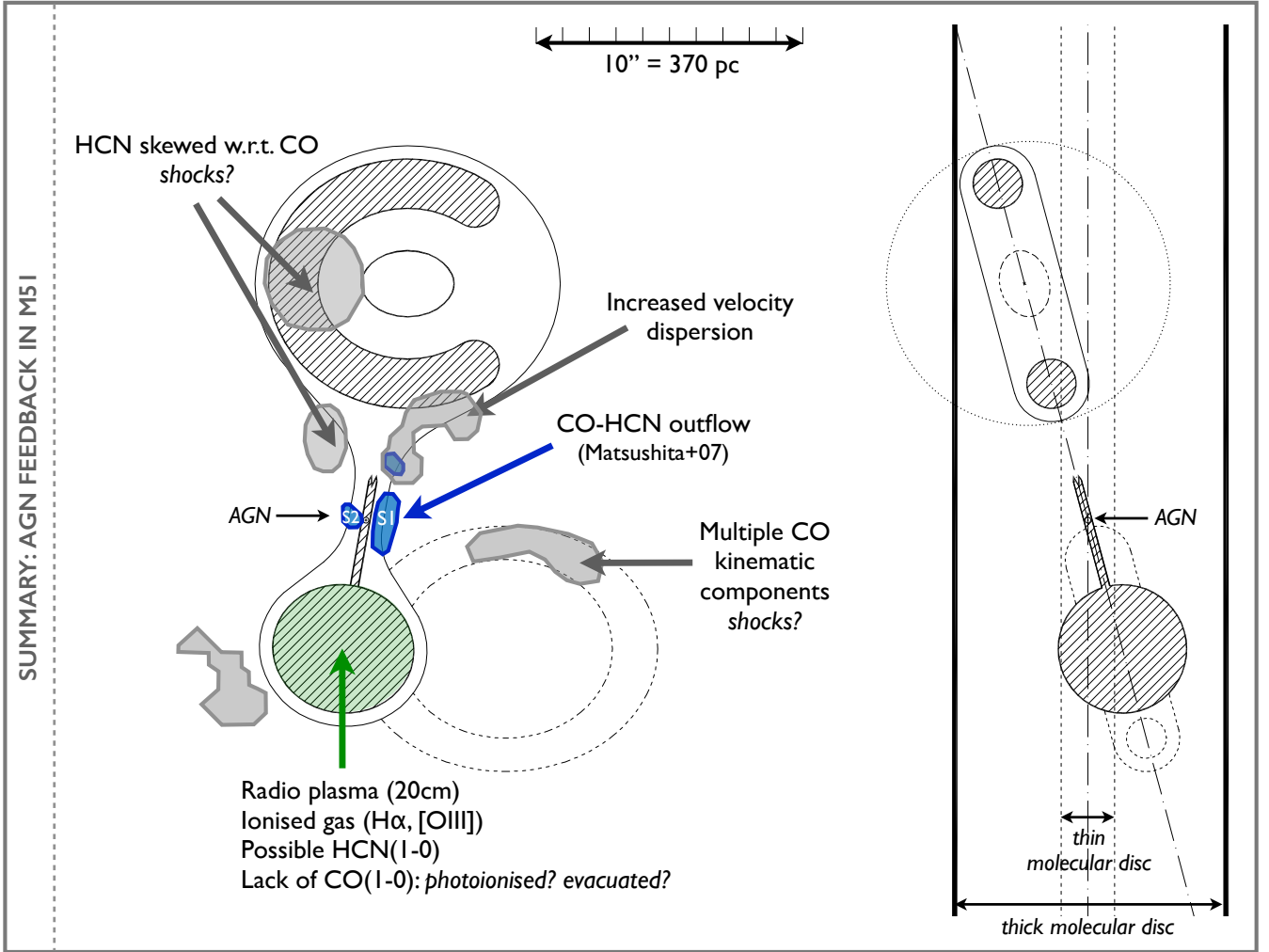


Fig. 14. Cartoon showing the scales relevant to the different processes involved in AGN feedback in the nucleus of M51. The striped areas delineate the main elements of the radio plasma jet (synchrotron emission); the nuclear collimated jet was resolved by Crane & van der Hulst (1992), and the rest of the structures have been identified on the maps from Dumas et al. (2011). The left panel corresponds to a face-on view, whereas the right panel shows a possible edge-on deprojection.

to the dense gas, which would not be surprising because both photoionisation and mechanical evacuation are in principle expected to affect both phases of the molecular gas similarly. However, higher-resolution observations of the whole ionisation cone in HCN are required to confirm this conjecture.

4.2. HCN-CO differences along the jet

We have calculated the difference between HCN and CO profiles, after scaling them to match the same peak brightness temperature, as a diagnostic tool to identify potential regions in which molecular gas is impacted by the radio jet. The agreement of this HCN-CO offset emission with the area covered by the radio jet is very good, and we interpret this as direct evidence that the AGN is impacting molecular gas through the radio plasma jet; at the same time, the fact that this effect becomes visible when looking at the difference between CO and HCN profile shapes implies that this is a *differential effect*, with enhanced HCN excitation which could reveal a larger impact of AGN feedback through radio jets on the dense gas than on the bulk molecular gas.

Kinematically, the situation highlighted by the HCN-CO velocity map is complex, with a quickly varying net velocity offset between CO and HCN. This can be the result of intrinsically rapid positional variations in the differential response imprinted on the gas traced by HCN and CO; alternatively, perhaps a relatively smooth variation results in the observed map due to projection and beam dilution effects. New observations at matched $1''$ are required to disentangle beam dilution from other effects and build a sharper picture of the feedback kinematics in the different phases of molecular gas in M51.

But not only is the response of HCN different from CO; when looking at the two tracers individually, we also find distinct kinematic components in their line profiles for some regions. These differences have motivated our attempt to automatically separate the emission into multiple Gaussian contributions. The first (main) Gaussian component reflects the intensity distribution and velocity field expected for a differentially rotating disc; the second component, however, shows a velocity gradient from north-east (blueshifted) to south-west (redshifted), probably the result of galactic rotation of shocked gas in combination with the outflow. There are some intrinsic difficulties in performing

Gaussian separations on a pixel-by-pixel basis, especially when the properties of the second components change quickly with position (as in M51), and do not have a very high signal-to-noise ratio. However, the mere presence of these secondary components, and the fact that they are so susceptible to local changes, is already telling us something important: similarly to the effects that we identified when analysing the differential HCN-CO kinematic behaviour, the analysis of the CO and HCN profile shapes independently points to a complex feedback situation, compatible with the jet pushing laterally (which due to projection leads to quickly changing red- or blueshifted components). It is also important to emphasise that both effects are not always redundant: in some positions, CO and HCN show important relative differences, while none of them has a second Gaussian component (HCN is typically broader or skewed). In other positions, we see multiple components, but no difference between the HCN and CO lines: they are scaled replicas, and both have multiple components which coincide in velocity and shape.

The radio jet is far from being a smooth structure when inspected closely, showing kinks, asymmetries, and irregularities; the molecular gas distribution is also far from smooth, and rather clumpy (Leroy et al. 2013; Colombo et al. 2014a). Therefore, if the expanding jet is pushing on the clumpy gas, we can expect quickly varying kinematic components, especially if the imprinted velocities are essentially coplanar with the galaxy. In other words, the complex kinematic response in the molecular gas might reflect the underlying non-smooth distribution of the ISM (and the geometrical irregularities of the radio jet itself).

Altogether, this is clear evidence that the molecular gas is impacted by the radio jet, out to scales of ~ 500 pc, even in a system with an AGN as weak as the one in M51.

4.3. Consequences of AGN feedback

One of the most important consequences of AGN feedback as we see it in M51 is that it will contribute to inject turbulence on the molecular disc, which has the potential of making the gas unable to form new stars. With our new observations, we have found that velocity dispersion is enhanced at least out to $r \sim 5''$, further out than the nuclear outflowing structure identified by Matsushita et al. It is worthwhile noting that what we resolve as multiple Gaussian components would be attributed to mere turbulence when observed at lower resolution (e.g. from single-dish data, or from interferometric observations with lower resolution); therefore, we speculate that part of the increased velocity dispersion measured in other galaxies at lower spatial resolution could ultimately be resolved into independent components which vary rapidly from position to position. Increased turbulence from AGN feedback is now recognised as an agent which can regulate star formation, with quantitative measurements of such star formation suppression existing for some early-type galaxies such as NGC 1266 (Alatalo et al. 2011; Nyland et al. 2013; Alatalo et al. 2014).

The increase of turbulence and the appearance of strong kinematic effects as jets propagate through a molecular medium are expected on theoretical grounds, especially at the interaction points between jets and dense gas clouds (e.g. Wilson 1992). Here we find that the feedback is spatially extended, and does not only involve the collimated nuclear jet, but also the large-scale plasma structures. We also find that HCN is more affected than CO, perhaps due to different excitation conditions (enhanced radiative transfer effects triggered by shocks).

Observations of more molecular species could help confirm the precise role of shocks. The flux measurements of the differ-

ent CO transitions (the ‘‘CO ladder’’) from *Herschel*/SPIRE fits by Schirm (2015) for the nucleus of M51 show a characteristic flattening at high-J values; an analogous situation has been found in Mrk 231 and NGC 6240, and explained using PDR, XDR, and shocks (van der Werf et al. 2010; Meijerink et al. 2013). This suggests that, probably, both XDR and shocks are important in the nucleus of M51; to perform a more quantitative analysis in this sense, however, observations of additional molecular transitions will be essential, ideally at sufficiently high spatial resolution to probe the different regions that we have identified in this paper.

4.4. Nuclear outflow

As we have already pointed out, there is a strong bimodality between the line profiles (both CO and HCN) in the central $\sim 5''$ and the rest of our field of view. In the central area, it becomes essentially impossible to isolate different Gaussian contributions, and all we find is a very broad approximately Gaussian line, which is preferentially redshifted. This explains the strong flux at redshifted velocities in the p-v diagrams of Fig. 12. In HCN, a small blueshifted counterpart also becomes clear, symmetrical with respect to the centre. When looking at the variation of velocity with position within this area, we also find a noticeable velocity gradient in the northeast-southwest direction (from blue- to redshifted), especially clearly traced by HCN (Fig. 11). This is compatible with the velocity gradients found by Matsushita et al. (2007, 2015b), who attribute them to a molecular gas outflow; the emission they observe is coming from a number of resolved clumps. Our continuous gradient could be the result of an intrinsically smooth velocity variation (with part of the flux missed by the Matsushita et al. interferometer-only observations, see below), or because we are smoothing the structures that Matsushita identifies, producing a continuous appearance.

Even though Matsushita et al. (2015) do not quote the integrated fluxes for CO(1-0) and HCN(1-0), we can estimate them from their Fig. 2 and Fig. 6 to be ~ 10 Jy km/s and ~ 5 Jy km/s, respectively, in the inner $r < 3''$. With our maps, which include short-spacing corrections and therefore recover all the flux, we measure 25.0 Jy km/s in CO(1-0) and 7.2 Jy km/s in HCN(1-0) for the same region ($r < 3''$); therefore, Matsushita et al. seem to be missing $\sim 50\%$ of the flux in CO and $\sim 30\%$ of the flux in HCN for the central area. Comparing our HCN map with and without the short spacing correction out to $r < 20''$, we confirm that the interferometer recovers 43% of the total HCN flux from the 30m single-dish telescope; in CO, 37% of the flux is recovered by the interferometer at $1''$ resolution, and about 50% at $3 - 6''$ resolution (Pety et al. 2013). This means that, while part of the differences observed between Matsushita et al. and this work could stem from the different resolutions achieved, part could also be due to the lack of flux coming from diffuse structures, which get filtered by the interferometer.

Now, we briefly discuss the geometry of the outflow identified by Matsushita et al. (2007), and how it fits in the global picture of AGN feedback that emerges from our work. The overlay with the radio jet map shown by Matsushita et al. (2015a) makes it clear that the structures S1 and S2 (first identified by Scoville et al. 1998) lie at opposite sides of the radio jet (next to the estimated position of the AGN), whereas S3 lies $1.5''$ towards the north, precisely where the putative counter-jet seems to dissolve (see Fig. 14). Even though Matsushita et al. (2007) and Matsushita et al. (2015a) claim good agreement between the molecular outflow and the ionised outflow, this is in tension with the ionised gas observations: Bradley et al. (2004) assume that

the entrained ionised component is Cloud 1, which is blueshifted in the south, as expected from the geometry for a radial outflow if we assume that the southern cone is closer to us (Bradley et al. 2004). However, the gradient that Matsushita et al. measure goes exactly in the opposite direction, with redshifted velocities *in the south*. This apparently contradicting result can be reconciled if we reverse the assumed geometry of the jet, so that the southern cone is pointing away from us, as we briefly commented in Sect. 3.1 and Sect. 4.2. This possibility would also explain the entrainment of a higher amount of the ionised clouds identified by Bradley et al. (2004); instead of only Cloud 1 being compatible with entrainment along the jet, at least Clouds 4, 4a, and 3 would be. We note that the HCN blueshifted counterpart identified in the p-v diagram on Fig. 12, which lies $\sim 1''$ at the east of the nucleus (as opposed to the prominent redshifted material at the west), might be indicative of a dense molecular outflow which is *perpendicular to the jet*, propagating in the plane of the galaxy. This idea would be supported by the velocity gradient from north-east to south-west that we found in Fig. 11; if true, we would be resolving an outflow perpendicular to the line-of-nodes.

With our observations, we can also estimate the kinetic energy and momentum of the molecular gas that is presumably outflowing. These have already been estimated by Matsushita et al. (2004, 2007); however, our estimates should be more accurate, as they include short spacings corrections, and therefore recover all the flux. The kinetic luminosity is given by:

$$L_{\text{kin}} = \frac{1}{2} \times \frac{dM}{dt} \times \left(\frac{V_{\text{out}}}{\cos(\alpha)} \right)^2, \quad (5)$$

and the momentum flux can be obtained as:

$$\frac{dP}{dt} = \frac{dM}{dt} \times \frac{V_{\text{out}}}{\cos(\alpha)}. \quad (6)$$

Following the conservative assumptions made in Sect. 3.3.1 (multi-conical outflow uniformly filled by molecular gas), for $\dot{M}_{\text{H}_2} = 0.3 M_{\odot}/\text{yr} \times \tan(\alpha)$ and $\dot{M}_{\text{dense}} = 0.2 M_{\odot}/\text{yr} \times \tan(\alpha)$, taking again $V_{\text{out}} = 100 \text{ km/s}$ as the characteristic velocity, for CO we obtain $L_{\text{kin}} = 2.35 \times 10^{40} \text{ erg/s}$ ($1.5 \times 10^{40} \text{ erg/s}$ for HCN), $dP/dt = 1.6 \times 10^{33} \text{ g cm s}^{-2}$ (for HCN, $1.0 \times 10^{33} \text{ g cm s}^{-2}$). Matsushita et al. (2007) provide the related quantities kinetic energy and momentum instead; our equivalent measurements would be: $E_{\text{kin}} = 3 \times 10^{54} \text{ erg}$, $P = 2.4 \times 10^{47} \text{ g cm s}^{-1}$, whereas the results from Matsushita et al. (2007) were $E_{\text{kin}} = 3 \times 10^{52} \text{ erg}$, $P = 8 \times 10^{45} \text{ g cm s}^{-1}$. Therefore, the differences are very significant (our results being about two orders of magnitude higher). These values are still an order of magnitude lower than the energies involved in NGC 1068, for example ($L_{\text{kin}} = 5 \times 10^{41} \text{ erg/s}$, $dP/dt = 6 \times 10^{34} \text{ g cm s}^{-2}$; García-Burillo et al. 2014).

The star formation rate in the centre of M51 is very low, $\text{SFR}(r < 3'') \sim 0.01 M_{\odot}/\text{yr}$ in the central area involved in the putative outflow (Kennicutt et al. 2007; Fang et al. 2015). Given that the star formation rate is two orders of magnitude lower than the outflow rate, it is in principle not possible that the outflow is driven by a nuclear starburst. The bolometric luminosity of the AGN is $L_{\text{bol}} \sim 10^{44} \text{ erg s}^{-1}$ (Woo & Urry 2002); therefore, on energetic grounds, it is well possible that the AGN is driving the outflow. The question is how: in principle, gas could be expelled directly by radiation pressure, but as we have seen, CO emission seems to avoid the ionisation cone (which also seems to apply to the central $\sim 3''$, judging from our moment-0 map, and the

higher resolution maps from Matsushita et al.). Consequently, it looks like entrainment through the radio jet is the most probable mechanism. However, while the energy of the jet is estimated to be $6.9 \times 10^{51} \text{ erg}$, the momentum is only $2 \times 10^{41} \text{ g cm s}^{-1}$ (assuming a jet velocity of $0.9c$; Crane & van der Hulst 1992). As already discussed by Matsushita et al. (2004, 2007), the energy is sufficient, but the power of the jet is too low to explain this coupling directly; perhaps a continuous transfer between energy and momentum could explain this apparent mismatch. Finally, another possibility would be to abandon the idea of a molecular outflow, and interpret the velocity gradient observed as evidence of molecular gas *inflow*.

4.5. Relation between inflow and AGN feedback

In Querejeta et al. (2016) we have shown that there is molecular gas inflow down to our resolution limit of $1.7''$ (although the inner region, $r \lesssim 3''$ is highly uncertain). This molecular gas inflow can be explained by the gravitational torques exerted by the $\sim 1.5 \text{ kpc}$ -long stellar bar. However, in this paper we have shown that in the innermost region of M51 the interplay between AGN, molecular gas and stars becomes very complex. The apparently chaotic response of molecular gas to AGN feedback through radio jets could actually explain the discrepancies between AGN activity and large-scale inflow (for example, the lack of correlation, or only weak correlation, between presence of bars and AGN activity; Knapen et al. 2000; Laine et al. 2002; Cisternas et al. 2013). Overall, this would contribute to limit the amount of gas that can reach the SMBH, and, thus, control the AGN duty cycles. A scenario in which gas can easily make it to the central $\sim 100 \text{ pc}$ through secular evolution mechanisms, but is then trapped in a number of cyclical motions triggered by the omnidirectional pressure from the radio jets is well compatible with our data. It is quite remarkable that the inflow rate estimated in Querejeta et al. (2016) in the central $\sim 3''$ coincides so well with the outflow rate estimated here, $\sim 1 M_{\odot}/\text{yr}$. This could be coincidence, of course, but it could also be reflecting some self-regulating balance between inflow and outflow.

It is worth briefly discussing the uncertainties involved in the outflow rates that we have calculated here. First and foremost, these rates rely on a strong methodological assumption, namely that all the molecular gas observed to have peculiar velocities near the centre is flowing out, and that it is doing so by uniformly filling a multi-conical volume. Judging from what we have seen in Sect. 3.1.3, this hypothesis is highly questionable for M51 (as optical ionised emission does fill an approximate bicone, but CO emission seems to accumulate towards its edges). Additionally, a number of systematic uncertainties are inevitably part of the estimation of outflow rates: the uncertain X_{CO} (which could easily vary by a factor of ~ 2), the range of velocities selected, and the characteristic radius of the outflow, which cannot be easily determined. This means that, all in all, the outflow rate should only be regarded as an approximation to the order of magnitude.

The outflow rate in NGC 1068 ($\sim 60 M_{\odot}/\text{yr}$; García-Burillo et al. 2014) is an order of magnitude higher than our estimation for M51 ($\sim 1 M_{\odot}/\text{yr}$); interestingly, the AGN bolometric luminosity is also one order of magnitude higher. The outflow rate in M51 is closer to that found by Combes et al. (2013) in NGC 1433, $\sim 7 M_{\odot}/\text{yr}$ (for a $L_{\text{bol}} \sim 10^{43} \text{ erg s}^{-1}$); the datapoint for M51 would appear as a lower outlier in the outflow rates–bolometric luminosity compilation from García-Burillo et al. (2015).

Of course, for (much) more active galaxies, such as those observed by Cicone et al. (2014) at intermediate and high redshifts,

the estimated outflow rates can be several orders of magnitude higher than what we find in M51. The question that immediately arises is whether the manifestations of AGN feedback in M51 are intrinsically different from those at play in very active galaxies, or if they are to some extent scaled versions. Specifically, we wonder if our finding that molecular gas seems to be largely depleted in the ionisation cone of M51 is also applicable to active galaxies undergoing powerful outflows. If CO is photoionised in M51, with such a low-luminosity AGN, it seems surprising that CO could survive in galaxies with even more intense nuclear radiation fields. In any case, it would be necessary to spatially resolve more spectacular outflows (with the handicap that they tend to be much more distant) to confirm the tantalising evidence provided by M51 and other nearby galaxies.

5. Summary and conclusions

We have studied AGN feedback effects in a nearby spiral galaxy, M51, which hosts a low-luminosity active nucleus ($L_{\text{bol}} \sim 10^{44}$ erg s $^{-1}$) and a kpc-scale radio jet. The first important conclusion is that *even with such a modest AGN*, the effects of feedback can be significant out to a distance of ~ 500 pc.

The particular spatial configuration of M51 has allowed us to directly witness the interplay between the radio jet and molecular gas, because the galaxy is almost face-on and its radio jet is expanding through the disc, at least in the inner 1 kpc (the jet has an inclination $\sim 15^\circ$ with the plane of the galaxy). The area of the jet where optical ionised lines are detected, the ionisation cone, is largely depleted of molecular gas as traced by CO(1-0) at $1''$ resolution. Instead, CO emission seems to accumulate *towards the edges* of the ionisation cone. This is an important result, as it indicates that molecular gas may not survive under the strong radiation field produced by the AGN, and questions the applicability of (bi)conical outflow models to more distant, unresolved molecular outflows.

We find evidence for multiple components and disturbed kinematics in the molecular gas across the whole extent of the radio plasma jet. This becomes particularly clear when looking at the different kinematic response shown by CO and HCN, tracers of the bulk and dense phases of molecular gas, respectively. Therefore, relative differences between CO and HCN prove to be a useful diagnostic tool when it comes to probing feedback effects from radio jets. Mechanical shocks are the most likely explanation for the observed differences between both tracers. We also find increased turbulence (higher velocity dispersion) in the molecular gas across the whole region covered by the radio jet.

The situation found in M51 is analogous to that recently observed in other nearby galaxies with similarly modest radio jets (e.g. Krause et al. 2007; Morganti et al. 2015), and agrees with numerical simulations of radio jets expanding through a clumpy medium (Wagner & Bicknell 2011; Wagner et al. 2012). Therefore, a new paradigm seems to be emerging, in which feedback through radio jets has complex implications for molecular gas (and, therefore, for star formation), probably pushing it in different directions and increasing its turbulence. It seems that outflows are not the only important consequences of AGN feedback; in addition to potential removal of molecular gas, injecting turbulence and therefore preventing molecular gas from forming new stars is an important part of the AGN response.

Overall, we have shown that the feedback from the AGN in M51 is a multi-scale phenomenon. In addition to the large-scale impact on molecular gas across the radio jet area, the central $5''$ (180 pc) display a more extreme version of feedback, which has

been interpreted as a molecular outflow before (Matsushita et al. 2007). We have estimated the corresponding outflow rates with our data, $\dot{M}_{\text{H}_2} \sim 0.9 M_\odot/\text{yr}$ and $\dot{M}_{\text{dense}} \sim 0.6 M_\odot/\text{yr}$, and discussed geometrical caveats. It is worth noting that the typical velocities of this “outflow” (100 km/s) are well below escape velocity; therefore, this will ultimately also contribute to increase turbulence and recirculate molecular gas in the galaxy, but not really to expel a significant amount of gas from the host.

It would be important to confirm whether similar multi-scale mechanisms operate in more active galaxies, which do indeed have significant amounts of gas at velocities large enough to escape their host. However, this will prove to be observationally challenging, as those very active sources tend to be more distant, and therefore much longer integration times are required to achieve the same sensitivity with current-day interferometers; ALMA and NOEMA should be able to undoubtedly contribute in this direction.

One of the important conclusions from our study is that both high spatial *and spectral* resolution are necessary to obtain a complete picture of feedback effects, as multiple velocity components and kinematic differences between tracers can only be robustly characterised when sufficient velocity resolution is available. In a similar way, we have confirmed that the response of tracers of gas at different densities (CO, HCN) are not redundant, and provide important hints as to what regions are impacted by the radio plasma jets. Therefore, future observations should go in the direction of high-resolution, multi-species observations of active nuclei, probing sufficiently large spatial regions to cover the various spatial effects involved.

References

- Alatalo, K., Blitz, L., Young, L. M., et al. 2011, *ApJ*, 735, 88
 Alatalo, K., Nyland, K., Graves, G., et al. 2014, *ApJ*, 780, 186
 Antonucci, R. 1993, *ARA&A*, 31, 473
 Bae, H.-J. & Woo, J.-H. 2014, *ApJ*, 795, 30
 Blanc, G. A., Heiderman, A., Gebhardt, K., Evans, II, N. J., & Adams, J. 2009, *ApJ*, 704, 842
 Blanc, G. A., Schrubba, A., Evans, II, N. J., et al. 2013, *ApJ*, 764, 117
 Bradley, L. D., Kaiser, M. E., & Baan, W. A. 2004, *ApJ*, 603, 463
 Braithwaite, J. 2010, *MNRAS*, 406, 705
 Cecil, G. 1988, *ApJ*, 329, 38
 Ciardullo, R., Feldmeier, J. J., Jacoby, G. H., et al. 2002, *ApJ*, 577, 31
 Cicone, C., Feruglio, C., Maiolino, R., et al. 2012, *A&A*, 543, A99
 Cicone, C., Maiolino, R., & Marconi, A. 2016, *ArXiv e-prints*
 Cicone, C., Maiolino, R., Sturm, E., et al. 2014, *A&A*, 562, A21
 Cisternas, M., Gadotti, D. A., Knapen, J. H., et al. 2013, *ApJ*, 776, 50
 Colombo, D., Hughes, A., Schinnerer, E., et al. 2014a, *ApJ*, 784, 3
 Colombo, D., Meidt, S. E., Schinnerer, E., et al. 2014b, *ApJ*, 784, 4
 Combes, F., García-Burillo, S., Casasola, V., et al. 2013, *A&A*, 558, A124
 Comerón, S., Knapen, J. H., Beckman, J. E., et al. 2010, *MNRAS*, 402, 2462
 Crane, P. C. & van der Hulst, J. M. 1992, *AJ*, 103, 1146
 Croton, D. J., Springel, V., White, S. D. M., et al. 2006, *MNRAS*, 365, 11
 Dasyra, K. M., Combes, F., Novak, G. S., et al. 2014, *A&A*, 565, A46
 Dumas, G., Schinnerer, E., Tabatabaei, F. S., et al. 2011, *AJ*, 141, 41
 Fabian, A. C. 2012, *ARA&A*, 50, 455
 Fang, L.-L., Jiang, X.-L., He, Z.-C., & Bian, W.-H. 2015, *Research in Astronomy and Astrophysics*, 15, 802
 Fendt, C. & Sheikhnezami, S. 2013, *ApJ*, 774, 12
 Feruglio, C., Fiore, F., Maiolino, R., et al. 2013, *A&A*, 549, A51
 Feruglio, C., Maiolino, R., Piconcelli, E., et al. 2010, *A&A*, 518, L155
 Fruscione, A., McDowell, J. C., Allen, G. E., et al. 2006, in *Proc. SPIE*, Vol. 6270, Society of Photo-Optical Instrumentation Engineers (SPIE) Conference Series, 62701V
 Gao, Y. & Solomon, P. M. 2004, *ApJS*, 152, 63
 García-Burillo, S., Combes, F., Usero, A., et al. 2015, *A&A*, 580, A35
 García-Burillo, S., Combes, F., Usero, A., et al. 2014, *A&A*, 567, A125
 García-Burillo, S., Usero, A., Alonso-Herrero, A., et al. 2012, *A&A*, 539, A8
 Grillmair, C. J., Faber, S. M., Lauer, T. R., et al. 1997, *AJ*, 113, 225
 Hagiwara, Y. 2007, *AJ*, 133, 1176
 Hagiwara, Y. & Edwards, P. G. 2015, *ApJ*, 815, 124
 Ho, L. C., Filippenko, A. V., & Sargent, W. L. W. 1997, *ApJS*, 112, 315

- Israel, F. P. 2009a, A&A, 493, 525
 Israel, F. P. 2009b, A&A, 506, 689
 Józsa, G. I. G., Kenn, F., Klein, U., & Oosterloo, T. A. 2007, A&A, 468, 731
 Kennicutt, Jr., R. C., Calzetti, D., Walter, F., et al. 2007, ApJ, 671, 333
 Kewley, L. J. & Ellison, S. L. 2008, ApJ, 681, 1183
 Knapen, J. H., Shlosman, I., & Peletier, R. F. 2000, ApJ, 529, 93
 Kormendy, J. & Ho, L. C. 2013, ARA&A, 51, 511
 Krause, M., Fendt, C., & Neininger, N. 2007, A&A, 467, 1037
 Laine, S., Shlosman, I., Knapen, J. H., & Peletier, R. F. 2002, ApJ, 567, 97
 Lee, J. H., Kim, S. C., Park, H. S., et al. 2011, ApJ, 740, 42
 Leroy, A. K., Walter, F., Sandstrom, K., et al. 2013, AJ, 146, 19
 Leslie, S. K., Kewley, L. J., Sanders, D. B., & Lee, N. 2016, MNRAS, 455, L82
 Maiolino, R., Gallerani, S., Neri, R., et al. 2012, MNRAS, 425, L66
 Matsushita, S., Muller, S., & Lim, J. 2007, A&A, 468, L49
 Matsushita, S., Sakamoto, K., Kuo, C.-Y., et al. 2004, ApJ, 616, L55
 Matsushita, S., Trung, D.-V., Boone, F., et al. 2015a, Publication of Korean Astronomical Society, 30, 439
 Matsushita, S., Trung, D.-V., Boone, F., et al. 2015b, ApJ, 799, 26
 Meidt, S. E., Schinnerer, E., Garcia-Burillo, S., et al. 2013, ApJ, 779, 45
 Meijerink, R., Kristensen, L. E., Weiß, A., et al. 2013, ApJ, 762, L16
 Morganti, R., Oosterloo, T., Oonk, J. B. R., Frieswijk, W., & Tadhunter, C. 2015, A&A, 580, A1
 Moster, B. P., Somerville, R. S., Maulbetsch, C., et al. 2010, ApJ, 710, 903
 Mutchler, M., Beckwith, S. V. W., Bond, H., et al. 2005, in Bulletin of the American Astronomical Society, Vol. 37, American Astronomical Society Meeting Abstracts #206, 452
 Nyland, K., Alatalo, K., Wrobel, J. M., et al. 2013, ApJ, 779, 173
 Obied, G., Zakamska, N. L., Wylezalek, D., & Liu, G. 2016, MNRAS, 456, 2861
 Pety, J. 2005, in SF2A-2005: Semaine de l'Astrophysique Francaise, ed. F. Casoli, T. Contini, J. M. Hameury, & L. Pagani, 721
 Pety, J., Schinnerer, E., Leroy, A. K., et al. 2013, ApJ, 779, 43
 Querejeta, M., Meidt, S. E., Schinnerer, E., et al. 2015, ApJS, 219, 5
 Querejeta, M., Meidt, S. E., Schinnerer, E., et al. 2016, A&A, 588, A33
 Rampadarath, H., Morgan, J. S., Soria, R., et al. 2015, MNRAS, 452, 32
 Sandstrom, K. M., Leroy, A. K., Walter, F., et al. 2013, ApJ, 777, 5
 Schawinski, K., Koss, M., Berney, S., & Sartori, L. F. 2015, MNRAS, 451, 2517
 Schinnerer, E., Meidt, S. E., Pety, J., et al. 2013, ApJ, 779, 42
 Schirm, M. 2015, PhD thesis, McMaster University
 Schuster, K. F., Kramer, C., Hirschfeld, M., Garcia-Burillo, S., & Mookerjee, B. 2007, A&A, 461, 143
 Scoville, N. Z., Yun, M. S., Armus, L., & Ford, H. 1998, ApJ, 493, L63
 Silk, J. 2013, ApJ, 772, 112
 Somerville, R. S. & Davé, R. 2015, ARA&A, 53, 51
 Spekkens, K. & Sellwood, J. A. 2007, ApJ, 664, 204
 Terashima, Y. & Wilson, A. S. 2001, ApJ, 560, 139
 Tremonti, C. A., Heckman, T. M., Kauffmann, G., et al. 2004, ApJ, 613, 898
 Turner, J. L. & Ho, P. T. P. 1994, ApJ, 421, 122
 van der Werf, P. P., Isaak, K. G., Meijerink, R., et al. 2010, A&A, 518, L42
 Wagner, A. Y. & Bicknell, G. V. 2011, ApJ, 728, 29
 Wagner, A. Y., Bicknell, G. V., & Umemura, M. 2012, ApJ, 757, 136
 Wilson, A. S. 1992, in Physics of Active Galactic Nuclei, ed. W. J. Duschl & S. J. Wagner, 307
 Woo, J.-H. & Urry, C. M. 2002, ApJ, 579, 530

Acknowledgements. Based on observations carried out with the IRAM Interferometer NOEMA. IRAM is supported by INSU/CNRS (France), MPG (Germany) and IGN (Spain). We would like to thank Larry Bradley for kindly providing the data on the ionised outflow in M51 (published in Bradley et al. 2004), and Mark Norris, Brent Groves, and Diederik Kruijssen for helpful suggestions. We acknowledge financial support to the DAGAL network from the People Programme (Marie Curie Actions) of the European Union's Seventh Framework Programme FP7/2007- 2013/ under REA grant agreement number PITN-GA-2011-289313. M.Q. acknowledges the International Max Planck Research School for Astronomy and Cosmic Physics at the University of Heidelberg (IMPRS-HD). S.G.B. thanks support from Spanish grant AYA2012-32295. J.P. acknowledges support from the CNRS programme "Physique et Chimie du Milieu Interstellaire" (PCMI). G.B. is supported by CONICYT/FONDECYT, Programa de Iniciación, Folio 11150220. M.Q., S.E.M., D.C. and A.H. acknowledge funding from the Deutsche Forschungsgemeinschaft (DFG) via grants SCHI 536/7-2, SCHI 536/5-1, and SCHI 536/7-1 as part of the priority program SPP 1573 "ISM-SPP: Physics of the Interstellar Medium."

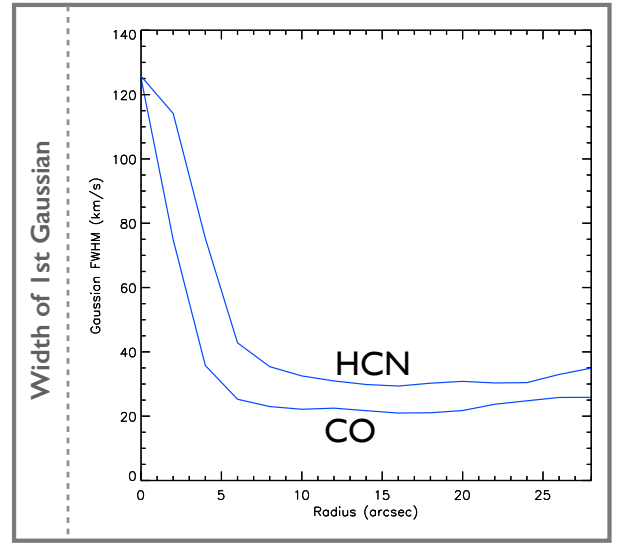


Fig. B.1. Width of the first fitted Gaussian (the one that carries most flux, Sect. 3.2.2) as a function of radius.

Appendix A: Kinematic model of the central region of M51

Here we use a synthetic kinematic model of the CO(1-0) cube of M51 (PAWS at 3'' resolution) to verify that the emission assigned to the first Gaussian does indeed correspond to the disc kinematic component. For that, we have constructed a TiRiFiC model (Józsa et al. 2007) of M51, implementing a differentially rotating disc and an idealised $m = 2$ bar (Spekkens & Sellwood 2007). We start imposing the rotation curve of M51 parametrised by Meidt et al. (2013), and allow for the surface brightness and amplitudes of the $m = 2$ bar to be fitted in radial bins of 3'', out to a radius of $r = 22''$ (where the bar ends; Comerón et al. 2010). Additionally, we allow for the PA and inclination of the disc to vary as a function of radius; this is because the tilted-ring strategy from TiRiFiC assumes a circular disc which projects into ellipses, but, as argued in Querejeta et al. (2016), there seems to be an oval in the central region of M51, probably as the result of the interaction with NGC 5195. Fig. A.1 shows the velocity centroid of the final TiRiFiC model, compared to the velocity centroid from PAWS (at 3'' resolution). We note that the TiRiFiC model becomes meaningless in the inner $\sim 5''$, as the emission is dominated by the molecular outflow, and therefore the amplitudes of the bar in that innermost region cannot be constrained with our dataset; this area is marked with a white dashed circle on Fig. A.1.

The TiRiFiC model confirms that the velocity centroid of our "Disc Gaussian" is in good agreement with the smooth disc-bar velocity model that we have constructed, as shown by the right panel of Fig. A.1. The velocity difference between Gaussian fit and model is typically 5 km/s, and virtually always below 10 km/s (the limits of the green region of the colourbar we use, except in the central $r \lesssim 5''$, as commented above).

Appendix B: Maximum disc contribution in $r \lesssim 5''$

Here we estimate the maximum contribution from a regularly rotating disc component to the molecular emission in the central $\sim 5''$ of M51. Indeed, as we move towards the centre of the galaxy, there is a point at which one can no longer distinguish the Gaussian line associated with the disc from the outflowing component, which becomes more and more dominant in flux (Sect. 3.2.2). This is obvious from Fig. B.1, where it becomes clear that the width of the first fitted Gaussian increases dramatically below $r \lesssim 5''$ ($r \lesssim 7''$ for HCN). In this central region, we estimate the maximum possible contribution from the disc (as illustrated in Fig. B.2) following a simple argument. We assume that the

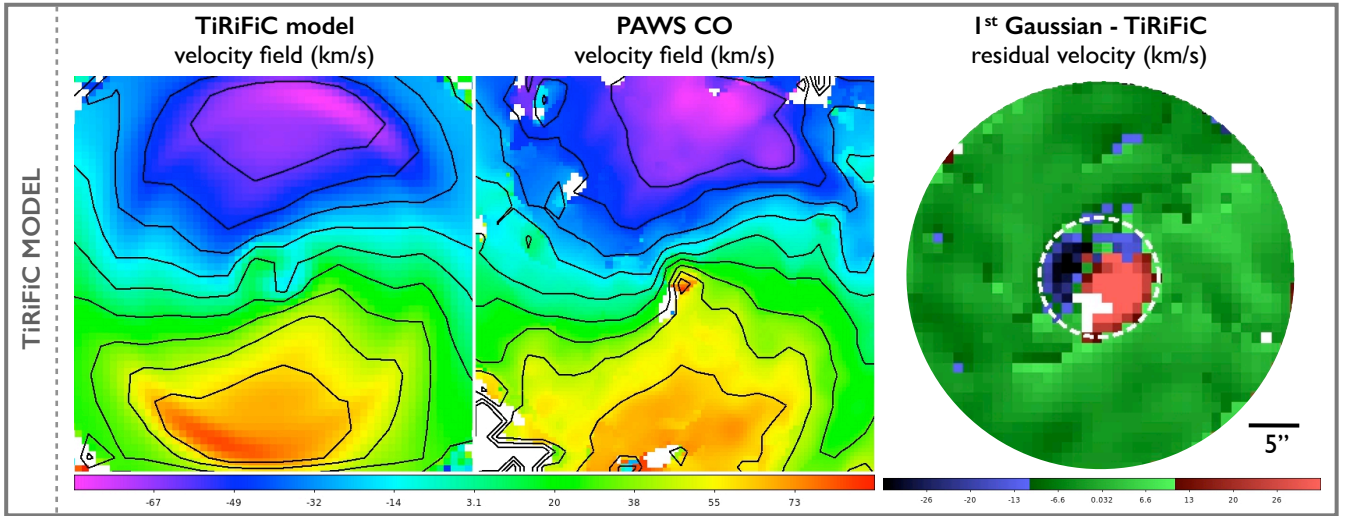


Fig. A.1. Velocity field of our TiRiFiC model compared to the velocity field from PAWS (moment-1, at 3'' resolution). The isovelocity contours correspond to the range [-60 km/s, 60 km/s] in increments of $\Delta v = 15$ km/s. The right panel shows the velocity difference between the first Gaussian fit (Sect. 3.2.2) and the velocity centroid from our TiRiFiC model, highlighting their good agreement except in the central $r \lesssim 5''$.

disc component has approximately the same line width as outside that central region: as we have seen (Fig. B.1), the line width at $r \gtrsim 5''$ is well confined between 20–30 km/s for CO ($r \lesssim 7''$ for HCN, widths in the range 30–40 km/s); therefore, we assume an intermediate characteristic width of 25 km/s for the hypothetical disc contribution in this central area (35 km/s for HCN). Then, we interpolate its velocity centroid linearly in this small region, along 16 different azimuthal regions, starting from the average value in the immediate vicinity (at $r = 5''$ or $r = 7''$), and imposing that the central position must coincide with the systemic velocity of the galaxy ($v_{\text{sys}} = 472$ km/s). We have confirmed that varying the number of azimuthal zones or extending the maximum radius out to which we interpolate does not affect the velocity centroids significantly ($\Delta v \lesssim 5$ km/s). The peak of this Gaussian is given by the maximum height allowed by the actual line profile at the interpolated velocity centroid (Fig. B.2). The flux of this interpolated Gaussian is assigned, as an upper limit, to the first Gaussian (“disc”), and the remaining flux, as a lower limit, to the second Gaussian (“outflow”).

Appendix C: Outflow Geometry

The angle α that is part of the formula to calculate the outflow rate (Eq. 3.3.1) is well-constrained for M51. From careful modelling of the observed kinematics in the southern XNC, Cecil (1988) concluded that the shock working surface that they analyse is inclined $\sim 20^\circ$ to the line of sight. This result is robust, in any case well-bounded between 20° and 25° , and compatible with a number of additional constraints (disc scale-height, observed velocities, etc.). It is important to emphasise, though, that to our best knowledge there is no compelling reason to assume that the southern cone is near us, as we discuss in Sect. 3.1, Sect. 4.2. In any case this implies that, if the axis of the jet is perpendicular to the shock working surface, as expected, the angle between the jet and the line of sight must be 70° .

We are now in a position to deproject this value (and assess uncertainties) and provide the true value of the inclination of the jet with respect to the plane of the disc. The scalar product of a (unitary) vector pointing along the axis of the jet and a (unitary) vector normal to the plane of the galaxy is:

$$\mathbf{j} \cdot \mathbf{n} = \begin{pmatrix} \cos \alpha \\ \sin \alpha \cos \phi \\ -\sin \alpha \sin \phi \end{pmatrix} \begin{pmatrix} \cos i \\ 0 \\ \sin i \end{pmatrix} = \sin \xi \quad (\text{C.1})$$

For the geometry assumed in Fig. 1 (corresponding to the orientation of M51), where α is the (smallest) angle between the jet and the line of sight, ϕ is the *projected* azimuthal angle between the jet axis and the line of nodes, and i is the inclination of the galaxy with respect to the line of sight ($i = 0$ for face-on), and ξ is the (smallest) angle between the jet axis and the plane of the galaxy (from the definition of scalar product, $\mathbf{j} \cdot \mathbf{n} = |\mathbf{j}| |\mathbf{n}| \cos \hat{jn}$, with $\hat{jn} = 90^\circ - \xi$). In the case of M51, adopting the orientation of the jet measured by Bradley et al. (2004) (PA = 163° , with a projected opening angle of 74°), and the inclination of the galaxy determined by PAWS (Colombo et al. 2014b) this expression reduces to:

$$\mathbf{j} \cdot \mathbf{n} = \begin{pmatrix} \cos(70^\circ) \\ \sin(70^\circ) \cos(10^\circ) \\ -\sin(70^\circ) \sin(10^\circ) \end{pmatrix} \begin{pmatrix} \cos(22^\circ) \\ 0 \\ \sin(22^\circ) \end{pmatrix} = \sin \xi \quad (\text{C.2})$$

Which implies an angle of 15° between the jet and the plane of the galaxy. As a sanity check, we can make use of the gaseous disc scale-heights measured by Pety et al. (2013) and the extent of the narrow-line emission clearly associated with the biconic jet (Bradley et al. 2004) to obtain an independent estimation of the angle between the outflow and the plane of the galaxy. We assume that the narrow-line emission comes from the interaction between radio jet and thin gaseous disc, roughly extending vertically up to the scale-height of the molecular gas traced by PdBI at that radius. In the maps from Bradley et al. (2004), both the radio emission and the NLR emission closely follow a (projected) biconic geometry, and drop off quite sharply at a (projected) radius of $4''$. This corresponds to a (deprojected) radius of 148 pc, and at this radius, the scale-height of the thin disc is ~ 35 pc. If the limit of the NLR and radio continuum correspond to this scale-height, this would imply an angle of 13° , in good agreement with the value of 15° implied by Cecil (1988). This is also in agreement with the fact that M51 is a Seyfert 2 galaxy; thus, the inclination of the jet could not be much higher or we would, otherwise, see the broad line region.

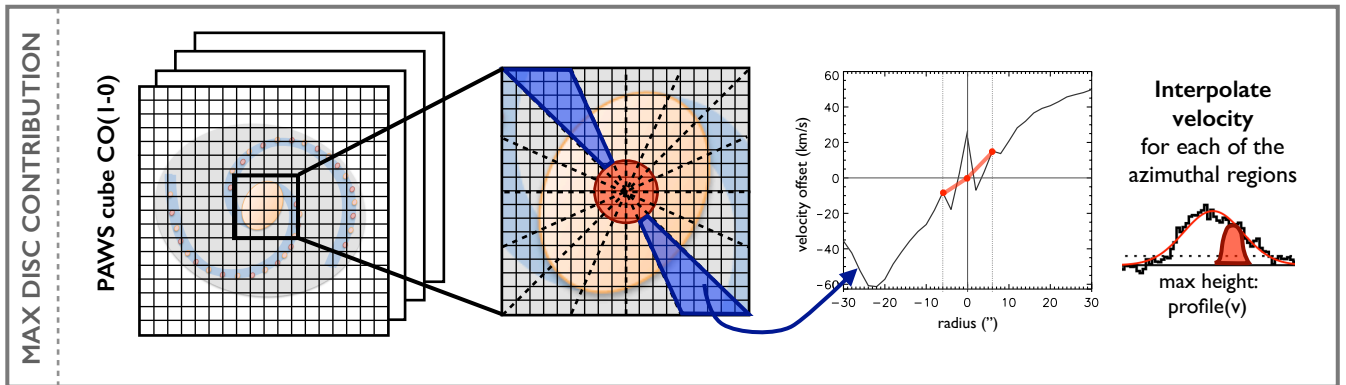


Fig. B.2. In the central $r \lesssim 5''$ it becomes extremely hard to separate a line associated with the disc from the extremely broad outflowing component that dominates its flux. This is a visual illustration of how we estimate the maximum emission from disc, assuming that its emission line has the same width as in the rest of the disc, ~ 25 km/s, and that its velocity centroid can be linearly interpolated in this small region from the surroundings. We perform this interpolation along 16 different azimuthal regions, forcing the central position to coincide with the systemic velocity, 472 km/s.

Chapter 5

Making discs passive with major mergers: photometry

In this chapter we use numerical simulations to show that major mergers of spiral galaxies can result in lenticular galaxies, in agreement with photometric observations. While discs are initially destroyed by the merging process, the debris from the collision settles into a disc shortly (~ 1 Gyr) after the full merger. The resulting lenticular systems follow the observed photometric scaling relations of real lenticulars, and even host pseudo-bulges. Therefore, major mergers are viable candidates to make discs passive, rapidly suppressing star formation. This work has been published in *Astronomy & Astrophysics*, 573, 78 (Querejeta et al. 2015a).

Formation of S0 galaxies through mergers[★]

Bulge-disc structural coupling resulting from major mergers

M. Querejeta^{1,2}, M. C. Eliche-Moral², T. Tapia³, A. Borlaff², C. Rodríguez-Pérez², J. Zamorano², and J. Gallego²

¹ Max Planck Institute for Astronomy, Königstuhl 17, 69117 Heidelberg, Germany
 e-mail: querejeta@mpia-hd.mpg.de

² Departamento de Astrofísica y Ciencias de la Atmósfera, Universidad Complutense de Madrid, 28040 Madrid, Spain

³ Instituto de Astrofísica de Canarias, C/ Vía Láctea, 38200 La Laguna, Tenerife, Spain

Received 29 May 2014 / Accepted 15 September 2014

ABSTRACT

Context. Observations reveal a strong structural coupling between bulge and disc in S0 galaxies, which seems difficult to explain if they have formed from supposedly catastrophic events such as major mergers.

Aims. We face this question by quantifying the bulge-disc coupling in dissipative simulations of major and minor mergers that result in realistic S0s.

Methods. We have studied the dissipative N -body binary merger simulations from the GalMer database that give rise to realistic, relaxed E/S0 and S0 remnants (67 major and 29 minor mergers). We simulate surface brightness profiles of these S0-like remnants in the K band, mimicking typical observational conditions, to perform bulge-disc decompositions analogous to those carried out in real S0s. Additional components have been included when needed. The global bulge-disc structure of these remnants has been compared with real data.

Results. The S0-like remnants distribute in the $B/T - r_e - h_d$ parameter space consistently with real bright S0s, where B/T is the bulge-to-total luminosity ratio, r_e is the bulge effective radius, and h_d is the disc scalelength. Major mergers can rebuild a bulge-disc coupling in the remnants after having destroyed the structures of the progenitors, whereas minor mergers directly preserve them. Remnants exhibit B/T and r_e/h_d spanning a wide range of values, and their distribution is consistent with observations. Many remnants have bulge Sérsic indices ranging $1 < n < 2$, flat appearance, and contain residual star formation in embedded discs, a result which agrees with the presence of pseudobulges in real S0s.

Conclusions. Contrary to the popular view, mergers (and in particular, major events) can result in S0 remnants with realistically coupled bulge-disc structures in less than ~ 3 Gyr. The bulge-disc coupling and the presence of pseudobulges in real S0s cannot be used as an argument against the possible major-merger origin of these galaxies.

Key words. galaxies: bulges – galaxies: evolution – galaxies: formation – galaxies: interactions – galaxies: structure

1. Introduction

Traditionally regarded as a transition class between ellipticals and spirals, S0 galaxies have deserved relatively marginal attention for decades, but have recently made their way to centre stage in the context of astronomical research. It was Hubble (1936) who classified these lentil-shaped passive galaxies (lenticulars) as some kind of primordial spirals devoid of spiral arms and star formation; therefore, in his well-known tuning-fork diagram S0s are depicted in between elliptical and spiral galaxies. As part of an increasing interest in these astronomical objects, three independent studies have drawn attention to the fact that lenticulars constitute a heterogeneous family of galaxies, with structural and rotational properties more similar to those of spirals than to ellipticals (see Laurikainen et al. 2010; Cappellari et al. 2011; Kormendy & Bender 2012).

Strenuous effort has been devoted in the last few decades, via observations and modelling, to try to understand the processes that give rise to and transform these galaxies. In any case, there are observational constraints that any evolutionary mechanisms should preserve. Laurikainen et al. (2010, L10 hereafter) have

recently studied the photometric scaling relations in a sample of 175 early-type galaxies containing almost 120 S0s. They have found noticeable correlations between the bulge and disc photometric parameters in S0s (in particular, between their scalelengths and magnitudes), clearly pointing to a strong bulge-disc structural coupling in these galaxies. This result imposes a strong constraint to any mechanisms that try to explain the origin and evolution of lenticulars.

Observations support the idea that gas stripping due to ram pressure in clusters can effectively transform spirals into S0s (Crowl et al. 2005; Crowl & Kenney 2006, 2008; Rasmussen et al. 2008; Vollmer et al. 2008, 2009, 2012; Sivanandam et al. 2010; Million et al. 2010; Abramson et al. 2011). If we also consider that the fraction of lenticular galaxies decreases with redshift, whereas the fraction of spirals increases, it is tempting to conclude that lenticulars come out of spirals which have had their gas stolen (see e.g. Aragón-Salamanca et al. 2006).

Nevertheless, according to Wilman et al. (2009), S0s are at least as common in groups as they are in clusters, and clearly more common in groups than in the less dense field. Moreover, cluster S0s are usually located within groups in the cluster, and usually exhibit traces of past mergers (Rudick et al. 2009, 2010; Janowiecki et al. 2010; Mihos et al. 2013). The dominant galaxy

[★] Table 3 is available in electronic form at <http://www.aanda.org>

evolution mechanisms in groups are tidal interactions and mergers (Mazzei et al. 2014a,b), so the gas stripping mechanism can only account for the origin of a fraction of S0s.

Similarly, internal secular evolution is often invoked to explain how S0s emerge out of spirals. This is supported by the fact that many S0s host pseudobulges (Laurikainen et al. 2006; Graham 2013, L10) i.e. bulges with bulge-to-total luminosity ratios and concentrations typical of late-type spiral galaxies ($B/T < 0.2$ and $n \sim 1$), which often contain embedded discs, inner spiral patterns, nuclear bars, some star formation, and which present rotational support more similar to spiral galaxies than to classical bulges (see Kormendy & Kennicutt 2004). These properties seem incompatible with the smooth spheroidal structure that usually results from major merger events. So, they are usually attributed to the evolution induced by bars and other internal components in the galaxies, which direct material towards the centre, enhancing the bulge component (Pfenniger & Norman 1990). However, the bulges that emerge out of gas-free bar models do not show concentrations and sizes compatible with the parameters observed in real S0s (see the comparison in Eliche-Moral et al. 2012, 2013, EM12 and EM13 henceforth).

Current hierarchical models of galaxy formation assume that the bulges of S0s formed by means of a major merger of early discs or by a sequence of minor merger events, followed by a later disc rebuilding out of the left-over gas and stripped stars (Somerville & Primack 1999). This scenario seems compatible with the fact that most S0s reside in groups and with observations reporting merging relics in many S0s (see references above and in EM12).

Concerning the minor merger mechanism (mass ratios above 7:1), these are known to induce gentle transformations to the global structure of the progenitor (Aguerre et al. 2001; Eliche-Moral et al. 2006, 2011; Moster et al. 2010). In fact, recent simulations of gas-free intermediate and minor mergers onto S0s show that these events can preserve or even enhance the structural bulge-disc coupling by triggering internal secular evolution in the surviving disc (EM12; EM13). So, in principle, minor mergers are consistent with bulge-disc coupling.

On the contrary, the bulges and discs of S0s formed through major mergers (mass ratios below 4:1) are expected to be structurally decoupled, as the encounters must destroy the original structure of the progenitors, rebuilding the remnant bulges and discs through independent processes (bulges from the merger and discs from later material reaccretion). This expected bulge-disc decoupling in major mergers directly contradicts the observations of nearby S0s commented above (see Laurikainen et al. 2009, L10). Nevertheless, recent observational and theoretical studies support the idea that major mergers must have been relevant for the evolution of present-day massive E-S0s since $z \sim 1.5-2$ (Eliche-Moral et al. 2010a,b; Bernardi et al. 2011a,b; Tirit et al. 2011; Weinzirl et al. 2011; Prieto et al. 2013). Therefore, the question is whether this popular view of major mergers as catastrophic events that destroy any bulge-disc coupling in a galaxy is realistic or not. Recent studies show that discs can survive even 1:1 mergers, mostly depending on the initial gas content (Hopkins et al. 2009), but whether major mergers can account for the bulge-disc structural coupling observed in real S0s has not yet been explored.

We address this question using N -body dissipative simulations of major galaxy mergers provided by the GalMer project (Chilingarian et al. 2010). We have also analysed the minor merger simulations onto an S0 progenitor available in the database. These simulations consider different morphological types and mass ratios for the colliding galaxies, covering a wide

range of orbital parameters. We have identified the encounters that end up in relaxed remnants with realistic S0-like morphology, to determine whether the photometric structures of these merger-built S0s are compatible with those observed for real S0s or not. In a forthcoming paper (Querejeta et al., in prep.), we will analyse in detail whether our S0 remnants can additionally reproduce the photometric scaling relations reported by L10 for real S0s.

A brief description of the models is presented in Sect. 2. The methodological approach is summarised in Sect. 3. In Sect. 3.1 we explain the criteria used to identify what encounters result in E/S0 or S0 galaxies. Then, we simulate realistic 1D surface brightness profiles of the remnants in the K band and perform multi-component decompositions (Sects. 3.2 and 3.3). In Sect. 4, we compare the characteristic photometric parameters of the bulges and discs derived from the decompositions of the S0-like remnants with the parameters of real S0s. Model limitations are commented in Sect. 5. The discussion and final conclusions derived from this study are presented in Sects. 6 and 7, respectively. We assume a concordance cosmology ($\Omega_M = 0.3$, $\Omega_\Lambda = 0.7$, $H_0 = 70 \text{ km s}^{-1} \text{ Mpc}^{-1}$, see Spergel et al. 2007), and magnitudes are provided in the Vega system.

2. Description of models

Part of the HORIZON collaboration, GalMer¹ is a public database containing ~ 1000 hydrodynamic N -body simulations of galaxy mergers with intermediate resolution, sampling various mass ratios, morphological properties of the progenitors, and orbital characteristics. The project and the database are thoroughly described in Chilingarian et al. (2010), so we will just provide a brief summary here.

A representative sample of galaxy morphologies is considered, ranging from giants to dwarfs (g , i , d) and from ellipticals to spirals (E0, S0, Sa, Sb, Sd). The orbits differ in the relative orientation of the spins of the progenitors with respect to the orbital angular momentum, the pericentral distance, and the initial motion energy. The stellar mass ratios of the encounters range from 1:1 to 20:1 depending on the progenitors (see Table 1). Up to date, the database contains 876 giant-giant interactions and 126 gS0-dwarf encounters. As we are interested in S0-like remnants, we have initially considered all the merger experiments within the database as possible candidates to give rise to an E/S0 or S0. We will comment on the selection of the dynamically relaxed S0-like remnants in Sect. 3.1.

The progenitor galaxies are modelled using spherical non-rotating dark-matter haloes, with optional stellar and gaseous discs, and central non-rotating bulges. The E0 progenitor lacks any stellar or gaseous discs, the S0 initial model does not have a gaseous disc, and the Sd progenitor is bulgeless. The bulge-to-disc ratios are 2.0, 0.7, and 0.4 for the S0, Sa, and Sb progenitors, respectively; the ratio of dark to baryonic matter ranges from 0.43 (gE) to 3 (gSd). Haloes and bulges are constructed using Plummer spheres with characteristic mass and radius M_{Bulge} and r_{Bulge} for the bulge and M_{Halo} and r_{Halo} for the dark matter halo, as indicated in Table 2. The discs follow Miyamoto & Nagai (1975) density profiles, with masses and vertical and radial scalelengths as described in the same Table. The total number of particles is 120 000 for each giant galaxy and 48 000 for the dwarfs, distributed among each galaxy component depending on the morphology, except for the gS0 progenitor, which has

¹ GalMer project: <http://galmer.obspm.fr>

M. Querejeta et al.: Bulge-disc structural coupling in S0s resulting from major mergers

Table 1. Mass ratios of the GalMer merger experiments.

		Major mergers (giant – giant)				
Type 1	Type 2	gE0	gS0	gSa	gSb	gSd
gE0		1:1	–	1.5:1	3:1	3:1
gSa		–	–	1:1	2:1	2:1
gSb		–	–	–	1:1	1:1
gSd		–	–	–	–	1:1
		Minor mergers (gS0 – dwarf)				
Type 1	Type 2	dE0	dS0	dSa	dSb	dSd
gS0		7:1	10:1	10:1	20:1	20:1

Notes. The present study has considered all merger simulations available from the GalMer database up to February 2014 (876 major events and 126 minor ones, 1002 experiments in total). The stellar mass ratios of the encounters depend on the morphological type of the progenitors, as indicated in this table.

480 000 particles. This means that we have a total of 240 000 particles in the major merger experiments and 528 000 in minor merger ones (see Table 2). The gS0 progenitor is barred at the start of the simulation, whereas the other giant progenitors are not. Total stellar masses in the giant progenitors range $\sim 0.5\text{--}1.5 \times 10^{11} M_{\odot}$. Therefore, the final stellar mass of the remnants ranges between $\sim 1\text{--}3 \times 10^{11} M_{\odot}$ in the major mergers and $\sim 1.2\text{--}1.3 \times 10^{11} M_{\odot}$ in the minor ones, depending on the efficiency of the star formation induced by the encounter and on the masses of the progenitors. This will be relevant when comparing to real data in Sect. 4.

The simulations make use of a TreeSPH technique, using the code described in Semelin & Combes (2002). Gravitational forces are calculated using a hierarchical tree method (Barnes & Hut 1986), the resulting forces are then softened to a Plummer potential, and finally use smooth particle hydrodynamics to follow gas evolution (Lucy 1977; Gingold & Monaghan 1982). The softening length is fixed to $\epsilon = 280$ pc in the giant-giant encounters, and to $\epsilon = 200$ pc in giant-dwarf runs. All experiments have been evolved for a total time period of 2.95–3.50 Gyr.

One of the most important features of these simulations is that they take into account the effects of gas and star formation. Gas is modelled as isothermal ($T_{\text{gas}} = 10^4$ K), and star formation is implemented using the method described in Mihos & Hernquist (1994): a prescription for the star formation rate (SFR) is first defined, assuming the Schmidt-Kennicutt law, and then the formation of stars out of the gaseous component is implemented via hybrid particles, which contain a gas and stellar fraction that vary with time (depending on the conditions in the surroundings). Enrichment of the interstellar medium (ISM), stellar mass loss, metallicity changes, and energy injection out of supernova explosions are also considered.

For each combination of progenitors, a wide set of orbits is sampled. The initial distance between galaxies is always set equal to 100 kpc, but initial velocity is allowed to take up the discrete values 200, 300, 370 and 580 km s^{-1} . Secondly, for each case, both retrograde and prograde orbits are taken into account. Orbits with different pericentre distances are also simulated (8, 16, and 24 kpc). Finally, six possible values of inclination are considered: $i = 0, 33, 45, 60, 75, \text{ and } 90^{\circ}$.

We refer to the simulations using a notation that aims to make the initial conditions of the encounter explicit. We first refer to the morphology of the primary galaxy, followed by the

morphology of the secondary (g, i, d for giant, intermediate and dwarf; E0, S0, Sa, Sb, Sd for the corresponding Hubble types); then an “o” followed by the numerical identifier of the orbit used in the GalMer database, which is unique for each combination of orbital parameters under consideration. For example, gS0dSao6 means that a dwarf Sa (galaxy 2) is accreted by a giant S0 (galaxy 1), following the orbit identified as number 6 in the database (i.e. the one with an orbital inclination of 33° , pericentre of 16 kpc, initial motion energy of $2.5 \times 10^4 \text{ km}^2 \text{ s}^{-2}$, and retrograde spin-orbit coupling).

The GalMer database provides the simulations in FITS binary tables, one per stored time step of the total computed time period (intervals of 50 Myr are considered). The tables contain the mass, position, velocity, and other relevant properties for each particle in the simulation at each time. Figure 1 represents the time evolution of the stellar and gaseous component of the accretion of a dwarf Sb by a giant S0 galaxy, obtained using the snapshots previewer of the GalMer database.

We stress that the GalMer database only contained giant – giant major merger encounters and minor mergers over a giant S0 progenitor when the present study was carried out.

3. Methodology

We have first identified all the merger simulations that end up in a dynamically-relaxed remnant with morphology, structure, kinematics, SFRs and gas content typical of E/S0 and S0 galaxies (S0-like galaxies hereafter). The selection of the sample of S0-like relaxed remnants will be presented in detail in Eliche-Moral et al. (in prep.), so we only provide a short summary in Sect. 3.1.

We have simulated realistic surface brightness profiles in the K band for these S0-like relaxed remnants, mimicking the observing conditions of recent samples of nearby S0s with which we have compared the products of our merger simulations (see Sect. 3.2). We then worked out structural decompositions for such remnants (Sect. 3.3), to ultimately perform a detailed comparison of the resulting photometric parameters with those obtained for real galaxies (Sect. 4). This will allow us to assess whether a major merger origin of S0s is compatible with the observational constraints imposed by real S0 data or not. We have also included in this analysis the relaxed S0 remnants resulting from the minor merger experiments available from the GalMer database (gS0 – dwarf encounters).

3.1. Identification of S0 remnants

3.1.1. Preselection of relaxed, apparently disc-like remnants

From the initial sample of 1002 merger simulations available from GalMer, we rejected all merger experiments that do not result in a one-body remnant at the end of the simulation. Using the previewer of the database, three co-authors independently identified visually the models that resulted in final stellar remnants with disc components and apparently relaxed morphologies. A total of 215 major merger experiments and 72 minor merger ones were selected as candidates to give rise to relaxed S0 remnants at the end of the simulation. We then determined which remnants have really reached a relaxed dynamical state, obtaining two final subsamples of 173 major merger and 29 minor merger models. Time periods from full merger to the end of the simulation range between ~ 1 and ~ 2 Gyr.

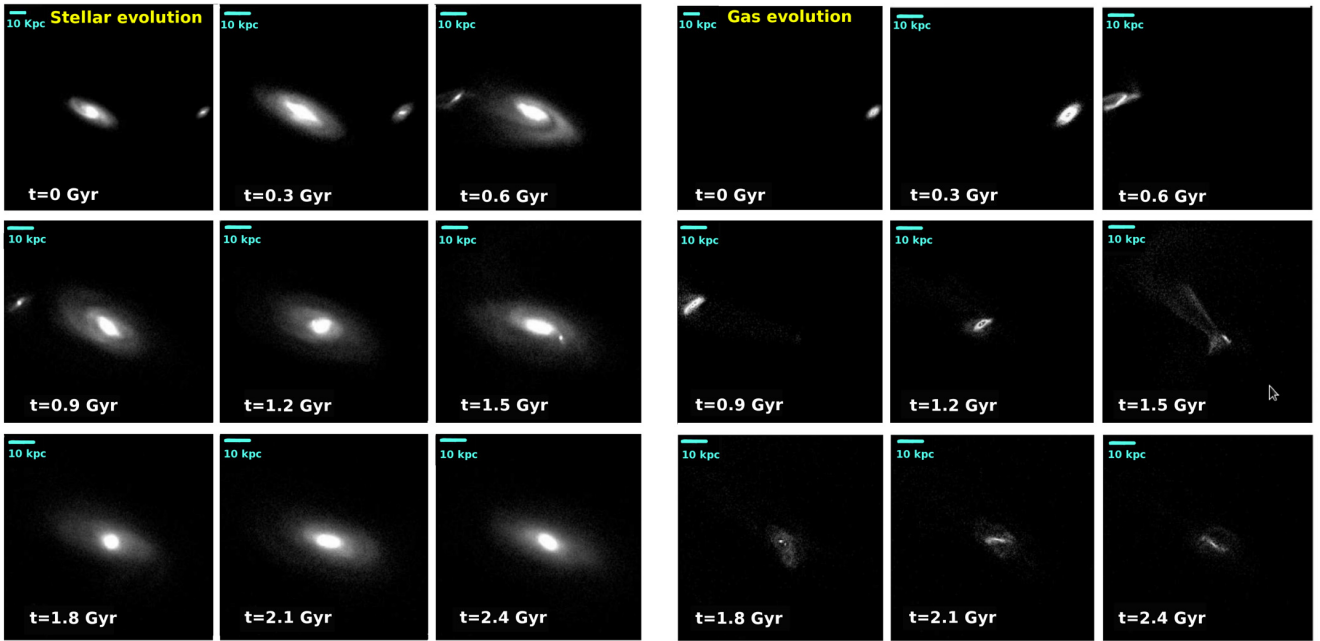


Fig. 1. Time evolution of the stellar and gaseous material in the minor merger model gS0dSbo99 (left and right panels, respectively). Time is shown at the bottom left corner of each frame. At each snapshot, the line of sight has been set to $\theta = 30^\circ$ and $\phi = -90^\circ$ and nearly centred on the giant S0. The field of view has been increased in the frames corresponding to $t = 0$ to show the original location of the dSb satellite. In this experiment, only the dwarf galaxy contains gas at the start of the simulation. This simulation has been run for a total period of 3 Gyr. The snapshots have been obtained with the previewer of the GalMer database.

Table 2. Masses, scalelengths, scaleheights, and number of particles of the different components in the progenitor galaxies.

Characteristic parameters	gE0	gS0	gSa	gSb	gSd	dE0	dS0	dSa	dSb	dSd
(a) $M_{\text{Bulge}} [2.3 \times 10^9 M_\odot]$	70	10	10	5	0	7	1	1	0.5	0
$M_{\text{Halo}} [2.3 \times 10^9 M_\odot]$	30	50	50	75	75	3	5	5	7.5	7.5
$r_{\text{Bulge}} [\text{kpc}]$	4	2	2	1	–	1.3	0.6	0.6	0.3	–
$r_{\text{Halo}} [\text{kpc}]$	7	10	10	12	15	2.2	3.2	3.2	3.8	4.7
(b) $M_{\star, \text{Disc}} [2.3 \times 10^9 M_\odot]$	0	40	40	20	25	0	4	4	2	2.5
$M_{\text{g, Disc}} / M_{\star, \text{Disc}}$	0	0	0.1	0.2	0.3	0	0	0.1	0.2	0.3
$a_{\star, \text{Disc}} [\text{kpc}]$	–	4	4	5	6	–	1.3	1.3	1.6	1.9
$h_{\star, \text{Disc}} [\text{kpc}]$	–	0.5	0.5	0.5	0.5	–	0.16	0.16	0.16	0.16
$a_{\text{g, Disc}} [\text{kpc}]$	–	–	5	6	7	–	–	1.6	1.9	2.2
$h_{\text{g, Disc}} [\text{kpc}]$	–	–	0.2	0.2	0.2	–	–	0.06	0.06	0.06
(c) N_{hybrid}	–	–	20 000	40 000	60 000	–	–	8000	16 000	24 000
N_{stellar}	80 000	320 000	60 000	40 000	20 000	32 000	32 000	24 000	16 000	8000
N_{DM}	40 000	160 000	40 000	40 000	40 000	16 000	16 000	16 000	16 000	16 000

Notes. Rows: (a) Plummer sphere parameters used to model the bulges and haloes of the progenitor galaxies, as a function of the considered morphological types: M_{Bulge} is the (stellar) mass of the bulge, M_{Halo} is the total mass of the dark matter halo, while r_{Bulge} and r_{Halo} are their corresponding effective radii. (b) Parameters of the Miyamoto-Nagai density profiles used to model the gaseous and stellar discs of the different progenitors: the sub-index \star denotes the stellar disc, and the sub-index g refers to the gaseous disc, M is mass, a is effective radius, and h is the vertical scalelength. (c) Number of hybrid particles (initially fully gaseous), collisionless stellar particles, and dark matter particles used for each progenitor galaxy.

3.1.2. Simulation of realistic images of the remnants

Visual classification has proven to be more reliable than quantitative criteria when it comes to identifying faint structures (such as external discs or spirals, see Abraham et al. 1999; Bamford et al. 2009), so we have performed a visual morphological

classification of the final remnants. Our intention was to make sure that we have selected the remnants that would be classified as E/S0 or S0 types by observers, to incur a fair comparison with real data. Therefore, we simulated realistic photometric images of the remnants in several broad bands (B , V , R , I , and K) mimicking mean properties of current observational surveys of

M. Querejeta et al.: Bulge-disc structural coupling in S0s resulting from major mergers

nearby galaxies, and then classify them morphologically attending to these images. In Eliche-Moral et al. (in prep.), we show several examples of how relevant accounting for the observational effects is to distinguish between E and S0 remnants.

The stellar mass of each particle ($\sim(3.5-20.0) \times 10^5 M_\odot$) was converted into light flux in the different photometric bands considering the M/L ratio in the band of a stellar population with the average age and metallicity of the stellar content within the particle at each time. We considered star formation histories (SFH) characteristic of each morphological type according to observations, and using the stellar population synthesis models by Bruzual & Charlot (2003). A Chabrier initial mass function and the Padova 1994 evolutionary tracks have been used (Bertelli et al. 1994).

For the collisionless stellar particles, we have assumed SFHs that are characteristic of real galaxies of the same morphological type as the progenitor that initially hosted the particle (E, S0, Sa, Sb, or Sd), according to the parametrisations described in Eliche-Moral et al. (2010a). Old stellar particles do not have an assigned age in the GalMer simulations, so we have assumed the typical age of the old stellar population located in the outer discs of nearby S0 galaxies (~ 10 Gyr, see Sil'chenko et al. 2012; Sil'chenko 2013), independently of the type of the progenitor the particle initially belonged to. The SFH experienced by the hybrid particles is different for each particle. We have approximated the SFH of each one by a simple stellar population model (SSP) with the average age and metallicity of the mass in stars contained in the particle.

We have also simulated the effects of the typical observing conditions of current surveys of nearby S0 galaxies in our photometric images, mimicking their characteristic limiting magnitudes, signal-to-noise, spatial resolution, and seeing values in each band. We have added photonic noise considering that the limiting magnitude in each band corresponds to $S/N = 3$ in the reference observational samples. A distance of 30 Mpc has been considered to all our remnants, as it is the average distance of the S0 galaxies within the Near-InfraRed S0 Survey² (NIRS0S; Laurikainen et al. 2011), which is the reference observational sample that we will base our comparisons on (see Sect. 4). Assuming this distance, we have transformed intrinsic physical lengths in the remnants into sky projected angular ones and we have implemented the effects of the cosmological dimming, assuming a concordance Λ CDM cosmology. We have not simulated dust extinction effects in these artificial images.

3.1.3. Visual identification of S0-like remnants

It is often difficult to distinguish between ellipticals and face-on lenticulars, due to the absence of prominent spiral arms; in such cases, only a break in the surface-brightness gradient can allow us to conclude that we are dealing with an S0 (Wilman et al. 2009). Therefore, we have simulated images in each band for face-on and edge-on views to make the identification of S0s easier. By assumption, the face-on view of each remnant corresponds to the direction of the total angular momentum of its baryonic material. We have defined the edge-on view as the perpendicular direction contained in the XY plane of the original coordinates system of the simulation. Some examples of the artificial face-on and edge-on images in the K band for some remnants are shown in Fig. 2.

The classification was performed visually by five co-authors independently. The morphological type assigned to each remnant is the median value of the five classifications. A complete agreement between all classifiers was obtained in 85% of the major merger remnants, ensuring the robustness of the classification. In the sample of 173 relaxed major merger remnants with possible detectable discs, we finally identified 106 Es, 25 E/S0s, and 42 S0s, which correspond to the following percentages: 61.3% of Es, 14.4% of E/S0, and 24.3% of S0s. We note that the elliptical galaxies in this subsample harbour a disc component detectable in their density maps, but not in realistic broad band images. All remnants from the minor merger simulations (gS0 – dwarf encounters) are still S0s after the encounter, according to all co-authors.

The morphology of the remnants has been analysed in detail. None of the S0-like major-merger remnants exhibits a strong bar. All minor mergers result in barred galaxies, but the progenitor gS0 has already a strong bar at the start of the simulation. The E/S0 and S0 remnants usually have lenses, ovals, and inner discs detectable in the images. We confirmed the morphological classification by analysing realistic simulations of their 1D surface brightness profiles in the V , R , and K bands (for more information, see Sect. 3.2). All of them presented clear bulge-disc structures. We have also derived the final rotational support, SFRs and final gas content of these S0-like remnants, and we have compared them to typical values measured in real S0s. We find remnants to be consistent with S0s also according to these properties.

Our S0-like remnants have a median ($B - R$) colour of ~ 0.9 , whereas local ETGs of similar masses typically have ($B - R$) colours of ~ 1.5 (Bell & de Jong 2001). This difference in the ($B - R$) colour is due to the youth of the starbursts induced by the encounters in the centres of the remnants. This makes the average K -band M/L ratios used in our models to be ~ 2 times smaller than the typical ones in quiescent early-type galaxies, and thus our remnants are ~ 1 mag brighter in K -band than real S0s with similar stellar masses. In any case, blue central structures are quite common in nearby E-S0 (in fact, they are usually considered as evidence of recent merging, see Kannappan et al. 2009; Huertas-Company et al. 2010; Wei et al. 2010), and the remnants would exhibit analogous colours to those observed in present-day S0s with $\sim 1-2$ Gyr of additional passive evolution. There are other sources of uncertainty in the determination of the M/L ratios used in the models, which are inherent to the assumptions adopted to estimate them, such as the age assigned to the collisionless stellar particles, the SFHs, or the considered IMF. We will take this into account for the interpretation of the results in Sect. 4.

3.2. Simulation of realistic surface brightness profiles

3.2.1. Simulating the conditions of NIRS0S

We have simulated realistic surface brightness profiles of our S0-like remnants reproducing the typical observing conditions in the photometric band of the NIRS0S data, in order to compare the parameters of the bulges and discs in our remnants with those exhibited by real S0 galaxies contained in that sample (L10).

The K -band images in NIRS0S have an average depth of $\mu_K \sim 22$ mag arcsec⁻² for a limiting signal-to-noise ratio of $S/N = 3$. We have adopted this limiting surface brightness for the same S/N to simulate the surface brightness profiles. The projected spatial resolution has been set to the average of NIRS0S data ($\sim 0.7''$). It is equivalent to ~ 100 pc for the distance

² More information on NIRS0S available at: <http://www.oulu.fi/astronomy/nirs0s/>

A&A 573, A78 (2015)

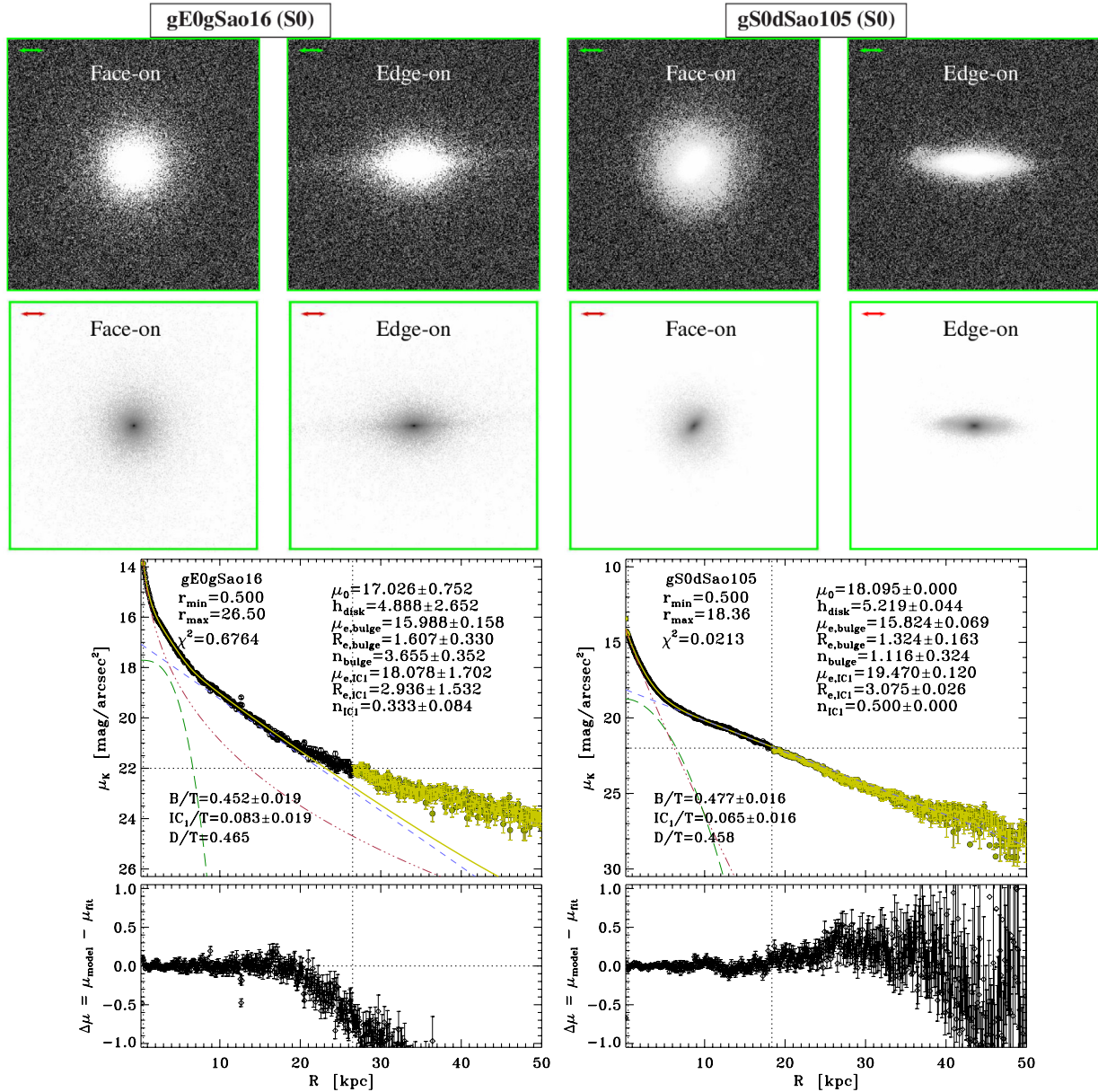


Fig. 2. Simulated K -band images and radial surface brightness profiles of some S0-like remnants from our sample of major and minor mergers. The simulations assume $D = 30$ Mpc, $\mu_{K,\text{lim}} = 22$ mag arcsec $^{-2}$ for $S/N = 3$, and a spatial resolution of $0.7''$. *First two rows of panels:* simulated K -band images of the final remnants for face-on and edge-on views. The horizontal arrow at the top left of each panel represents a physical length of 5 kpc. The field of view is $50 \text{ kpc} \times 50 \text{ kpc}$. We have used different logarithmic greyscales to highlight the structure of the outer discs (*first row of panels*) or of the central bulges (*second row of panels*). *Third row of panels:* simulated radial K -band surface brightness profiles and multicomponent decompositions performed to them. Dotted horizontal line: limiting surface brightness of the images. Dotted vertical lines: minimum and maximum radii considered in the fit. Black empty circles: data considered in the fit. Green filled circles: data excluded from the fit. Red dotted-dashed line: fitted Sérsic bulge. Blue dashed line: fitted exponential disc. Green long-dashed line: additional Sérsic component required in the fit (representing components such as ovals, bars, lenses, or embedded inner discs). Solid light green line: total profile resulting from the fit. *Fourth row of panels:* residuals of the fits as a function of radial location in the galaxy. (A colour version is available in the electronic edition.)

considered for our remnants ($D = 30$ Mpc, see Sect. 3.1), which is even lower than the softening length used in the simulations ($\epsilon = 280$ pc in the major mergers and $\epsilon = 200$ pc in minor events). Therefore, the minimum spatial resolution is ultimately set by ϵ in each case. As commented in Sect. 3.1, we have also included photonic noise to the data considering the limiting magnitude indicated above for $S/N = 3$. No dust extinction effects have been included, as they are expected to be negligible in the K band.

L10 obtained their parameters from 2D multi-component decompositions to deep K -band images of the galaxies, not from 1D surface brightness profiles. We will discuss next why this strategy is problematic when applied to the simulated images from GalMer, and will justify our decomposition method based on 1D azimuthally-averaged surface brightness profiles. In any case, as we will see in 3.2.3, the 1D profiles clearly show a “three-zone” structure very similar to that found in observations like NIRS0S.

M. Querejeta et al.: Bulge-disc structural coupling in S0s resulting from major mergers

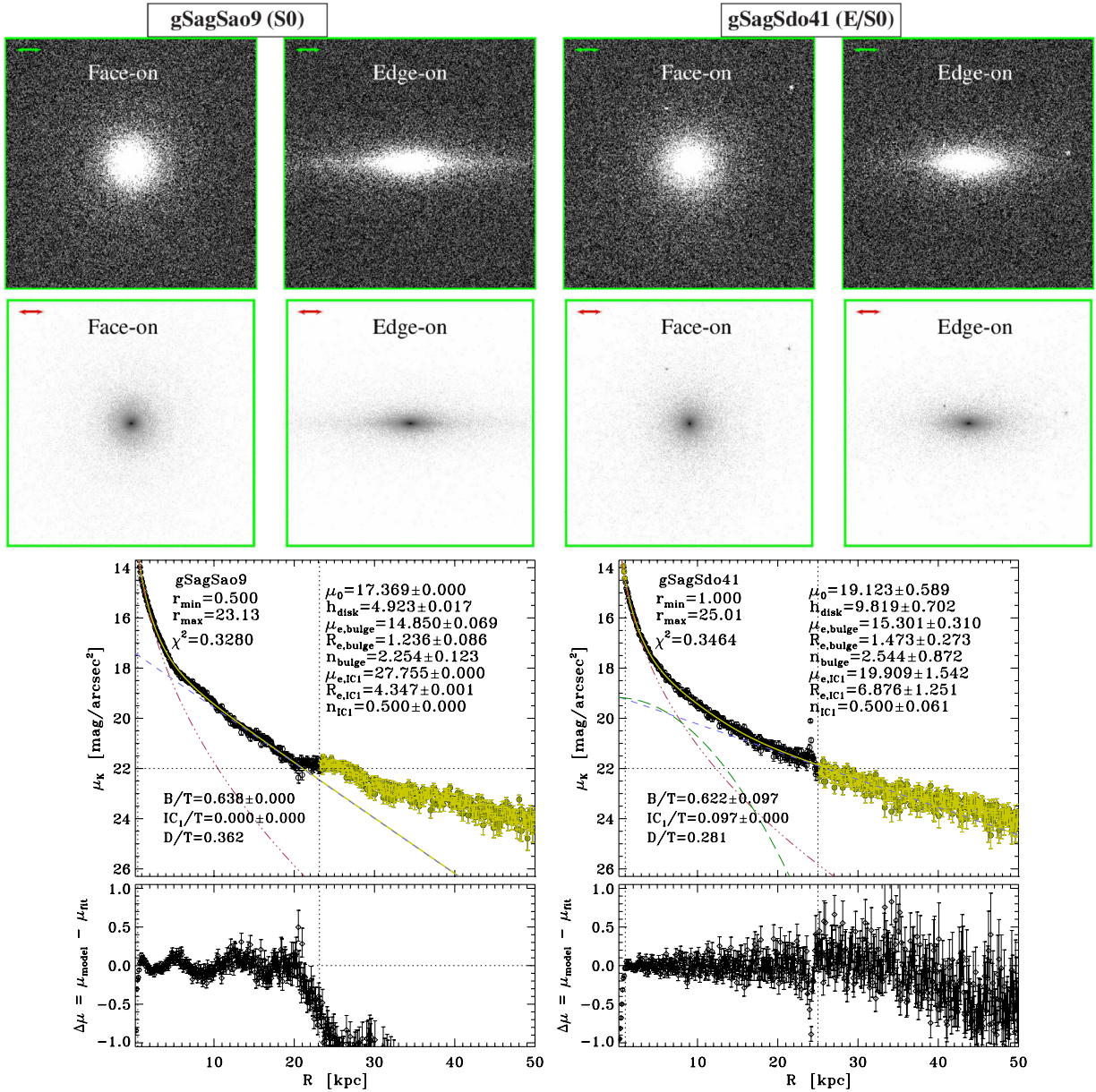


Fig. 2. continued.

3.2.2. Optimal decomposition method: 1D vs 2D

We initially reproduced the procedure from L10 by carrying out multi-component decompositions to our artificial K -band images for face-on views of the remnants using GALFIT³, a highly efficient algorithm for 2D fitting of analytic functions to digital images of galaxies (Peng et al. 2002, 2010). However, we found several problems when comparing with real data.

One of the problems was that the decompositions required too many components in the centre to reproduce the original image realistically (~ 3 – 5 subcomponents beside the bulge and the disc, see an example in Fig. 3), whereas the decompositions performed to the S0 galaxies in NIRSOS required ~ 2 at most (L10). Real S0s exhibit a more diffused and smooth appearance than

our remnants in K -band images, in the sense that they look less structured in inner components at the central regions. However, we know that the basic structure of the bulges and discs in our S0-like remnants are consistent with those observed in real S0s in optical bands (Eliche-Moral et al., in prep.), so the problem was not that the central structure in our remnants was unrealistic, but that the bulge substructures were much more noticeable in our simulated K -band images than in real cases. Therefore, the flux of the bulge component in the remnants got divided into several subcomponents in our 2D decompositions. As commented in Sect 3.1, this effect would probably disappear by simply allowing the remnants to evolve passively for a few Gyr more.

The fact that we have not included dust extinction in our simulated images may also have an effect here, as it would contribute to blur the appearance of the bright and young inner components formed at the centre of the remnants. In fact, dust lanes

³ GALFIT home page: <http://users.obs.carnegiescience.edu/peng/work/galfit/galfit.html>

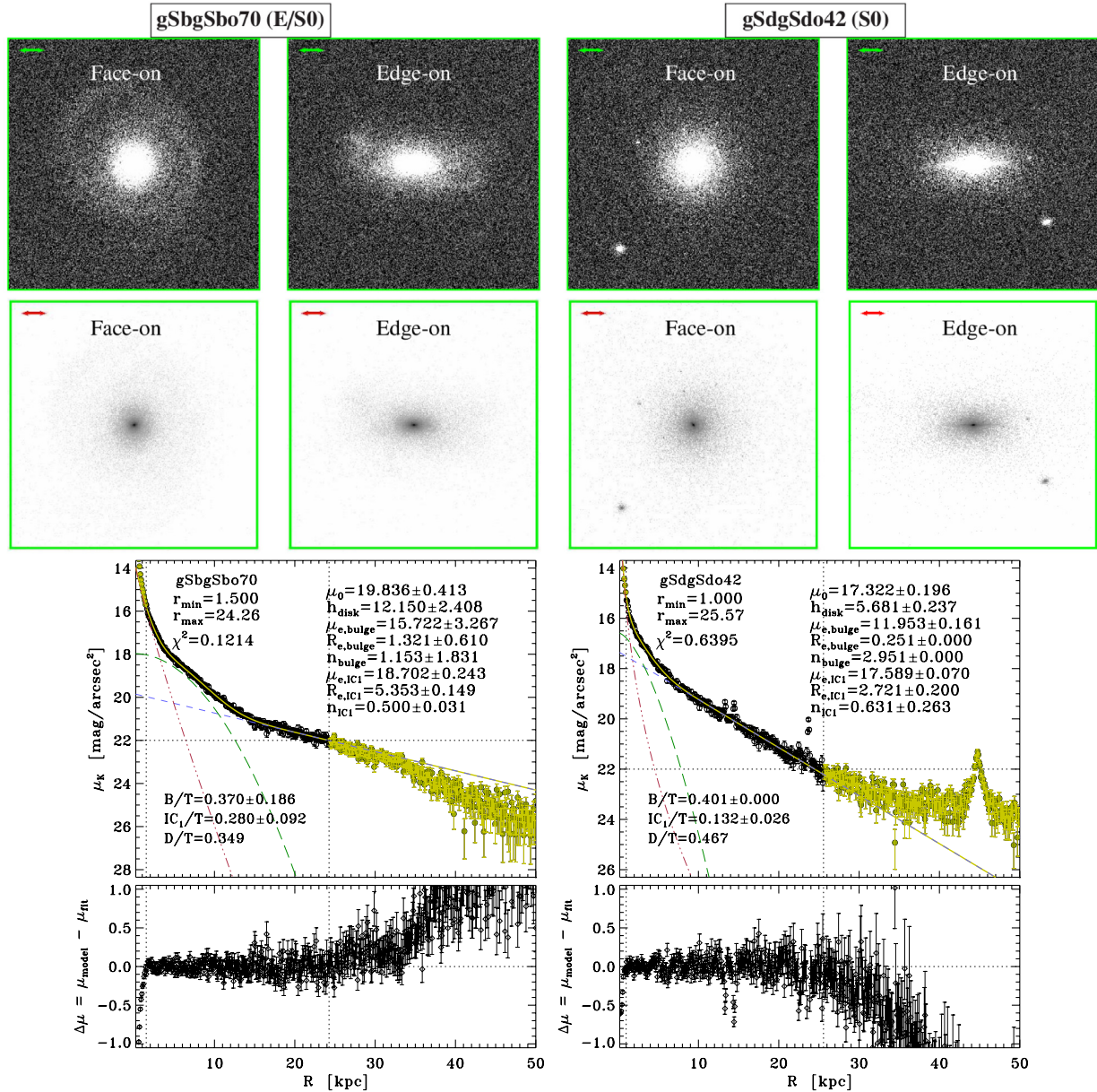


Fig. 2. continued.

are frequent central features in nearby S0s (Annibali et al. 2010; Finkelman et al. 2010). Additionally, present-day massive S0s must have evolved passively for much longer periods of time than our remnants (Fritz et al. 2009; Eliche-Moral et al. 2010a; Sil'chenko et al. 2012; Davidzon et al. 2013; Prieto et al. 2013; Choi et al. 2014); so nearby S0s tend to be dynamically more relaxed and mixed, and their young stellar populations are dimmer. Consequently, we would expect present-day S0s to look more fuzzy than our S0-like remnants.

In addition, the simulated remnants present an inherent grainy appearance at the galaxy outskirts due to the high mass of the stellar particles in the simulation ($\sim(3.5\text{--}20.0) \times 10^5 M_\odot$). At large radii, light accumulates at the pixels where the particles are located, instead of displaying a homogeneous distribution in space (see Fig. 2). Since light distributed in disjointed pixels cannot be identified as a unique component by fitting codes such as

GALFIT, the scalelength of the outer discs in our remnants is significantly underestimated.

Figure 3 illustrates this problem for the remnant of gSbgSbo70. The original K -band image, the best GALFIT model, and its residuals are shown on the left panels. We used five Sérsic components to generate a model with a similar appearance to the original image, trying to minimise the residuals. However, we had to fix the outer disc parameters to those obtained from the exponential fit to the 1D surface brightness profile, because the light (mass) was distributed in isolated pixels towards the outskirts, making it difficult for GALFIT to fit a continuous light distribution there. This is noticeable in the pixels with positive residuals at large radii and the extended circular region with negative residuals (which is tracing the modelled disc). This problem also affected the inner disc region (fitted with the fourth GALFIT component). The central panels of

M. Querejeta et al.: Bulge-disc structural coupling in S0s resulting from major mergers

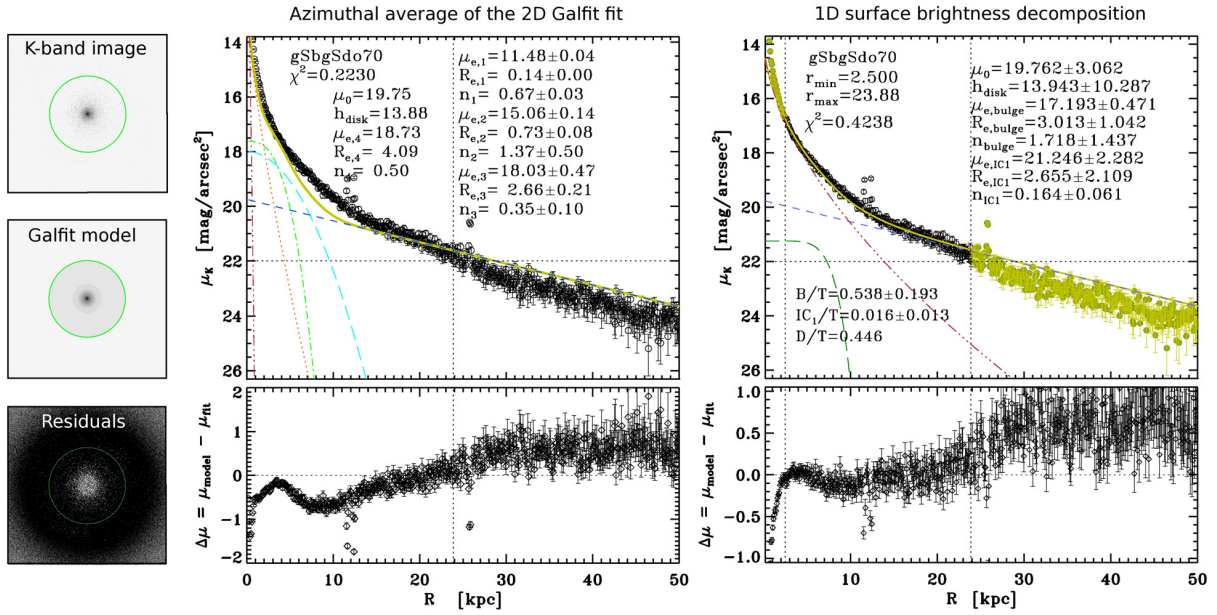


Fig. 3. Comparison between the best GALFIT multi-component decomposition of the 2D K -band image of the remnant gSbgSdo70 and the corresponding 1D decomposition. *Left panels:* artificial K -band image of the remnant for a face-on view (*top*), 5-component model obtained with GALFIT (free of noise, *middle*), and residuals resulting from the subtraction of the model to the image (*bottom*). The same logarithmic greyscale is used in the two upper panels, whereas the linear greyscale in the bottom panel emphasises the background noise at the outskirts. The field of view corresponds to 100 kpc \times 100 kpc, and the green circle represents $R = 25$ kpc in the galaxy. *Middle panels:* azimuthal average of the GALFIT model (green solid line) compared to the 1D surface brightness profile (circles). The five axisymmetric Sérsic components required by the modelling are plotted in the top panel: a nuclear component (component 1, red dotted-dashed line), a thin inner disc with $n = 1.37$ (component 2, orange dotted line), a lens with $n = 0.35$ (component 3, green dotted-dashed line), a fixed extended lens component with $n = 0.5$ (component 4, light blue long-dashed line), and the outer exponential disc, fixed to the result obtained in the 1D fit (dark blue dashed line). The residuals are plotted as a function of radius in the bottom panel. *Right panels:* for comparison, 1D decomposition obtained fitting the azimuthally-averaged K -band surface brightness profile. The legend is the same as in Fig. 2. (A colour version is available in the electronic edition.)

Fig. 3 show the 1D profile derived by azimuthally averaging the 2D GALFIT model, compared to the 1D surface brightness profile of the remnant. The model clearly loses light in the inner disc (traced by component 4 in the GALFIT model). The problem of the too complex structure of the bulges in the simulated images is also illustrated by this panel. The GALFIT model loses light in the centre compared to the 1D surface brightness profile (we note also the positive residuals at the centre of the remnant, in the leftmost panel).

We found that these problems could be solved by performing multi-component decompositions based on 1D face-on azimuthally-averaged surface brightness profiles instead of performing them on 2D photometric images. The 1D profiles already average the 2D spatial information at each radius, blurring the complex central structure of the remnant bulges. They also improve the signal-to-noise at the outskirts compared to 2D surface brightness maps, avoiding the problem of the granularity of the discs in the artificial images. In the right panels of Fig. 3, we show how the decomposition performed directly on the 1D surface brightness profile of model gSbgSbo70 overrides the problems of the structured appearance of the bulge and the grainy structure of the disc in the 2D artificial images.

Therefore, we have simulated realistic surface brightness profiles of our S0-like remnants in the K band, mimicking the observing conditions of the NIRS0S data, to perform 1D multi-component decompositions.

Our major merger remnants are quite axisymmetric, and 1D and 2D decompositions have been proven to provide similar photometric parameters in such case (within typical observational

errors, see de Jong 1996; Courteau et al. 1996; MacArthur et al. 2003; Peng et al. 2010). This ensures that the comparison between the photometric decompositions performed to NIRS0S and to our remnants is fair. However, all remnants in the minor merger experiments are still barred at the end of the simulation (in fact, the original gS0 progenitor is already barred). In these cases, the 1D decompositions provide a description of the azimuthally-averaged light distribution of the bar.

3.2.3. Constructing 1D surface brightness profiles

We have converted the projected radial mass density profiles of the remnants into surface brightness profiles in the K band, following an analogous procedure to the one described in Sect. 3.1 for simulating photometric images (see details there). We have derived azimuthally-averaged 1D surface density profiles of the stellar remnants in face-on views, so we do not have to apply any correction for galaxy inclination to the obtained profiles.

We plot the azimuthally-averaged surface brightness profiles of some remnants in Fig. 2. All the remnants exhibit typical bulge-disc structures. The majority of them clearly show “three-zone” profiles proving the existence of additional subcomponents in the centre, such as the lenses in models gE0gSao16 and gSbgSbo70, the nuclear bar in experiment gS0dSao105, or the inner disc in model gSdgSdo42 (compare their profiles with their images in the figure). This is very frequent in real S0s (L10; Laurikainen et al. 2011; Siil’chenko et al. 2011). The remnants coming from gas-rich progenitors usually have several tidal satellites orbiting around, which are responsible for the

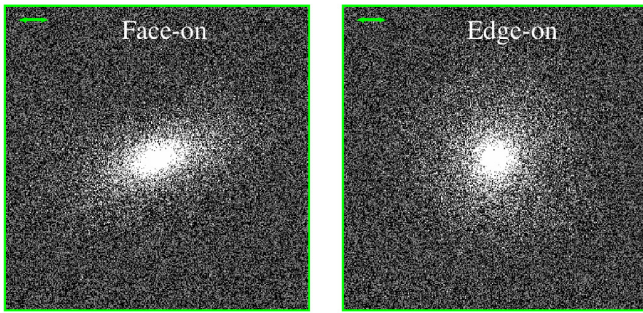


Fig. 4. Artificial K -band photometric images of remnant gSdgSdo51 (E/S0), for the face-on and edge-on views defined on the basis of the total stellar angular momentum (see Sect. 3.1). The remnant contains a high-rotating embedded disc, very inclined with respect to the main outer disc, which dominates the total stellar spin of the galaxy. This is biasing the “face-on view” towards a face-on view of this embedded inner disc, instead of a face-on view of the outer disc. The field of view in all panels corresponds to $50 \text{ kpc} \times 50 \text{ kpc}$. The arrows indicate a physical length of 5 kpc . (A colour version is available in the electronic edition.)

peaks that appear in their surface brightness profiles (as it occurs in gSdgSdo42).

In some merger experiments with very inclined orbits, the remnant contains high-rotating inner discs, completely embedded in the light distribution of the bulge, which are very inclined with respect to the orientation of the main disc of the remnant. In these cases, the face-on view derived from the total angular momentum of the stars in the galaxy (as commented in Sect. 3.1) was biased to show a face-on view of this inner disc, not of the external remnant disc. In these cases, the line of sight was corrected to provide a true face-on view of the main remnant disc. One example is shown in Fig. 4.

3.3. Photometric decompositions of the remnants

We have performed multi-component decompositions to the simulated 1D surface brightness profiles in the K band to compare with the results by L10. The majority of remnants had profiles that required an additional component besides the bulge and the disc to be adequately modelled (see Sect. 3.2.3). To account for this, we performed bulge+disc (B+D) and bulge+[inner component]+disc (B+C+D) decompositions for all S0-like remnants, and selected the one that reproduced better the total galaxy profile in each case.

3.3.1. Fitting functions

For the bulges, we assumed the traditional Sérsic profile (Sérsic 1968; Caon et al. 1993; Prieto et al. 2001; Baes & Gentile 2011),

$$I_B(r) = I_{e,B} \exp \left[-b_n \left(\left(\frac{r}{r_e} \right)^{1/n} - 1 \right) \right], \quad (1)$$

where r_e is the bulge effective radius, $I_{e,B}$ is the surface brightness at r_e , and n is the Sérsic index. The factor b_n is a function of the parameter n , which may be approximated by $b_n = 1.9992n - 0.3271$ in the range $1 < n < 10$ with an error $< 0.15\%$ (Graham 2001). We had to constrain n to the observational range of values during the fitting ($1 \leq n \leq 4$, see L10), because many remnants had small nuclear bars and ovals embedded in

the bulges (which biased n towards $n \sim 0.2-0.5$) or central cusps resulting from the merger-induced starbursts (which led to unrealistically high n values $n \gtrsim 5$). In two models (gSdgSdo1 and gSdgSdo74), we had to force $n = 4$ since the beginning to obtain reasonable decompositions.

The exponential law adequately describes the global radial profiles of most remnant discs down to the limiting magnitude considered (see Fig. 2), but many discs in our remnants exhibit breaks at deeper magnitudes (see Borlaff et al. 2014). We have thus adopted a simple Freeman exponential profile to model the discs in the remnants (Freeman 1970),

$$I_D(r) = I_{0,D} \exp \left(-\frac{r}{h_D} \right), \quad (2)$$

where h_D is the disc scalelength (radius at which the surface brightness is reduced by $1/e$) and $I_{0,D}$, its central surface brightness.

The additional inner components have been fitted including another Sérsic component,

$$I_C(r) = I_{e,C} \exp \left[-b_{n,C} \left(\left(\frac{r}{r_{e,C}} \right)^{1/n_C} - 1 \right) \right], \quad (3)$$

where $r_{e,C}$ is the effective radius of the additional inner component, $I_{e,C}$ is its surface brightness at $r_{e,C}$, and n_C is its Sérsic index. According to observations, lenses, ovals, and bars have Sérsic profiles with $n_C < 1$, while embedded inner discs typically have $n_C \sim 1$ (Laurikainen et al. 2005, 2009; Sil’chenko 2009, L10). We left the Sérsic index n_C as a free parameter in the fits and checked that the fitted values agreed well with the morphology of the inner components visible in the artificial photometric images.

3.3.2. Fitting strategy

We performed the B+D and B+C+D fits (depending on the profile) using a Levenberg-Marquardt nonlinear fitting algorithm to locate the χ^2 minimum solution by iterative changes to the parameters in Eqs. (1)–(3). We initially consider a minimum fitting radius of $r_{\min} = 0.3 \text{ kpc}$ (which is approximately the highest softening length used in the simulations). However, most remnants had nuclear compact sources or discs embedded within the spheroidal light distribution of the bulge, which have been produced by merger-induced nuclear starbursts and which are still very bright in K band at the end of the simulation (see some examples in the second row of panels in Fig. 2). These nuclear components have their observational counterparts in real early-type galaxies (see e.g. Erwin & Sparke 2002; Balcells et al. 2007a; Laurikainen et al. 2009). Compact sources steepen the profile at the centre (artificially raising n of the fitted bulge), while young nuclear discs bias n towards $n \sim 1$ in the central regions. We have thus excluded the innermost regions from the profiles affected by these nuclear components by raising r_{\min} in the fit, only if there was another component that clearly dominated the profile in the centre and extended beyond this minimum radius (i.e. if the compact source or nuclear disc was embedded in a spheroidal bulge-like component). Some experiments also give rise to core-type profiles in the centres of the remnants, that deviated downwards the inward extrapolation of the bulge Sérsic profile (observational analogues can be found in Kormendy et al. 2009; Dullo & Graham 2013). We have excluded these regions from the fits by raising r_{\min} too.

M. Querejeta et al.: Bulge-disc structural coupling in S0s resulting from major mergers

The maximum radius (r_{\max}) in all fits has been set to the radius of the isophote corresponding to the limiting surface brightness in the images ($\mu_K \sim 22$ mag arcsec $^{-2}$). In some major mergers involving a gE0 progenitor, an outer spheroidal envelope of stellar material from the gE0 remains in the remnant, dominating the surface brightness at the external radii over the disc profile (cf. gE0gSao16 in Fig. 2). Sometimes, these outskirts biased the slope of the fitted disc towards a shallower solution, so we slightly decreased r_{\max} in these cases to avoid that problem. A similar procedure was adopted when a tidal satellite induced a peak in the profile near r_{\max} that was clearly biasing the fitted slope of the disc.

We performed several tests changing r_{\min} , r_{\max} , and the initial guesses of the parameters by up to a factor of 10 to check the robustness of the obtained solutions. We found that the B+D fits were reasonably stable, whereas the addition of an extra component in the centre strongly degenerated the solutions, in the sense that there were two to four different sets of components that adequately reproduced the global surface brightness profile and provided similar minima of χ^2 . The strong degeneracy of multi-component decompositions is also usual when dealing with real galaxies (see e.g. L10). However, it was easy to discard many of these solutions and select the most appropriate one simply by considering the edge-on morphology of the galaxy and the radial profile of the residuals of each fit (see Fig. 2). We consider the fits with the lowest χ^2 values and inspect visually the results and the artificial images, which makes it relatively straightforward to select the most appropriate decomposition. When a given model had two feasible solutions, the scalelengths, characteristic surface brightness, and the total magnitudes of the bulges and discs differed by ~ 10 – 20% at most, lying within the typical observational errors. This means that the fitted values of these parameters can be considered robust, as well as the bulge-to-total (B/T) and disc-to-total (D/T) ratios derived from them. On the contrary, n changed noticeably between the different possible solutions. The errors of the fitted parameters were obtained through the bootstrap method (Efron & Tibshirani 1993; Press et al. 1994) accounting for the errors of the surface brightness profiles. We performed Monte Carlo simulations ($N = 100$) of the surface brightness profiles considering the errors associated with each data point (related to particle counting) and performed a B+D or B+C+D decomposition to each realisation. We then estimated the standard deviation of the photometric parameters obtained from the N fits with respect to the nominal values derived by fitting the original profile. We used 3σ rejection in this computation to discard outliers resulting from some failed automatic fits. This procedure of estimating errors for the fitted photometric parameters includes to some extent the uncertainties due to the degeneracy of very similar solutions. As commented above, this degeneracy affected noticeably the bulge Sérsic index. This is the reason why we have obtained relatively large errors for n in some models.

All our S0-like remnants were well described by a B+D or B+C+D profile. Figure 2 shows the multi-component decompositions performed to the radial surface brightness profiles of six S0-like remnants in the K band. We plot the residuals of each fit as a function of radius in the galaxy at the bottom panels. Very few remnants were better reproduced by a B+D fit than by a B+C+D decomposition (one example of B+D fit is model gSagSao9 in Fig. 2). The additional component included in the B+C+D fits may represent a lense or oval (as in model gSbgSbo70 in Fig. 2), an embedded inner disc (as in model gSdgSdo42, see the same figure), or an azimuthally-averaged bar (see model gS0dSao105 in the figure).

In Table 3 we list the bulge and disc photometric parameters derived from the multicomponent decompositions performed to our S0-like remnants that have been analysed in the present study, as well as the main characteristics of these decompositions: number and type of components included (i.e. whether it is B+D or B+C+D), r_{\min} and r_{\max} considered in each case, and χ^2 of the fit in mag 2 . χ^2 is typically below ~ 1 mag 2 in total for the whole fitted radial range in most cases. It rises up to ~ 3 mag 2 in the cases with tidal satellites within the fitted radial profile. The decompositions performed to the original progenitors are also listed in Table 3.

4. Results

In order to quantify to what extent major mergers destroy, preserve, or rebuild bulge-disc coupling, here we compare the photometric parameters derived for our relaxed S0-like remnants with real observational data. We have also included the minor merger models that give rise to a relaxed S0 remnant in the comparison. In particular, we check the overlap of our parameters in various photometric planes with those obtained by Laurikainen et al. (L04 hereafter 2004), Weinzirl et al. (2009, W09 henceforth), and L10 from near-infrared observations of spirals and S0s. For reference, we also compare our results with the dry minor mergers simulated by Aguerri et al. (2001, A01 hereafter) and Eliche-Moral et al. (2006, EM06 henceforth; EM12; EM13).

4.1. Bulge-disc structural coupling

We start by analysing the coupling between the scalelengths of discs and bulges. Figure 5 shows the distribution of the final S0-like remnants in the $\log(h_d)$ - $\log(r_c)$ plane. Each filled circle represents the fate of a different merger event, with the colour code going from red to purple reflecting that later Hubble-type progenitors are involved (and, consequently, it roughly corresponds to a sequence of increasing gas content). With less saturated colours and smaller symbols, at the background, the observational results from L04, W09, and L10 are depicted. For reference, the remnants of the collisionless simulations of minor mergers onto an S0 are also shown with grey diamonds (A01; EM06; EM12; EM13). These collisionless models are scalable, i.e. they can be moved diagonally in this diagram just considering a different length unit. We have also overplotted the least-squares linear fits performed to the observational distributions of spirals and S0s, whenever the Pearson correlation coefficient ρ is larger than 0.5.

Observationally, all disc galaxies, from S0s to spirals, populate a diagonal region in the plane $\log(h_d)$ - $\log(r_c)$, as it can be seen in Fig. 5. Scatter exists, but it is still remarkable that bulges of a certain size predominantly exist in galaxies with a given disc scalelength. Moreover, it is important to emphasise that the distributions of the different types of galaxies overlap: a similar increasing tendency seems to hold for all kinds of disc galaxies, with a steeper slope in the case of S0s.

The merger remnants that we are studying cluster towards the upper-right corner of the plane (Fig. 5), but this is because we are dealing with remnants which have masses similar to the most massive S0s in the NIRS0S sample, at the upper end of the sizes and luminosities of observed lenticulars. This is natural, as the masses of the progenitors ranged ~ 0.5 – $1.5 \times 10^{11} M_\odot$ (Sect. 2). The distribution of scalelengths for the bulges and discs of our remnants overlaps with that of the largest S0s; even the scatter introduced by the different types of encounter is compatible with the scatter of real galaxies.

A&A 573, A78 (2015)

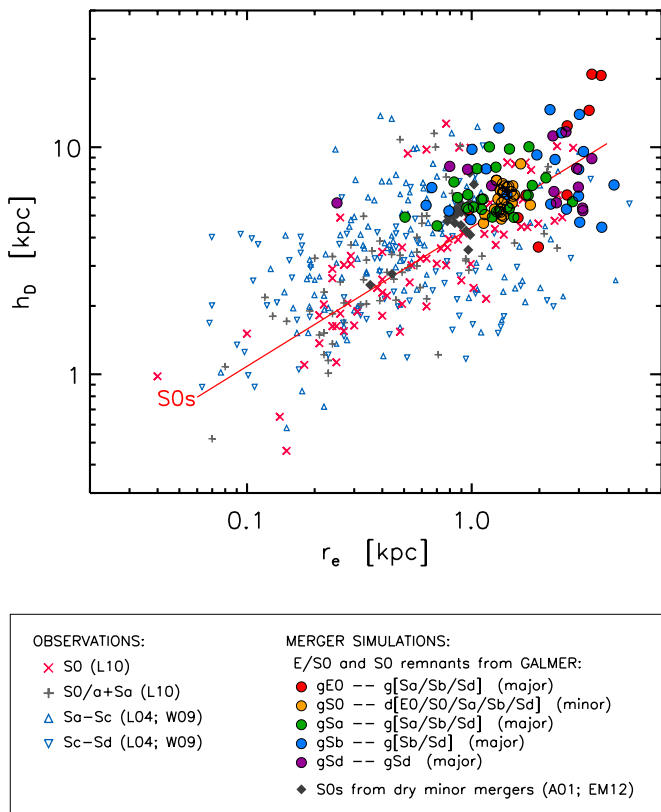


Fig. 5. Location of our S0-like remnants in the $\log(h_d)$ - $\log(r_e)$ plane, compared to the observational results (L04; W09; L10) and previous simulations of dry minor mergers (A01; EM06; EM12; EM13). Details on the symbols and colour-coding used can be found on the legend. The linear fits performed to the observational distributions of S0 and spiral galaxies are overplotted in the diagram with solid lines only when Pearson's correlation coefficient is greater than 0.5, in this case only for S0s ($\rho_{S0} = 0.59$, $\rho_{Sp} = 0.21$). (A colour version is available in the electronic edition.)

For the largest bulge effective radii, from Fig. 5 it seems like, on bulk, lenticulars have slightly larger disc scalelengths than spirals. It is precisely towards this upper side of the observational distribution of S0s where our remnants are located. The S0 remnants of our minor mergers cover a rather small area of the $\log(h_d)$ - $\log(r_e)$ plane, and they lie close to the results from previous studies based on dry minor merger simulations (A01; EM12). The different sets of major mergers, however, span a much larger range of values, reproducing well the scatter observed in real S0s. Finally, it is also interesting to note that the experiments with the largest gas fractions are the ones that show the largest deviations in positions on the plane. Our S0-like remnants exhibit a bulge-disc coupling in terms of sizes that is consistent with the one observed in real S0s.

In Fig. 6, we plot the distribution of real and simulated S0s in the $M_K(\text{disc})$ - $M_K(\text{bulge})$ plane. The linear fits performed to the distributions of real S0s and spirals indicate that the total K -band magnitudes of their bulges and discs correlate linearly, although the linear trend of the S0s is tilted with respect to the one of spirals. All our remnants accumulate towards the upper end area covered by the brightest real S0s. More importantly, the remnants from both minor and major mergers fulfill well the observational constraint of bulge-disc coupling also in terms of luminosity: the magnitude of the disc takes up a value which is

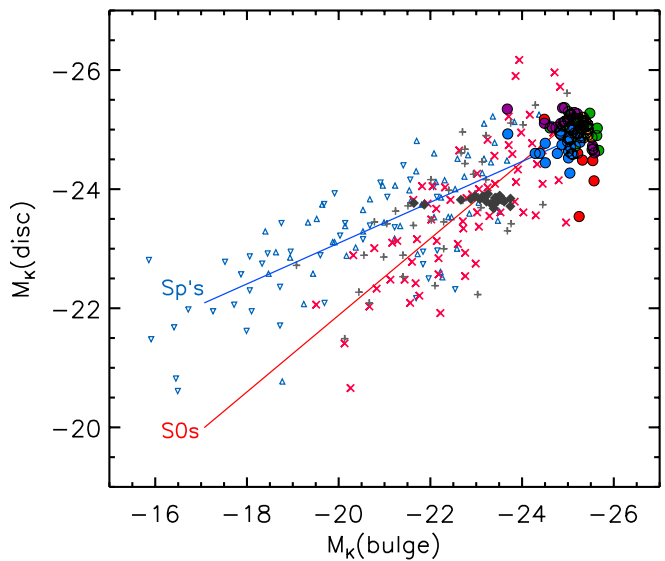


Fig. 6. Distribution of our S0-like remnants in the $M_K(\text{disc})$ - $M_K(\text{bulge})$, compared to the observational distributions of nearby S0s and spirals (L04; W09; L10) and to previous simulations of dry minor mergers (A01; EM06; EM12; EM13). The linear fits performed to the observational distributions of S0 and spiral galaxies are overplotted in the diagram with solid lines (Pearson $\rho_{S0} = 0.76$, $\rho_{Sp} = 0.70$). The symbols represent the same models and observations as in the previous figure; consult the legend in Fig. 5. (A colour version is available in the electronic edition.)

proportional to the bulge magnitude within some scatter (shared both by simulations and observations).

We have again overplotted the collisionless minor merger models by A01 and EM12 in Fig. 6 for comparison. They can be moved diagonally in the plane considering a different mass unit (i.e. luminosity unit), up to the region where our dissipative minor mergers are located. Therefore, the inclusion of gas and star formation effects does not seem to be relevant to preserve the bulge-disc coupling in satellite accretions onto gas-poor progenitors.

As commented in Sect. 3.1, our remnants are brighter than real S0s of analogous masses in the NIRSOS sample by a factor of ~ 2 , due to recent merger-driven starbursts. If the remnants were allowed to relax passively for an additional period of ~ 1 - 2 Gyr, their colours would become more similar to those of nearby S0s and the remnants would experience a dimming of ~ 1 mag in the K band. Assuming that the average M/L ratios of the bulge and the disc are similar, the remnants would move diagonally towards fainter magnitudes up to ~ 1 mag in Fig. 6, nearly following the line fitted to the distribution of real S0s. Therefore, a global dimming of the remnants by ~ 1 mag in K -band would keep the agreement between real and simulated S0s in the $M_K(\text{disc})$ - $M_K(\text{bulge})$ diagram.

Figures 5 and 6 prove that the S0-like remnants resulting from major and minor mergers present a bulge-disc coupling consistent with observations in terms of scalelengths and luminosities. In the minor merger experiments, the global structure of the main progenitor disc is mostly preserved at the end of the simulation in all cases. In the right panels of Fig. 7, we show the time evolution of the stellar surface brightness profile of the gS0 progenitor in the minor merger experiment gS0dSao103 (blue). We have overplotted the additional contribution from accreted stellar material coming from the dSa satellite at each time, as the

M. Querejeta et al.: Bulge-disc structural coupling in S0s resulting from major mergers

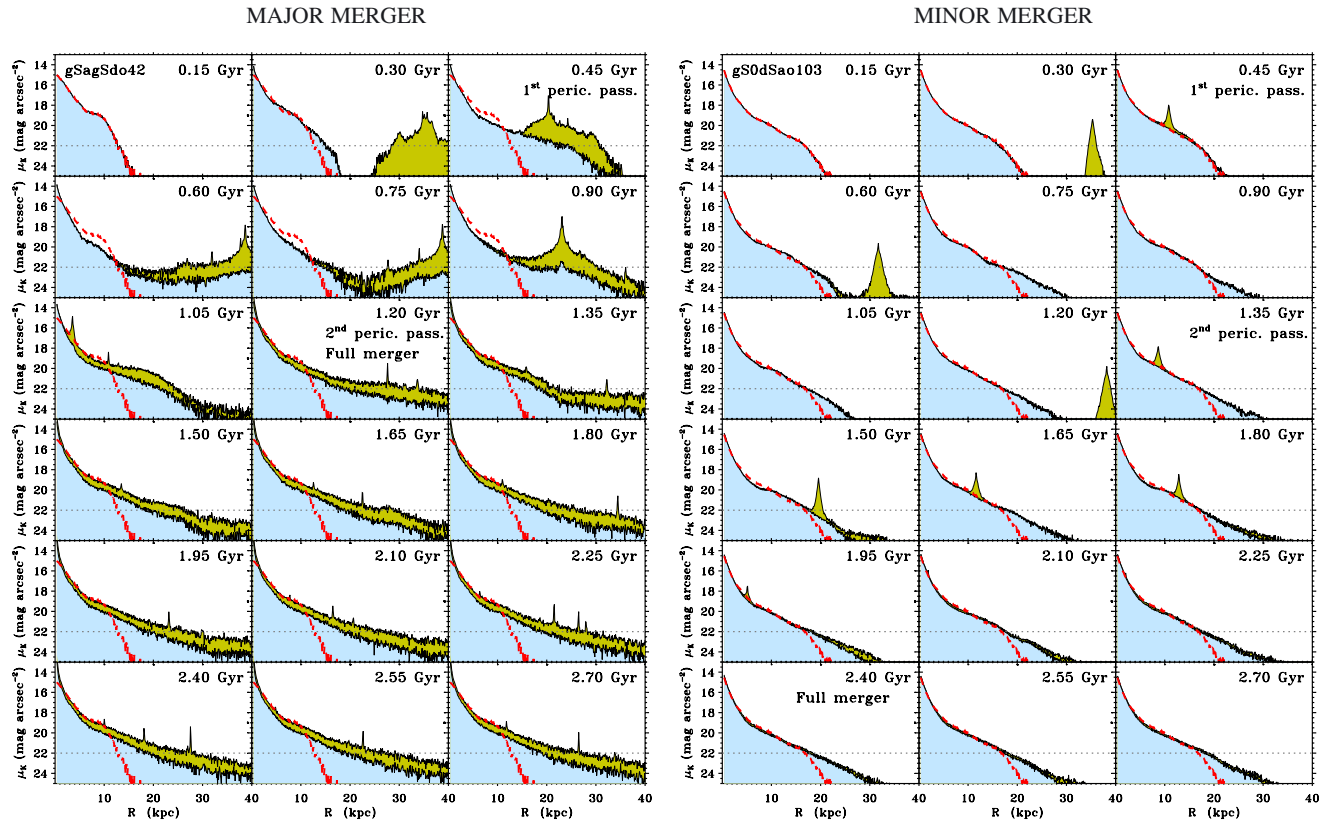


Fig. 7. Time evolution of the surface brightness profiles of the stellar material in two models that result in an S0-like remnant, centred on the mass centroid of the most massive (primary) progenitor at each time. *Left panels:* for the major merger gSagSdo42. *Right panels:* for the minor merger gS0dSao103. The contribution of the stellar material of each progenitor to the total profile at each time is marked with a different colour (blue: primary progenitor; green: secondary progenitor). We have plotted with red dashed lines the original surface brightness profile of the primary progenitor in all panels, to stress that minor merger events essentially preserve the profile, whereas major encounters completely rebuild the bulge and disc profiles in the remnants out of material from both progenitors. The limiting surface brightness that we consider is shown with a horizontal dotted line. We also indicate the first and second pericentre passages, as well as the moment when the full merger is reached. (A colour version is available in the electronic edition.)

disruption process evolves (green). The original surface brightness profile of the gS0 progenitor is shown in all panels for comparison (red dashed line). At the end of the simulation, the total profile due to the stars from the gS0 and the dSa in the remnant is very similar to the original profile of the gS0 progenitor at all radii down to the limiting magnitude under consideration. Therefore, in minor mergers, the changes experienced by the bulge and disc structures are small in general, mostly driven by internal secular processes induced by the encounters (see EM13), so it is not surprising that bulge and disc preserve their coupling at the end of the accretion. The original bar that the gS0 progenitor has at the start of the simulation in the minor merger experiments is strengthened at each pericentre passage of the satellite that takes place before the full merger (see Fig. 1).

The bulges and discs in the S0-like remnants resulting from major mergers exhibit a realistic structural coupling, even if the progenitor discs are basically destroyed in such major encounters. In the left panels of Fig. 7, we show the time evolution of the stellar surface brightness profile for the gSa progenitor in the major merger model gSagSdo42. Here, we also highlight with different colours the contribution to the total profile at each time of the stars coming from each progenitor, as well as the original profile of the gSa galaxy (red dashed line). At the end of the simulation, the distribution of the stellar mass coming from the gSa progenitor (blue) is completely different at all radii from

its original profile. There has been considerable mass migration from intermediate radii to the core and to the outskirts. The material originally belonging to the gSd has also been accreted at different radii, rebuilding a new bulge+disc structure. Then, in major mergers, the processes after the bulge relaxation and the disc rebuilding seem to force both components to keep a structural connection. This suggests that the bulge-disc coupling of all disc galaxies (and not just of S0s) may arise from fundamental physics. This would explain why both S0 and spiral galaxies exhibit a similar bulge-disc coupling in terms of sizes and luminosities (despite having different evolutionary pathways), as well as why the S0 galaxies resulting from events as violent as major mergers do still fulfill this coupling.

These results confirm, both from the sizes point of view and from the perspective of the luminosity, that the analysed S0-like remnants show a similar coupling between their bulges and discs to that observed in real S0s. This proves that, contrary to the widespread belief, major mergers can produce S0 remnants with coupled bulge-disc structures analogous to those observed in real S0s.

4.2. Trends of the bulge and disc scalelengths with B/T

The correlation between r_c/h_d and B/T or n in spirals has undergone significant debate in the last couple of decades: the

A&A 573, A78 (2015)

apparent lack of observed correlation in the earlier studies lead some authors to claim that the Hubble sequence was scale-free (de Jong 1996; Courteau et al. 1996; Graham 2001; MacArthur et al. 2003; Balcells et al. 2007b); on the contrary, others found a slight increasing trend in those planes, suggesting that earlier Hubble types (with higher B/T) tend to host bulges of relatively larger sizes (Graham & Prieto 1999; Gadotti 2009; Mosenkov et al. 2010). L10 found a slight decreasing trend of r_e/h_d with the morphological galaxy type T (de Vaucouleurs et al. 1991) from $T = -3$ (SO⁻) to $T = 2$ (Sa), which becomes essentially constant from $T = 2$ to $T = 6$ (Sa to Sc; see their Fig. 5).

Independently of whether r_e/h_d exhibits significant trends with B/T and n or not, we have studied if our S0-like remnants overlap with real S0s in the r_e/h_d - B/T and r_e/h_d - n planes. In Fig. 8 we first plot r_e/h_d as a function of the B/T ratio, compared to observational data (top panel). From the linear fit to observational S0s and late-type spirals we notice that, in spite of the large scatter, there is a similar increasing trend in both galaxy types, but with a systematic offset upwards in the case of spirals. When we overplot our remnants in this plane, it becomes clear that we are mostly reproducing the S0s, preferentially overlapping the area around the linear fit to lenticulars rather than the late-type spirals. There are only three outliers exhibiting the highest r_e/h_d values, corresponding to gas-rich major mergers. In any case, the scatter in the resulting r_e/h_d of the remnants as a function of B/T is large, but the distribution of the simulated S0s is consistent with the increasing trend that the observational S0s seem to follow (within the scatter).

It is also remarkable that the S0-like remnants resulting from our major merger experiments span the observational ranges of r_e/h_d and B/T values in the top panel of Fig. 8, although their stellar masses cover a relatively narrow range ($\sim 1-3 \times 10^{11} M_\odot$). This means that major mergers can give rise to S0 galaxies with very different global properties starting from similar progenitors, just depending on the initial conditions of the encounters.

The intermediate and bottom panels of Fig. 8 can shed some light on the origin of the systematic shift between spirals and S0s in the r_e/h_d - B/T plane, and explain why our remnants end up covering the area they do. The intermediate panel shows that spirals tend to have systematically larger bulge effective radii for a given bulge-to-total luminosity ratio. The distributions overlap, but most of our remnants tend to align where most S0s lie, on average corresponding to smaller r_e than their spiral counterparts. It is also interesting to note that remnants with the largest dispersions (which still lie close to some of the S0 outliers in the plane) are those with the highest gas fractions. For completeness, the bottom panel shows the relation between h_d and B/T , but no linear fit to observations is attempted here, since the Pearson correlation coefficients are low. In any case, it is reassuring to find that the merger remnants that we are studying populate an area which is observationally covered by lenticulars.

In conclusion, the S0-like remnants resulting from major and minor mergers are consistent with the distribution of real S0s in the r_e/h_d , r_e , and h_d versus B/T planes.

4.3. Pseudobulges resulting from major mergers

Figure 9 shows the distribution of our S0-like remnants in the n - B/T and r_e/h_d - n planes (left and right panels, respectively), compared to the distributions of real S0s and spirals and to previous simulations of dry minor mergers. The left panel indicates that real galaxies distribute diagonally in the n - B/T plane, with earlier types tending to accumulate towards higher B/T and n values. Half of our major merger remnants exhibit bulges with

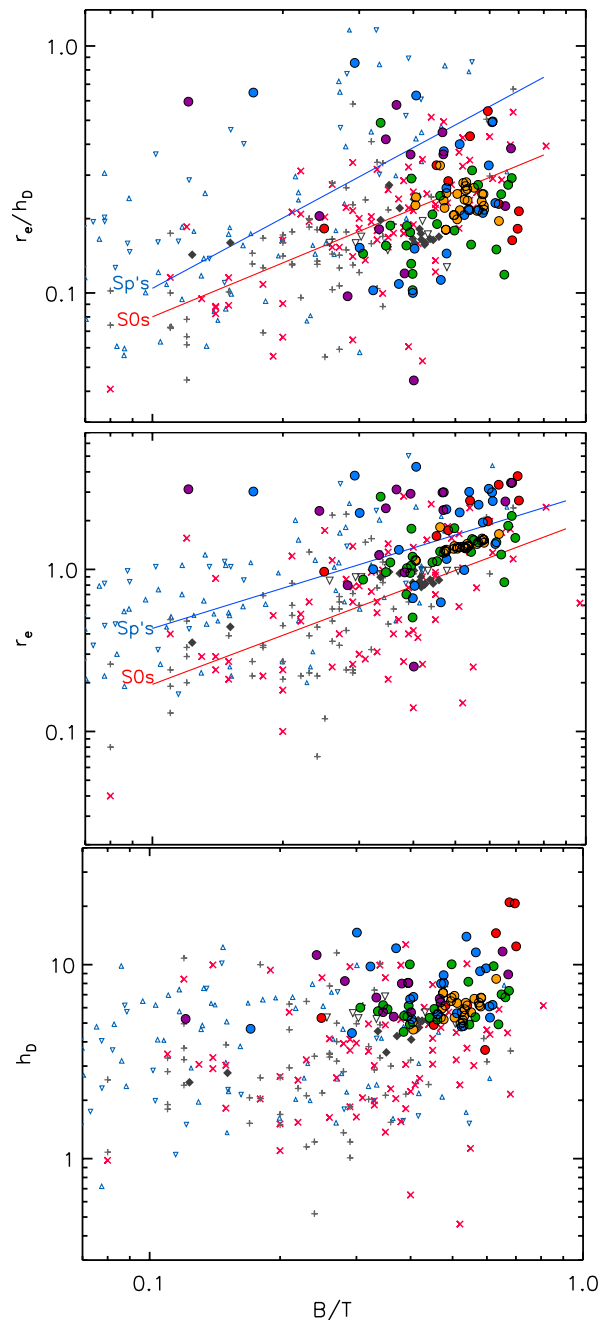


Fig. 8. Distribution of r_e/h_d , r_e , and h_d versus B/T for our S0-like remnants resulting from major and minor mergers, compared to real observations of S0s and spirals (L04; W09; L10) and to previous collisionless simulations of minor mergers (A01; EM06; EM12; EM13). The linear fits to the observational distributions of S0 and spiral galaxies are overplotted with solid lines only when Pearson’s correlation coefficient exceeds 0.5 (here, in the top and middle panels: top panel: $\rho_{S0} = 0.64$, $\rho_{Sp} = 0.63$; middle panel: $\rho_{S0} = 0.60$, $\rho_{Sp} = 0.55$; bottom panel: $\rho_{S0} = 0.0021$, $\rho_{Sp} = -0.20$). The symbols represent the same models and observations as in the previous figures; consult the legend in Fig. 5. (A colour version is available in the electronic edition.)

concentrations (n) and light contents relative to the total (B/T) compatible with the observations of S0 galaxies, whereas the other half exhibit too low n values for their B/T ratios. All minor merger remnants present less concentrated bulges (i.e. lower

M. Querejeta et al.: Bulge-disc structural coupling in S0s resulting from major mergers

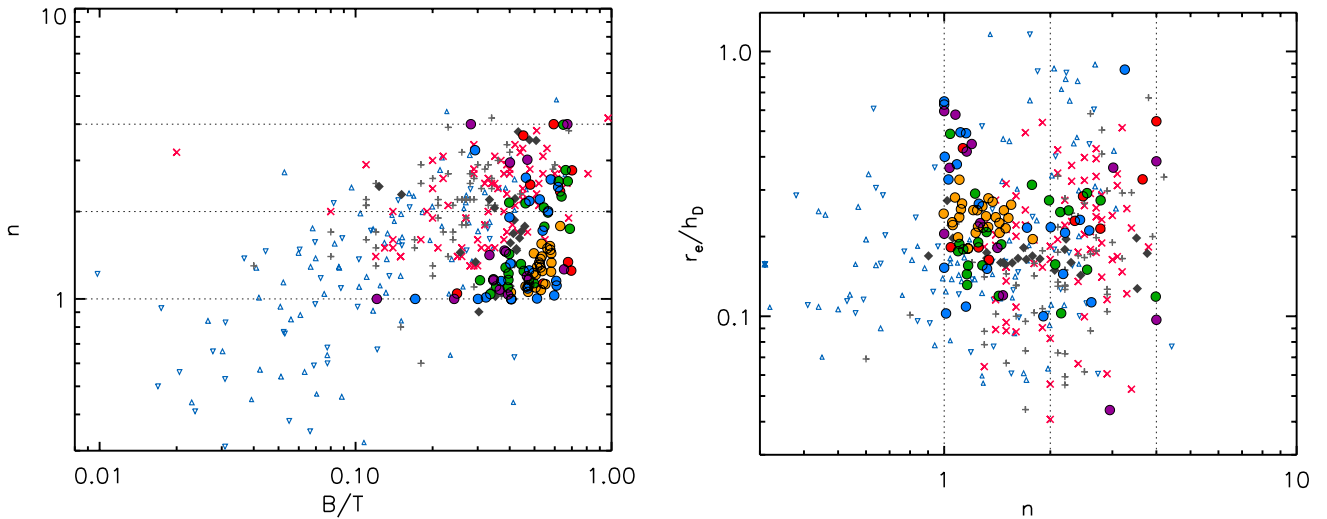


Fig. 9. Distribution of Sérsic indices n with B/T and r_e/h_d in our S0-like remnants (left and right panels, respectively), compared to the observational parameters from real S0s and spirals (L04; W09; L10). We also represent the locations of previous simulations of dry minor mergers (A01; EM06; EM12; EM13). The dotted lines indicate the location of $n = 1, 2,$ and 4 in each diagram. The symbols represent the same models and observations as in the previous figures; consult the legend in Fig. 5. (A colour version is available in the electronic edition.)

n) than real S0s with similar B/T . These models accumulate in a clump below the diagonal distribution of real galaxies at $n \sim 1$ and $0.3 < B/T < 0.8$. L10 showed that real S0s tend to exhibit lower n values than popularly thought (they usually have $n \lesssim 2$, instead of the widespread belief of typical $n > 3$ bulges). However, although our remnants tend to exhibit $n < 2$ bulges accordingly to L10 results, many of them are too displaced from the location of real S0s in the n - B/T diagram (see Fig. 9).

The low n values of the remnants coming from a minor merger are an artefact of the initial conditions. The original gS0 is already offset from the location of S0s in this diagram ($B/T = 0.2$ and $n = 1$, see Table 3). Therefore, even though all minor mergers onto this progenitor induce an increment of the concentration (n) and relative luminosity of the bulge (B/T), this bulge growth is not enough to counteract the initial conditions. So, these minor merger experiments would probably give rise to S0s with higher n for similar B/T ratios if the gS0 progenitor already had a more realistic Sérsic index. The dry minor mergers simulated by A01 and EM12 provide more realistic n values for their B/T , just because the original S0 progenitor used in these encounters laid onto the observational cloud since the beginning.

In major mergers, the reason for the offset in Sérsic indices is related to the collapse of gas particles towards the centre. In some cases, gas accumulates at the remnant centre, giving rise to inner discs of ~ 3 – 4 kpc size made of newborn stars. These flat central structures made of young stars dominate the light distribution and bias the bulge Sérsic index towards $n \sim 1$. However, in other cases, the inner discs made of young stars are too small (~ 2 kpc) to explain the $n \sim 1$ bulges which dominate the profile out to $R \sim 5$ kpc, and which are basically made up of old stars. In these cases, the explanation of the bulge flattening may arise from gas dynamics. Gas particles are known to transfer angular momentum to the old stellar particles during the encounter, providing rotational support to them and flattening their spatial distribution. This might lead to the $n \sim 1$ bulges built out of old stellar material. One example is shown in Fig. 10. The contribution of the new stars (light blue) in the final remnant of gSbSbo9 (black) only dominates the light distribution at the core

of the galaxy ($R < 1$ kpc), which has been excluded from the decomposition. The region of the $n \sim 1$ bulge (red dashed line) basically consists of old stellar material, from $R \sim 1$ kpc out to $R \sim 5$ kpc, where the lense component starts to dominate.

This situation would probably change if the models were allowed to relax for a longer time period, as relaxation usually entails dynamical mixing and reduces rotation. The bulge could potentially puff up and raise its Sérsic index. Moreover, these inner discs made up of young stars are expected to fade by ~ 1 mag in K in ~ 1 – 2 Gyr (see Sect. 3.1); in that case, they would negligibly contribute to the surface brightness profile at the centre. Most present-day massive S0s have passively evolved for much longer time periods than these particular models (Davidzon et al. 2013; Choi et al. 2014), so this is a natural explanation of why such low n are rare in the local universe.

Many S0s host pseudobulges, i.e. bulges with $B/T < 0.4$ and $n \sim 1$, with high levels of star formation and disc-related phenomena, such as spiral patterns or bars (see Laurikainen et al. 2006, L10). The properties of these bulges have usually been attributed to a secular origin, mainly to bar evolution. Our models demonstrate that a major merger can give rise to an S0 galaxy hosting a pseudobulge without requiring any bars (none of our major merger remnants develops a significant bar, see Sect. 3.1).

In the right panel of Fig. 9 we plot r_e/h_d as a function of the Sérsic index. Although many of our remnants exhibit too low n values compared to real S0s, the large scatter in r_e/h_d at each n value of observational data masquerades the offset of these models in n with respect to real S0s. However, there is a clump of models with $n \sim 1$ and $r_e/h_d > 0.4$ that clearly deviates from the rest of models in this plane. All these S0-like remnants come from gas-rich major encounters with very inclined orbits. The existence of very young (and thus bright) inclined inner discs in the centres of these remnants biases r_e towards higher values than expected for their h_d . Cosmological simulations indicate that encounters with very inclined orbits have been rare in the Universe, so it is understandable that these encounters populate a region of the plane only sparsely covered by

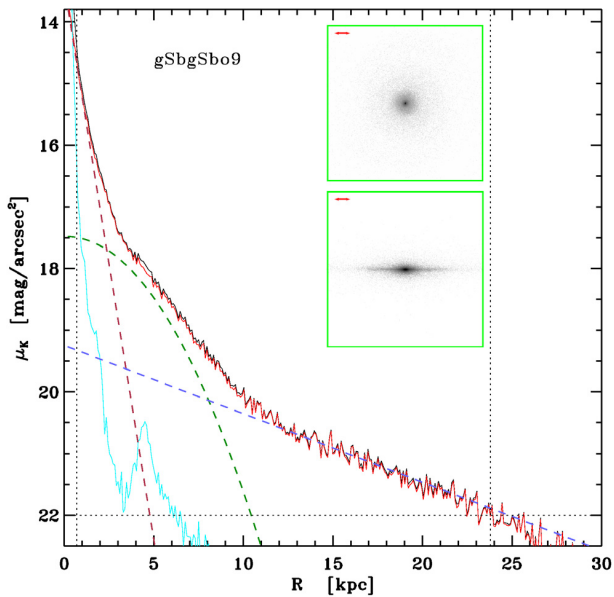


Fig. 10. Bulge-lens-disc decomposition performed to an S0-like remnant with an $n \sim 1$ bulge (model gSbgSbo9). Solid black line: total surface brightness profile in the K band. Red solid line: contribution of the old stars to the total profile. Light blue solid line: contribution of the young stars to the total profile. Red dashed line: fitted bulge ($n \sim 1.0$). Green dashed line: fitted lens component. Blue dashed line: fitted disc. We have overplotted the limiting magnitude and the minimum and maximum radii considered in the decomposition (dotted straight lines). The subframes of each panel show the artificial K -band images of the remnant for face-on and edge-on views, using a logarithmic greyscale to highlight the substructures at the centre (in particular, the flattened, disc-shaped bulge). The field of view is $50 \text{ kpc} \times 50 \text{ kpc}$. (A colour version is available in the electronic edition.)

observations (Zentner et al. 2005; Gómez-Flechoso et al. 2010; Benjouali et al. 2011).

Figure 11 is an alternative way of checking that our mergers reproduce the upper end of the observed S0 mass spectrum, and that, for such sizes, our remnants preferentially correspond to the lowest observed Sérsic indices. When the disc and bulge scalelengths are plotted against the Sérsic index, we see that the remnants reproduce the upper half of the observational cloud in the r_c - n and h_d - n planes. Our results agree well with previous collisionless simulations of dry minor mergers in both diagrams. The lower half of the observational distributions of S0s in these two photometric planes could be probably reproduced by mergers onto less massive progenitors than those used here.

Finally, any trends with gas content and even mass ratios seem to be subdominant as to where galaxies end up in all the photometric diagrams shown in Figs. 5–11. It is true that the most gas-rich major merger models disseminate more in the planes, whereas the minor mergers cover much tighter areas (just because they share the same main progenitor). The minor merger remnants are surrounded by those of our major merger events. Therefore, the mass ratio or gas content alone lack the predictive power to dictate the specific region of these planes into which remnants will fall.

Summarising, these simulations show that major mergers can build up S0s hosting pseudobulges without requiring the development of a bar, as already shown by EM13 for dry minor merger events. The presence of gas and star formation are, however, essential to explain the formation of S0s with disc-like bulges through major merger events.

5. Limitations of the models

GalMer models survey a wide set of initial conditions, but they are also limited. Here we comment on the limitations inherent to the present models.

1. Mass ratios of encounters and progenitor masses.

GalMer models cover a significant range of mass ratios (1:1 to 20:1, see Table 1), but they are fixed for each pair of progenitor morphologies, so the effects of different mass ratios cannot be analysed for a given set of initial conditions (and in particular, for a given couple of progenitor types). In fact, intermediate mergers (with mass ratios from 4:1 to 7:1) are not present in the database, but many studies suggest that intermediate encounters and multiple minor mergers may have been as relevant for the evolution of S0 galaxies as major merger events (see Maller et al. 2006; Bournaud et al. 2007; Wilman et al. 2013; Tapia et al. 2014, and references therein).

More than the limitations in terms of mass ratios, the reason why our remnants only cover the largest observational S0s is that at least one of the progenitors is always a giant galaxy, of initial stellar mass $M_\star \gtrsim 5 \times 10^{10} M_\odot$. Therefore, it would be interesting to complement the present study with examples from the intermediate-merger regime and with galaxies of more modest initial masses.

2. Gas and star formation effects.

Dissipative effects have been proven to be essential for establishing the global structure and kinematics of merger remnants (see e.g. Jesseit et al. 2007; Di Matteo et al. 2007; di Matteo et al. 2008). A major advantage of GalMer models is that they include the dynamical effects of gas and star formation, providing a more realistic picture of the merger event than collisionless models, but it also entails a series of constraints.

Firstly, we must bear in mind that our S0-like remnants correspond to the outcome of a merger between progenitor galaxies that are analogous to those found in our local Universe. At higher redshifts, where the actual encounters that led to present-day S0s took place, the gas fractions were even higher. For instance, the gas fraction can be up to $\sim 50\%$ of the total stellar mass at $z \sim 1$ (Papovich et al. 2005; Genzel et al. 2008; Tacconi et al. 2008; Förster Schreiber et al. 2009; Law et al. 2009). As we will argue in the discussion, this increases the likelihood of forming an S0-like remnant, reinforcing the relevance of our results. In any case, expanding the present analysis to simulations with larger gas fractions would be helpful to interpret this point.

Secondly, the conversion from mass into light is not a trivial issue. We have adopted a number of simplifications: (a) we assign a single age to every old stellar particle (10 Gyr); (b) we assume a given SFH per morphological type, typical of each progenitor, and independent of the location of the particles within the galaxy; (c) for gas particles transforming into stars, we approximate the SFH by a SSP model. There is some observational evidence of variation in the age of stars contributing to K -band, both from galaxy to galaxy and across individual galaxies (van Dokkum & Franx 2001; MacArthur et al. 2004; Sil'chenko et al. 2012); however, this is still a highly-debated issue from the observational point of view, and trying to adopt more complex distributions of stellar ages and/or SFHs would only introduce additional uncertainties and complicate further the interpretation of our results. In any case, with the present conversion of mass into light, we account for the morphological appearance of

M. Querejeta et al.: Bulge-disc structural coupling in S0s resulting from major mergers

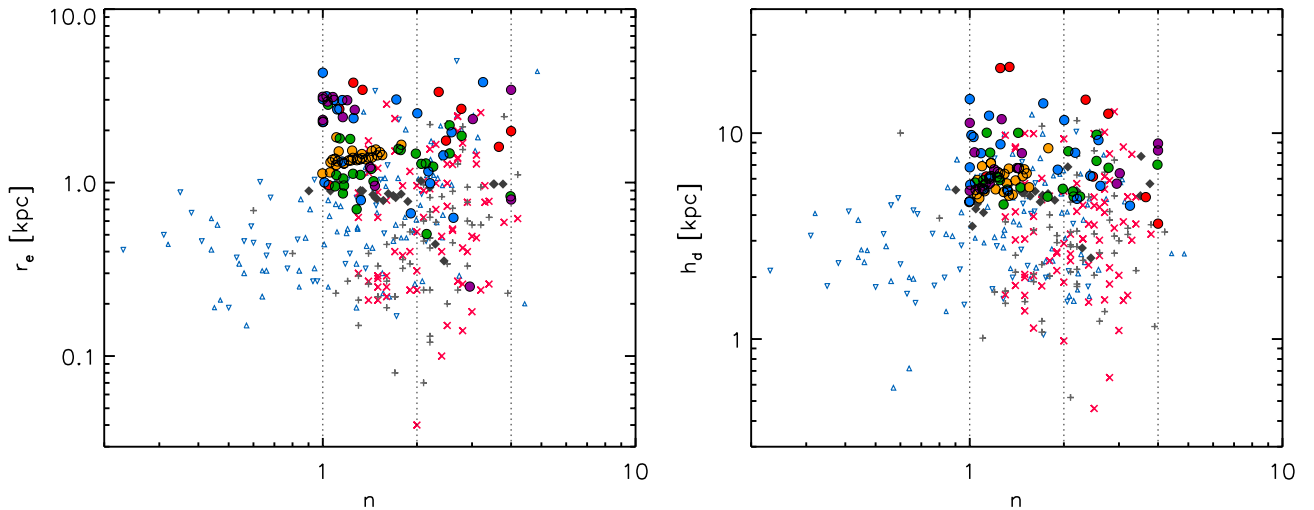


Fig. 11. Distribution of our S0-like remnants in the $\log(r_e)$ - $\log(n)$ and $\log(h_d)$ - $\log(n)$ planes (left and right panels, respectively), compared to the observational distributions of S0s and spirals (L04; W09; L10). The location of previous collisionless simulations of minor mergers is also shown (A01; EM06; EM12; EM13). The vertical dotted line indicates the location of $n = 1, 2,$ and 4 in each diagram. The symbols represent the same models and observations as in the previous figures; consult the legend in Fig. 5. (A colour version is available in the electronic edition.)

remnants, including the important effects of the recent starbursts in the structure of the central bulge (see Sect. 4.3).

3. Total simulation time.

The models have been evolved for up to 3.5 Gyr, involving relaxing periods of ~ 2 Gyr at most. Even though we have checked that all the remnants analysed were dynamically relaxed at the end of the simulation, the stellar material acquired during the merger may have not had enough time to be properly mixed. This may be the reason for the over-structured bulge that we found in 2D decompositions in comparison to NIRS0S galaxies (Sect. 3.2). Moreover, the youth of these substructures made them brighter than usual even in the K band. Stellar populations with these ages would decrease their flux by up to ~ 1 mag in the K -band during the next ~ 1 – 2 Gyr (Prieto et al. 2013), becoming completely smooth within the global bulge light distribution. Anyway, some nearby E-S0 galaxies of lower masses than those of our S0-like remnants exhibit blue nuclear structures, which are usually considered as traces of past merging activity (Kannappan et al. 2009; Huertas-Company et al. 2010; Wei et al. 2010). Blue colours in massive S0s are also more common at intermediate redshifts (Fritz et al. 2009).

6. Discussion

It is well known that mergers (even major events) can, under favourable conditions, preserve discs (Springel & Hernquist 2005), but major mergers in particular are expected to produce remnants with decoupled bulge and disc structures. Contrary to this widespread belief, we have shown that S0-like remnants resulting from dissipative major and minor mergers exhibit bulge-disc structural coupling coherent with observations, extending the results obtained from dry minor merger simulations (EM12; EM13).

As commented in Sect. 4.1, minor merger events directly preserve the bulge-disc coupling of the original main progenitor. EM13 showed that, even in the absence of gas and star formation, satellite accretions induce internal secular evolution in the progenitor disc that can even enhance this structural link. The addition of small amounts of gas to the satellites can only boost

internal secular processes in the main progenitor, as observed in the minor merger models analysed here. On the contrary, major mergers destroy the original bulge and disc structures during the first phases of the encounter, *but* the final bulge and disc structures are rebuilt (partially based on the relics of the original progenitor structures) to give rise to S0 remnants that overlap in the $n - B/T - r_e/h_d$ parameter space with the distribution of bright S0s. Except for a few outliers, especially in terms of concentration (Sérsic index n), we otherwise reproduce the tail of the most massive lenticulars in NIRS0S in the various photometric planes as the consequence of both major or minor mergers. Therefore, S0s with realistically coupled bulge-disc structures may result from the relaxation process that follows certain mergers, even in such violent events as major mergers. This process occurs within timescales that are reasonable in a cosmological sense (just ~ 2 – 4 Gyr), and it is therefore a plausible mechanism to explain the formation of a fraction of the current population of S0s. The bulge-disc coupling observed in all disc galaxies may thus be the consequence of basic physical processes. This would explain the observational fact that both spirals and S0s present similar linear trends (slightly offset or tilted) in photometric planes such as h_d - r_e , $M_K(\text{disc})$ - $M_K(\text{bulge})$, or r_e/h_d - B/T .

Our remnants span a relatively narrow range of final stellar masses, ~ 1 – $3 \times 10^{11} M_\odot$, because one of the members of the encounter is always a giant galaxy, even if both major and minor mergers are considered. In this context, one advantage of the merger origin picture is that, even considering such a narrow range in stellar masses, they can explain the trends and dispersions observed in the $n - B/T - r_e - h_d$ planes for up to one dex. Mergers that differ only slightly in their initial conditions are capable of producing quite different sort of remnant systems, and all of them with bulge-disc structural coupling consistent with observations. If we also account for the observational and computational evidence that points to a merger origin for a significant fraction of S0s (and in particular, for the most massive ones, see Eliche-Moral et al. 2010a; Bernardi et al. 2011a,b; Méndez-Abreu et al. 2012; Barway et al. 2013; Wilman et al. 2013; Tapia et al. 2014), it seems unjustified to exclude major mergers from the current scenarios of S0 formation and evolution.

Another relevant point is the role of gas fraction when producing S0s out of mergers. It has already been mentioned that our S0-like remnants arise from progenitor galaxies that are analogous to those found in our local Universe, with gas fractions typical of present-day spiral galaxies (see Table 2). However, many authors claim that massive S0s have evolved passively since $z \sim 0.8$, but they seem to have undergone strong star formation episodes at higher redshifts (Davidzon et al. 2013; Choi et al. 2014). These results fit in a hierarchical formation picture in which a significant fraction of present-day massive S0s derive from mergers of spiral discs occurred at $z \sim 1$. In those early epochs, the typical gas fraction in spirals was higher than at present, reaching up to $\sim 50\%$ of the total stellar mass at $z \sim 1$ (Papovich et al. 2005; Genzel et al. 2008; Tacconi et al. 2008; Förster Schreiber et al. 2009; Law et al. 2009). With such large amounts of gas, the formation of disc components in major merger events becomes more probable, and so does the probability of forming an S0-like remnant instead of an elliptical (Yang et al. 2009; Hammer et al. 2010, 2013; Puech et al. 2009). Even the lower gas amounts contemplated by the present models already point to major mergers producing S0 remnants with coupled bulges and discs; therefore, the buildup of a relevant fraction of present-day S0 galaxies through major mergers at $z \sim 1$, when gas fractions were higher, seems to be quite feasible.

The fact that our results point to a merger origin of some S0s should not, of course, be overinterpreted. Naturally, it is not reasonable to claim that all lenticular galaxies derive from mergers, and we are far from being able to quantify what amount of the S0s in the local Universe are the direct consequence of one or several galaxy encounters. It is widely accepted that, within the densest environments, effects like ram-pressure stripping or galaxy harassment can explain the gas loss and consequent change of spirals into S0s (Aragón-Salamanca et al. 2006). Moreover, such mechanisms help explain the rise of the fraction of lenticulars with redshift, and the corresponding decline of spirals (Dressler 1980). However, here we would like to point out that, whatever that contribution has been, any S0s deriving from the major merger between two spirals would also contribute to the trend observed by Dressler of transformation of spirals into S0s. It is beyond the scope of the present paper to quantify the relevance of major mergers in terms of creating S0s (recent estimates indicate that they may have been essential in the buildup of $\sim 50\%$ of present massive S0s at most, see Tapia et al. 2014), but it is a mechanism that surely needs to be taken into account, and may especially explain the origin of the S0s that reside in groups and less dense environments. S0s are at least as common in groups as in clusters, and galaxy interactions are the dominant evolution mechanism in this regime (Wilman et al. 2009; Mazzei et al. 2014a,b). Moreover, the role of merging in “pre-processing” galaxies in filaments before falling into a cluster and in “post-processing” them during their infall might also be underestimated at present (see Vijayaraghavan & Ricker 2013; Head et al. 2014).

7. Summary and conclusions

Because galaxy mergers are highly violent phenomena, it has often been claimed that they cannot possibly give rise to S0 galaxies in which a strong bulge-to-disc coupling holds. Since such structural coupling has been measured observationally, this has led most authors to rule out mergers as a possible origin of S0 galaxies. We have thus studied the bulge-disc coupling in a set of major and minor merger simulations from the GalMer database that result in E/S0 or S0 types. We have sim-

ulated realistic surface brightness profiles of the remnants in K -band, mimicking the typical observational conditions, to perform structural photometric decompositions analogous to the ones that would have been obtained by observers. We have finally compared the distribution of the S0-like remnants with real S0 galaxies from the NIRS0S survey (Laurikainen et al. 2011) in photometric planes relating basic parameters of the bulges and discs. In particular, we have found that:

1. S0-like remnants reproduce well the observed distribution of real bright S0s in the $B/T - r_e - h_d$ parameter space.
2. Although our remnants span a narrow range of stellar masses, they reproduce the observational values of r_e , h_d , r_e/h_d , and B/T over an order of magnitude. Therefore, a wide variety of final structures consistent with observations can be achieved from mergers that differ only slightly in their initial conditions.
3. The majority of the experiments analysed ($\sim 64\%$ of major mergers and $\sim 100\%$ of minor events) exhibit low bulge Sérsic indices ($1 < n < 2$), in agreement with the observed trend of real S0s to host $n < 2$ bulges.
4. However, nearly one half of the major-merger remnants present too low n values compared to real analogues. These remnants host young inner discs formed in the starbursts induced by the encounters, biasing the bulge fit towards $n \sim 1$; the effects of these inner components are expected to vanish in $\geq 2-3$ Gyr additional relaxation time.
5. The presence of young disc-like structures in the bulges of these major merger remnants and their global properties ($n < 2$ and $B/T < 0.4$) indicate that pseudobulges can also come out of major mergers without requiring bar phenomena (as none of these major merger experiments develops a relevant bar).
6. While minor mergers tend to preserve the original bulge-disc coupling of the main progenitor, major mergers are capable of rebuilding a bulge-disc coupling in the remnants after having destroyed the original structures of the progenitors. This suggests that the mechanisms after the bulge-disc coupling found in both S0 and spiral galaxies may be associated with fundamental physics.

Therefore, these simulations demonstrate that realistic S0 galaxies with photometric parameters showing a bulge-disc coupling compatible with the one observed in real objects can emerge out of galaxy mergers in less than ~ 3.5 Gyr, and, in particular, from major mergers. Considering that mergers are complementary to other evolutionary mechanisms that probably operate preferentially over regions of different density, we conclude that mergers (and in particular, major ones) cannot be discarded from the formation scenarios of S0s on the basis of the strong bulge-disc coupling observed in these galaxies or their tendency to host pseudobulges.

Acknowledgements. The authors would like to thank the anonymous reviewer for a very helpful and constructive referee report. We would also like to acknowledge I. Chilingarian, P. Di Matteo, F. Combes, A.-L. Melchior, and B. Semelin for creating the GalMer database. We also appreciate valuable comments by P.G. Pérez-González and E. Laurikainen, as well as the GALFIT code made publicly available by his author C. Peng. We also acknowledge the usage of the HyperLeda database (<http://leda.univ-lyon1.fr>). This research has made use of the NASA’s Astrophysics Data System and NASA/IPAC Extragalactic Database (NED) which is operated by the Jet Propulsion Laboratory, California Institute of Technology, under contract with the National Aeronautics and Space Administration. M.Q. acknowledges financial support to the DAGAL network from the People Programme (Marie Curie Actions) of the European Union’s Seventh Framework Programme FP7/2007-2013/ under REA grant agreement number PITN-GA-2011-289313. Supported

M. Querejeta et al.: Bulge-disc structural coupling in S0s resulting from major mergers

- by the Spanish Ministry of Economy and Competitiveness (MINECO) under projects AYA2006-12955, AYA2009-10368, AYA2012-30717, and AYA2012-31277, and by the Madrid Regional Government through the AstroMadrid Project (CAM S2009/ESP-1496, <http://www.laeff.cab.inta-csic.es/projects/astromadrid/main/index.php>). Funded by the Spanish MICINN under the Consolider-Ingenio 2010 Programme grant CSD2006-0070: "First Science with the GTC" (<http://www.iac.es/consolider-ingenio-gtc/>), and by the Spanish programme of International Campus of Excellence Moncloa (CEI).
- ## References
- Abraham, R. G., Merrifield, M. R., Ellis, R. S., Tanvir, N. R., & Brinchmann, J. 1999, *MNRAS*, 308, 569
- Abramson, A., Kenney, J. D. P., Crowl, H. H., et al. 2011, *AJ*, 141, 164
- Aguerri, J. A. L., Balcells, M., & Peletier, R. F. 2001, *A&A*, 367, 428 (A01)
- Annibaldi, F., Bressan, A., Rampazzo, R., et al. 2010, *A&A*, 519, A40
- Aragón-Salamanca, A., Bedregal, A. G., & Merrifield, M. R. 2006, *A&A*, 458, 101
- Baes, M., & Gentile, G. 2011, *A&A*, 525, A136
- Balcells, M., Graham, A. W., & Peletier, R. F. 2007a, *ApJ*, 665, 1084
- Balcells, M., Graham, A. W., & Peletier, R. F. 2007b, *ApJ*, 665, 1104
- Bamford, S. P., Nichol, R. C., Baldry, I. K., et al. 2009, *MNRAS*, 393, 1324
- Barnes, J., & Hut, P. 1986, *Nature*, 324, 446
- Barway, S., Wadadekar, Y., Vaghmare, K., & Kembhavi, A. K. 2013, *MNRAS*, 432, 430
- Bell, E. F., & de Jong, R. S. 2001, *ApJ*, 550, 212
- Benjouali, L., Gómez Flechoso, M. A., Domínguez-Tenreiro, R., Martínez-Serrano, F., & Serna, A. 2011, in *Highlights of Spanish Astrophysics VI, Proc. of the IX Scientific Meeting of SEA Madrid*, eds. M. R. Zapatero Osorio, J. Gorgas, J. Maíz Apellániz, J. R. Pardo, & A. Gil de Paz, 148
- Bernardi, M., Roche, N., Shankar, F., & Sheth, R. K. 2011a, *MNRAS*, 412, 684
- Bernardi, M., Roche, N., Shankar, F., & Sheth, R. K. 2011b, *MNRAS*, 412, L6
- Bertelli, G., Bressan, A., Chiosi, C., Fagotto, F., & Nasi, E. 1994, *A&AS*, 106, 275
- Borlaff, A., Eliche-Moral, M. C., Rodríguez-Pérez, C., et al. 2014, *A&A*, 570, A103
- Bournaud, F., Jog, C. J., & Combes, F. 2007, *A&A*, 476, 1179
- Bruzual, G., & Charlot, S. 2003, *MNRAS*, 344, 1000
- Caon, N., Capaccioli, M., & D'Onofrio, M. 1993, *MNRAS*, 265, 1013
- Cappellari, M., Emsellem, E., Krajnović, D., et al. 2011, *MNRAS*, 416, 1680
- Chilingarian, I. V., Di Matteo, P., Combes, F., Melchior, A.-L., & Semelin, B. 2010, *A&A*, 518, A61
- Choi, J., Conroy, C., Moustakas, J., et al. 2014, *ApJ*, 792, 95
- Courteau, S., de Jong, R. S., & Broeils, A. H. 1996, *ApJ*, 457, L73
- Crowl, H. H., & Kenney, J. D. P. 2006, *ApJ*, 649, L75
- Crowl, H. H., & Kenney, J. D. P. 2008, *AJ*, 136, 1623
- Crowl, H. H., Kenney, J. D. P., van Gorkom, J. H., & Vollmer, B. 2005, *AJ*, 130, 65
- Davidzon, I., Bolzonella, M., Coupon, J., et al. 2013, *A&A*, 558, A23
- de Jong, R. S. 1996, *A&A*, 313, 45
- de Vaucouleurs, G., de Vaucouleurs, A., Corwin, Jr., H. G., et al. 1991, 3rd Reference Catalogue of Bright Galaxies, Vol. 1–3, XII, 2069 (New York: Springer-Verlag, Berlin Heidelberg), 7
- Di Matteo, P., Combes, F., Melchior, A., & Semelin, B. 2007, *A&A*, 468, 61
- di Matteo, P., Bournaud, F., Martig, M., et al. 2008, *A&A*, 492, 31
- Dressler, A. 1980, *ApJ*, 236, 351
- Dullo, B. T., & Graham, A. W. 2013, *ApJ*, 768, 36
- Efron, B., & Tibshirani, R. 1993, *An Introduction to the Bootstrap* (New York: Chapman & Hall)
- Eliche-Moral, M. C., Balcells, M., Aguerri, J. A. L., & González-García, A. C. 2006, *A&A*, 457, 91 (EM06)
- Eliche-Moral, M. C., Prieto, M., Gallego, J., et al. 2010a, *A&A*, 519, A55
- Eliche-Moral, M. C., Prieto, M., Gallego, J., & Zamorano, J. 2010b, *ArXiv e-prints* [[arXiv:1003.0686](https://arxiv.org/abs/1003.0686)]
- Eliche-Moral, M. C., González-García, A. C., Balcells, M., et al. 2011, *A&A*, 533, A104
- Eliche-Moral, M. C., González-García, A. C., Aguerri, J. A. L., et al. 2012, *A&A*, 547, A48 (EM12)
- Eliche-Moral, M. C., González-García, A. C., Aguerri, J. A. L., et al. 2013, *A&A*, 552, A67 (EM13)
- Erwin, P., & Sparke, L. S. 2002, *AJ*, 124, 65
- Finkelman, I., Brosch, N., Funes, J. G., Kniazev, A. Y., & Väisänen, P. 2010, *MNRAS*, 407, 2475
- Förster Schreiber, N. M., Genzel, R., Bouché, N., et al. 2009, *ApJ*, 706, 1364
- Freeman, K. C. 1970, *ApJ*, 160, 811
- Fritz, A., Böhm, A., & Ziegler, B. L. 2009, *MNRAS*, 393, 1467
- Gadotti, D. A. 2009, *MNRAS*, 393, 1531
- Genzel, R., Burkert, A., Bouché, N., et al. 2008, *ApJ*, 687, 59
- Gingold, R. A., & Monaghan, J. J. 1982, *J. Comput. Phys.*, 46, 429
- Gómez-Flechoso, M. A., Benjouali, L., & Domínguez Tenreiro, R. 2010, in *Highlights of Spanish Astrophysics V*, eds. J. M. Diego, L. J. Goicoechea, J. I. González-Serrano, & J. Gorgas, *Astrophys. Space Sci. Proc.*, 295
- Graham, A. W. 2001, *MNRAS*, 326, 543
- Graham, A. W. 2013, *Elliptical and Disk Galaxy Structure and Modern Scaling Laws*, ed. T. D. Oswalt & W. C. Keel, 91
- Graham, A. W., & Prieto, M. 1999, *ApJ*, 524, L23
- Hammer, F., Yang, Y. B., Wang, J. L., et al. 2010, *ApJ*, 725, 542
- Hammer, F., Yang, Y., Fouquet, S., et al. 2013, *MNRAS*, 431, 3543
- Head, J. T. C. G., Lucey, J. R., Hudson, M. J., & Smith, R. J. 2014, *MNRAS*, 440, 1690
- Hopkins, P. F., Cox, T. J., Younger, J. D., & Hernquist, L. 2009, *ApJ*, 691, 1168
- Hubble, E. P. 1936, *Realm of the Nebulae* (New Haven: Yale University Press)
- Huertás-Company, M., Aguerri, J. A. L., Tresse, L., et al. 2010, *A&A*, 515, A3
- Janowiecki, S., Mihos, J. C., Harding, P., et al. 2010, *ApJ*, 715, 972
- Jesseit, R., Naab, T., Peletier, R. F., & Burkert, A. 2007, *MNRAS*, 376, 997
- Kannappan, S. J., Guie, J. M., & Baker, A. J. 2009, *AJ*, 138, 579
- Kormendy, J., & Bender, R. 2012, *ApJS*, 198, 2
- Kormendy, J., & Kennicutt, Jr., R. C. 2004, *ARA&A*, 42, 603
- Kormendy, J., Fisher, D. B., Cornell, M. E., & Bender, R. 2009, *ApJS*, 182, 216
- Laurikainen, E., Salo, H., Buta, R., & Vasylyev, S. 2004, *MNRAS*, 355, 1251 (L04)
- Laurikainen, E., Salo, H., & Buta, R. 2005, *MNRAS*, 362, 1319
- Laurikainen, E., Salo, H., Buta, R., et al. 2006, *AJ*, 132, 2634
- Laurikainen, E., Salo, H., Buta, R., & Knapen, J. H. 2009, *ApJ*, 692, L34
- Laurikainen, E., Salo, H., Buta, R., Knapen, J. H., & Comerón, S. 2010, *MNRAS*, 405, 1089 (L10)
- Laurikainen, E., Salo, H., Buta, R., & Knapen, J. H. 2011, *MNRAS*, 418, 1452
- Law, D. R., Steidel, C. C., Erb, D. K., et al. 2009, *ApJ*, 697, 2057
- Lucey, L. B. 1977, *AJ*, 82, 1013
- MacArthur, L. A., Courteau, S., & Holtzman, J. A. 2003, *ApJ*, 582, 689
- MacArthur, L. A., Courteau, S., Bell, E., & Holtzman, J. A. 2004, *ApJS*, 152, 175
- Maller, A. H., Katz, N., Kereš, D., Davé, R., & Weinberg, D. H. 2006, *ApJ*, 647, 763
- Mazzei, P., Marino, A., & Rampazzo, R. 2014a, *ApJ*, 782, 53
- Mazzei, P., Marino, A., Rampazzo, R., Galletta, G., & Bettoni, D. 2014b, *Adv. Space Res.*, 53, 950
- Méndez-Abreu, J., Aguerri, J. A. L., Barrena, R., et al. 2012, *A&A*, 537, A25
- Mihos, J. C., & Hernquist, L. 1994, *ApJ*, 437, 611
- Mihos, J. C., Harding, P., Rudick, C. S., & Feldmeier, J. J. 2013, *ApJ*, 764, L20
- Million, E. T., Allen, S. W., Werner, N., & Taylor, G. B. 2010, *MNRAS*, 405, 1624
- Miyamoto, M., & Nagai, R. 1975, *PASJ*, 27, 533
- Mosenkov, A. V., Sotnikova, N. Y., & Reshetnikov, V. P. 2010, *MNRAS*, 401, 559
- Moster, B. P., Macciò, A. V., Somerville, R. S., Johansson, P. H., & Naab, T. 2010, *MNRAS*, 403, 1009
- Papovich, C., Dickinson, M., Giavalisco, M., Conselice, C. J., & Ferguson, H. C. 2005, *ApJ*, 631, 101
- Peng, C. Y., Ho, L. C., Impey, C. D., & Rix, H.-W. 2002, *AJ*, 124, 266
- Peng, C. Y., Ho, L. C., Impey, C. D., & Rix, H.-W. 2010, *AJ*, 139, 2097
- Pfenniger, D., & Norman, C. 1990, *ApJ*, 363, 391
- Press, W. H., Teukolsky, S. A., Vetterling, W. T., & Flannery, B. P. 1994, *Numerical Recipes in Fortran* (New York: Cambridge University Press)
- Prieto, M., Aguerri, J. A. L., Varela, A. M., & Muñoz-Tuñón, C. 2001, *A&A*, 367, 405
- Prieto, M., Eliche-Moral, M. C., Balcells, M., et al. 2013, *MNRAS*, 428, 999
- Puech, M., Hammer, F., Flores, H., Neichel, B., & Yang, Y. 2009, *A&A*, 493, 899
- Rasmussen, J., Ponman, T. J., Verdes-Montenegro, L., Yun, M. S., & Borthakur, S. 2008, *MNRAS*, 388, 1245
- Rudick, C. S., Mihos, J. C., Frey, L. H., & McBride, C. K. 2009, *ApJ*, 699, 1518
- Rudick, C. S., Mihos, J. C., Harding, P., et al. 2010, *ApJ*, 720, 569
- Semelin, B., & Combes, F. 2002, *A&A*, 388, 826
- Sersic, J. L. 1968, *Atlas de galaxias australes* (Cordoba, Argentina: Observatorio Astronomico)
- Sil'chenko, O. 2013, *Mem. Soc. Astron. It. Suppl.*, 25, 93
- Sil'chenko, O. K. 2009, in *IAU Symp.*, 254, eds. J. Andersen, J. Bland-Hawthorn & B. Nordström, 173
- Sil'chenko, O. K., Chilingarian, I. V., Sotnikova, N. Y., & Afanasiev, V. L. 2011, *MNRAS*, 414, 3645
- Sil'chenko, O. K., Proshina, I. S., Shulga, A. P., & Kuposov, S. E. 2012, *MNRAS*, 427, 790
- Sivanandam, S., Rieke, M. J., & Rieke, G. H. 2010, *ApJ*, 717, 147

A&A 573, A78 (2015)

- Somerville, R. S., & Primack, J. R. 1999, MNRAS, 310, 1087
Spergel, D. N., Bean, R., Doré, O., et al. 2007, ApJS, 170, 377
Springel, V., & Hernquist, L. 2005, ApJ, 622, L9
Tacconi, L. J., Genzel, R., Smail, I., et al. 2008, ApJ, 680, 246
Tapia, T., Eliche-Moral, M. C., Querejeta, M., et al. 2014, A&A, 565, A31
Tiret, O., Salucci, P., Bernardi, M., Maraston, C., & Pforr, J. 2011, MNRAS, 411, 1435
van Dokkum, P. G., & Franx, M. 2001, ApJ, 553, 90
Vijayaraghavan, R., & Ricker, P. M. 2013, MNRAS, 435, 2713
Vollmer, B., Braine, J., Pappalardo, C., & Hily-Blant, P. 2008, A&A, 491, 455
Vollmer, B., Soida, M., Chung, A., et al. 2009, A&A, 496, 669
Vollmer, B., Soida, M., Braine, J., et al. 2012, A&A, 537, A143
Wei, L. H., Kannappan, S. J., Vogel, S. N., & Baker, A. J. 2010, ApJ, 708, 841
Weinzirl, T., Jogee, S., Khochfar, S., Burkert, A., & Kormendy, J. 2009, ApJ, 696, 411 (W09)
Weinzirl, T., Jogee, S., Conselice, C. J., et al. 2011, ApJ, 743, 87
Wilman, D. J., Oemler, Jr., A., Mulchaey, J. S., et al. 2009, ApJ, 692, 298
Wilman, D. J., Fontanot, F., De Lucia, G., Erwin, P., & Monaco, P. 2013, MNRAS, 433, 2986
Yang, Y., Hammer, F., Flores, H., Puech, M., & Rodrigues, M. 2009, A&A, 501, 437
Zentner, A. R., Kravtsov, A. V., Gnedin, O. Y., & Klypin, A. A. 2005, ApJ, 629, 219

Pages 21 to 23 are available in the electronic edition of the journal at <http://www.aanda.org>

M. Querejeta et al.: Bulge-disc structural coupling in S0s resulting from major mergers

Table 3. Characteristic photometric parameters of the bulges and discs of the S0-like relaxed remnants in the K band.

No.	Model	Morph	Fit	r_{\min} [kpc]	r_{\max} [kpc]	χ^2 [mag]	r_e [kpc]	n	l_{d} [kpc]	B/T	D/T	$M_K(\text{total})$ [mag]
(1)	(2)	(3)	(4)	(5)	(6)	(7)	(8)	(9)	(10)	(11)	(12)	(13)
–	Original gE0	E	B	0.5	13.4	0.069	3.67863 ± 0.712	0.99 ± 0.15	...	1.0	0.0	–25.11
–	Original gS0	S0	B+C+D	0.5	16.1	0.063	0.88957 ± 0.078	1.00 ± 0.12	4.1 ± 2.9	0.20 ± 0.039	0.555027 ± 0.000013	–24.74
–	Original gSa	Sa	B+C+D	0.3	11.6	0.022	2.53212 ± 0.577	0.89 ± 0.25	4.2 ± 1.0	0.40 ± 0.18	0.59 ± 0.12	–25.16
–	Original gSb	Sb	B+C+D	0.5	15.0	0.173	0.96842 ± 2.712	1.8 ± 1.0	4.2 ± 2.3	0.27 ± 0.12	0.72030 ± 0.00073	–24.55
–	Original gSd	Sd	D	0.5	18.0	0.265	4.677 ± 0.032	0.0	1.0	–24.77
1	gE0gSao1	S0	B+C+D	0.5	21.4	0.082	1 ± 16	2.47 ± 0.67	6.15 ± 0.95	0.48140 ± 0.00026	0.27 ± 0.33	–26.01
2	gE0gSao5	S0	B+C+D	0.5	23.5	0.071	0.9 ± 7.8	1.0 ± 1.7	5.30 ± 0.65	0.24 ± 0.20	0.46 ± 0.17	–25.99
3	gE0gSao16	S0	B+C+D	0.5	26.5	0.676	1.60 ± 0.33	3.65 ± 0.35	4.8 ± 2.6	0.452 ± 0.018	0.4647 ± 0.0015	–26.02
4	gE0gSao44	S0	B+C+D	1.0	14.4	0.261	1.98 ± 0.10	4.00 ± 0.88	3.633 ± 0.086	0.594 ± 0.082	0.363 ± 0.048	–26.00
5	gE0gSbo5	S0	B+C+D	0.7	22.3	0.126	3.33 ± 0.40	2.34 ± 0.40	14.5 ± 6.6	0.629 ± 0.087	0.131 ± 0.094	–25.75
6	gE0gSbo44	S0	B+C+D	1.0	23.5	0.205	3.42 ± 0.18	1.339 ± 0.092	20 ± 18	0.67 ± 0.17	0.31 ± 0.20	–25.74
7	gE0gSdo5	S0	B+C+D	1.0	20.0	0.286	3.76 ± 0.24	1.251 ± 0.086	20.6 ± 1.7	0.696 ± 0.091	0.261 ± 0.013	–25.94
8	gE0gSdo16	S0	B+C+D	0.5	27.9	0.672	2.660 ± 0.069	2.773 ± 0.071	12.4 ± 6.8	0.70 ± 0.12	0.18 ± 0.14	–25.96
9	gE0gSdo44	S0	B+C+D	0.7	28.7	1.692	2.65 ± 0.80	1.12 ± 0.50	6.1 ± 2.8	0.54 ± 0.13	0.37 ± 0.14	–25.95
10	gS0dE0o98	S0	B+D	0.5	19.0	0.032	1.552 ± 0.016	1.477 ± 0.042	6.175 ± 0.058	0.5764 ± 0.0045	0.4235 ± 0.0045	–24.89
11	gS0dE0o99	S0	B+C+D	0.5	19.0	0.018	1.39 ± 0.36	1.400 ± 0.082	5.8 ± 1.7	0.533 ± 0.031	0.414453 ± 0.00007	–24.89
12	gS0dE0o100	S0	B+C+D	0.5	19.2	0.015	1.43 ± 1.65	1.49 ± 0.82	6.6 ± 16.5	0.56 ± 0.11	0.367982 ± 0.00002	–24.89
13	gS0dE0o101	S0	B+C+D	0.5	19.6	0.018	1.65 ± 0.10	1.78 ± 0.14	8.44 ± 4.5	0.630 ± 0.033	0.3442 ± 0.0096	–24.89
14	gS0dE0o102	S0	B+C+D	0.5	20.2	0.022	1.52 ± 0.24	1.43 ± 0.20	6.76 ± 0.13	0.581 ± 0.062	0.3935 ± 0.0075	–24.89
15	gS0dE0o103	S0	B+C+D	0.5	18.1	0.015	1.384 ± 0.056	1.334 ± 0.010	4.9636 ± 0.0037	0.52139 ± 0.00075	0.468352 ± 0.00001	–24.89
16	gS0dE0o104	S0	B+C+D	0.5	19.0	0.019	1.26 ± 0.28	1.1 ± 1.1	5.3 ± 15.9	0.46 ± 0.18	0.450404 ± 0.00024	–24.89
17	gS0dE0o105	S0	B+C+D	0.5	18.2	0.016	1.346 ± 0.029	1.28 ± 0.10	5.17 ± 0.28	0.528 ± 0.019	0.427 ± 0.034	–24.89
18	gS0dE0o106	S0	B+C+D	0.5	18.6	0.021	1.388 ± 0.026	1.247 ± 0.063	6.36 ± 0.31	0.536 ± 0.010	0.343 ± 0.023	–24.89
19	gS0dE0o109	S0	B+C+D	0.5	19.4	0.018	1.49 ± 0.61	1.52 ± 0.69	6.3 ± 3.7	0.575 ± 0.075	0.408585 ± 0.000012	–24.89
20	gS0dE0o110	S0	B+C+D	0.5	18.4	0.029	1.82 ± 0.52	1.104 ± 0.010	5.56 ± 0.13	0.461 ± 0.029	0.439322 ± 0.000007	–24.89
21	gS0dE0o111	S0	B+C+D	0.5	19.5	0.020	1.37 ± 0.19	1.29 ± 0.38	6.3 ± 6.3	0.512 ± 0.060	0.394 ± 0.053	–24.89
22	gS0dE0o113	S0	B+C+D	0.5	18.7	0.016	1.36 ± 0.24	1.31 ± 0.61	5.6 ± 4.9	0.525 ± 0.092	0.411068 ± 0.000002	–24.89
23	gS0dE0o115	S0	B+C+D	0.5	19.2	0.034	1.28 ± 0.50	1.16 ± 0.28	7.14 ± 0.39	0.475 ± 0.091	0.365 ± 0.011	–24.89
24	gS0dE0o117	S0	B+C+D	0.5	19.2	0.034	1.28 ± 0.38	1.16 ± 0.31	7.14 ± 0.40	0.47 ± 0.10	0.365 ± 0.013	–24.89
25	gS0dS0o97	S0	B+D	0.5	19.6	0.033	1.514 ± 0.014	1.124 ± 0.021	5.679 ± 0.019	0.5519 ± 0.0027	0.4480 ± 0.0027	–24.85
26	gS0dS0o98	S0	B+C+D	0.5	20.4	0.025	1.3 ± 2.3	1.435 ± 0.010	6.7 ± 3.5	0.497 ± 0.047	0.412 ± 0.042	–24.85
27	gS0dS0o99	S0	B+C+D	0.5	19.6	0.020	1.30 ± 0.13	1.057 ± 0.010	5.92 ± 0.31	0.4721 ± 0.0063	0.444035 ± 0.000006	–24.85
28	gS0dS0o100	S0	B+C+D	0.5	18.8	0.015	1.4 ± 1.2	1.333 ± 0.010	6.72 ± 0.35	0.582 ± 0.019	0.389 ± 0.030	–24.85

Notes. *Columns:* (1) Number ID. (2) Model code: `g[type][lg[type2]o[#orbit]`, see Sect. 2. (3) Visual morphological type assigned according to realistic broad-band simulated images (see Sect. 3.1). (4) Multicomponent decomposition performed to the K -band surface brightness profile: bulge+disc (B+D) or bulge+[inner component]+disc (B+C+D). We have assumed only an spheroidal component to fit the gE0 progenitor (B) and just an exponential disc in the gSd progenitor (D). The additional inner component has been modelled with a Sérsic profile, and it may correspond to a lense, oval, bar, inner disc, or to several of them depending on the case (see Sect. 3.3). (5) Minimum radius of data included in the fit, in kpc. (6) Maximum radius of data included in the fit, in kpc. (7) χ^2 of the fit, in mag². (8) Bulge effective radius r_e , in kpc. (9) Bulge Sérsic index n . (10) Disc e-folding scalelength l_{d} , in kpc. (11) Bulge-to-total luminosity ratio. (12) Disc-to-total luminosity ratio. (13) Total absolute magnitude of the galaxy in the K band. All parameters have been derived from the multicomponent decompositions performed to the simulated K -band surface brightness profiles of the stellar progenitors and remnants. The bulge Sérsic index had to be fixed to $n = 4$ in two models (no errors are thus indicated in these cases).

Table 3. continued.

No.	Model	Morph	Fit	r_{\min} [kpc]	r_{\max} [kpc]	χ^2 [mag]	r_c [kpc]	n	h_d [kpc]	B/T	D/T	$M_K(\text{total})$ [mag]
(1)	(2)	(3)	(4)	(5)	(6)	(7)	(8)	(9)	(10)	(11)	(12)	(13)
29	gS0dS0o101	S0	B+C+D	1.0	20.0	0.023	1.3 ± 2.2	1.094 ± 0.010	6.9 ± 5.1	0.504 ± 0.020	0.380 ± 0.049	-24.85
30	gS0dS0o102	S0	B+C+D	0.5	19.6	0.021	1.339 ± 0.037	1.228 ± 0.064	6.481 ± 0.017	0.495 ± 0.053	0.402017 ± 0.000014	-24.85
31	gS0dS0o103	S0	B+C+D	0.3	18.0	0.029	1.12 ± 0.39	0.99 ± 0.57	4.623 ± 0.032	0.405 ± 0.051	0.485484 ± 0.000004	-24.85
32	gS0dS0o105	S0	B+C+D	0.5	17.7	0.017	1.36 ± 0.27	1.37 ± 0.69	5.0 ± 5.0	0.527 ± 0.066	0.443 ± 0.017	-24.85
33	gS0dS0o10	S0	B+C+D	0.5	18.4	0.023	1.34 ± 0.14	1.20 ± 0.22	5.332 ± 0.011	0.505 ± 0.010	0.449624 ± 0.000004	-24.91
34	gS0dS0o103	S0	B+C+D	0.5	18.4	0.017	1.43 ± 0.35	1.549 ± 0.040	5.458 ± 0.017	0.532 ± 0.020	0.430047 ± 0.000009	-24.91
35	gS0dS0o105	S0	B+C+D	0.5	18.3	0.021	1.32 ± 0.16	1.11 ± 0.32	5.219 ± 0.043	0.476 ± 0.015	0.457874 ± 0.000006	-24.91
36	gS0dS0o106	S0	B+C+D	0.5	17.9	0.018	1.14 ± 0.15	1.05 ± 0.25	5.04 ± 0.74	0.404 ± 0.012	0.451761 ± 0.000014	-24.91
37	gS0dS0o106	S0	B+D	0.3	17.7	0.042	1.355 ± 0.053	1.073 ± 0.010	4.824 ± 0.024	0.52 ± 0.34	0.47 ± 0.34	-24.84
38	gS0dS0o100	S0	B+D	0.3	18.6	0.032	1.529 ± 0.015	1.241 ± 0.021	6.082 ± 0.036	0.5805 ± 0.0026	0.4194 ± 0.0026	-24.87
39	gS0dS0o1	S0	B+C+D	0.5	26.9	0.229	2.139 ± 0.034	2.54 ± 0.11	7.329 ± 0.040	0.674 ± 0.011	0.263 ± 0.011	-26.10
40	gS0dS0o5	S0	B+D	0.3	23.9	0.264	1.540 ± 0.062	1.77 ± 0.10	4.9110 ± 0.0057	0.54 ± 0.17	0.45 ± 0.17	-26.13
41	gS0dS0o9	S0	B+D	0.5	23.1	0.328	1.235 ± 0.086	2.25 ± 0.12	4.922 ± 0.017	0.637969 ± 0.000002	0.362003 ± 0.000001	-26.13
42	gS0dS0o1	S0	B+C+D	0.5	25.2	0.588	1.10 ± 0.80	1.3 ± 1.6	5.3 ± 9.1	0.44 ± 0.25	0.382913 ± 0.000003	-25.89
43	gS0dS0o2	S0	B+C+D	0.5	20.6	0.262	1.46 ± 0.73	1.9 ± 1.3	5.3 ± 9.8	0.56 ± 0.16	0.38485 ± 0.00018	-25.90
44	gS0dS0o5	E/S0	B+C+D	0.5	22.3	0.106	1.12 ± 0.45	1.2 ± 1.2	5.9 ± 11.1	0.45 ± 0.17	0.43 ± 0.15	-25.91
45	gS0dS0o9	S0	B+C+D	1.7	24.3	0.132	1.797 ± 0.097	1.13 ± 0.62	10.04 ± 0.81	0.497 ± 0.075	0.331 ± 0.031	-25.92
46	gS0dS0o21	S0	B+C+D	0.8	16.6	0.046	1.28 ± 0.43	2.13 ± 0.62	5.210 ± 0.028	0.461 ± 0.035	0.452291 ± 0.000006	-25.91
47	gS0dS0o22	S0	B+C+D	0.5	22.7	0.266	0.50 ± 0.21	2.147 ± 0.010	4.920 ± 0.023	0.398 ± 0.010	0.403996 ± 0.000001	-25.92
48	gS0dS0o24	S0	B+C+D	0.5	26.3	0.128	0.83 ± 0.24	3.983 ± 0.010	7.02 ± 0.20	0.648 ± 0.015	0.289063 ± 0.000027	-25.92
49	gS0dS0o42	E/S0	B+C+D	1.1	25.1	0.138	0.86 ± 0.39	1.159 ± 0.010	6.001 ± 0.065	0.306 ± 0.010	0.450835 ± 0.000001	-25.89
50	gS0dS0o43	E/S0	B+C+D	1.5	25.6	0.127	0.9 ± 2.2	1.16 ± 0.58	6.1 ± 1.9	0.34 ± 0.15	0.454 ± 0.020	-25.89
51	gS0dS0o71	E/S0	B+C+D	0.5	20.7	0.114	0.701 ± 0.089	1.2830 ± 0.0081	4.5038 ± 0.0098	0.3854 ± 0.0052	0.435689 ± 0.000001	-25.88
52	gS0dS0o2	S0	B+C+D	2.0	25.7	0.235	1.78 ± 0.86	1.2 ± 1.5	6.1 ± 2.7	0.39 ± 0.27	0.47 ± 0.17	-26.07
53	gS0dS0o5	S0	B+C+D	0.7	30.9	3.771	0.95 ± 0.10	1.094 ± 0.097	5.4 ± 6.9	0.393 ± 0.059	0.469 ± 0.058	-26.07
54	gS0dS0o9	S0	B+C+D	0.5	24.8	0.395	1.28 ± 0.12	2.065 ± 0.405	8.16 ± 0.64	0.543 ± 0.041	0.394 ± 0.023	-26.07
55	gS0dS0o14	E/S0	B+D	1.0	28.3	1.085	2.70 ± 0.49	2.145 ± 0.010	16.4 ± 1.0	0.651 ± 0.019	0.348 ± 0.019	-26.03
56	gS0dS0o18	E/S0	B+C+D	0.5	24.6	0.236	2.8 ± 1.2	1.03 ± 0.44	5.7 ± 5.2	0.33 ± 0.13	0.39 ± 0.13	-26.03
57	gS0dS0o41	E/S0	B+C+D	1.0	25.0	0.346	1.47 ± 0.27	2.54 ± 0.87	9.81 ± 0.70	0.621 ± 0.096	0.280 ± 0.087	-26.04
58	gS0dS0o42	S0	B+C+D	1.0	31.7	3.530	1.01 ± 0.11	1.452 ± 0.010	5.4482 ± 0.0078	0.3864 ± 0.0016	0.505225 ± 0.000001	-26.04
59	gS0dS0o43	E/S0	B+C+D	1.2	27.9	0.714	1.10 ± 0.75	1.10 ± 0.49	5.8 ± 2.5	0.353 ± 0.052	0.530 ± 0.055	-26.06
60	gS0dS0o70	E/S0	B+C+D	1.0	25.7	0.352	1.05 ± 0.25	1.16 ± 0.81	8.0 ± 1.8	0.395 ± 0.089	0.401 ± 0.049	-26.04
61	gS0dS0o71	E/S0	B+C+D	1.5	30.1	0.434	1.19 ± 0.45	1.4 ± 1.5	10.0 ± 1.6	0.39 ± 0.16	0.323 ± 0.091	-26.05
62	gS0dS0o73	E/S0	B+D	1.5	26.5	0.364	1.8596 ± 0.0085	2.7784 ± 0.0083	6.786 ± 0.010	0.661 ± 0.010	0.338 ± 0.010	-26.08
63	gS0dS0o9	S0	B+C+D	0.7	23.7	0.093	1.00 ± 0.26	1.012 ± 0.010	9.78 ± 3.9	0.323 ± 0.022	0.394 ± 0.036	-25.61
64	gS0dS0o16	E/S0	B+C+D	1.0	23.3	0.117	2.50 ± 0.35	2.00 ± 0.36	11.568 ± 0.99	0.56 ± 0.10	0.361 ± 0.019	-25.63
65	gS0dS0o17	E/S0	B+D	1.5	22.5	0.121	2.641 ± 0.047	1.112 ± 0.068	5.335 ± 0.20	0.609 ± 0.025	0.390 ± 0.025	-25.62
66	gS0dS0o19	E/S0	B+C+D	0.5	20.6	0.080	3.79 ± 0.71	3.25 ± 0.44	4.4415 ± 0.0019	0.29 ± 0.10	0.391338 ± 0.000004	-25.62
67	gS0dS0o22	S0	B+D	1.0	22.6	0.196	1.43 ± 0.11	2.42 ± 0.20	6.2040 ± 0.0051	0.61 ± 0.23	0.38 ± 0.23	-25.63
68	gS0dS0o41	E/S0	B+C+D	0.5	20.6	0.055	3.02 ± 0.38	1.00 ± 0.14	4.6704 ± 0.0035	0.170 ± 0.060	0.535280 ± 0.000001	-25.61
69	gS0dS0o42	E/S0	B+C+D	0.5	21.3	0.106	0.62 ± 0.61	2.61 ± 0.54	5.5 ± 2.5	0.462 ± 0.057	0.396057 ± 0.000010	-25.60
70	gS0dS0o69	E/S0	B+C+D	2.5	24.1	0.105	3.14 ± 0.22	1.02 ± 0.45	9.5 ± 3.1	0.597 ± 0.051	0.293 ± 0.055	-25.60
71	gS0dS0o70	E/S0	B+C+D	1.5	24.2	0.121	1.32 ± 0.61	1.1 ± 1.8	12.1 ± 2.4	0.37 ± 0.18	0.349 ± 0.094	-25.59

M. Querejeta et al.: Bulge-disc structural coupling in S0s resulting from major mergers

Table 3. continued.

No.	Model	Morph	Fit	r_{\min} [kpc]	r_{\max} [kpc]	χ^2 [mag]	r_c [kpc]	n	h_d [kpc]	B/T	D/T	$M_K(\text{total})$ [mag]
(1)	(2)	(3)	(4)	(5)	(6)	(7)	(8)	(9)	(10)	(11)	(12)	(13)
72	gSbgSbo72	S0	B+D	2.0	24.2	0.108	1.9 ± 1.0	2.580 ± 0.010	9.2 ± 2.9	0.57 ± 0.16	0.42 ± 0.16	-25.65
73	gSbgSdo5	S0	B+C+D	0.5	22.6	0.456	0.791 ± 0.040	1.32 ± 0.21	5.23 ± 0.20	0.402 ± 0.026	0.426 ± 0.019	-25.84
74	gSbgSdo9	S0	B+C+D	0.5	24.6	0.181	0.66 ± 0.74	1.91 ± 0.74	6.6 ± 2.9	0.39 ± 0.11	0.442 ± 0.063	-25.82
75	gSbgSdo14	S0	B+C+D	1.5	22.8	0.453	2.2 ± 3.3	1.0 ± 1.8	14.6 ± 9.5	0.30074 ± 0.00061	0.38 ± 0.21	-25.81
76	gSbgSdo17	S0	B+C+D	0.5	21.8	0.659	0.991 ± 0.095	2.202 ± 0.064	4.795 ± 0.035	0.524288 ± 0.000002	0.475646 ± 0.000001	-25.83
77	gSbgSdo18	S0	B+C+D	1.5	24.9	0.560	2.3 ± 1.4	1.253 ± 2.080	8.8 ± 12.1	0.47 ± 0.28	0.41 ± 0.19	-25.83
78	gSbgSdo19	S0	B+C+D	0.3	26.6	0.395	2.24 ± 0.49	1.00 ± 0.36	5.6 ± 4.3	0.511 ± 0.094	0.467 ± 0.094	-25.81
79	gSbgSdo23	E/S0	B+C+D	1.0	26.4	0.399	4.29 ± 0.52	1.00 ± 0.29	6.8 ± 2.3	0.40 ± 0.10	0.361 ± 0.042	-25.85
80	gSbgSdo41	S0	B+D	0.3	24.4	0.311	2.989 ± 0.082	1.153 ± 0.074	6.0 ± 1.3	0.607 ± 0.015	0.392 ± 0.015	-25.81
81	gSbgSdo69	S0	B+C+D	0.3	26.0	0.356	2.993 ± 0.075	1.08 ± 0.10	7.98 ± 0.39	0.470 ± 0.042	0.392 ± 0.010	-25.81
82	gSbgSdo70	S0	B+C+D	2.5	23.8	0.423	3.0 ± 1.0	1.7 ± 1.4	13.9 ± 10.2	0.53 ± 0.19	0.44 ± 0.18	-25.82
83	gSbgSdo71	E/S0	B+C+D	1.2	23.4	0.695	1.15 ± 0.43	2.1 ± 1.7	8.0 ± 1.8	0.47 ± 0.18	0.33 ± 0.11	-25.82
84	gSdgSdo1	E/S0	B+C+D	1.0	27.4	1.801	0.7 ± 5.0	4.0	8.2 ± 2.2	0.282 ± 0.095	0.404461 ± 0.000005	-26.03
85	gSdgSdo2	S0	B+C+D	1.3	27.3	0.267	2.93 ± 0.68	1.03 ± 0.26	8.0 ± 3.5	0.39 ± 0.18	0.45 ± 0.11	-26.04
86	gSdgSdo5	S0	B+C+D	2.0	27.8	0.559	2.2 ± 5.8	1.0 ± 1.2	11.2 ± 3.1	0.24 ± 0.28	0.42 ± 0.21	-26.02
87	gSdgSdo9	S0	B+C+D	1.3	28.3	0.654	2.32 ± 0.34	3.01 ± 0.14	6.380 ± 0.042	0.4690 ± 0.0088	0.496339 ± 0.000002	-26.03
88	gSdgSdo16	E/S0	B+D	0.3	31.8	2.354	2.98 ± 0.16	1.197 ± 0.093	6.67 ± 0.42	0.466 ± 0.033	0.533 ± 0.033	-25.97
89	gSdgSdo17	S0	B+C+D	1.0	29.4	2.561	3.11 ± 0.50	1.07 ± 0.34	5.3 ± 7.9	0.36 ± 0.10	0.446 ± 0.063	-26.00
90	gSdgSdo21	E/S0	B+C+D	1.5	29.5	0.411	0.9 ± 1.4	1.467 ± 0.010	7.9 ± 2.6	0.381 ± 0.042	0.460 ± 0.039	-25.99
91	gSdgSdo42	S0	B+C+D	1.0	25.5	0.639	0.251 ± 0.010	2.951 ± 0.010	5.68 ± 0.23	0.401019 ± 0.000013	0.466 ± 0.025	-25.99
92	gSdgSdo45	E/S0	B+C+D	1.0	24.4	0.286	2.383 ± 0.048	1.158 ± 0.010	5.6 ± 1.8	0.345 ± 0.022	0.439 ± 0.029	-25.99
93	gSdgSdo51	E/S0	B+C+D	1.5	26.1	0.257	1.2 ± 1.0	1.41 ± 0.51	6.7 ± 1.1	0.333 ± 0.036	0.51926 ± 0.00088	-26.07
94	gSdgSdo69	S0	B+C+D	1.0	28.3	1.122	3.12 ± 0.17	1.000 ± 0.066	5.2505 ± 0.0055	0.121 ± 0.017	0.562326 ± 0.000001	-25.97
95	gSdgSdo71	S0	B+C+D	0.3	27.1	0.689	2.627 ± 0.021	1.264 ± 0.052	11.68 ± 0.14	0.6520 ± 0.0093	0.3090 ± 0.0058	-26.00
96	gSdgSdo74	S0	B+C+D	1.0	30.2	0.838	3.4 ± 3.9	4.0	8.9 ± 1.8	0.671 ± 0.097	0.275 ± 0.074	-26.01

Chapter 6

Making discs passive with major mergers: kinematics

Here we confirm that the findings from Chapter 5 also agree with recent observational results on the kinematics of lenticular galaxies. Major mergers of spirals simultaneously make galaxies more concentrated and lower their rotational support, in agreement with observations from the CALIFA team. This letter has been published in *Astronomy & Astrophysics*, 579, 2 (Querejeta et al. 2015b).

L E

Formation of S0 galaxies through mergers[★]

Explaining angular momentum and concentration change from spirals to S0s

M. Querejeta¹, M. C. Eliche-Moral², T. Tapia³, A. Borlaff⁴, G. van de Ven¹, M. Lyubenova⁵, M. Martig¹,
 J. Falcón-Barroso⁴, and J. Méndez-Abreu⁶

¹ Max Planck Institute for Astronomy, Königstuhl 17, 69117 Heidelberg, Germany
 e-mail: querejeta@mpia-hd.mpg.de

² Departamento de Astrofísica y Ciencias de la Atmósfera, Universidad Complutense de Madrid, 28040 Madrid, Spain

³ Instituto de Astronomía, Universidad Nacional Autónoma de México, BC-22800 Ensenada, Mexico

⁴ Instituto de Astrofísica de Canarias, C/vía Láctea, 38200 La Laguna, Tenerife, Spain

⁵ Kapteyn Astronomical Institute, University of Groningen, Postbus 800, 9700 Groningen, The Netherlands

⁶ School of Physics and Astronomy, University of St Andrews, North Haugh, St Andrews, KY16 9SS, UK

Received 19 April 2015 / Accepted 26 May 2015

ABSTRACT

The CALIFA team has recently found that the stellar angular momentum and concentration of late-type spiral galaxies are incompatible with those of lenticular galaxies (S0s), concluding that fading alone cannot satisfactorily explain the evolution from spirals into S0s. Here we explore whether major mergers can provide an alternative way to transform spirals into S0s by analysing the spiral-spiral major mergers from the GalMer database that lead to realistic, relaxed S0-like galaxies. We find that the change in stellar angular momentum and concentration can explain the differences in the $\lambda_{\text{Re}}-R_{90}/R_{50}$ plane found by the CALIFA team. Major mergers thus offer a feasible explanation for the transformation of spirals into S0s.

Key words. galaxies: interactions – galaxies: evolution – galaxies: kinematics and dynamics – galaxies: elliptical and lenticular, cD

1. Introduction

A kinematic classification of early-type galaxies (ETGs) might more closely reflect their true physical nature than photometry-based morphological classifications, which can be biased by inclination effects. In this sense, the ratio between ordered and random motion, V/σ , has long been used as a proxy for the rotational support of a galaxy: disc-like, rotation-dominated galaxies are intuitively associated with the highest V/σ , while the lowest values are expected in spheroidal-like, dispersion-dominated galaxies. With the advent of integral field spectroscopy, the SAURON and ATLAS^{3D} teams developed an improved parameter, λ_{Re} , which divides galaxies into two groups: fast and slow rotators (FRs and SRs, respectively; Emsellem et al. 2007, 2011; Cappellari et al. 2011a). Based on this kinematic definition, most spirals and lenticulars (S0s) are classified as FRs, while ellipticals are found in both groups.

In the quest to understand the origin of FRs and SRs, a number of studies have focused on simulations. Jesseit et al. (2009) showed that λ_{Re} is a good indicator of the true stellar angular momentum in ETGs, and studied their possible merger origin, including the effect of gas. They already stated that the mass ratio of the encounter is crucial to determining the outcome as a SR or FR. This is in agreement with studies pointing to equal-mass mergers as the most likely origin of elliptical galaxies (Naab & Burkert 2003; Springel et al. 2005; Hoffman et al. 2010; Duc et al. 2011; Tsatsi et al. 2015). The results from Bois et al. (2011) also support this idea, and underline the role of spin (within 1:1 and 1:2 mergers, SRs are associated with retrograde and FRs

with prograde encounters). These authors study the incidence of kinematic misalignments and kinematically decoupled cores, which are found primarily in SRs; however, they cannot explain the round SRs observed in ATLAS^{3D}. A similar study with an exhaustive exploration of the parameter space was undertaken by Moody et al. (2014), who conclude that round SRs can emerge from the accumulation of many minor mergers, while FRs may be formed through a variety of pathways. The idea that ETGs might have been sculpted through multiple mergers is not new (Barnes 1985; Weil & Hernquist 1996; Bekki 2001; Bournaud et al. 2007), and in fact different studies have analysed the effects of minor and intermediate mergers onto early-type progenitors (see e.g. Bournaud et al. 2004; Di Matteo et al. 2009; Eliche-Moral et al. 2011; Hilz et al. 2013; Mapelli et al. 2015; Zinchenko et al. 2015). Using mock kinematic maps extracted from cosmological simulations, Naab et al. (2014) have recently confirmed that, even if the formation histories can be complex, the main results in a cosmological context are in full agreement with the conclusions drawn from idealised mergers.

As a consequence of the kinematic classification of ETGs, it has become apparent that most S0s are FRs and have kinematic properties that make them comparable to spirals (Cappellari et al. 2011b; Krajnović et al. 2011). Together with the fact that S0s span a whole range of bulge-to-disc ratios, this led Laurikainen et al. (2010), Cappellari et al. (2011b), and Kormendy & Bender (2012) to propose a sequence of S0s parallel to that of spirals (i.e. S0a – S0b – S0c). This recovers the original idea of Spitzer & Baade (1951) and van den Bergh (1976), bringing back the question of whether the classification parallelism reflects an underlying physical connection: are S0s faded spirals?

[★] Table 1 is available in electronic form at <http://www.aanda.org>

A&A 579, L2 (2015)

Observations show that gas stripping, e.g. from ram pressure in clusters, can effectively transform spirals into S0s (Crowl et al. 2005; Aragón-Salamanca et al. 2006; Crowl & Kenney 2008; Maltby et al. 2015). This constitutes an example of fading (any processes resulting in the suppression of star formation), and it can contribute to explaining the observational morphology-density relation in high-density regimes (Dressler 1980; Dressler et al. 1997; but see Cappellari et al. 2011).

However, we know that S0s do not preferentially inhabit the densest cluster environments; they are equally common in groups (Wilman et al. 2009; Bekki & Couch 2011), where mergers and tidal effects dominate (Mazzei et al. 2014a,b). Additionally, traces of past mergers have been observed in some S0s (e.g. Falcón-Barroso et al. 2004). Therefore, it seems compelling to study under which conditions S0s could emerge out of mergers, and their impact on the observed kinematics.

The CALIFA team has recently raised further doubts about S0s as faded spirals through a new diagnostic diagram: the λ_{Re} -concentration plane (van de Ven et al., in prep.). The population of late-type spirals (Sb, Sc, Sd) shows a clear incompatibility with S0s when both angular momentum (λ_{Re}) and concentration (R_{90}/R_{50}) are simultaneously taken into account. Provided that simple fading is not expected to significantly change the angular momentum of the galaxy, this contradicts the idea that *most* S0s are faded spirals. Here, we study whether major mergers can explain those differences using N -body dissipative simulations from the GalMer database. We will analyse the encounters that end up in relaxed S0-like remnants, showing that the induced changes in ellipticity, stellar angular momentum, and concentration are in agreement with the CALIFA observations.

2. Binary merger models

GalMer¹ is a public database of binary N -body merger simulations that sample a wide range of mass ratios, morphological types, and orbital characteristics. The progenitor galaxies are modelled using a spherical non-rotating dark-matter halo, an optional disc and bulge, with a spatial resolution of 0.28 kpc and $\sim 10^5$ particles per galaxy. The simulations use a TreeSPH code (Semelin & Combes 2002), and take into account the effects of gas and star formation, with total simulation times in the range 3–4 Gyr, which typically implies ~ 1 Gyr of relaxation after full merger (see Chilingarian et al. 2010, for more details).

2.1. Lenticular remnants

We consider the major mergers (mass ratios 1:1 to 1:3) involving all possible combinations of two spiral progenitors (Sa, Sb, or Sd) that give rise to realistic, dynamically-relaxed S0-like remnants, based on quantitative criteria that impose structural, kinematic, SFR, and gas-content parameters typical of lenticular galaxies (Eliche-Moral et al., in prep.). In addition, we have performed a visual morphological classification to identify which remnants would have been classified as S0-like by observers (i.e. as disc galaxies without noticeable spiral arms). To this end, we have simulated photometric images of the resulting galaxies in several broad bands (B , V , R , I , and K), mimicking typical conditions of current observational surveys. We use a mass-to-light ratio which considers the stellar mass, age, and metallicity of each simulation particle according to Bruzual & Charlot (2003), with a Chabrier IMF and the Padova evolutionary tracks; for details, see Borlaff et al. (2014) and Querejeta et al. (2015). This provides us with a final sample of 67 S0-like remnants, which will be the focus of this Letter (see Table 1).

¹ GalMer project: <http://galmer.obspm.fr>

2.2. Stellar angular momentum, ellipticity, and concentration

We assume that the simulated merger remnants are observed at the median distance of the 300 CALIFA galaxies in Falcón-Barroso et al. (in prep.): $D_{\text{median}} = 67$ Mpc. We also consider the same spatial resolution and field of view as the survey, $\text{PSF}_{\text{FWHM}} = 1.6''$, $R_{\text{max}} = 35''$ (Sánchez et al. 2012).

We calculate λ_e according to Emsellem et al. (2011),

$$\lambda_e = \frac{\sum F_i R_i |V_i|}{\sum F_i R_i \sqrt{V_i^2 + \sigma_i^2}}, \quad (1)$$

where F_i , R_i , V_i , and σ_i are the flux (using an appropriate mass-to-light ratio), radius, velocity, and velocity dispersion measured within each spatial bin out to the effective radius of the galaxy ($R \leq R_e$). The ellipticity at the effective radius ε_e is obtained from interpolation of the curve of growth of the luminosity-weighted ellipticities within increasingly larger isophotes.

The Petrosian concentration parameter R_{90}/R_{50} is defined as the ratio of the radii enclosing 90% and 50% of the Petrosian flux, measured on the 1D azimuthally averaged radial surface brightness profile in the simulated SDSS r band. According to Gadotti (2009), there is an equivalence between R_{90}/R_{50} and bulge-to-total ratio: $R_{90}/R_{50} = 1.93 + 2.02(B + \text{bar})/T$, which we add on top of our plot for reference. This relation is valid for $(B + \text{bar})/T < 0.6$, but then flattens for higher values; thus, the upper axis in the right panel of Fig. 1 must be interpreted with caution for $(B + \text{bar})/T > 0.6$.

3. Results

3.1. Angular momentum versus ellipticity

We compare the distribution of the remnants in the $\lambda_{\text{Re}} - \varepsilon_e$ plane with the real galaxies from the CALIFA survey. The spiral progenitor models lie in the region of FRs, as expected.

Naturally, for a meaningful comparison with observational data, one has to consider projection effects: the maximum λ_{Re} is attained for an edge-on view, and it is closer to the real angular momentum (Jesseit et al. 2009); for this reason, we compare our results with the CALIFA measurements *corrected for inclination*. The deprojection of λ_{Re} to edge-on follows van de Ven et al. (in prep.), assuming $\delta = 0.5$ for the global anisotropy (the mean value of the distribution proposed by Cappellari et al. 2007), but we check that varying it by $\pm 1\sigma$ has a $< 3\%$ effect on the resulting deprojected values. When deprojecting ε_e , due to observational uncertainties in the inclination, the result is unfeasible for a few cases, in which we assume the maximum $\varepsilon_{\text{intr}} = 1$.

The left panel of Fig. 1 shows that major mergers can produce both fast- and slow-rotating S0s (9 out the 67 S0-like remnants are SRs). While only one SR S0s is present in the first CALIFA kinematic sample, in ATLAS^{3D}, 13 out of the 36 SRs were S0-like (Cappellari et al. 2011a). We also find that, in agreement with previous studies, mergers tend to reduce both the stellar angular momentum λ_{Re} and ellipticity ε_e by an amount that varies largely depending on the mass ratio, gas fractions, and orbital characteristics (Jesseit et al. 2009; Bois et al. 2011; Tapia et al. 2014; Naab et al. 2014). In this diagram, real spirals (especially Sb and Sc) have a very limited overlap with S0s. Remarkably, the S0-like remnants that we find in these simulations are in excellent agreement with the real S0s, and far from the progenitor spirals that they originate from. This is a first hint that a good fraction of S0s could have originated through a mechanism involving mergers.

M. Querejeta et al.: Origin of S0s: Disentangling major mergers from fading

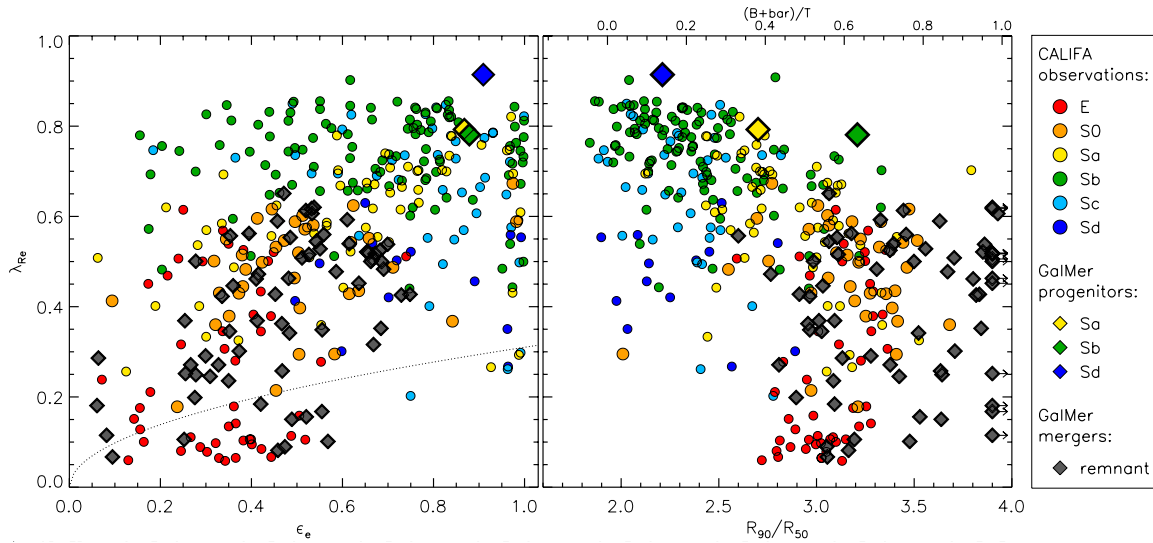


Fig. 1. Stellar angular momentum (λ_{Re}) plotted against the ellipticity (ϵ_e , *left*) and concentration (R_{90}/R_{50} , *right*) for the GalMer simulations (original models and merger remnants), in comparison to CALIFA galaxies. All the parameters correspond to an edge-on view. The dotted line in the *left plot* represents the division between fast and slow rotators, and the top axis in the *right plot* is from Gadotti (2009), valid only up to $(B + \bar{b})/T < 0.6$. See legend at the right for the symbols and colour-coding.

3.2. Angular momentum versus concentration

As mentioned in Sect. 1, the differences between spirals and S0s become more striking in the λ_{Re} -concentration plane introduced by van de Ven et al. (in prep.). The right panel of Fig. 1 compares the distribution of our remnant S0s with that of real galaxies from CALIFA in λ_{Re} versus R_{90}/R_{50} , showing that S0s resulting from major mergers are consistent with real lenticulars. In this plane, Sb and Sc galaxies clearly cluster towards the top-left corner; Sa galaxies show a larger scatter, extending down diagonally towards the bottom-right, where S0 and E galaxies are located. The number of Sd galaxies in this first CALIFA kinematic sample is small, but they also show little overlap with S0s.

The novel and main result presented in this Letter is that major mergers can transform spiral progenitors on the region of high λ_{Re} and low concentration into realistic S0 systems of lower λ_{Re} and higher concentration, in agreement with the CALIFA observations. The bulk shift between spirals and lenticulars is significant both observationally and according to these simulations. This confirms that *major mergers are a plausible mechanism to explain this observed change, which is incompatible with simple fading.*

It might seem paradoxical that the progenitor Sa galaxy has a lower R_{90}/R_{50} concentration than the Sb galaxy, but this should not be seen as unrealistic: in the CALIFA sample, many Sa indeed show lower R_{90}/R_{50} than a great deal of Sb galaxies. Even if B/T and concentration are often invoked as a proxy for the morphological type, there is not a one-to-one relation between them (see e.g. Graham & Worley 2008).

Within the S0 merger remnants there are some outliers, especially in terms of concentration, R_{90}/R_{50} , because for these remnants the total simulated time after coalescence is short (typically $\lesssim 0.5$ Gyr after full merger). Since we consider a mass-to-light ratio (M/L) that varies according to the age and metallicity of the stellar particles in the simulation, when star formation takes place in the centre (which is very frequent in mergers, see Barnes & Hernquist 1991), we end up having an unusually high light concentration due to young stars, which reflects on the R_{90}/R_{50} parameter (see also Naab & Trujillo 2006; Hopkins et al. 2009a, on the evolution of surface density profiles for elliptical

galaxies resulting from simulated mergers). In fact, the most extreme concentration outliers ($R_{90}/R_{50} > 4.5$) correspond to the encounters involving the highest initial gas fractions ($\gtrsim 20\%$), and the highest fractions of merger-triggered star formation (new stars $\gtrsim 15\%$ of total stellar mass). The variation of M/L in simulations is often overlooked (assuming a constant value), and this is another important result: if we want to measure concentrations for wet merger remnants, the effects of young stellar populations on the light distribution cannot be ignored, as already pointed out by Jesseit et al. (2009). After an extra ~ 1 Gyr of relaxation, the central young populations will decrease their r -band luminosity by at least a factor of 2 (see Querejeta et al. 2015), and this would probably shift the points to the left and fully overlap the observational values. Additionally, it must be emphasised that most remnants have reasonable concentrations even after the short relaxation periods considered ($\sim 90\%$ with $R_{90}/R_{50} < 4$), fully compatible with the observed values for S0s.

The dependence on initial conditions is complex, but we have found a clear trend for the highest reduction in angular momentum to be associated with retrograde encounters, in agreement with Bois et al. (2011). In fact, the emergence of SRs is almost only associated with retrograde mergers (8 out of 9, see Table 1). We have observed some degree of dependence with the pericentre distance, with a preference for short pericentres in the formation of SRs, but the dependence is milder than the correlation with the spin-orbit coupling. Within the range of major mergers considered, the mass ratio 1:1 to 1:3 does not seem to affect the outcome significantly. Interestingly, the change in λ_{Re} does not show any systematic dependence on the gas content or measured SFRs. In terms of concentration, however, there is some relation with the gas content and newborn stars, as commented above: the highest concentrations are preferentially associated with the most gas-rich encounters.

4. Discussion

As we have seen, the systematic offset between spirals and S0s in the λ_{Re} -concentration plane reported by the CALIFA team can be attributed to the effect of major mergers. A number of studies have already made it clear that disc-like remnants can

emerge from mergers, even those with equal mass-ratios (Barnes 2002; Springel & Hernquist 2005; Robertson et al. 2004, 2006; Hopkins et al. 2009b; Moster et al. 2011; but see the doubts raised by Bournaud et al. 2011 about the need to include supersonic turbulence in such simulations of gas-rich mergers). In this sense, in Querejeta et al. (2015) we proved that not only can discs survive major mergers, but also that they can produce remnants with disc-bulge coupling in perfect agreement with observations of S0s (e.g. Laurikainen et al. 2010). Moreover, we have found that the discs of our S0-like remnants tend to exhibit antitruncations in agreement with those in real S0s (even reproducing their tight scaling relations, see Borlaff et al. 2014). If we combine these results with the angular momentum and concentration changes presented in this Letter, major mergers stand out as a plausible transformation mechanism to explain the origin of many S0s.

The role of mergers with other mass ratios (intermediate and minor mergers) and the combined effect of multiple mergers remains to be quantified. Based on the dry minor mergers considered by Tapia et al. (2014), and the studies by Bois et al. (2011), Moody et al. (2014) and Naab et al. (2014), we would expect intermediate and minor mergers to induce more modest changes on λ_{Re} and concentrations, but a series of mergers (which is very probable in a cosmological context) could add up and produce a net effect similar to the one that we have presented here. A major merger origin of a significant fraction of S0s would also be in agreement with the fact that higher gas fractions are expected in the early Universe, making it more likely to obtain disc-like remnants out of major mergers (keeping in mind that the gas fractions of our progenitors are representative of present-day spirals).

The fact that our results are compatible with a merger origin of S0s should not, of course, be overinterpreted. We are claiming it as a *plausible* mechanism, but not necessarily the only one, to explain the observed offset between most spirals and S0s in the λ_{Re} -concentration plane. In fact, some spirals and S0s clearly overlap (especially Sa galaxies); in these cases, simple fading cannot be ruled out. Remarkably, from their analysis of pseudobulges, Vaghmare et al. (2015) have recently pointed out that gas stripping alone is a viable process to transform early-type spirals into S0s, but not for late-type spirals, which agrees with the overlap found by CALIFA. Thus, it is not reasonable to claim that all lenticular galaxies are the by-products of mergers, but their relative relevance is probably higher in the transformation starting from late-type spirals. Additionally, the role of merging in “pre-processing” galaxies in filaments before falling into a cluster and in “post-processing” them during their infall should also be considered (see Vijayaraghavan & Ricker 2013; Head et al. 2014).

Acknowledgements. The authors would like to acknowledge the referee for a helpful report, and the GalMer team for creating such a powerful tool, with especial thanks to Paola Di Matteo for her kind support with the database. M.Q., G.v.d.V. and J.F.B. acknowledge financial support to the DAGAL network from the People Programme (Marie Curie Actions) of the European Union’s Seventh Framework Programme FP7/2007-2013/ under REA grant agreement number PITN-GA-2011-289313. Supported by the Spanish Ministry of Economy and Competitiveness (MINECO) under projects AYA2012-31277 and AYA2013-48226-C3-1-P. J.M.A. acknowledges support from the European Research Council Starting Grant (SEDMorph; P.I. V. Wild).

References

Aragón-Salamanca, A., Bedregal, A. G., & Merrifield, M. R. 2006, *A&A*, 458, 101

- Barnes, J. 1985, *MNRAS*, 215, 517
 Barnes, J. E. 2002, *MNRAS*, 333, 481
 Barnes, J. E., & Hernquist, L. E. 1991, *ApJ*, 370, L65
 Bekki, K. 2001, *ApJ*, 546, 189
 Bekki, K., & Couch, W. J. 2011, *MNRAS*, 415, 1783
 Bois, M., Emsellem, E., Bournaud, F., et al. 2011, *MNRAS*, 416, 1654
 Borlaff, A., Eliche-Moral, M. C., Rodríguez-Pérez, C., et al. 2014, *A&A*, 570, A103
 Bournaud, F., Combes, F., & Jog, C. J. 2004, *A&A*, 418, L27
 Bournaud, F., Jog, C. J., & Combes, F. 2007, *A&A*, 476, 1179
 Bournaud, F., Chapon, D., Teyssier, R., et al. 2011, *ApJ*, 730, 4
 Bruzual, G., & Charlot, S. 2003, *MNRAS*, 344, 1000
 Cappellari, M., Emsellem, E., Krajnović, D., et al. 2011a, *MNRAS*, 413, 813
 Cappellari, M., Emsellem, E., Krajnović, D., et al. 2011b, *MNRAS*, 416, 1680
 Chilingarian, I. V., Di Matteo, P., Combes, F., Melchior, A.-L., & Semelin, B. 2010, *A&A*, 518, A61
 Crowl, H. H., & Kenney, J. D. P. 2008, *AJ*, 136, 1623
 Crowl, H. H., Kenney, J. D. P., van Gorkom, J. H., & Vollmer, B. 2005, *AJ*, 130, 65
 Di Matteo, P., Jog, C. J., Lehnert, M. D., Combes, F., & Semelin, B. 2009, *A&A*, 501, L9
 Dressler, A. 1980, *ApJ*, 236, 351
 Dressler, A., Oemler, Jr., A., Couch, W. J., et al. 1997, *ApJ*, 490, 577
 Duc, P.-A., Cuillandre, J.-C., Serra, P., et al. 2011, *MNRAS*, 417, 863
 Eliche-Moral, M. C., González-García, A. C., Balcells, M., et al. 2011, *A&A*, 533, A104
 Emsellem, E., Cappellari, M., Krajnović, D., et al. 2007, *MNRAS*, 379, 401
 Emsellem, E., Cappellari, M., Krajnović, D., et al. 2011, *MNRAS*, 414, 888
 Falcón-Barroso, J., Peletier, R. F., Emsellem, E., et al. 2004, *MNRAS*, 350, 35
 Gadotti, D. A. 2009, *MNRAS*, 393, 1531
 Graham, A. W., & Worley, C. C. 2008, *MNRAS*, 388, 1708
 Head, J. T. C. G., Lucey, J. R., Hudson, M. J., & Smith, R. J. 2014, *MNRAS*, 440, 1690
 Hilz, M., Naab, T., & Ostriker, J. P. 2013, *MNRAS*, 429, 2924
 Hoffman, L., Cox, T. J., Dutta, S., & Hernquist, L. 2010, *ApJ*, 723, 818
 Hopkins, P. F., Cox, T. J., Dutta, S. N., et al. 2009a, *ApJS*, 181, 135
 Hopkins, P. F., Cox, T. J., Younger, J. D., & Hernquist, L. 2009b, *ApJ*, 691, 1168
 Jesseit, R., Cappellari, M., Naab, T., Emsellem, E., & Burkert, A. 2009, *MNRAS*, 397, 1202
 Kormendy, J., & Bender, R. 2012, *ApJS*, 198, 2
 Krajnović, D., Emsellem, E., Cappellari, M., et al. 2011, *MNRAS*, 414, 2923
 Laurikainen, E., Salo, H., Buta, R., Knapen, J. H., & Comerón, S. 2010, *MNRAS*, 405, 1089
 Maltby, D. T., Aragón-Salamanca, A., Gray, M. E., et al. 2015, *MNRAS*, 447, 1506
 Mapelli, M., Rampazzo, R., & Marino, A. 2015, *A&A*, 575, A16
 Mazzei, P., Marino, A., & Rampazzo, R. 2014a, *ApJ*, 782, 53
 Mazzei, P., Marino, A., Rampazzo, R., Galletta, G., & Bettoni, D. 2014b, *Adv. Space Res.*, 53, 950
 Moody, C. E., Romanowsky, A. J., Cox, T. J., Novak, G. S., & Primack, J. R. 2014, *MNRAS*, 444, 1475
 Moster, B. P., Macciò, A. V., Somerville, R. S., Naab, T., & Cox, T. J. 2011, *MNRAS*, 415, 3750
 Naab, T., & Burkert, A. 2003, *ApJ*, 597, 893
 Naab, T., & Trujillo, I. 2006, *MNRAS*, 369, 625 (N06)
 Naab, T., Oser, L., Emsellem, E., et al. 2014, *MNRAS*, 444, 3357
 Querejeta, M., Eliche-Moral, M. C., Tapia, T., et al. 2015, *A&A*, 573, A78
 Robertson, B., Yoshida, N., Springel, V., & Hernquist, L. 2004, *ApJ*, 606, 32
 Robertson, B., Hernquist, L., Cox, T. J., et al. 2006, *ApJ*, 641, 90
 Sánchez, S. F., Kennicutt, R. C., Gil de Paz, A., et al. 2012, *A&A*, 538, A8
 Semelin, B., & Combes, F. 2002, *A&A*, 388, 826
 Spitzer, Jr., L., & Baade, W. 1951, *ApJ*, 113, 413
 Springel, V., & Hernquist, L. 2005, *ApJ*, 622, L9
 Springel, V., Di Matteo, T., & Hernquist, L. 2005, *ApJ*, 620, L79
 Tapia, T., Eliche-Moral, M. C., Querejeta, M., et al. 2014, *A&A*, 565, A31
 Tsatsi, A., Macciò, A. V., van de Ven, G., & Moster, B. P. 2015, *ApJ*, 802, L3
 Vaghmare, K., Barway, S., Mathur, S., & Kembhavi, A. K. 2015, *MNRAS*, 450, 873
 van den Bergh, S. 1976, *ApJ*, 206, 883
 Vijayaraghavan, R., & Ricker, P. M. 2013, *MNRAS*, 435, 2713
 Weil, M. L., & Hernquist, L. 1996, *ApJ*, 460, 101
 Wilman, D. J., Oemler, Jr., A., Mulchaey, J. S., et al. 2009, *ApJ*, 692, 298
 Zinchenko, I. A., Berczik, P., Grebel, E. K., Pilyugin, L. S., & Just, A. 2015, *ApJ*, submitted [arXiv:1504.07483]

M. Querejeta et al.: Origin of S0s: Disentangling major mergers from fading

Table 1. Properties of the simulated progenitors and remnants.

No.	Model	Spin	Inclination [deg]	Pericentre [kpc]	Velocity [km s ⁻¹]	Mass ratio	Gas fraction %	ε_e	R_{90}/R_{50}	λ_{Re}
(1)	(2)	(3)	(4)	(5)	(6)	(7)	(8)	(9)	(10)	(11)
–	Original gSa	–	–	–	–	–	–	0.87	2.70	0.79
–	Original gSb	–	–	–	–	–	–	0.88	3.21	0.78
–	Original gSd	–	–	–	–	–	–	0.91	2.21	0.91
1	gE0gSao1	P	0	8	200	3:2	3	0.37	3.71	0.30
2	gE0gSao5	P	0	16	200	3:2	3	0.41	3.09	0.37
3	gE0gSao16	R	0	8	200	3:2	3	0.52	3.53	0.16
4	gE0gSao44	R	0	16	200	3:2	3	0.47	3.63	0.26
5	gE0gSbo5	P	0	16	200	3:1	4	0.35	3.09	0.24
6	gE0gSbo44	R	0	16	200	3:1	4	0.33	3.38	0.27
7	gE0gSdo5	P	0	16	200	3:1	7	0.31	3.42	0.25
8	gE0gSdo16	R	0	8	200	3:1	7	0.28	2.90	0.20
9	gE0gSdo44	R	0	16	200	3:1	7	0.28	3.64	0.25
10	gSagSao1	P	0	8	200	1:1	8	0.75	3.83	0.43
11	gSagSao5	P	0	16	200	1:1	8	0.67	4.18	0.52
12	gSagSao9	P	0	24	200	1:1	8	0.61	3.33	0.59
13	gSagSbo1	P	0	8	200	2:1	10	0.73	3.82	0.43
14	gSagSbo2	P	0	8	300	2:1	10	0.68	3.84	0.35
15	gSagSbo5	P	0	16	200	2:1	10	0.65	3.85	0.52
16	gSagSbo9	P	0	24	200	2:1	10	0.61	3.39	0.54
17	gSagSbo21	P	75	8	300	2:1	10	0.56	2.97	0.35
18	gSagSbo22	P	90	8	300	2:1	10	0.48	3.52	0.34
19	gSagSbo24	R	45	8	300	2:1	10	0.47	3.05	0.09
20	gSagSbo42	P	75	16	200	2:1	10	0.55	3.56	0.53
21	gSagSbo43	P	90	16	200	2:1	10	0.51	3.70	0.51
22	gSagSbo71	P	90	24	200	2:1	10	0.52	3.45	0.61
23	gSagSdo2	P	0	8	300	2:1	15	0.64	4.80	0.45
24	gSagSdo5	P	0	16	200	2:1	15	0.70	3.86	0.54
25	gSagSdo9	P	0	24	200	2:1	15	0.66	4.44	0.52
26	gSagSdo14	P	75	8	200	2:1	15	0.59	3.67	0.48
27	gSagSdo18	R	75	8	200	2:1	15	0.09	3.06	0.07
28	gSagSdo41	P	45	16	200	2:1	15	0.56	3.46	0.56
29	gSagSdo42	P	75	16	200	2:1	15	0.54	3.06	0.54
30	gSagSdo43	P	90	16	200	2:1	15	0.53	3.11	0.52
31	gSagSdo70	P	75	24	200	2:1	15	0.53	3.93	0.61
32	gSagSdo71	P	90	24	200	2:1	15	0.53	4.38	0.62
33	gSagSdo73	R	45	24	200	2:1	15	0.08	4.61	0.11
34	gSbgSbo9	P	0	24	200	1:1	16	0.69	3.31	0.48
35	gSbgSbo16	R	0	8	200	1:1	16	0.57	3.48	0.10
36	gSbgSbo17	R	45	8	200	1:1	16	0.27	2.81	0.27
37	gSbgSbo19	R	90	8	200	1:1	16	0.25	3.19	0.11
38	gSbgSbo22	P	90	8	300	1:1	16	0.49	3.64	0.15
39	gSbgSbo41	P	45	16	200	1:1	16	0.34	2.96	0.42
40	gSbgSbo42	P	75	16	200	1:1	16	0.41	3.80	0.46
41	gSbgSbo69	P	45	24	200	1:1	16	0.35	2.60	0.56
42	gSbgSbo70	P	75	24	200	1:1	16	0.46	3.63	0.59
43	gSbgSbo72	R	0	24	200	1:1	16	0.55	4.24	0.17
44	gSbgSdo5	P	0	16	200	1:1	23	0.66	4.88	0.50
45	gSbgSdo9	P	0	24	200	1:1	23	0.68	3.38	0.52
46	gSbgSdo14	P	75	8	200	1:1	23	0.35	3.03	0.35
47	gSbgSdo17	R	45	8	200	1:1	23	0.47	2.96	0.36
48	gSbgSdo18	R	75	8	200	1:1	23	0.26	4.14	0.25
49	gSbgSdo19	R	90	8	200	1:1	23	0.30	3.28	0.29
50	gSbgSdo23	R	0	8	300	1:1	23	0.42	3.09	0.18
51	gSbgSdo41	P	45	16	200	1:1	23	0.45	2.91	0.43
52	gSbgSdo69	P	45	24	200	1:1	23	0.42	2.77	0.47
53	gSbgSdo70	P	75	24	200	1:1	23	0.49	3.10	0.55
54	gSbgSdo71	P	90	24	200	1:1	23	0.39	3.18	0.56
55	gSdgSdo1	P	0	8	200	1:1	30	0.54	5.55	0.62

Notes. Columns: (1) ID number. (2) GalMer model code: g[type1]g[type2]o[#orbit]. (3) Spin-orbit coupling of the encounter (P, prograde; R, retrograde). (4) Initial inclination between the planes of the discs involved in the merger. (5) Pericentre distance of the initial orbit, in kpc. (6) Absolute value of the initial relative velocity, in km s⁻¹. (7) Stellar mass ratio. (8) Initial gas fraction involved in the encounter. (9) Ellipticity of the remnant (ε_e) measured in edge-on view. (10) Concentration of the remnant, R_{90}/R_{50} . (11) Angular momentum of the remnant (λ_{Re}) measured in edge-on view.

A&A 579, L2 (2015)

Table 1. continued.

No.	Model	Spin	Inclination [deg]	Pericentre [kpc]	Velocity [km s ⁻¹]	Mass ratio	Gas fraction %	ε_e	R_{90}/R_{50}	λ_{Re}
(1)	(2)	(3)	(4)	(5)	(6)	(7)	(8)	(9)	(10)	(11)
56	gSdgSdo2	P	0	8	300	1:1	30	0.67	0.54	0.32
57	gSdgSdo5	P	0	16	200	1:1	30	0.67	5.40	0.51
58	gSdgSdo9	P	0	24	200	1:1	30	0.69	3.50	0.50
59	gSdgSdo16	R	0	8	200	1:1	30	0.46	3.16	0.08
60	gSdgSdo17	R	45	8	200	1:1	30	0.36	3.03	0.45
61	gSdgSdo21	P	75	8	300	1:1	30	0.25	3.01	0.37
62	gSdgSdo42	P	75	16	200	1:1	30	0.48	4.85	0.46
63	gSdgSdo45	R	45	16	200	1:1	30	0.06	3.13	0.29
64	gSdgSdo51	R	0	16	300	1:1	30	0.06	5.06	0.18
65	gSdgSdo69	P	45	24	200	1:1	30	0.47	3.06	0.65
66	gSdgSdo71	P	90	24	200	1:1	30	0.28	2.98	0.50
67	gSdgSdo74	R	75	24	200	1:1	30	0.37	3.50	0.33

Summary and discussion

In this thesis, we have looked at two basic processes that regulate star formation in galaxies: AGN feedback and galaxy mergers. Both of them are good candidates to explain the rapid quenching of star formation, which is likely to be responsible for the observed dichotomy between actively star-forming spiral galaxies (the blue cloud) and comparatively passive early-type galaxies (the red sequence; see Chapter 1). In particular, we paid special attention to methodological limitations, and given the importance of knowing the exact stellar mass distribution in galaxies, we developed an algorithm to automatically construct stellar mass maps for more than 1500 nearby galaxies, a catalogue which we have made publicly available (Chapter 2). Along the same lines, one of the main conclusions of this thesis is the need to establish new bridges between simulations and observations, and the importance of carefully translating between numerical and empirical results.

In the introduction (Chapter 1), we listed a number of specific questions; some of them were major barriers to our understanding of the interplay between stellar structure, gas flows, and star formation in galaxies. Here, we come back to the questions raised in the introduction, and assess whether we have been able to answer them. Afterwards, we will consider new questions and challenges that our investigation has triggered, and outline possible ways to address them in the future.

7.1 Conclusions of the thesis

7.1.1 An important observational tool: stellar mass maps

- How accurately can we estimate stellar masses in nearby galaxies?
- What type of data do we need? What are our limitations and uncertainties?

Accessing the 2D stellar mass distribution in galaxies is far from trivial, but in Chapter 2 we have shown that $3.6\ \mu\text{m}$ imaging corrected for dust emission is arguably one of the best possible ways to do so (if not the best); it allows us to achieve an uncertainty in M/L_* of $\lesssim 0.1$ dex, better than currently available alternatives. We have emphasised that it is crucial to correct $3.6\ \mu\text{m}$ images of star-forming galaxies for dust emission when stellar masses are to be computed, as dust typically contributes as much as 20-30% *globally*, and it can become the dominant source of emission locally (e.g. in HII

regions). As a case study, in Chapter 3 we have confirmed and quantified the importance of the dust correction in the case of the spiral galaxy M51 for the analysis of gravitational torques and gas transport.

We have shown how a method such as ICA can be used to correct for dust contamination in nearby galaxies if we have access to two NIR bands, *Spitzer*/IRAC 3.6 and 4.5 μm . After correcting the 3.6 μm images for dust emission, this results in an accurate view of the stellar mass surface density. However, this algorithm cannot be applied blindly, and a number of requirements need to be met: 1) data at sufficiently high spatial resolution, so that ICA has a representative sample of the different physical conditions present in the galactic disc; 2) sufficiently high signal-to-noise ratio ($S/N \gtrsim 10$); 3) good masks that exclude all sources external to the galaxy; and, 4) galaxies with little dust content need to be excluded from the ICA procedure. The latter is because galaxies with little dust emission ($\lesssim 10\%$ of the 3.6 μm flux) can lead to an unphysical separation driven by noise variations when the flux due to dust per pixel is too low; these cases can be easily excluded in an automated way, as they manifest themselves empirically as blue original [3.6]-[4.5] colours. Therefore, one important conclusion is that we cannot always use ICA to correct 3.6 μm images for dust emission, and good-quality data is an imperative condition for its applicability.

One of the most important challenges that we faced is the fact that more than two physical sources of emission can contribute to the S⁴G images. For example, very hot dust in star-forming regions (e.g. HII regions), or dust close to sublimation temperatures in the immediate vicinity of AGN, have more extreme [3.6]-[4.5] colours than old stars and the extended dust component, and can thus bias the ICA solution towards a separation which is not representative of the large-scale dust emission. However, this problem can be alleviated by an iterative approach in which the first ICA solution is used to re-define the masks, and then ICA is applied a second time, converging to a meaningful separation of the two remaining components: the stellar flux and the spatially extended dust emission.

In sum, coming back to the big questions we posed in the introduction, we conclude that we can estimate stellar masses accurately down to ~ 0.1 dex, ignoring the bulk offset in M/L_* introduced by the choice of IMF (which can lead to an additional shift of ~ 0.3 dex). The main uncertainty at 3.6 μm is dust emission, but ICA can solve for this under favourable circumstances (data with sufficient spatial resolution and S/N); ICA cannot be applied if the amount of dust is small ($\lesssim 10\%$ of 3.6 μm flux), but the bias will be very limited in these cases (comparable to the uncertainty introduced by trying to correct for it). Therefore, taking the optimistic 0.06 dex uncertainty in M/L_* from Meidt et al. (2014) (if all the flux is due to old stars), and adding a representative 10% uncertainty from the ICA correction itself, we conclude that our mass estimates can be trusted down to a typical uncertainty of 0.1 dex. Even under the conservative assumption of an 0.1 dex error in M/L_* , and a less favourable scenario of 20% uncertainty associated with ICA (Appendix of Chapter 2), the resulting stellar mass would still have a final accuracy well below 0.2 dex. This is comparable to (or even slightly better than) the results that can be achieved with the most sophisticated alternative techniques (e.g. Zibetti et al. 2009), which typically require ancillary observations and are considerably more time-consuming.

Therefore, the availability of a uniform dataset in the near-infrared (S⁴G) has allowed us to improve by an order of magnitude the amount of resolved stellar mass maps of nearby galaxies, leading to

the public release of a catalogue with an important ancillary value for the astronomical community. For example, these maps have been or are currently being used for a diverse set of purposes, which include: computing specific star formation rates in galaxies (Knapen et al. 2015), estimating the baryonic contribution to rotation curves (Erroz-Ferrer et al. 2016), defining spiral perturbations in the gravitational potential (Chandar et al. in preparation), and quantifying the mid-plane pressure in galaxy discs and its impact on molecular gas turbulence (Leroy et al. in preparation).

7.1.2 AGN feeding and feedback in M51

- Is there evidence for molecular gas inflow towards the active nucleus of M51? What are the inflow rates and how accurately can we constrain them?
- How large is the impact of AGN feedback on molecular gas? How exactly is this process orchestrated?

We have used the stellar mass map of the nearby AGN host M51 (Chapter 2) to reveal the gravitational torques that are currently at play in this grand-design spiral galaxy. In conjunction with a high-resolution map of the molecular gas distribution (from PAWS) we find evidence for molecular gas inflow towards the active nucleus of M51. This secular transport of gas towards the nucleus is happening at an approximate rate of $1 M_{\odot}/\text{yr}$ down to our resolution limit of $1.7'' = 60 \text{ pc}$. Even though our radial profiles point to molecular inflow also in the innermost bin (down to $R = 0$), we cannot consider that measurement conclusive, as it is subject to increasingly large uncertainties. In any case, mechanisms such as viscous torques are expected to bring molecular gas down to the AGN on those small scales, as discussed in Chapter 3.

Additionally, we have shown that this net gas inflow clearly results from the torques exerted by the nuclear stellar bar of M51, which extends out to $R = 22'' = 800 \text{ pc}$. Simulations of galaxy mergers, like the ones that we have analysed in Chapters 5 and 6, suggest that tidal forces created by an infalling companion can reinforce the presence of a bar and drive gas inwards. Therefore, the present-day feeding of the AGN could be indirectly triggered by the merging process that M51 is undergoing.

Our analysis of the uncertainties involved emphasise how difficult it is to quantify inflow rates in galaxies. All in all, we can regard our estimates as accurate to an order of magnitude, but not much more. We have also identified the most critical aspects when computing torques and estimating gas flows, and these warnings can be useful for future studies. Linked to the discussion in the previous section (on stellar mass maps), we have shown that the dust correction applied to $3.6 \mu\text{m}$ images is essential to obtain meaningful torques. Since other methods to access the mass distribution in galaxies lead to similar (or higher) uncertainties, they will also, presumably, face similar problems when estimating torques. In conclusion, first, a proper stellar mass map is essential to obtain accurate torques (and, indirectly, gas flows). It is equally important to have a gas tracer at sufficiently high angular resolution, which restricts the targets for which gas flows can be currently computed to a handful (but this is expected to change with ALMA and NOEMA, see Sect 7.2). Extrapolating from

our study of M51 (and with the caveat that this might depend on the properties of each galaxy), we suggest that a minimum spatial resolution of $\sim 100\text{--}150$ pc in the gas tracer is necessary to obtain reliable gas flow estimates. As already demonstrated by van der Laan et al. (2011), short-spacing correction of the interferometric data is also a strong requirement to sample the full molecular gas reservoir. Finally, we have shown that a correct and accurate centring of the NIR image and the gas map are crucial (in agreement with Haan et al. 2009), which underlines the importance of carefully determining the astrometry of the images (to less than ~ 40 pc); the deprojection of the stellar mass map also plays a relevant role, but the inclination and PA of the disc can be typically inferred to a reasonable degree of accuracy from the gas observations (approximately $\pm 5^\circ$, e.g. via modelling of the velocity field). Summing up, estimating inflow rates can only be done accurately in galaxies with high-quality observational datasets; this also applies to the dynamical interpretation which can be inferred from an analysis of the torque map (e.g. presence and location of resonances).

One of the interesting questions from the ICA separation was if the thus derived dust map (s_2 component) could be used as a tracer of molecular gas, assuming that the gas-to-dust ratio is approximately constant in nearby galaxies. This would have opened new horizons, as these maps are uniformly available for our entire sample (more than 1500 galaxies), and they would have superseded the shortcoming of gas observations at sufficiently high resolution (~ 100 pc) for a large sample of galaxies. Although tempting, as this would have afforded the advantage of robust statistics, in Chapter 3 we have demonstrated that this is not a viable option: s_2 provides only a crude approximation of the ISM distribution, insufficient when it comes to the subtle task of quantifying torques and gas flows (given all the limitations discussed above). It is still true that, for other purposes, a first-order approximation of the ISM distribution could be sufficient, and the s_2 map might still prove useful as a tracer of dust for large samples of galaxies (e.g. as a substitute of *Spitzer* $8\ \mu\text{m}$ imaging at comparable resolution).

Taking one step back, now we discuss our results on AGN feeding and feedback in M51, and their implications for other galaxies. Our analysis clearly shows that AGN feedback on molecular gas is a multi-scale process, with at least three well-differentiated domains in M51: 1) very broadened molecular emission lines (~ 100 km/s) in the central ~ 100 pc, with preferentially redshifted velocities, which is probably indicative of a molecular gas outflow; 2) lack of CO emission in the area covered by ionised gas (traced through $\text{H}\alpha$ and [OIII]); and, 3) strong kinematic effects in the molecular gas extending out to ~ 500 pc, the region spanned by the radio jet. This is overall suggestive of lateral pushing of molecular gas by the radio jet, and not only radial entrainment by the jet; the fact that the dense gas tracer HCN is more strongly affected points to mechanical shocks. This result nicely connects to recent findings from other nearby radio galaxies (e.g. Morganti et al. 2015), which suggests that the behaviour observed in M51 is probably not an exception, and rather the dominant mechanism of feedback through radio jets, at least in low-luminosity AGN. It has only recently been recognised that injection of turbulence in the galactic gaseous disc could be as important as expelling gas from the host galaxy in terms of controlling star formation (Alatalo et al. 2014).

Another important conclusion which is revealed when combining the results from Chapters 3 and 4 is that the estimated molecular inflow and outflow rates are comparable in M51 ($\sim 1 M_\odot/\text{yr}$). This

is suggestive of a picture in which AGN feeding and feedback is a mutually regulated process. It can well be that, even though gas can make it to the central region (thus, providing energy to feed the nuclear engine), it is then recirculated by AGN feedback, allowing for the nuclear activity to be sustained over relatively long timescales. This can be regarded as a ‘maintenance’ feedback mode in M51, but, of course, in more active galaxies, the effects achieved through this self-regulated process could be much more spectacular.

Summing up, there seems to be sufficient molecular gas inflow in M51 to currently feed the AGN, and the feedback effects are considerable, at least in the central ~ 1 kpc. Taking into account the fact that M51 hosts a (very) low-luminosity AGN, if these effects scale with AGN power (which would not be too surprising; see García-Burillo et al. 2014), analogous feedback effects could be very significant in other galaxies. Our study suggests that, in order to better understand the physics of AGN feedback, the most promising direction is to analyse the interplay between jets and molecular gas in detail in other radio galaxies, rather than constructing large samples of gas observations at low resolution.

7.1.3 Creating lenticular galaxies with mergers

- Can major mergers of spiral galaxies simultaneously quench star formation and preserve discs?
- Do the scaling relations observed between bulges and discs of lenticular galaxies rule out (major) mergers as their possible origin?
- Can mergers explain the mismatch between spiral and lenticular galaxies in terms of specific angular momentum and light concentration?

The answer to the first question is relatively simple, but it has created a great deal of confusion due to the different lexical uses of the verb *preserve*. If by *preserve* we understand that the disc of a spiral progenitor is ‘unaffected’ by the collision, the answer is clearly *no*: in major mergers (1:1 to 1:4 mass ratios), discs are essentially destroyed by the time the full merger is achieved (or, at the very least, discs are very strongly disturbed). However, if by *preserve* we mean that, once the merging process has finished, the relaxed remnant that emerges is a disc galaxy, then the answer is *yes, sometimes*.

Indeed, the destruction of pre-existing stellar structures in major mergers can give rise to the subsequent rebirth of a disc, in which most of the material from the progenitor galaxies is combined into a single disc galaxy: it will usually have the properties observed in lenticular galaxies (relatively low star formation rates, red colours) after only 1 – 2 Gyr of post-merger relaxation. Of course, not all major mergers of spirals eventually relax into a lenticular system; depending on the initial conditions, the spheroidal component can dominate over any possible discs: in that case, the merger will have produced an elliptical galaxy. The necessary conditions for the formation of a lenticular galaxy out of a major merger of spirals are: 1) sufficiently high gas fractions; and, 2) a favourable orbital configuration, namely, sufficiently low orbital energy. The gas fractions of the simulated mergers that we have studied in Chapters 5 and 6 are representative of spiral galaxies in the local Universe; therefore, it is not imperative to have extremely high gas fractions to ‘preserve’ discs. In any case, large gas fractions

are expected for high-redshift galaxies, which would increase the probability of creating discs through major mergers (Springel & Hernquist 2005).

The tight photometric scaling relations observed between the discs and bulges of lenticular galaxies, and the presence of pseudo-bulges in their centres, have been interpreted as evidence supporting a ‘gentle’ scenario for the formation of S0s: ram pressure stripping (or strangulation), and secular evolution. This conclusion seems reasonable, especially taking into account the very intuitive (and partially true) idea that mergers destroy any pre-existing stellar structures. However, we have shown that discs can sometimes be rebuilt after major mergers, so the question that immediately arises is: would those discs obey the scaling relations of real S0s? This seemed unlikely *a priori*, and the possibility of finding flattened pseudo-bulges in their centres appeared even more improbable; pseudo-bulges are thought to grow through slow, secular processes, as opposed to classical (spheroidal) bulges, which are expected to be built-up by mergers (Kormendy & Kennicutt 2004). Against all expectations, we have demonstrated that: 1) the lenticular-looking galaxies that emerge from our simulations of major mergers obey those photometric scaling relations (as tightly as observed lenticulars); and, 2) we find plenty of flat ($n \sim 1$) pseudo-bulges in those remnants, in agreement with observations.

The answer to the last question that we posed in the introduction is clearly *yes*: major mergers can explain the simultaneous change in specific angular momentum (λ_{Re}) and light concentration that the CALIFA team have measured to be significant between (late-type) spirals and lenticular galaxies. Even though some of our remnants are too concentrated compared to real S0s, we have shown that this is due to residual star formation in their centres, which will fade in 1 – 2 Gyr of additional secular evolution. Therefore, assuming that these mergers happened before $z \sim 0.3$ (~ 3.5 Gyr ago), observationally we would find the remnants in full agreement with local lenticulars. We have also emphasised how important it is to properly translate simulations into the parameter space of observers; in particular, it is essential to use an M/L which reflects the age and metallicity of each stellar particle in the simulation in order to convert the stellar mass distribution into luminosity and measure parameters such as light concentration (interestingly, the inverse problem of what we did in Chapter 2).

Of course, these results should not be over-interpreted, as we do not claim that most lenticulars have been created through *major* mergers; this is something that appears unlikely from simple arguments based on merger rates (e.g. Rodriguez-Gomez et al. 2015). Nevertheless, our results do imply that: 1) photometric scaling relations and the presence of pseudo-bulges cannot be used as an argument to rule out mergers as mechanisms to create lenticular galaxies out of spirals; 2) mergers can explain an observational result (simultaneous change of angular momentum and concentration) which other mechanisms have not yet been able to explain. Therefore, mergers could have played a major role in transforming spiral galaxies into S0s, and their exact relevance for the buildup of this population of galaxies remains to be quantified.

7.1.4 Towards an integral picture of star formation suppression in galaxies

As we explained in the introduction, star formation modulates the exchange of matter and energy between the various components of a galaxy: the stars and the different phases of the ISM. The lack of gas, or external factors which modify the ability of the gas to form stars, can therefore largely constrain the evolution and fate of a given galaxy. The sudden suppression of star formation, known as quenching, is thought to trigger a number of morphological transformations.

The main conclusion from our work is that both *internal* processes (gas transport and AGN feedback) and *external* mechanisms (mergers) have the potential to control star formation in galaxies. Many of these processes are interdependent: our results suggest an intimate connection between gas inflow and AGN feedback; nuclear activity is indirectly controlled by the transport of gas to the centre of the galaxy, and, at the same time, the feedback from the nucleus regulates the amount of gas that can reach the AGN. These mutually regulated processes might be crucial to explain why we still see spiral galaxies in the local Universe, and why many of them host Seyfert nuclei.

In a cosmological context, the balance between external gas accretion (through intergalactic filaments) and any potential outflows (with a substantial amount of gas above escape velocity) will determine the total budget of gas that is available in the galaxy as a function of time. At the same time, at galaxy scales, dynamical mechanisms such as gravitational torques will constrain the mobility of the gas across the disc of the galaxy; torques can arise from the stellar structure of the galaxy, or they can be tidally induced by a companion (e.g. in the case of a merger or galaxy harassment). Also at galaxy scales, AGN feedback, indirectly controlled by the transport of gas to the centre, can drive outflows and result in shocks and injection of turbulence in the gaseous disc; this has the ability to change the phase balance of the ISM and eventually decrease the fraction of gas which can be converted into stars. The combination of all these mechanisms can lead to the rapid suppression of star formation (for example, through the cascade of effects involved in the major merging process), or it can exert a more gradual and gentle control on star formation, such as the AGN feedback effects we find in M51. Presumably, more powerful AGN, characteristic of high-redshift galaxies, could undergo a scaled version of these effects, which could rapidly quench star formation.

As we will see next, our results are especially relevant in the context of the upcoming ALMA and NOEMA era. The distribution and kinematics of molecular gas will be mapped with unprecedented detail in galaxies, both near and far, with access to different phases of molecular gas traced by a myriad of molecular lines. This thesis can be regarded as a preparatory study for what ALMA and NOEMA will provide, including some important tools (catalogue of stellar mass maps, which we have publicly released), and methodological issues (e.g. limitations and uncertainties in the estimations of gas inflow and outflows). We advance towards a picture in which all these effects can be integrated, and their relative importance, quantified. The most exciting avenues to explore include establishing the details of AGN feeding and feedback in other galaxies to confirm that M51 is not a special case; this will likely require high-resolution studies. Similarly interesting open questions remain in the quest to understand the origin of lenticular galaxies and the transformation from late- to early-type galaxies in general; these will also benefit from the new instrumental capabilities. Pursuing these

goals will require advancements both from the observations and simulations perspective, hopefully in permanent contact and providing reciprocal feedback. Next, we will describe a number of specific experiments which might contribute to clarify some of these open questions.

7.2 Open questions and future perspectives

From the previous section it is clear that the work presented in this thesis has found answers to some important issues, but it has also triggered a new set of questions. For example:

- Given the advantages of the $3.6\mu\text{m}$ band to map the stellar mass distribution in galaxies, and the effectiveness of our ICA technique to correct for dust emission, can our catalogue of stellar mass maps be extended to (many) more galaxies?
- Provided that the use of an accurate stellar mass map is critical to estimate gravitational torques and gas flows, would the results on gas flows obtained so far change if higher-quality data had been available?
- Are the AGN feedback characteristics of M51 universal and scalable?
- Can mergers of intermediate to low mass ratios, or the accumulation of multiple minor mergers, explain the photometric and kinematic constraints from observations of lenticular galaxies?

The importance of stellar mass and the large uncertainties involved in its observational determination have been stressed a number of times in this thesis. Now, thanks to our public data release¹, future studies will benefit from a comprehensive and consistent sample of stellar mass maps for more than 1500 nearby galaxies. While the *Spitzer* Space Telescope is still operative under the so-called *warm mission*, a survey of deep observations for a large sample of nearby galaxies, comparable to S⁴G, is not planned (to our knowledge). However, in the mid-term future, *James Webb* Space Telescope (JWST) will open up exciting new possibilities in this direction; the 6.5 m space telescope (to be launched in 2018) is expected to deliver near-infrared observations at a resolution of $0.1''$ (more than $15\times$ better than *Spitzer*, and comparable to the resolution from *Hubble* Space Telescope in the optical). The Near Infrared Camera (NIRCam) will operate in the spectral range 0.6 to $5\mu\text{m}$, covering the wavelengths that we have suggested are best to map stellar mass distributions, and which allow for the application of dust corrections with a method like ICA. Meanwhile, and for sources that lack resolved imaging at sufficient quality, the empirical calibration that we have provided between NIR colours ($[3.6]-[4.5]$) and M/L_* will prove helpful in constraining stellar masses.

Resolved maps of stellar mass surface density will become especially important in the upcoming ALMA/NOEMA era. High-quality datasets of molecular gas emission from galactic discs will be delivered by these world-class interferometers for an increasing number of local galaxies, and quantifying the transport of gas will require an accurate knowledge of the stellar mass distribution (any

¹<http://irsa.ipac.caltech.edu/data/SPITZER/S4G>

calculations of spatially resolved specific star formation rates will also rely on a good determination of how stellar mass distributes). For example, the combination of our high-quality stellar mass maps with these new maps of molecular gas will permit to discern whether the apparently inconsistent results between gas transport and AGN activity are real or not, once the uncertainties examined in Chapter 3 are overcome. These future studies might allow us to access valuable statistics which could help clarifying the timescales at which the transport of gas varies, and connect it to the variability timescales of AGN duty cycles.

The maps of molecular gas emission and kinematics from ALMA and NOEMA will undoubtedly cast new light on the important process of AGN feedback through radio jets, for which we have made a number of suggestions based on our case study of M51. Specifically, we have argued that it is important to consider the impact of AGN on molecular gas at relatively large distances from the centre, at the interface between the radio plasma jets and the molecular disc, with sufficiently high spatial and spectral resolution; this remark should be taken into account when designing new observations. If confirmed in other nearby galaxies, this mode of AGN feedback through radio jets should be incorporated into numerical simulations of galaxy evolution.

Finally, ALMA also opens up a new window to explore the evolution of galaxies across cosmic time, their transformation from LTGs to ETGs, and the puzzling origin of lenticular galaxies. Deep observations of the molecular gas distribution and kinematics in early-type galaxies could reveal signatures of recent merging (or rule out that possibility); in a similar vein, very deep optical observations are starting to uncover an increasing number of faint structures in the outskirts of ETGs (Duc et al. 2015). A comparison with simulations of mergers could be extremely enlightening in this sense: numerical simulations can help to constrain how long after full merger will certain types of signatures be observed down to a given observational magnitude limit (e.g. tidal tails). Therefore, careful comparison of simulations of galaxy mergers with observations of gas, dust, and stellar structure in ETGs are important, as it could conclusively demonstrate what fraction of present-day lenticular and elliptical galaxies have a merger origin, and discriminate between formation mechanisms.

Moreover, the ATLAS^{3D} team have shown that a kinematic classification of galaxies might be physically more meaningful than traditional morphological schemes; in particular, in terms of their rotational support, disc-dominated lenticulars form an indistinguishable continuum with some elliptical galaxies. Therefore, our investigation could be extended to the rotational component of ETGs in general, and try to address how the disc that dominates morphologically in lenticulars can be extrapolated to the fastest-rotating elliptical galaxies, and what this can reveal about their formation channels.

Provided that minor mergers are much more frequent than major mergers in the Universe (e.g. Rodriguez-Gomez et al. 2015), it would be compelling to test whether intermediate and minor mergers, or a sequence of minor mergers, could also explain the change from spiral to lenticular galaxies. Such simulations of minor, intermediate, and sequential mergers currently exist, and we plan to analyse them in the near future.

Summing up, the main lesson learned from this thesis could well be that it is important to be aware of the uncertainties and limitations intrinsic to a certain method, and that it can be extremely fruitful

to explore synergies between observations and numerical simulations. We live in exciting times for the study of galaxy evolution, with ALMA and NOEMA eventually reaching their full power; in that sense, this thesis has presented some results which can be easily built upon in the near future, and which are useful in guiding the exploitation of the datasets that these new instruments are just starting to deliver.

Bibliography

- Abbott, B. P., Abbott, R., Abbott, T. D., et al. 2016, *Physical Review Letters*, 116, 061102
- Alam, S., Albareti, F. D., Allende Prieto, C., et al. 2015, *ApJS*, 219, 12
- Alatalo, K., Nyland, K., Graves, G., et al. 2014, *ApJ*, 780, 186
- Andreon, S. 1998, *ApJ*, 501, 533
- Antonucci, R. 1993, *ARAA*, 31, 473
- Aragón-Salamanca, A., Bedregal, A. G., & Merrifield, M. R. 2006, *A&A*, 458, 101
- Athanassoula, E. 2013, *Bars and secular evolution in disk galaxies: Theoretical input*, ed. J. Falcón-Barroso & J. H. Knapen, 305
- Baldry, I. K., Glazebrook, K., Brinkmann, J., et al. 2004, *ApJ*, 600, 681
- Bedregal, A. G., Aragón-Salamanca, A., & Merrifield, M. R. 2006, *MNRAS*, 373, 1125
- Bekki, K. 1998, *ApJL*, 502, L133
- Bekki, K., Couch, W. J., & Shioya, Y. 2002, *ApJ*, 577, 651
- Bell, E. F. & de Jong, R. S. 2001, *ApJ*, 550, 212
- Bennett, C. L., Banday, A. J., Gorski, K. M., et al. 1996, *ApJL*, 464, L1
- Bialas, D., Lisker, T., Olczak, C., Spurzem, R., & Kotulla, R. 2015, *A&A*, 576, A103
- Bigiel, F., Leroy, A., Walter, F., et al. 2008, *AJ*, 136, 2846
- Blandford, R. D. & Znajek, R. L. 1977, *MNRAS*, 179, 433

- Bolatto, A. D., Leroy, A. K., Rosolowsky, E., Walter, F., & Blitz, L. 2008, *ApJ*, 686, 948
- Bosma, A. 1978, PhD thesis, PhD Thesis, Groningen Univ., (1978)
- Bournaud, F., Jog, C. J., & Combes, F. 2007, *A&A*, 476, 1179
- Brinchmann, J., Charlot, S., White, S. D. M., et al. 2004, *MNRAS*, 351, 1151
- Bruzual, G. & Charlot, S. 2003, *MNRAS*, 344, 1000
- Burstein, D., Ho, L. C., Huchra, J. P., & Macri, L. M. 2005, *ApJ*, 621, 246
- Cappellari, M., Emsellem, E., Krajnović, D., et al. 2011a, *MNRAS*, 413, 813
- Cappellari, M., Emsellem, E., Krajnović, D., et al. 2011b, *MNRAS*, 416, 1680
- Chabrier, G. 2003, *PASP*, 115, 763
- Cicone, C., Feruglio, C., Maiolino, R., et al. 2012, *A&A*, 543, A99
- Cielo, S., Antonuccio-Delogu, V., Macciò, A. V., Romeo, A. D., & Silk, J. 2014, *MNRAS*, 439, 2903
- Colombo, D., Hughes, A., Schinnerer, E., et al. 2014, *ApJ*, 784, 3
- Courteau, S., Cappellari, M., de Jong, R. S., et al. 2014, *Reviews of Modern Physics*, 86, 47
- Crane, P. C. & van der Hulst, J. M. 1992, *AJ*, 103, 1146
- Croton, D. J., Springel, V., White, S. D. M., et al. 2006, *MNRAS*, 365, 11
- Daddi, E., Cimatti, A., Renzini, A., et al. 2004, *ApJ*, 617, 746
- de Vaucouleurs, G., de Vaucouleurs, A., Corwin, Jr., H. G., et al. 1991, *Third Reference Catalogue of Bright Galaxies, Vol. Volume 1-3, XII, 2069* (Springer-Verlag Berlin Heidelberg New York), 7
- Dressler, A. 1980, *ApJ*, 236, 351
- Dressler, A., Oemler, Jr., A., Couch, W. J., et al. 1997, *ApJ*, 490, 577
- Duc, P.-A., Cuillandre, J.-C., Karabal, E., et al. 2015, *MNRAS*, 446, 120
- Elbaz, D., Daddi, E., Le Borgne, D., et al. 2007, *A&A*, 468, 33
- Eliche-Moral, M. C., González-García, A. C., Aguerri, J. A. L., et al. 2012, *A&A*, 547, A48
- Elmegreen, D. M. & Elmegreen, B. G. 1984, *ApJS*, 54, 127
- Erroz-Ferrer, S., Knapen, J. H., Leaman, R., et al. 2016, *MNRAS*
- Faber, S. M., Willmer, C. N. A., Wolf, C., et al. 2007, *ApJ*, 665, 265 (F07)
- Fabian, A. C. 2012, *ARAA*, 50, 455

- Falcón-Barroso, J., Lyubenova, M., & van de Ven, G. 2015, in IAU Symposium, Vol. 311, IAU Symposium, ed. M. Cappellari & S. Courteau, 78–81
- Famaey, B. & McGaugh, S. S. 2012, *Living Reviews in Relativity*, 15
- Fanaroff, B. L. & Riley, J. M. 1974, *MNRAS*, 167, 31P
- Fendt, C. & Sheikhnezami, S. 2013, *ApJ*, 774, 12
- Ferrarese, L. & Ford, H. 2005, *Space Science Reviews*, 116, 523
- Ferrarese, L. & Merritt, D. 2000, *ApJL*, 539, L9
- Gao, Y. & Solomon, P. M. 2004, *ApJ*, 606, 271
- García-Burillo, S., Combes, F., Usero, A., et al. 2014, *A&A*, 567, A125
- García-Burillo, S., Combes, F., Usero, A., & Graciá-Carpio, J. 2007, *New Astronomy Reviews*, 51, 160
- Genzel, R., Tacconi, L. J., Lutz, D., et al. 2015, *ApJ*, 800, 20
- Gonçalves, T. S., Martin, D. C., Menéndez-Delmestre, K., Wyder, T. K., & Koekemoer, A. 2012, *ApJ*, 759, 67
- Gültekin, K., Richstone, D. O., Gebhardt, K., et al. 2009, *ApJ*, 698, 198
- Gunn, J. E. & Gott, III, J. R. 1972, *ApJ*, 176, 1
- Haan, S., Schinnerer, E., Emsellem, E., et al. 2009, *ApJ*, 692, 1623
- Häring, N. & Rix, H.-W. 2004, *ApJL*, 604, L89
- Heckman, T. M. 1980, *A&A*, 87, 152
- Hopkins, P. F., Cox, T. J., Younger, J. D., & Hernquist, L. 2009, *ApJ*, 691, 1168
- Hoyle, F. & Fowler, W. A. 1963, *Nature*, 197, 533
- Hubble, E. 1929, *Proceedings of the National Academy of Science*, 15, 168
- Hubble, E. P. 1936, *Realm of the Nebulae* (New Haven: Yale University Press, 1936. ISBN 9780300025002)
- Hughes, A., Meidt, S. E., Colombo, D., et al. 2013a, *ApJ*, 779, 46
- Hughes, A., Meidt, S. E., Schinnerer, E., et al. 2013b, *ApJ*, 779, 44
- Illingworth, G. D., Magee, D., Oesch, P. A., et al. 2013, *ApJS*, 209, 6
- Kennicutt, Jr., R. C. 1998, *ApJ*, 498, 541

- Knapen, J. H., Cisternas, M., & Querejeta, M. 2015, *MNRAS*, 454, 1742
- Kormendy, J. & Bender, R. 2012, *ApJS*, 198, 2
- Kormendy, J. & Kennicutt, Jr., R. C. 2004, *ARAA*, 42, 603
- Krajnović, D., Emsellem, E., Cappellari, M., et al. 2011, *MNRAS*, 414, 2923
- Kroupa, P. 2001, *MNRAS*, 322, 231
- Larson, R. B., Tinsley, B. M., & Caldwell, C. N. 1980, *ApJ*, 237, 692
- Laurikainen, E., Salo, H., Buta, R., Knapen, J. H., & Comerón, S. 2010, *MNRAS*, 405, 1089
- Lemaître, G. 1927, *Annales de la Société Scientifique de Bruxelles*, 47, 49
- Lintott, C. J., Schawinski, K., Slosar, A., et al. 2008, *MNRAS*, 389, 1179
- Liu, L., Gao, Y., & Greve, T. R. 2015, *ApJ*, 805, 31
- Maraston, C. 2005, *MNRAS*, 362, 799
- Masters, K. L., Mosleh, M., Romer, A. K., et al. 2010, *MNRAS*, 405, 783
- Meidt, S. E., Schinnerer, E., García-Burillo, S., et al. 2013, *ApJ*, 779, 45
- Meidt, S. E., Schinnerer, E., van de Ven, G., et al. 2014, *ApJ*, 788, 144
- Milgrom, M. 1983, *ApJ*, 270, 365
- Moore, B., Katz, N., Lake, G., Dressler, A., & Oemler, A. 1996, *Nature*, 379, 613
- Morganti, R., Oosterloo, T., Oonk, J. B. R., Frieswijk, W., & Tadhunter, C. 2015, *A&A*, 580, A1
- Moster, B. P., Somerville, R. S., Maulbetsch, C., et al. 2010, *ApJ*, 710, 903
- Moustakas, J., Coil, A. L., Aird, J., et al. 2013, *ApJ*, 767, 50
- Noeske, K. G., Weiner, B. J., Faber, S. M., et al. 2007, *ApJL*, 660, L43
- Norris, M. A., Meidt, S., Van de Ven, G., et al. 2014, *ApJ*, 797, 55
- Osterbrock, D. E. & Ferland, G. J. 2006, *Astrophysics of gaseous nebulae and active galactic nuclei*
- Penzias, A. A. & Wilson, R. W. 1965, *ApJ*, 142, 419
- Popping, G., Behroozi, P. S., & Peebles, M. S. 2015, *MNRAS*, 449, 477
- Querejeta, M., Eliche-Moral, M. C., Tapia, T., et al. 2015a, *A&A*, 573, A78
- Querejeta, M., Eliche-Moral, M. C., Tapia, T., et al. 2015b, *A&A*, 579, L2
- Querejeta, M., Meidt, S. E., Schinnerer, E., et al. 2015c, *ApJS*, 219, 5

- Querejeta, M., Meidt, S. E., Schinnerer, E., et al. 2016, *A&A*, 588, A33
- Rees, M. J. 1977, *Quarterly Journal of the Royal Astronomical Society*, 18, 429
- Rix, H.-W. & Zaritsky, D. 1995, *ApJ*, 447, 82
- Robertson, B., Yoshida, N., Springel, V., & Hernquist, L. 2004, *ApJ*, 606, 32
- Robson, I. 1996, *Active galactic nuclei*
- Rodriguez-Gomez, V., Genel, S., Vogelsberger, M., et al. 2015, *MNRAS*, 449, 49
- Rubin, V. C. & Ford, Jr., W. K. 1970, *ApJ*, 159, 379
- Salpeter, E. E. 1955, *ApJ*, 121, 161
- Schawinski, K., Lintott, C., Thomas, D., et al. 2009, *MNRAS*, 396, 818
- Schawinski, K., Urry, C. M., Simmons, B. D., et al. 2014, *MNRAS*, 440, 889
- Schmidt, M. 1959, *ApJ*, 129, 243
- Schmidt, M. 1963, *Nature*, 197, 1040
- Schweizer, F., Seitzer, P., Faber, S. M., et al. 1990, *ApJL*, 364, L33
- Seyfert, C. K. 1943, *ApJ*, 97, 28
- Solomon, P. M., Rivolo, A. R., Barrett, J., & Yahil, A. 1987, *ApJ*, 319, 730
- Speagle, J. S., Steinhardt, C. L., Capak, P. L., & Silverman, J. D. 2014, *ApJS*, 214, 15
- Spitzer, Jr., L. & Baade, W. 1951, *ApJ*, 113, 413
- Springel, V. 2010, *ARAA*, 48, 391
- Springel, V. & Hernquist, L. 2005, *ApJL*, 622, L9
- Springel, V., White, S. D. M., Jenkins, A., et al. 2005, *Nature*, 435, 629
- Stein, W. A., Odell, S. L., & Strittmatter, P. A. 1976, *ARAA*, 14, 173
- Toomre, A. 1977, in *Evolution of Galaxies and Stellar Populations*, ed. B. M. Tinsley & R. B. Larson, 401
- Urry, C. M. & Padovani, P. 1995, *PASP*, 107, 803
- van den Bergh, S. 1976, *ApJ*, 206, 883
- van der Laan, T. P. R., Schinnerer, E., Boone, F., et al. 2011, *A&A*, 529, A45
- van der Wel, A., Rix, H.-W., Wuyts, S., et al. 2011, *ApJ*, 730, 38

- Vijayaraghavan, R. & Ricker, P. M. 2013, *MNRAS*, 435, 2713
- Vogelsberger, M., Genel, S., Springel, V., et al. 2014, *MNRAS*, 444, 1518
- Wagner, A. Y., Bicknell, G. V., & Umemura, M. 2012, *ApJ*, 757, 136
- Wuyts, S., Förster Schreiber, N. M., van der Wel, A., et al. 2011, *ApJ*, 742, 96
- Young, L. M., Bureau, M., Davis, T. A., et al. 2011, *MNRAS*, 414, 940
- Zibetti, S., Charlot, S., & Rix, H.-W. 2009, *MNRAS*, 400, 1181
- Zwicky, F. 1933, *Helvetica Physica Acta*, 6, 110

Acknowledgements

I would like to use this space to thank the many people who have assisted me through the journey of my PhD. The starting point is my main supervisor, Eva Schinnerer, and Sharon Meidt, for brilliant scientific advice, and for being so supportive and available. They have always found the right way to offer me the most interesting challenges, and also to keep a good eye on me so that I would stay focused and not feel overwhelmed. A gigantic thank you once again for your help and support these years, and for guiding me through this wonderful adventure.

It goes without saying that I would like to warmly thank the rest of my fantastic colleagues at MPIA: this is a great place to work, and that is mostly due to the welcoming atmosphere that you all have contributed to creating and maintaining. It has been fantastic to share so much scientific discussion (and also non-scientific activities) with many of you these years; I would like to avoid listing specific names, as I am too afraid of forgetting someone! One of the best things about my stay in Heidelberg is clearly the amazing people that I have got to know through astronomy. I hope that we can keep in touch in the future.

I would also like to have some words of appreciation for the collaborators who are abroad. It is a pleasure to thank Santiago García-Burillo and Jérôme Pety for their help and patience while I learned interferometry, and to the whole PAWS team for great scientific feedback. Connected to the work that I started in Madrid as a Bachelor student, which I have continued as part of my PhD, I would like to send my warmest thanks to Carmen Eliche-Moral, who guided me through light and darkness, and always constituted a motivating supervisor and collaborator. I also feel indebted to the rest of my lecturers and colleagues at Universidad Complutense de Madrid, and at the University of Nottingham, for fostering my passion for astronomy and confirming that I wanted to make it an important part of my life.

A number of specific acknowledgements are due at MPIA. First and foremost, I would like to thank Christian Fendt for his monumental efforts in successfully coordinating the IMPRS programme, and

for taking such good care of all of us, making us feel welcome in Heidelberg since the first day. In this direction, Heide Seifert also contributed a great deal, with extensive support in the challenging task of flat-hunting in Heidelberg. I would also like to have some thankful words for the extremely helpful IT department at MPIA (especially to Uli Hiller and Björn Binroth).

I would also like to thank Hans-Walter Rix and Simon Glover for their kind acceptance to review this thesis, and I would like to make my gratitude extensive to the other two members of the PhD examination committee (Eva Grebel, Karl-Heinz Meier), and to the third member of my IMPRS thesis committee (Ralf Klessen).

The work presented in this thesis has been possible with generous funding from the European Union, channelled through the DAGAL initial training network. In addition to funding, DAGAL has provided a great scientific framework to develop my PhD (and also some good friends!); I would like to thank the whole “DAGAL family”, with a special mention to its scientific coordinator, Johan Knapen, and my member and mentor, Marc Verheijen and Glenn van de Ven, to whom I owe very much.

I would like to close these acknowledgements by reiterating how grateful I am to my parents, and by making it extensive to my whole family and friends. As a final celebration of friendship, in the last words of this thesis, I would like to echo the closing remarks from the wonderful *Cantar de mio Cid*, one of the oldest and most admirable literary works in Spanish language:

E el romanz es leído,
datnos del vino;
Si non tenedes dineros,
echad allá unos peños,
que bien nos los darán sobr'ellos.²

²*Cantar de mio Cid* (Spanish medieval epic poem, anonymous), vv. 3733-3735, Edition: A. Montaner (Galaxia Gutenberg, 2007).